NICOLAUS COPERNICUS ASTRONOMICAL CENTER
POLISH ACADEMY OF SCIENCE

DOCTORAL THESIS

Extra Galactic Globular Cluster machinery based on MOCCA code for Star Cluster simulations

---

Author:
Agostino LEVEQUE

Supervisor:
Prof. Mirosław GIERSZ

A thesis submitted in fulfillment of the requirements for the degree of Doctor of Philosophy

in

Astronomy

February 12, 2023

Contents

Abstract

In this thesis, I present the machinery that has been developed to reproduce globular cluster (GC) populations around galaxies. The machinery combines the semi-analytical MASinGA code with the results from the MOCCA-Survey I Database. The ability to model both the large scale dynamics (0.01–10 kpc) controlling their orbital evolution and the small scale dynamics (sub–pc–AU) controlling the internal dynamics of each GC is necessary for a thorough study of the co-evolution of GC systems in galaxies.

In a preliminary work, we have shown that MOCCA models can be used to identify GCs' properties that could be used to identify the dynamic state of a GC also in extra-galactic GC populations. To achieve this, a sub-sample of the MOCCA-Survey Database I was selected in order to mimic the observational limits of extra-galactic GCs. The sub-sample has also been compared with the observations of Milky Way GCs, finding good agreement with previous studies for the considered properties.

The second paper presented in this thesis introduces our machinery for the first time and presents its main features along with that of the MASinGa code. We compared the distributions of global properties of our simulated GC populations with those observed in both the Milky Way and Andromeda galaxies. We found that our models can recover the spatial and mass distributions of GCs in both galaxies, together with the half-light radius distribution. Also, we compared the total mass of the nuclear star cluster (NSC) and super-massive black hole (SMBH) found in our simulations with the observed values, with the masses reported in our simulations being about two orders of magnitude smaller compared to the observations.

In the third paper, we investigated the BH populations in Milky Way and Andromeda - like galaxies. The number, mass, and half-light radius distributions of GCs in different dynamical states (that is, the presence of an intermediate-massive BH, a BH subsystem, or neither) have been studied. We also show that the nature of the dynamical formation of BH binaries would be imprinted onto the orbital properties of the binaries. Depending on the adopted assumptions, the merger rate of BH-BH binaries found in our simulations in the local Universe is $1.0 - 23$ $\mathrm{yr}^{-1}\,\mathrm{Gpc}^{-3}$. The orbital parameter distributions for the BH-BH binaries that would survive until the present-day have been investigated. Finally, we found that the dynamics in GCs can considerably enhance the efficiency of BH binary formation, being nearly twice as efficient compared to isolated stellar/binary evolution in the Galactic field.

In another paper presented in this thesis, the study of the embedded gas phase in the evolution of GCs has been carried out in the framework of the Monte Carlo method. In this study, the survival of GCs after the removal of primordial gas s been followed. The results have been compared to N-body simulations, finding good agreement for the Lagrangian radii and mass evolution. Our study outlines the range of initial conditions that can cause clusters to dissolve as well as those that can help them survive this early stage of their evolution. Initially, it was expected to use the prescription introduced in this work to create MOCCA-Survey Database II. However, due to issues with the integration of the most recent upgrades to the MOCCA code, the development of the MOCCA-Survey Database II was strongly

delayed. Nonetheless, this work involved the development of an important feature in the MOCCA code.

I also briefly discuss works that have been submitted and are in progress which deal with the updates to the MOCCA code related to the upgrades of the stellar/binary evolution in the BSE code and the introduction of the possibility to follow the evolution of multiple stellar populations and the first application of the machinery introduced in this thesis to other projects. These updates introduced in these works (including the prescription presented in the forth paper) were intended to be used to create a new MOCCA-Survey Database. This was initially planned to be used to populate GCs in external galaxies in the local Universe. Also, a mass growth prescription for the NSC and SMBH has been applied to the results presented in the second paper for the Milky Way and Andromeda galaxies. Our results show that in order to explain the observed masses in the studied galaxies, an *in-situ* accretion has to be considered in the mass-growth evolution of the NSC and SMBH. The SMBH would accrete the pristine gas in the central region of the galaxy, and trigger star formation events that would contribute to the NSC mass too.

Streszczenie

W pracy przedstawiliśmy środowisko programistyczne, które zostało opracowane do odtwarzania populacji gromad kulistych (GC) wokół galaktyk. Środowisko to łączy w sobie półanalityczny kod MASinGa z wynikami symulacji ewolucji gromad gwiazdowych zawartych w bazie danych MOCCA-Survey Database I. Modelowanie zarówno dynamiki w dużych (0,01–10 kpc) i małych (AU-pc) skalach przestrzennych kontrolujących odpowiednio ewolucję orbit gromad i ich wewnętrzną dynamikę jest niezbędne do śledzenia koewolucji systemów GC w galaktykach.

W pierwszej pracy wykazaliśmy, że modele MOCCA mogą być używane do identyfikacji właściwości GC, które z kolei mogą być wykorzystane do określenia ich typu ewolucji, również w innych galaktykach. W tym celu wybrano modele z MOCCA-Survey Database I, tak aby naśladowały one parametry obserwacyjne pozagalaktycznych populacji GC. Tak wybrane modele zostały także porównane z obserwacjami GC Drogi Mlecznej, wykazując dobrą zgodność z ich obserwacyjnymi właściwościami.

W drugiej pracy zaprezentowaliśmy szczegółowy opis środowiska programistycznego oraz kodu MASinGA wraz z jego zastosowaniami dla Drogi Mlecznej i galaktyki Andromeda. Pokazaliśmy, że modele GC z MOCCA-Survey I Database mogą odtworzyć rozkład przestrzenny, mas i promieni charakterystycznych GC w obu galaktykach. Porównaliśmy również całkowite masy centralnej gromady gwiazd (NSC) i supermasywnych czarnych dziur (SMBH) uzyskane w naszych symulacjach z obserwowanymi wartościami. Masy tych obiektów otrzymane w symulacjach były o około dwa rzędy wielkości mniejsze niż wartości obserwacje, co sugeruje że za budowę NSC i SMBH musi być także odpowiedzialna akrecji gazu galaktycznego, a nie tylko GC.

W trzeciej pracy zbadaliśmy populację BH w Drodze Mlecznej i galaktykach podobne do galaktyki Andromedy. Przeanalizowaliśmy liczbę, rozkłady masy i promienia charakterystycznego GC w różnych stanach dynamicznej ewolucji – obecności średniomasywnej BH, podsystemu BH, lub żadnego z nich. Wykazaliśmy również, że procesy fizyczne związane z powstawaniem układów podwójnych BH w oddziaływaniach dynamicznych pozastawiają wyraźną sygnaturę w ich właściwościach orbitalnych. W zależności od przyjętych założeń, tempo fuzji BH w układach podwójnych, w lokalnym Wszechświecie, wyznaczone z symulacji wynosi 1 - 23 rok-1 Gpc-3. Wykazaliśmy także, że oddziaływania dynamiczne w GC mogą znacznie zwiększyć wydajność powstawania układów podwójnych BH, która jest około dwa razy większa w porównaniu do izolowanej ewolucji układów podwójnych w polu galaktycznym.

W czwartej pracy zbadaliśmy efektywność odrzutu pierwotnego gazu pozostałego po uformowaniu się GC na ich dalszą ewolucję i przetrwanie. W tym celu został napisana specjalna wersja kodu MOCCA (MOCCA-C), wersja z ewolucja gwiazd pojedynczych oraz bez dynamicznych oddziaływań trój- i cztero-ciałowych. Wyniki symulacji nowym kodem porównano z symulacjami wykonanymi kodem N-ciałowym, uzyskując dobrą zgodność ewolucji promieni Lagrange'a i masy gromad. Uzyskane wyniki pozwoliły określić zakres warunków początkowych, które mogą prowadzić

do rozerwania gromad, lub przetrwania etapu ewolucji związanego z odrzutem pozostałości pierwotnego gazu. Kod MOCCA-C był rozwijany w celu użycia jego wraz z innymi elementami, związanymi z szeroką rozbudową kodu MOCCA, do budowy nowej bazy danych MOCCA-Survey Database II. Jednak ze względu na problemy z integracją najnowszych aktualizacji w kodzie MOCCA, rozwój bazy danych MOCCA-Survey Database II został mocno opóźniony, co uniemożliwiło skorzystanie z niego w projekcie doktorskim. Niemniej jednak praca ta przyniosła dodanie ważnych funkcjonalności do kodu MOCCA.

Omawiamy pokrótce również prace, które zostały opublikowane lub są w toku. Dotyczą one rozbudowy kodu MOCCA związanych z aktualizacjami w kodzie BSE ewolucji gwiazd i układów podwójnych oraz wprowadzeniem możliwości śledzenia ewolucji wielu populacji gwiazdowych. Omawiamy także wyniki zastosowania zbudowanego, w ramach pracy doktorskiej, środowiska programistycznego w innych projektach. Aktualizacje wprowadzone w tych pracach miały służyć do stworzenia nowej bazy danych MOCCA-Survey Database II, która miała być użyta do analizy populacji GC w innych galaktykach. Wyniki uzyskane w drugiej pracy projektu doktorskiego posłużyły do zbudowania modelu wzrostu masy NSC i SMBH w Drodze Mlecznej i galaktyce Andromedy. Argumentujemy, że w celu wyjaśnienia obserwowanych mas NSC i SMBH w badanych galaktykach, należy uwzględnić akrecję gazu galaktycznego. SMBH akreował by gaz budując swoją masę, jednocześnie procesy gwiazdotwórcze budowały by masę NSC.

Acknowledgements

As I write this dissertation, a chapter of my life is closing. The experiences I had during my doctoral studies had a significant impact on my life. I broadened my knowledge, had a chance to meet wonderful people, work with many of them, and share with others the hardships of PhD student's everyday life. I would like to thank everyone, including those who are not named here, who supported me and with whom I shared important experiences.

Firstly, I would like to express my deepest appreciation to my supervisor, Mirek, who always believed in me and taught me everything I know about the beauty of globular clusters. I am extremely grateful for his unwavering dedication, guidance and relentless support throughout my PhD journey. This work could not have been accomplished without his careful supervision. I would also like to extend my deepest gratitude to all my collaborators who helped me with the projects presented in this thesis. In particular, I would like to thank Abbas Askar, Manuel Arca-Sedda, Diogo Belloni, Rainer Spurzem, Enrico Vesperini, Sambaran Banerjee and Jongsuk Hong. Their feedback, practical suggestions and valuable advices were tremendously useful in the development of these articles.

I am also grateful to my parents and siblings for their support throughout my life. I would not have come this far without their endless love and encouragement. They sparked my interest in astrophysics and inspired me to study it

When I flew from home to Warsaw, I did not expect to make such strong friendships here. I met people who became like family to me, they have been source of joy and support throughout my PhD. I would like to thank Abbas, David, Dominik, Filip, Jose, Katarzyna, Marco and Saikruba for making this path more enjoyable, for sharing the pain and struggles we have encountered during this time, and for all the help and support they have given me. I would like to thank also Marta and Karolina, the other two important people I have met during this time.

Despite the distance between us, Flavia and Lorenzo have always remained close to me: for such friendship, space and time does not matter. I would like to thank both of them for always being a light in my life, before, during and after my PhD.

As stars dance in stellar systems of our Universe, so we go through life dancing with people of this world. Just as the orbit of a star is perturbed by interactions with other stars, so our lives and ourselves are changed due to interactions with the people around us. We often experience brief interactions with people who just fly through our lives, only occasionally are we lucky enough to form strong and binding relationships. And I am lucky to have found my life companion and my future wife, Dorota. She was an important support in this part of my life and my PhD journey. I want to thank her for her presence and for all the times we have had together over the past few years: for the laughs, all the joyful moments, the journeys we have made together, and the sharing of life's struggles. Even though we shared the same one-room apartment during the last years of the pandemic, we managed not to kill each other, but actually deepened our relationship.

Chapter 1

Introduction

In this introductory chapter, the outline of the thesis is discussed in Section 1.1. A general introduction to globular clusters (GCs) and their astrophysical importance is provided (Section 1.2). The dynamical evolution of these systems is shortly discussed (Section 1.3), together with the numerical tools used to simulate their evolution (Section 1.4). In Section 1.5, an overview on the GCs population around galaxies is provided, together with an introduction to the numerical machinery used to model the GCs population around the Milky Way (MW) and external galaxies. Finally, the contents of the other chapters are briefly described (Section 1.6).

1.1 Motivation and thesis outlines

In the past years, important discoveries about compact objects, the formation and evolution of intermediate-massive black hole (IMBHs), super-massive black holes (SMBH) and nuclear star clusters (NSCs), and their connection with galaxy evolution have been achieved. At the same time, it has become evident that the influence of GC populations in these astrophysical processes is not negligible. The main aim of this thesis is to create machinery that could be used, among other tools, to simulate the GC populations around external galaxies in the local Universe. We seek to constrain and determine the GCs' observable characteristics, evolutionary histories, and compact object content, such as IMBHs, black holes (BH) subsystems (BHSs), BH-BH binaries, X-ray binaries, etc. Also, the machinery could be used to constrain, among others, the NSCs and the central SMBH mass build-up, the local universe's BH-BH merger rate as well as the event rates of tidally disruptive events (TDEs) between the SMBH and infalling stars.

In our initial and ambitious goal, it was planned to use simulations of GC evolution from the MOCCA-Survey Database II. The Database should have been created in the initial stages of the PhD project as a part of the NCN grant project. The project involved the development of an important upgrade of the MOCCA code introduced in Leveque et al. (2022a). Namely, this upgrade consisted of an addition to the MOCCA code corresponding to the removal of the pristine gas during the initial embedded phase of the stellar cluster evolution, allowing for the ability to follow the dynamical evolution of GCs from their first stages up to a Hubble time. The survival and the further evolution of GCs importantly depends on this initial phase, where significant expansion and mass loss is experienced by the system over a very short time scale. Introducing this process into the MOCCA code was extremely difficult and time consuming with the physical process of gas removal and the violent relaxation taking place on a dynamical time scale (connected to the crossing time). Meanwhile, the MOCCA code works on an evolution time scale that is fraction of the relaxation time and very much larger than the crossing time. For this purpose, a special version of the MOCCA code was created from scratch and successfully used for the evolution of

massive and large GCs (Leveque et al., 2022a). The simulations confirmed previous findings from N-body simulations of small-N systems. Unfortunately, issues with the MOCCA code integrity after the introduction of the most recent and very extensive upgrades for stellar/binary evolution and a detailed treatment of the evolution for multiple stellar populations caused a significant delay in the production of the MOCCA-Survey Database II. For this reason, it was decided to use the old, slightly out-of-date MOCCA-Survey Database I despite it having old stellar/binary evolution formulae (but still in good agreement with the observed Galactic GCs, see for example Askar et al., 2017). This makes it possible to create and test the machinery for real GC populations in Milky Way (MW) and Andromeda (M31) galaxies.

The project's objective was to create the tools necessary to replicate the observationally driven properties of GC populations in external galaxies using MOCCA models of GC evolution. Much attention has been paid to recover the maximum amount of information about the observational properties of GC populations. The main research goals of the thesis are summarized below:

- **Distribution of global GC properties:** The GC system properties strongly depend on the local galaxy density and potential in which the star clusters are located. That is, the cluster dissolution and mass loss are strongly connected to the galactic tidal field experienced by the system. Hence, the mass, the half-mass radius (or similarly the half-light radius), as well as the orbital properties of the star cluster around its host galaxy are expected to depend on the galactocentric distance. As a first step, we aimed to verify that our machinery could reproduce the observational properties of GCs around the MW and M31 galaxies. The comparisons for the spatial distribution of GC masses, their half-light radii and their orbital properties were carried out in the papers presented in Chapter 3 and Chapter 4.

- **Spatial distribution of various evolutionary GC models:** The dynamical evolution of a GC harbouring an IMBH, a BHS or neither can be wildly different. The different dynamical evolution would shape the GC's observable properties accordingly. One of the goals of our research was to determine observable properties that would help to distinguish the dynamical signature of each dynamical model. In the paper presented in Chapter 2, we firstly considered models from the MOCCA Database I to establish the properties that might be used in observations to distinguish between the different dynamical models. Then, in the paper presented in Chapter 4, we studied the distribution of the different dynamical models with their galactocentric distances, and how their properties are distributed within the galactic halo.

- **Compact objects properties in GC populations:** The observed GCs host an important number of exotic binary systems, whose formations are facilitated by the dynamical interactions in the dense environments of GCs. One of the goals for the thesis was to investigate the potential number and the property distribution of such populations produced in GCs, and how they would relate to the GC galactocentric distances. In particular, the third paper presented in this thesis in Chapter 4 investigated the BH-BH binary population distribution that could potentially be observed at 12 Gyr.

- **Compact object binary mergers in GCs population:** Exotic binaries can be also an important source of gravitational waves and luminous observational events. The properties of the merged binaries as well as the relative merger rates

can be inferred from gravitational waves studies using data from LIGO/Virgo. In Chapter 4, we also investigated the distribution properties of the BH-BH binaries that would merge within a cosmological cube of 1 Gyr, togheter with the BH-BH binaries merger rate.

- **NSC and SMBH mass growth:** The *in-situ* formation and the GC infall and merger with the galactic center are the two main mechanics that are mostly taken into account while discussing the formation mechanics of NSCs, which is still an open topic. The pristine gas would fall towards the galactic center in the *in-situ* formation scenario, triggering a powerful burst of star formation. In the second scenario, the GCs would gradually spiral inward due to dynamical friction, and finally would be accreted into the galaxy's center. One of our goals is to investigate the contribution of the infalling GCs into the galaxy center to the mass-growth of both the NSC and SMBH. In Chapter 3, we followed the mass evolution of the NSC as the accretion of GCs that have fallen into the NSC during the simulation and the mass evolution of the central massive BHs as the accretion of the IMBHs hosted in the GCs which have fallen into the NSC.

1.2 Overview of Globular Clusters

GCs are bound and self-gravitating spherical systems of tens of thousands to millions of stars, orbiting around their host galaxies. GCs are characterized by older and redder stars in comparison with other stellar clusters and by very high densities. The typical mass range is of $10^4 - 10^6\ M_\odot$ with diameters that range from a few to several tens of parsecs (pc), implying a mass density of stars in their core being as high as a few $10^6\ M_\odot/\mathrm{pc}^3$. Thanks to their high luminosity, GCs are easily observable in the MW and in external galaxies. The dense central cores of GCs are enclosed by much lower density stellar halos. In the present day, more than 150 GCs have been observed around the MW (Harris, 1996, updated 2010). The Milky Way GCs (MWGCs) can be found at any distance from the Galaxy, from a few kiloparsecs up to 50 kpc away from the Galactic center. However, approximately half of the MWGC population is found within 5 kpc from the Galactic center. While the thin disk in the Galaxy contains most of the stars and young open clusters, GCs are instead found in the Galactic halo, evidencing the very old age of GCs. Indeed, the stellar content in GCs is mostly composed of metal-poor population II stars. Finally, from kinematic and visual observations, it is shown that GCs contain neither dark matter nor gas.

It has been observed that all galaxies ranging from dwarf to giant and covering the whole Hubble sequence of morphological categories host GCs systems in their halos (Brodie and Strader, 2006). The distributions of GC structural parameters in external galaxies are similar to the distributions of Galactic GCs, as observational surveys in the local group and in the Virgo and Fornax galaxy clusters have shown (Côté et al., 2004; Peng et al., 2006; Jordán et al., 2005; Puzia et al., 2014).

A variety of different exotic stellar objects have been observed within GCs, including blue straggler stars (Knigge, 2015), cataclysmic variables (Knigge, 2012; Rivera Sandoval et al., 2018), X-ray binaries (Pooley, 2010), and millisecond pulsars (Manchester et al., 2005; Ransom, 2008). These exotic objects are the results of the interplay of dynamical interactions within the GCs and their stellar/binary evolution.

In general, GCs are capable of offering a potent diagnostic for galaxy formation, star formation within galaxies, galaxy interaction and mergers, and the distribution of dark matter in galaxies. In fact, interactions between galaxies may cause bursts of star formation to occur as well as the growth of massive star clusters. The formation and

evolution of the host galaxies might be constrained by the characteristics of the GC systems in different galaxies. Galactic GCs, in particular, may be utilized to constrain the halo structure and formation timeline of our Galaxy (Trujillo-Gomez et al., 2020; Bajkova et al., 2020; Beasley, 2020, and references therein), and to constrain its stellar and binary evolution (Thévenin et al., 2001; Ahumada, 2005; Lovisi et al., 2012; Korn, 2020).

1.3 Dynamical evolution of Globular Clusters

Similarly to how gas pressure prevents main sequence stars from gravitational collapse, the stability of self-gravitating system like GCs is driven by the balance between the inward gravitational pull and the outward pressure generated by stars movements in randomly orientated orbits in the central core of GCs.

The GC structure is characterized by three radii: the half-light radius (or half-mass radius), the core radius and the tidal radius. The observed half-light radius is the 2D distance from the GC center that contains half of the total luminosity of the GC. However, the half-light radius includes stars on the outer part of the cluster that just so happen to be in the line of sight. For this reason, theorists also use the half-mass radius, which is the 3D radius from the center that contains half of the total mass of the cluster. Instead, the 2D radius containing half of the GC central surface density or central surface brightness is defined as the core radius. Finally, the tidal radius is the distance from the GC's center at which the galaxy's external gravity has a stronger effect on the stars in the cluster than the cluster itself does.

Two main time scales are important in the study of self-gravitational systems as GCs: the relaxation time and the crossing time. The relaxation time of a GC is the timescale when the cumulative effect of distant two-body encounters become significant, in other words it is the amount of time needed for the star to completely forget its original orbit (determined by its energy and angular momentum). This timescale is called the relaxation time scale, and it is inversely proportional to the GC density, and directly proportional to the stellar velocity dispersion and number of stars in the system. Instead, the crossing time is the time needed for a star to cross the system's half-mass radius, and it is defined as the half-mass radius divided by the mean velocity of the stars. For collisional systems such as GCs, the crossing time is much smaller compared to the half-mass radius relaxation time, implying that the most crucial mechanism controlling the long-term evolution of systems like GCs is relaxation. The half-mass radius relaxation time for a GC is given by the Spitzer formula (Spitzer, 1987):

$$t_{rh} \sim \frac{0.138\, N^{1/2} r_h^{3/2}}{\langle m_\star \rangle^{1/2}\, G^{1/2}\, \ln(\gamma N)}, \tag{1.1}$$

where G is the gravitational constant, N is the total number of stars and $\langle m_\star \rangle$ is their average mass. The $\ln(\gamma N)$ term is called the Coulomb logarithm. Typically, the half-mass radius relaxation time is on the order of $10^8 \sim 10^9$ years. It is possible to show that the ratio between the crossing time and the half-mass radius relaxation time is inversely proportional to the number of the stars in the system.

The energy needed to support the dynamical balance of the GC is generated by the collapse of the cluster core and/or the interactions of binaries in the central core or intermediate BH, meanwhile the distant two-body interactions among stars are responsible for the energy transport through the system. Striving for energy equipartition resulting from the relaxation process would approximately imply that the kinetic

energy of all the stars in the GC does not depend on stellar mass. Consequently, less massive stars would have higher velocities compared to the more massive stars. So, more massive stars will fall deeper in the central core of the GCs, slowing down their velocities. On the other hand, the less massive stars would move faster and populate the GC halo. This process is known as mass segregation.

Anther process that is a consequence of two-body relaxation is evaporation. Stars can exchange and gain energy through the relaxation process. A star can become unbound and escape the cluster if it acquires enough kinetic energy. Interaction with the host galaxy (such as tidal shocks during passages through the galactic disk) or a strong tidal field can accelerate the evaporation process. The evaporation time is on the order of a hundred relaxation times for an isolated cluster, while clusters evolving in a tidal field have an evaporation time much smaller, of the order of few to dozen or so relaxation times.

The energy flow from the GC center towards the GC outskirts would imply a contraction of the core of the system. This is a consequence of the negative heat capacity in GCs: if a GC would be initially in virial equilibrium and some kinetic energy gets supplied to the system, in order to restore virial equilibrium, the length scale of the system would increase, meanwhile the velocity dispersion of the stars would decrease. A similar behaviour would be achieved in the case of mass loss. Also, the core and the halo of a GC could be very approximately considered as separate structures within the GC, with the core acting as a heat source, and the halo as a heat reservoir, with the energy flowing from the core to the halo. Consequently, the core would continue contracting until the central density would become relatively high and binaries at the center of the GC would be formed. These binaries would stop the cluster from further collapsing as their dynamical interactions would provide energy to the nearby stars regulating the cluster's future evolution. This process is known as core collapse, and it is consequence of two-body relaxation in GCs. GCs with small half-mass relaxation times would experience core collapse in the earlier stages of their evolution compared to the clusters with longer half-mass relaxation times. Also, the core collapse process can be sped up by the mass segregation process. Indeed, the time of core collapse is connected to the dynamical friction time-scale of the most massive stars, the latter being inversely proportional to the mass of the most massive star in the system (Fujii and Portegies Zwart, 2014).

During the GC core collapse, binary systems can be easily formed as a result of the strong dynamical interactions between three stars (Heggie, 1975; Heggie and Hut, 2003) due to the large number densities and hence high likelihood of strong interactions. Binaries can be divided between hard and soft: hard binaries are binary stars that have orbital velocities greater than the velocity dispersion of neighboring stars and are generally compact. On the other hand, soft binaries are binary systems where the stars' orbital velocities are smaller than the GC stars' velocity dispersion and generally have large seperations. Due to the strong interactions between binary-single stars and binary-binary stars, hard binaries are more likely to get even harder and soft binaries to get even softer, known as the Heggie-Hills law (Heggie, 1975; Hills, 1975). Consequently, dynamical interactions can cause soft binaries to disrupt and hard binaries to harden and eventually to escape or merge.

The GC's evolution can also be influenced by the stellar and binary evolution of its stars, in particular in the initial stages of the evolution. In the early stages, a strong mass loss from the cluster due to the stellar evolution and mass loss from massive stars is expected.

Finally, the dynamical evolution of GCs is determined by external factors, such as dynamical and static tides during the interactions with the different structures of the

host galaxies. GCs can experience strong tidal evaporation when passing through the galactic disk, bar, and bulge of the host galaxy. Furthermore, GCs can also fall towards their host galactic center due to dynamical friction (as discussed in Section 1.5).

1.4 Monte Carlo models for Globular Clusters evolution

Different physical processes with different characteristic time and length scales are involved in the evolution of GCs, making it hard to accurately simulate their evolution. The length scales of processes involved in the dynamical interactions in GCs can vary from few kilometers (for example, collisions or mergers of NSs or BHs) to the entire star cluster size on the order of few parsecs (for example the two-body relaxation). Similarly, the timescales can vary from seconds or milliseconds (for example stellar collision or mergers) up to the GC lifespan of dozen Gyr (the long-term GC evolution). In addition, the timescales for the stellar evolution differ for different stellar masses and during different stellar evolutionary stages. Moreover, the timescales of dynamic interactions differ in the case of collisions and three- and four-body interactions.

Thanks to advancements in computational technology over the past two decades, the dynamical evolution of GCs has been extensively modelled using a variety of numerical algorithms in comprehensive simulation codes, such as direct N-body, Monte Carlo, Fokker-Planck and gaseous model codes. These software must include prescriptions for stellar, binary, and tidal field effect with methods for computing the dynamical evolution of the GC. While N-body codes can handle the long-term evolution of a GC, they are generally too expensive to simulate initially dense GCs with large binary fraction in a decent amount of time. The Monte Carlo (MC) method offers an alternative approach to model the evolution of large GCs, and was firstly developed by Hénon (Hénon, 1971). The big advantage of using the MC method is computation time which is much faster compared to direct N-body codes. Indeed, with N being the number of stars in the GC, the computational time for a sequential N-body code scales as N^{3-4} (Heggie and Hut, 2003)[1], whereas for a MC code it scales as $N \ln N$. This implies that a MC code would simulate a realistic GC composed of 10^6 stars within a few days to a week. The Fokker-Planck and gaseous models have been developed in the past century because of their fast computing time. However, these codes have difficulties in handling continuous mass functions, dynamical interactions and energy generation and escape in a full tidal field.

In the Hénon MC prescription, the actual position for each star is picked up randomly (with probability inversely proportional to the radial velocity) between the orbital apses at each time step knowing the global potential, which is determined from the mass and radial position of each star using spherical shell approximations. This prescription assumes that all the weak interactions between one star and all other stars in the system during a time step are represented by one encounter between that star and its nearest neighbor. The two interacting stars' energy and angular momentum are modified throughout this encounter in accordance to the statistical description provided by the two-body relaxation process, which describes the change of the orbit for a star moving in the background of the other stars (Hénon, 1971; Stodółkiewicz, 1982).

The MC method comes however with its limitations and assumptions. Low N ($N < 10000$), nonspherical, and nonrotating clusters cannot be modelled with the MC method. Also, processes with characteristic timescales comparable to the

[1] However, with parallel codes to a bit less than 3.

crossing time are very difficult, but not impossible to model. A special treatment for these processes should be introduced, making the code less efficient. Because the system has to be in dynamical equilibrium, the time steps have to be much larger than the crossing time and a fraction of the half-mass relaxation time. This would imply that the MC method cannot be used to simulate the violent relaxation phase or the short-term evolution of star clusters (unless some special measures have been applied).

The treatment for binaries stars and the prescription for stellar evolution (altogether with other physical processes) have been introduced in the MC scheme by Stodółkiewicz (Stodółkiewicz, 1982; Stodółkiewicz, 1986). Single star-binary and binary-binary interactions were firstly introduced in Stodółkiewicz (1986) on the bases of simple cross section approximations. Cross sections for the three-body interactions (for single star-binary interactions) and four-body (for binary-binary interactions) have been determined. The recoil energy generated by these interactions would then be exchanged with the other stars in the clusters, heating the system. Further development and new MC developments came in the late nineties (Giersz, 1998; Giersz, 2001; Joshi, Rasio, and Portegies Zwart, 2000; Freitag and Benz, 2001), such as the following of the evolution of all individual stellar objects instead of the *superstar* concept developed in Hénon (1971) and Stodółkiewicz (1982). Three MC codes are currently developed and frequently used to simulate GCs models. These are the MOCCA code (Hypki and Giersz, 2013; Giersz et al., 2013), the CMC code (Pattabiraman et al., 2013; Kremer et al., 2020), and the implementation developed in Sollima and Mastrobuono Battisti (2014), Sollima (2021), and Sollima et al. (2022). The machinery introduced in this project utilizes the simulations generated with the MOCCA code to model GC populations in external galaxies. In the following subsection, the main features of the MOCCA code are described.

1.4.1 MOCCA

The MOCCA code (MOnte Carlo Cluster simulAtor) is a numerical code used to simulate the long-term evolution (10^{10} years) of real-sized star clusters. It is based on the Hénon MC prescription. The evolution of several million stars can be simulated within a few days to a week time (using a single processor).

Different options for setting the initial conditions in MOCCA are present. In particular, in the current version, the MOCCA code has been linked to the McLuster initial condition code (Küpper et al., 2011; Leveque et al., 2022a). The number of objects, the characteristic radii, and the initial position and velocities of the stars (for example isotropic, Plummer (1911), King (1962)) and primordial binary systems can be defined. Different initial mass functions, initial binary fractions, and initial binary property distribution are also defined. The initial conditions for multiple stellar populations can also be also defined.

The SSE (Hurley, Pols, and Tout, 2000) and the BSE (Hurley, Tout, and Pols, 2002) codes are used to follow the stellar and binary evolution in MOCCA. The position, velocity, mass, radius, and luminosities for each star in the system are known at each simulated time step. MOCCA's primary input file also includes the metallicity, supernova kick prescription, and distributions for masses of the stellar remnants, which are crucial in regulating the stellar/binary evolution.

A point mass approximation has been used in MOCCA to model the Galaxy tidal field. It is assumed that the Galaxy mass is equal to the mass contained inside the GC's circular orbit. The realistic treatment by Fukushige and Heggie (2000) for escaping stars in tidally limited clusters is used in MOCCA. Finally, the strong

dynamical interactions between two binary systems or a single star-binary system play an important role in the energy generation and energy flow through the GC, and they need to be computed fairly. The FEWBODY code (Fregeau et al., 2004) has been used to compute such interactions.

MOCCA can reasonably well reproduce the evolution of the cluster's properties, as well as the number and distribution of properties for binary systems and other objects, as shown in comparison with results of direct N-body codes (Giersz, Heggie, and Hurley, 2008; Giersz et al., 2013; Wang et al., 2016; Madrid et al., 2017; Giersz et al., 2019; Kamlah et al., 2022) for clusters hosting from a few tens of thousands up to a million stars.

1.4.2 MOCCA-Survey Database I

Thanks to its short simulation time, MOCCA is suitable for studying the multidimensional space of GC initial conditions by following the evolution of thousands of GC models. Exploring the initial parameter space, it is possible to understand the importance and the influence of the initial parameters on the evolution of GCs. The MOCCA-Survey Database I (Askar et al., 2017) consists of about 2000 GC models that were simulated using the MOCCA code, and span different initial conditions for the initial number of objects (from 4×10^4 to 1.2×10^6 stars), structure, central density, half-mass radii, relaxation time, primordial binary fraction, tidal and Galactocentric radii, metallicity, and black hole natal kicks. The models in the MOCCA-Survey Database I have been used in this thesis to simulate the GC populations in external galaxies through our machinery. Askar et al., 2017 showed that MOCCA-Survey Database I models can reproduce the observed properties of MWGCs, such as the cluster absolute magnitude and the average surface brightness inside the cluster half-light radius.

1.5 Globular cluster populations

A large variety of astrophysical processes can be constrained from observations of GCs themselves and their populations surrounding galaxies. Indeed, they can give a potent diagnostic for stellar and binary evolution, galaxy formation, star formation in galaxies, intergalactic interactions and mergers, and dark matter distributions in galaxies. In fact, interactions between galaxies can cause bursts of star formation events and the formation of massive star clusters. The features of GC systems in other galaxies can provide insight into their host galaxies' formation and evolution.

The bimodality of GCs in the color distribution has been a recent discovery, indicating two subpopulations of GCs around the host galaxy, with one peak shifted toward blue, indicating a metal-poor population, and the other red, indicating a metal-rich population. This feature appears to be common for all types of galaxies (Zepf and Ashman, 1993; Ostrov, Geisler, and Forte, 1993; Kundu and Whitmore, 2001; Larsen et al., 2001; Harris et al., 2006; Cantiello and Blakeslee, 2007). The positions of the two blue and red peaks vary from galaxy to galaxy. However, the $V - I$ color distribution for bright early-type galaxies (such as NGC 1023, NGC 3384, and NGC 4472) often exhibits a blue peak at $V - I = 0.95 \pm 0.02$, corresponding to $[Fe/H] \sim -1.5$, and a red peak at $V - I = 1.18 \pm 0.04$, corresponding to $[Fe/H] \sim -0.5$ (Larsen et al., 2001). To produce such a bimodal distribution, at least two star-formation events in the histories of such galaxies must be induced, which can be caused by major mergers (Ashman and Zepf, 1992) or occur in isolation (Forbes, Brodie, and Grillmair, 1997).

Another explanation might be the accretion of metal-poor GCs from lower-mass galaxies to more massive galaxies in the hierarchical scenario of galaxy formation, with the metal-rich GCs generated *in-situ* (Forbes, Brodie, and Grillmair, 1997; Harris, Harris, and Poole, 1999; D'Abrusco et al., 2016; Cantiello et al., 2018; Cantiello et al., 2020). However, no consensus has been reached regarding which scenario might explain the observed color distribution.

Peng et al. (2006) discovered a relationship between host galaxy brightness (and mass) and GC metallicity for metal-poor GCs in the analysis of early-type galaxies as part of the ACS Virgo Cluster Survey (Côté et al., 2004). This may reflect a universal enrichment during the birth of both the metal-rich and metal-poor populations. Furthermore, metal-rich GCs have a higher color dispersion than metal-poor GCs, implying that metal-rich GCs have roughly twice the color dispersion as metal-poor GCs. Finally, metal-rich GCs have a lower average half-light radius than metal-poor GCs (Jordán et al., 2005). The half-light radius increases with galactocentric distance (at least in the central areas of galaxies, see Puzia et al., 2014), although with a smaller slope when compared to GCs in other galaxies (the slope is ~ 0.07 compared to ~ 0.3 for Galactic GCs, see Jordán et al., 2005).

According to Harris, Harris, and Alessi (2013), the overall number (or mass) of GCs in a galaxy appears to rise with the host galaxy mass, or brightness. The authors discovered that low and very high luminosity galaxies have a larger number of surrounding GCs, and they interpret these findings as a result of the interaction of radiative feedback and gas ejection during star formation processes. Zepf and Ashman (1993) introduced the quantity T as the number of GCs per $10^9\ M_\odot$ of galaxy stellar mass to compare the richness of GCs (i.e., the number of GCs per each galaxy) for various galaxy types. It might be possible to set more strict limitations on the star-formation histories of galaxies if the metal-poor and metal-rich populations were considered separately (Kissler-Patig et al., 1997; Forbes, Brodie, and Larsen, 2001). In fact, T_{red} is expected to be substantially smaller for early elliptical galaxies than for elliptical galaxies, since they are likely to develop through violent and gas-rich mergers with metal-rich GCs within (Brodie and Strader, 2006). Instead, in a high-density environment, collapses are likely to produce metal-poor GCs first, implying that T_{blue} is expected to be bigger in the formation of hierarchical structures (Rhode, Zepf, and Santos, 2005).

1.5.1 The evolution of a globular cluster population

The GC's evolution and survival are driven by their host galaxy's evolutionary history and by their internal dynamical processes (Grudić et al., 2022; Rodriguez et al., 2022). Therefore, accurate descriptions of the interplay between the GC and their host galaxy (tidal mass loss, dynamical friction, shocks), and of the internal dynamics (mass loss, stellar evolution, compact remnants) are required in modelling the evolution of GC populations.

The stellar evolution, the relaxation process and the tidal field of the galaxy control the internal evolution of the GCs and their dissolution (as described in Sec. 1.5). The system mass loss and the evolution of the half-mass relaxation timescale are influenced by the presence of a tidal field: the stronger the tidal field the larger mass loss and the faster the cluster dissolution. The external evolution of a GC in its host galaxy is controlled by dynamical friction dragging the GCs towards the galactic center (Tremaine, Ostriker, and Spitzer, 1975; Capuzzo-Dolcetta, 1993; Antonini et al., 2012; Arca-Sedda and Capuzzo-Dolcetta, 2014b). The bulge and disc tidal shocks can also augment the GC mass loss and dissolution, by transferring kinetic energy

to every object in the cluster. Indeed, the interaction between the GC and the galaxy may be catastrophic, leading to the GCs' destruction if the galactic local density were greater than the densities of the GCs (Spitzer, 1958; Spitzer, 1987; Gnedin and Ostriker, 1997; Martinez-Medina et al., 2022).

The timescales of these three factors (internal dynamics, static and dynamical tides, and dynamical friction) define the importance of each process. The GCs would dissolve and perhaps contaminate the galactic NSC if the dynamical friction timescale were to be smaller than both the age and dissolution timescale of the GCs. However, the GCs would dissolve before merging into the galactic core if the dissolution timescale (associated with the interplay between the relaxation process and tides) were to be shorter than the dynamical friction timescale. The tides are strongly connected to the galactocentric position of the GCs. For each GC, the galactocentric position is influenced by dynamical friction, that would drag the GC in the galactic center. For really small galactocentric distances (within a few dozens of pc from the galactic center), the GC would be dissolved due to the high galactic density in this region (Gnedin and Ostriker, 1997; Arca-Sedda and Capuzzo-Dolcetta, 2014a; Rodriguez et al., 2022), if the galactic density would be larger than for the GC. If the GC would survive this process, the dynamical friction would drag the GC to the galactic center, where it would be accreted to the NSC.

When a GC is accreted to the NSC, it contributes to the NSC mass build up. The NSC is a star cluster that is in the center of most galaxies and contains a high stellar density and brightness. The *in-situ* formation and the GC in-fall and merger with the galactic center are the two primary mechanics that are mostly taken into account when discussing the formation mechanics of NSCs, which is still an open issue. The pristine gas would fall towards the galactic center in the *in-situ* formation scenario, triggering a powerful burst of star formation (Loose, Kruegel, and Tutukov, 1982; Milosavljević and Merritt, 2001; Bekki, 2007; Neumayer et al., 2011). The second possibility is that dynamical friction would gradually spiral the GCs inward until they have been accreted at the galaxy's center (Tremaine, Ostriker, and Spitzer, 1975; Capuzzo-Dolcetta, 1993; Capuzzo-Dolcetta and Mastrobuono-Battisti, 2009; Arca-Sedda and Capuzzo-Dolcetta, 2014a). However, the formation and evolution of the NSC may also be explained by the interplay of these two mechanics, with a massive star cluster forming in the galaxy's disc, migrating to the center, and gaining mass through interactions with other star clusters and substructures (Guillard, Emsellem, and Renaud, 2016; Urry and Padovani, 1995; van den Bosch et al., 2012; Kormendy and Ho, 2013; Emsellem, 2013).

1.5.2 MASinGa

In order to model the evolution of GC populations, it is necessary to be able to describe how the galactic tidal field influences the evolution of GC populations in terms of tidal mass loss, shocks, and dynamical friction, as well as to be able to closely monitor the GC internal dynamics and stellar/binary evolution, which control the GC mass loss, star populations, and compact remnants. The computational time required for such detailed evolution can be significantly high. For this reason, different semi-analytic studies and tools have been published in the past years to follow the evolution of GC populations and the central NSC (such as Gnedin, Ostriker, and Tremaine, 2014; Arca-Sedda and Capuzzo-Dolcetta, 2014b), enabling the rapid realization of hundreds of galaxy models within a few hours. Thanks to its flexibility, the MASinGa code (Arca-Sedda and Capuzzo-Dolcetta, 2014b; Arca-Sedda et al., 2015) can effectively utilize the benefits of both semi-analytical and N-body approaches. In order to

provide a thorough evolution of the internal and external GC dynamics, MASinGa can easily be interfaced with star cluster simulation catalogues. Therefore, in this study the evolution of GC populations have been described using a unique method that combines the MOCCA-Survey Database and the MASinGa semi-analytic tool.

The MASinGa (Modelling Astrophysical Systems in GAlaxies) code was firstly introduced to study the GC infall-merger with the galaxy center as part of the NSC formation and mass growth (Arca-Sedda and Capuzzo-Dolcetta, 2014b; Arca-Sedda et al., 2015). Also, the interplay of TDE rates and the infall of GCs, and their contribution to the mass build-up of the SMBH was studied with MASinGa (Arca-Sedda et al., 2015).

The GC populations have been evolved using a set of fitting formulas that describe the development of GC orbits, as described in Arca-Sedda and Capuzzo-Dolcetta (2014b) and Arca-Sedda (2022, private communication).

Galaxies are modeled in MASinGa using the Dehnen family (Dehnen, 1993) of potential density pairs, which are characterized by spherically symmetric density profiles of the following form:

$$\rho_G(r) = \frac{(3-\gamma)M_g}{4\pi r_g^3}\left(\frac{r}{r_g}\right)^{-\gamma}\left(1+\frac{r}{r_g}\right)^{\gamma-4}, \tag{1.2}$$

where M_g is the galaxy total mass in units of $M_\odot$, r_g the galaxy length scale in kpc and γ the density profile slope. The Dehnen density profile has the benefit of having a simple analytic form and being flexible enough to reproduce a variety of galaxy density profile distributions using only two parameters, r_g and γ. Indeed, the galaxy profile can be more or less cuspidal with the adjustment of those two parameters.

In earlier studies, Arca-Sedda and Capuzzo-Dolcetta (2014a) and Arca-Sedda et al. (2015) used N-body simulations of star clusters in Dehnen galaxy models to find the fitting formula for the dynamical friction timescale, τ_{df}, as:

$$\tau_{df} = 0.3\cdot g(E_{GC},\gamma)\cdot\left(\frac{r_g}{1\,\mathrm{kpc}}\right)^{3/2}\left(\frac{M_g}{10^{11}M_\odot}\right)^{1/2}\left(\frac{M_{GC}}{M_g}\right)^{-0.67}\left(\frac{R_{GC}}{r_g}\right)^{1.76}, \tag{1.3}$$

with M_{GC} as the GC mass, E_{GC} its orbital eccentricity, and R_{GC} its galactocentric position. The function $g(E_{GC},\gamma)$ is a dimensionless function given by

$$g(E_{GC},\gamma) = (2-\gamma)\left[a_1\left(\frac{1}{(2-\gamma)^{a_2}}+a_3\right)(1-E_{GC})+E_{GC}\right], \tag{1.4}$$

with $a_1 = 2.63\pm0.17$, $a_2 = 2.26\pm0.08$ and $a_3 = 0.9\pm0.1$ (Arca-Sedda et al., 2015).

The M_{GC} are selected randomly from the GC initial mass function (GCIMF). The orbital eccentricities E_{GC} have been randomly picked from a thermal distribution. Finally, the R_{GC} have been chosen randomly within the radial bins in which the galaxy density profile has been divided. This technique makes sure that the density profile of the galaxy and the GC system have initially the same functional form. Indeed, the initial distribution of the GC population in the galaxy is assumed to follow the host galaxy's density distribution, with the total mass of the GCs being a fraction of the overall galaxy mass, i.e. $\rho_{GCS}(r) = \alpha\cdot\rho_G(r)$, and $\alpha \leq 1$. The initial GC tidal radius r_{tidal} in MASinGa is computed by using galactocentric distance R_{GC}. The given r_{tidal} can be computed in the studied galaxy potential using the following formula,

assuming a GC circular orbit:

$$R_{GC}: \qquad r_{tidal} = R_C \cdot \sqrt[3]{\frac{M_{GC}}{3M_g(R_{GC})}}, \tag{1.5}$$

with $M_g(R)$ as the galaxy's mass at position R, given by the Dehnen model mass profile, and R_{GC} being the galactocentric distance. For the sake of simplicity, the tidal radius has been determined assuming that the GC is in a circular orbit, with the galactocentric distance for a circular orbit being equal to its actual galactocentric distance R_{GC}.

The initial half-mass radius $r_{h,GC}$ for the MASinGa models are determined by the Marks and Kroupa (2012) relationship, that is $r_{h,GC}/\mathrm{pc} = 0.1 \times (\mathrm{M_{GC}}/\mathrm{M_\odot})^{0.13}$. The initial half-mass radius value has been increased by a multiplicative factor, which was randomly selected from a uniform distribution between 1 and 15, in order to reproduce the expected cluster expansions after gas removal for different initially tidal underfilling states. For $r_{h,GC}$, 0.2 and 7 pc were set as the lowest and maximum values, respectively. A further restriction has been imposed on $r_{h,GC}$, preventing its value from exceeding $0.3 \times r_{tidal}$, that is, having initially tidally overfilling clusters. Indeed, the half-mass radius is around ten times smaller than the initial r_{tidal} for a cluster whose initial spatial distribution is characterized by a tidally filling King model (King, 1966) with $W_0 = 6.0$.

The actual galactocentric position $r(t)$ at each time t is governed by the dynamical friction time scale τ_{df}, and is given by

$$\tau_{df}(r_0) - \tau_{df}(r) = t, \tag{1.6}$$

with r_0 being the initial galactocentric position. Substituting the value for τ_{df}, it is possible to determine the galactocentric position at time t.

The eccentricity time evolution in MASinGa is described as (Arca-Sedda and Capuzzo-Dolcetta, 2014a)

$$E_{GC}(t) = E_{GC}(t=0) \cdot exp\,(-t/\alpha), \tag{1.7}$$

with $\alpha = g(0,\gamma)/(g(E_{GC},\gamma) \cdot \tau_{df})$ being the orbit circularization timescale due to dynamical friction, and $g(e,\gamma)$ as described in Eq. 1.4. According to this equation, the orbit will circularize as the GC gets closer to the center, as expected due to dynamical friction (Colpi, Mayer, and Governato, 1999).

A key factor in the GC mass loss is the evolution of the tidal radius and half-mass radius. When compared to less concentrated clusters (that is, with a large half-mass radius versus tidal radius ratio), more concentrated clusters would lose less mass because they would have fewer objects removed from their systems (such as stars or binary systems). The MOCCA-Survey Database I models do exhibit a distinct mass loss evolution for tidally filling and underfilling models since they do take into consideration the realistic evolution of star clusters. A prescription for the half-mass radius and tidal radius evolution was required in order to more accurately depict the mass loss for MASinGa models during their 12 Gyr evolution and to compare GC models from MASinGa with those from the MOCCA Database I.

At each time t_i, the tidal radius changes while accounting for the system's mass loss according to

$$r_{tidal}(t_i) = r_{tidal}(t_0) \cdot \sqrt[3]{M_{GC}(t_{i-1})/M_{GC}(t_0)}, \tag{1.8}$$

with $M_{GC}(t_0)$ being the initial GC mass, $t_0 = 0$ and $t_i > t_{i-1}$.

On the other hand, the evolution of the half mass radius is described as (Giersz and Heggie, 1996),

$$r_{h,GC}(t_i) = r_{h,GC}(t_0) \cdot b \cdot (t_i - T_0)^{(2+\nu)/3}, \tag{1.9}$$

with $b = 0.787 \pm 0.124$ pc/Myr, $\nu = -1.467 \pm 0.545$, $T_0 = -13.48 \pm 4.56$ Myr obtained by fitting the formula to the half-mass radius evolution for all the models used in Leveque, Giersz, and Paolillo (2021). The reported values are biased for the surviving clusters only, since the models used for estimating them are only models that survived 12 Gyr of evolution.

Finally, the mass evolution is described as a reasonable first-order approximation, and determined by the Spitzer formula (Spitzer, 1987):

$$M_{GC}(t_i) = M_{GC}(t_0) \cdot e^{-t_c/t_i}, \tag{1.10}$$

with $t_c = t_{relax}/\xi$ and t_{relax} as the initial Spitzer relaxation time (Spitzer, 1987). The initial half-mass radius is 10 times smaller than the initial tidal radius for the initially tidally filled King cluster with $W_0 = 6.0$ (King, 1966). This number has been used as a limiting parameter to define both isolated and non-isolated clusters. Hence, the value of ξ is determined by whether the model is isolated or not at each time step (Spitzer, 1987), that is:

$$\begin{aligned} \xi &= 8.5 \times 10^{-3} \qquad if\ r_{h,GC}(t_i)/r_{tidal}(t_i) \leq 0.1, \\ \xi &= 4.5 \times 10^{-2} \qquad if\ r_{h,GC}(t_i)/r_{tidal}(t_i) > 0.1. \end{aligned} \tag{1.11}$$

However, the tidally underfilling cluster will expand and eventually become tidally filled (after a relatively long time, depending on the degree of underfilling) because of the mass loss associated with stellar evolution and binary energy generation. In this situation, the galactic tidal field controls the mass loss.

The tidal dissolution caused by internal dynamics, the galactic tidal field, and the passages through the galactic bulge and across the galactic disc are all taken into consideration while performing the star cluster orbital evolution in MASinGa. Interactions with galactic center regions and the bulge and/or the galactic disk might accelerate the GC dissolution. Depending on how effectively energy is transmitted during these stages, the GC dissolution can be catastrophic or diffusive, with the GCs being disrupted over shorter or longer time scales, respectively. Additionally, the GC is disrupted if the galactic local density is larger than the densities of the GC.

1.5.3 MOCCA models in MASinGa

The MOCCA models cover the R_{GC} distances between 1 and 50 kpc from the Galactic center. The galaxy mass contained inside the R_{GC} was used as the central mass in a simplified point-mass model of the galactic potential. Over the whole range of galactocentric distances, the GC's rotational velocity was set at 220 km s^{-1}. This implies that several steps have to be carried out in order to establish the GC galactocentric position in the gravitational potential of the studied galaxy. In fact, the galaxy potential used in MASinGa is a Dehnen family distribution, as opposed to the simplistic assumption carried out in the MOCCA models. This implies that for a fixed tidal radius experienced by the GC and for a fixed total mass of the GC, the galaxy mass contained within the GC orbit in the MW and in the studied galaxy would differ.

A GC population has been firstly initialized and evolved in MASinGa as described in Section 1.5.2. Afterwards, models from the MOCCA-Survey Database I are linked

to the MASinGa results. A library of MOCCA models called the MOCCA-Library models has been created using the models from MOCCA-Survey Database I. The MOCCA-Library is made up of model representations from the MOCCA-Survey Database I in the studied galaxy. Namely, each model in the MOCCA-Library represent a MOCCA-Survey Database I model evolved in the examined galaxy, with various orbital properties and orbital positions within the gravitational field of the examined galaxy. This method allows us to populate the same MOCCA-Survey Database I model in various galactic field regions and with various orbital properties.

As mentioned above, the galactocentric position of the MOCCA-Library models in the examined galaxy's halo could be established in few steps. Firstly, the tidal radius and galactocentric distance for a circular orbit in the examined galaxy potential have been established. The correct galactocentric distance R_C for a circular orbit in an external galaxy, for a given tidal radius r_{tidal} and GC mass M_{GC}, may be calculated from Eq. 1.5, knowing the tidal radius for the MOCCA model and the density/potential distribution for the simulated galaxy.

The apocenter distance for a GC in an eccentric orbit, which has a lifetime comparable to a cluster with the same mass on a circular orbit, was estimated by Cai et al. (2016). Therefore, for each GC eccentric orbit, a circular orbit on which the GC will experience an equivalent mass loss can be found. The apocenter distance R_{apo}, scaled to R_C, for an eccentric orbit with an initial orbital eccentricity E_{GC} may be determined by fitting the data in their Fig. 6 Cai et al. (2016) as follows:

$$\frac{R_{apo}}{R_C} = (1 - 0.71 \cdot E_{GC})^{-5/3}. \tag{1.12}$$

The pericenter distance is then determined as $R_{peri} = 2.0 \cdot a - R_{apo}$, with a as the semi-major axis of the eccentric orbit ($a = R_{apo}/(1 + E_{GC})$). The orbital and galactocentric distances of the GC populations that have been detected in external galaxies are unknown. Because of this, the GC's galactocentric distance, R_{GC}, was selected randomly between the orbit's apocentre and pericentre (for details see Leveque et al., 2022b).

30 eccentricities have been chosen for every model in the selected subset. Each eccentricity marks a particular orbital representation in the galaxy under investigation. The MOCCA-Library eccentricity E_{GC} has been randomly chosen from the thermal distribution. R_{GC} has been sampled 30 times inside the orbit apsis for each orbital representation as mentioned above, yielding a total of 900 representations of each distinct MOCCA-Survey Database I model in the MOCCA-Library. Using this method, it is possible to populate the same model with various orbital eccentricities and galactic regions (i.e., galactocentric radial bins). The family of different model representations in the examined galaxy therefore implies that for each MOCCA-Survey Database I model a range of dynamical interactions with the galactic potential field are reproduced. Nevertheless, the mass loss for these models representations is similar to that in the MOCCA-Survey Database I models. Finally, MOCCA-Library models in a particular galactocentric bin are considered unique when they represent different MOCCA models. The internal dynamical evolution is diverse for different unique models, including mass loss, half-mass radius, and compact object composition. A comparable internal dynamical history, but with a significant variation in the external dynamical evolution, is produced by the several different representations of one particular model in the MOCCA-Library. Indeed, because of the large galactic density, a shorter dynamical friction timescale would actually draw the GCs closer to the galactic center and eventually disrupt them or possibly cause accretion into

the galactic center. At small galactocentric distances (less then a few hundred pc), the importance of the galactic halo density would be such that the GC would be dissolved, contaminating the galactic halo. If the GC would survive this catastrophic event, it would eventually be dragged into the galactic center, and merged with the NSC. However, if the GC would dissolve close to the galactic center (within a few pc), the dissolved GC would be gravitationally bound to the NSC and hence its stellar debris would be accreted onto the NSC.

The MOCCA models selected to populate external galaxies survived up to 12 Gyr. For this reason, the number of GCs for the MOCCA populations is set equal to the number of MASinGa models that survived up to 12 Gyr, sunk to the galactic center and were disrupted due to external interactions with the galaxy. This preserves both the initial number of GCs and the number of surviving GCs. As a result, each MASinGa model must be mapped to a model in the MOCCA Library given its initial mass and location. The MOCCA-Library has been partitioned into a 2D grid according to the GCs' initial galactocentric distance and initial mass bins in order to simplify the model selection process and decrease the number of repetitions of unique MOCCA Database models inside a 2D bin. Only one representation of each unique MOCCA model was chosen randomly within each matrix cell for each MASinGa model. The matrix cell was chosen using the same initial galactocentric bin from the MASinGa model, and the initial mass bin was chosen randomly from the GC IMF cumulative distribution. One model representation from the available model representations has been picked randomly to represent the chosen MASinGa model and has been successively removed from the MOCCA-Library (the detailed method description is given in Leveque et al., 2022b). This procedure was required to minimize the bias toward over-reproducing the MASinGa models with a limited number of distinctive MOCCA models. Indeed, each mass and galactocentric position bin is expected to include several instances (perhaps hundreds) of MOCCA representations, indicating repeated occurrences of the same unique MOCCA models. Our method ensures that the total number of GCs, the GC galactocentric distributions, and the GC IMF distribution for the MOCCA population would reproduce the initial conditions adopted in the MASinGa population.

1.6 Summary

This thesis comprises a collection of papers that stands as a basis for the study of GC populations around external galaxies (that is, non-MW) using simulation results from the MOCCA code.

Thus far, in Section 1.2 I gave a short introduction to GCs, describing their mean properties and their observational relevance to both the exotic stellar objects and galaxy formation and evolution. In Section 1.3, I described the main features and ingredients in the dynamical evolution of GCs, explaining the main physical processes that shape their time evolution. The two-body distant gravitational interactions among stars control the dynamical evolution of the clusters. Stellar evaporation, mass segregation, and core collapse are processes that are consequence of two-body interactions. Stellar evolution also influences the cluster evolution mainly its early stages, meanwhile the binaries provide the energy necessary to support the cluster in its post-collapse evolution. Finally, tidal interactions with the host galaxy also influence the survival of the cluster. Later, in Section 1.4, I presented the numerical techniques used to simulate the GC evolution, explaining in more detail the Monte Carlo prescription and the MOCCA code. The basic assumptions and limitation of

the Monte Carlo method are explained, together with its big advantage of being able to reproduce the dynamical evolution of large cluster within a week of compuational time. Indeed, it has been possible to build the MOCCA-Survey Database I, consisting of about 2000 GC models spanning different initial conditions. Finally, in Section 1.5, I briefly introduce the state of the art of GC population synthesis machinery. Successively, the important processes controlling their evolution are described. The computational time required to study the evolution of GC populations around external galaxies can be extremely important. As shown before, it is necessary to be able to describe how the galactic potential and tidal field influence the GC population evolution in terms of tidal mass loss, shocks, and dynamical friction. Similarly, it would be necessary to closely monitor the GC internal dynamics, which control GC mass loss, star population, and compact remnants. For this reason, I introduced a novel method that combines a semi-analytic code that describes the GC's orbital evolution with relatively good approximations, and the results from the MOCCA-Survey Database for their internal dynamical evolution. The MASinGa code used to populate and evolve the GC population has been described, and details on the approach and physical recipes used has been provided. The connection between the MOCCA-Survey Database I and the MASinGa code are explained too.

The remaining chapters consist of a set of publications, where the machinery used to populate GCs around external galaxies is introduced and its results compared with the observed properties of the Milky Way and Andromeda galaxies' GC populations. The work presented in Chapter 2 was a proof of concept work. In Leveque, Giersz, and Paolillo (2021), we determined a sub-sample of the MOCCA-Survey Database I, mimicking the observational limits of extra galactic GCs. We firstly compare the sub-sample with the observed properties of the Milky Way GCs for which we find good agreement. Successively, we identified some global features in our dataset that might be used to differentiate the dynamical state of a GC also in extra galactic GC populations.

In the second paper, Leveque et al. (2022b) included in Chapter 3, the machinery that will be used to populate the local Universe galactic GC populations with MOCCA models is presented. The semi-analytic code MASinGa was used to reproduce the Milky Way and Andromeda GC populations. The modelled GC populations are in agreement with the observed properties for both the Milky Way's and Andromeda's GC populations, showing that the machinery is working as expected. The spatial distribution of the observed GC population has been reproduced. Most of the population has been observed within 5 kpc from the galactic center, with an important increase in the observed mass profile in the central region of the galaxy, which was not fully reproduced by our simulations. The half-light radius in the simulated models are in agreement with the observed ones, with most of the GCs having a half-light radius smaller than 4 pc and hence being relatively compact as a consequence of the stronger tidal field and higher galactic density in the central galactic regions. According to the obtained results, the final NSC and SMBH masses are a few orders of magnitude less than the observed values. These discrepancies indicate that the mass build-up of the NSC and SMBH cannot be fully and solely explained by an infalling mass scenario and that the interplay of initially accreted mass, as well as interactions and merges with infalling GCs, are required.

In Chapter 4, further investigations of the Milky Way and Andromeda GC populations were carried out and presented in Leveque et al. (2022c). The results from the machinery introduced in the previous paper were extended to the BH population of globular clusters in the Milky Way and Andromeda galaxies. In particular, the properties of GCs that have either an IMBH, a BH subsystem (BHS), or neither were

determined. The typical number of GCs with a BHS, an IMBH, or neither become comparable in the galactic outskirts, whereas GCs without a significant dark matter component predominate in the inner galactic regions. According to our models, GCs with a BHS have slightly larger masses and greater half-mass radii than the rest of the population. Also, we determined the properties of binary BHs (BBHs) that have recently merged or have survived in their parent cluster up to the present day. Our results show that over 80% of merging binary BHs are formed by dynamical interactions, with the remaining merging binary BHs coming from the evolution of primordial binaries. The merger rate in the local Universe was determined, with values of $1.0 - 23\ \mathrm{yr}^{-1}\,\mathrm{Gpc}^{-3}$, depending on the assumption about the galaxy number density in the local Universe. The given value reported in our work is smaller but still comparable to that published in earlier publications. The number of BHs that are brought into the NSC by star clusters that are falling into it in during a period of 12 Gyr have been estimated as well.

The study of the evolution of the embedded gas phase in the initial evolution of GCs has been conducted in the fourth paper (Leveque et al., 2022a), included in Chapter 5. For the first time, the survival and initial evolution of GCs after the removal of primordial gas was studied in a Monte Carlo code. The mass and the Lagrangian radii evolution were followed and compared to the N-body simulation, finding good agreement. A new survey of simulations of GCs with up to $N = 500\,000$ stars for a range of different star formation efficiencies and half-mass radii was carried out in this work, finding the various initial conditions that can cause clusters to dissolve as well as those that can help them survive this early stage of their evolution. Also, an update of the Mcluster code (Küpper et al., 2011) was introduced in this work. The primary improvement of the new implementation is an updated procedure for self-consistently generating multiple stellar populations as initial conditions - up to ten at a time.

Chapter 2

Paper I - Method and first results

Monthly Notices of the ROYAL ASTRONOMICAL SOCIETY

MNRAS **501,** 5212–5228 (2021) doi:10.1093/mnras/staa4027
Advance Access publication 2021 January 4

MOCCA Survey Database: extra Galactic globular clusters. I. Method and first results

A. Leveque [1]★, M. Giersz [1] and M. Paolillo [2,3]

[1]*Nicolaus Copernicus Astronomical Center, Polish Academy of Sciences, ul. Bartycka 18, PL-00-716 Warsaw, Poland*
[2]*Dipartimento di Fisica 'E. Pancini', Universitá di Napoli Federico II, C.U. di Monte Sant'Angelo, Via Cintia, 80126 Naples, Italy*
[3]*INFN, Sezione di Napoli, via Cintia, I-80126 Napoli, Italy*

Accepted 2020 December 21. Received 2020 December 17; in original form 2020 September 1

ABSTRACT

Over the last few decades, exhaustive surveys of extra Galactic globular clusters (EGGCs) have become feasible. Only recently, limited kinematical information of globular clusters (GCs) were available through *Gaia* Data Release 2 spectroscopy and also proper motions. On the other hand, simulations of GCs can provide detailed information about the dynamical evolution of the system. We present a preliminary study of EGGCs' properties for different dynamical evolutionary stages. We apply this study to 12-Gyr-old GCs simulated as part of the MOCCA Survey Database. Mimicking observational limits, we consider only a subsample of the models in the data base, showing that it is possible to represent observed Milky Way GCs. In order to distinguish between different dynamical states of EGGCs, at least three structural parameters are necessary. The best distinction is achieved by considering the central parameters, those being observational core radius, central surface brightness, ratio between central and half-mass velocity dispersion, or similarly considering the central colour, the central V magnitude, and the ratio between central and half-mass radius velocity dispersion, although such properties could be prohibitive with current technologies. A similar but less solid result is obtained considering the average properties at the half-light radius, perhaps accessible presently in the Local Group. Additionally, we mention that the colour spread in EGGCs due to internal dynamical models, at fixed metallicity, could be just as important due to the spread in metallicity.

Key words: galaxies: star clusters: general.

1 INTRODUCTION

Star clusters are important natural laboratories for probing galaxy formation and evolution, stellar dynamics, and for testing stellar evolution theory, such as the physical nature of 'exotic' objects.

From observations, it is clear that globular clusters (GCs) are very common for all types of galaxies. They can provide a powerful diagnostic for galaxy formation, star formation in galaxies, galaxy interaction and mergers, and the distribution of dark matter in galaxies. Indeed, galaxy–galaxy interactions can trigger major star-forming events and the formation of massive star clusters. The properties of GCs systems in various galaxies can constrain the formation and the evolution of their host galaxies. In particular, Galactic GCs can be used to constrain our Galaxy's halo structure and its formation history (and references therein, Trujillo-Gomez et al. 2020; Bajkova et al. 2020; Beasley 2020).

Our knowledge about GCs increased dramatically over the last couple decades thanks to an enormous amount of very detailed observational data. In fact, the proper motion, the orbit, and the rotational signature of Galactic GCs have been determined with high precision thanks to *Gaia* Data Release 2 spectroscopy (Gaia Collaboration et al. 2018). Moreover, by taking advantage of the *Hubble Space Telescope* (*HST*) and the newest large ground-based telescopes, a detailed study of extra Galactic globular clusters (EGGCs) has become possible (Larsen et al. 2001; Côté et al. 2004; Peng et al. 2006, 2008; see Brodie & Strader 2006; Kruijssen 2014; Renaud 2020, and references therein). The main discovery in recent decades is the bimodality of GCs in the colour distribution, a common feature in all type of galaxies (Zepf & Ashman 1993; Ostrov, Geisler & Forte 1993; Kundu & Whitmore 2001, but see also Cantiello & Blakeslee 2007). The $V - I$ colour distribution for bright early-type galaxies usually shows a blue peak at $V - I = 0.95 \pm 0.02$, corresponding to [Fe/H] ~ -1.5 and a red peak at $V - I = 1.18 \pm 0.04$, corresponding to [Fe/H] ~ -0.5 (Larsen et al. 2001).

Peng et al. (2006) found, as part of the ACS Virgo Cluster Survey (Côté et al. 2004), a relation between host galaxy luminosity (and mass) and GC metallicity for metal-poor GCs in their study of early-type galaxies, which may suggest a universal enrichment during the formation of both the metal-rich and metal-poor populations. Moreover, a larger colour dispersion for metal-rich GCs was found, that is metal-rich GCs have nearly twice the colour dispersion as metal-poor GCs. Finally, metal-rich GCs show an average half-light radius smaller than the metal-poor GCs (Jordán et al. 2005). An increase of the half-light radius with galactocentric distance has been found (at least in the central regions of the galaxies, see Puzia et al. 2014), but with a shallower relationship when compared to Galactic GCs (the slope is ∼0.07 compared to ∼0.3 for Galactic GCs, see Jordán et al. 2005).

★ E-mail: agostino@camk.edu.pl

Different scenarios have been suggested to explain the observed colour distribution (Ashman & Zepf 1992; Forbes, Brodie & Grillmair 1997; Côté, Marzke & West 1998), although there is no consensus concerning its origin. At least two star formation events in the histories of such galaxies has to be invoked to generate such a bimodality, which can be triggered by major mergers (Ashman & Zepf 1992) or occur in isolation (Forbes et al. 1997). Another explanation could be, in the hierarchical scenario, the accretion of metal-poor GCs from lower mass galaxies to more massive galaxies, with the metal-rich GCs created *in situ* (Forbes et al. 1997; Harris, Harris & Poole 1999). This scenario has received support recently from the discovery of large populations of intracluster GCs (see, for instance D'Abrusco et al. 2016; Cantiello et al. 2018, 2020).

The knowledge of the dynamical state of EGGCs is even less established. The reason is that the spatial resolution of even the best telescopes is not enough to resolve the internal structure of distant GCs. Some of those GCs could be dissolving, in others an intermediate-mass black hole (IMBH) could be present, and others could be undergoing core collapse. Different GC dynamical states can reflect their different observational properties. Even if the observation cannot give such information, simulations can provide all the internal and structural properties of the system. Even if such studies may be available to Galactic GCs, they could not study all types of environments and evolutionary stages of the clusters that we see in outer galaxies, since the Milky Way (MW) is a late-type galaxy, in the relatively small Local Group (Rossi, Bekki & Hurley 2016; Shukirgaliyev et al. 2019).

Simulations show that GC systems containing a large number of black holes (BHs) are characterized by a large stellar core and half-light radii and low surface brightness values (Askar, Arca Sedda & Giersz 2018; Askar et al. 2019). On the other hand, it is expected that systems containing an IMBH should be characterized by a high central velocity dispersion and high central surface brightness (CSB) values. However, it is not easy to determine, using global observational properties, whether a particular GC could contain an IMBH, a BH subsystem (BHS), or neither (Askar et al. 2018; Arca Sedda, Askar & Giersz 2018, and reference therein).

In this series of papers, our goal is to find a correlation between the global properties of EGGCs and their internal dynamical state and to find some observational properties that would help us to distinguish between these dynamical states. Characteristics that differentiate between GC–galaxy interactions and internal GCs' dynamics could be crucial for the study of EGGCs and the history of their host galaxy. For this reason, it would be important to investigate the correlations between the internal dynamics and the observed global properties of GCs. Is the observed bimodality colour distribution due only to the spread in metallicity, or can the dynamical evolution also play a role? If yes, how important could it be? How important is the internal dynamical evolution for other observed parameters? Could the internal dynamical evolution influence the correlations between distance from host galaxies (such as size (Jordán et al. 2005; Puzia et al. 2014) or an observed link between the presence of a BHS and the structural properties of GCs (Paolillo et al. 2011) and the GC's properties?

In order to verify if our project goals are achievable, we will first compare our model data set with MW GCs (MWGCs), since it is easier to observe them and to determine their more detailed properties. Successively, we will try to apply our method to EGGCs, setting a distance limit for which our approach would be valid. This first paper is a proof of concept: we will identify a subsample in our data set that would mimic the observational limit of EGGCs, and immediately try to identify some global features in our data set. In the following papers, we would like to populate an external galaxy with its GCs population (with properties according to observed distributions) using models from the MOCCA Survey Database and to apply the procedure described in this paper to our simulated EGGC population.

The structure of the paper is as follows: in Section 2, we provide information on GC simulation models that were used in this study and we describe the method used to determine global parameters of the GCs and the selection of the models by comparison with the observations of Galactic GCs (Harris 1996, updated 2010). In Section 3, we present the results, in Section 4, we discuss the results, and in Section 5, we provide our final conclusions and describe our future work.

2 MODELS

For the scope of this work, we use the results from the MOCCA Survey Database (Askar et al. 2017) carried out using the MOCCA code (Hypki & Giersz 2013). The code simulates and follows the long-term dynamical evolution of spherically symmetric stellar clusters, based on Hénon's Monte Carlo method (Hénon 1971; Stodolkiewicz 1982, 1986; Giersz et al. 2013, and references therein, for details about MOCCA code). Stellar and binary evolution are followed using the prescription from the Single Star Evolution/Binary-Star Evolution (SSE/BSE) codes (Hurley, Pols & Tout 2000; Hurley, Tout & Pols 2002), whereas the strong interactions (binary–binary and binary–single) are handled by the FEWBODY code (Fregeau et al. 2004). Escaping stars from tidally limited clusters are treated as described in Fukushige & Heggie (2000).

The MOCCA Survey Database (Askar et al. 2017) consists of nearly 2000 real star cluster models that span a wide range of initial conditions, provided in table 1 in Askar et al. (2017). For half of the simulated models, supernovae (SNe) natal kick velocities for neutron stars (NSs) and BHs are assigned according to a Maxwellian distribution, with velocity dispersion of 265 $\mathrm{km\,s^{-1}}$ (Hobbs et al. 2005). In the remaining cases, BH natal kicks were modified according to the mass fallback procedure described by Belczynski, Kalogera & Bulik (2002). Metallicities of the models were selected as follows: $Z = 0.0002$, 0.001, 0.005, 0.006, and 0.02. All models were characterized by a Kroupa (2001) initial mass function (IMF), with a minimum and maximum initial stellar mass of 0.08 and 100 $\mathrm{M_\odot}$, respectively. The GC models were described by King (1966) with central concentration parameter values $W_0 = 3$, 6, and 9. They had tidal radii (R_t) equal to: 30, 60, and 120 pc, while the ratios between R_t and half-mass radius (R_h) were 50, 25 or the model was tidally filling. The primordial binary fractions were chosen to be 5 per cent, 10 per cent, 30 per cent, and 95 per cent. Models characterized by an initial binary fraction equal to or lower than 30 per cent had their initial binary eccentricities selected according to a thermal distribution (Jeans 1919), the logarithm of the semimajor axes according to a flat distribution, and the mass ratio according to a flat distribution. For models containing a larger binary fraction, the initial binary properties were instead selected according to the distribution described by Kroupa (1995), so-called eigen-evolution and mass feeding algorithms. The models consist of 4×10^4, 1×10^5, 4×10^5, 7×10^5, and 1.2×10^6 objects (stars and binaries). The Galactic potential was modelled as a simple point mass, taking as central mass the value of the Galaxy mass enclosed within the GC's orbital radius. The GC rotation velocity was set to 220 $\mathrm{km\,s^{-1}}$ for the whole range of Galactocentric distances. The GCs were assumed to move on a circular orbit at Galactocentric distances between 1 and 50 kpc. As shown by Askar et al. (2017) and will be

Table 1. Results of p-values from the KS test, for different hypotheses and for R_c (left), CRVD (centre), and CSB (right). The best p-values are marked in bold.

	R_c			CRVD			CSB		
Hypothesis	HB	HM	BM	HB	HM	BM	HB	HM	BM
Less	**0.834**	**0.989**	**0.749**	**0.904**	**0.658**	0.002	0.465	0.191	0.645
Two-sided	0.735	0.002	0.082	0.048	0.371	0.004	**0.840**	**0.214**	**0.798**
Greater	0.390	0.001	0.041	0.002	0.186	**0.660**	0.622	0.107	0.433

Notes: HB: Harris–Baumgardt catalogues comparison; HM: Harris–MOCCA catalogues comparison; and HB: Baumgardt–MOCCA catalogues comparison.

shown in Sections 3.1 and 3.3 also, the MOCCA models reproduce observational properties of MWGCs relatively well. Despite all of the weaknesses of the assumptions used to generate them, in Section 4 we will argue that the MOCCA models can be used to populate the GC systems of other galaxies. with some caution and with some additional assumptions.

The simulations present in the MOCCA Survey Database (Askar et al. 2017) project include, as output, snapshots of data containing the details for all stars and binaries in the cluster model. These are produced periodically during the cluster evolution and consist of, at a given time, information of spatial, kinematic, and stellar evolution properties of each stars (such as positions from the centre of the clusters, velocities, mass, and radius), plus binary parameters (such as semimajor axis and eccentricity) for each binary in the system. Information about the global properties of the GCs and about each star and binary in the system is available for such simulations.

2.1 Projection and photometry

As a first step, we projected the positions and velocities of stars from each snapshot on the plane of the sky. For binaries, we additionally computed the barycentric orbit of each star using the semimajor axis and eccentricity of the orbit and the mass of each star in the binary centre of mass. In this way, we can treat the binary as resolved, considering positions and velocities of single stars in the binary, or unresolved, considering position and velocity of the binary centre of mass: this will be useful to determine the importance of resolving binary systems to the integral properties of observed Galactic GCs and the determination of the velocity dispersion profile (VDP, with the next generation telescopes it may be possible for GCs in the Local Group e.g.). In this work, we will consider only MOCCA models at the 12 Gyr snapshot and unresolved binaries.[1]

The absolute magnitude for each star has been calculated and assigned using the FSPS code (Conroy, Gunn & White 2009; Conroy & Gunn 2010). FSPS is a stellar population synthesis code, returning the integrated spectra and the luminosity in different bands (e.g. Johnson–Cousins, *HST* WFPC2, *HST* ACS, etc.) for a given stellar population. The main advantage of this software is its flexibility, because the user can choose their preferred set of isochrones and stellar spectral libraries (see Conroy & Gunn 2010 for more details). Even though the FSPS code is principally aimed to study galaxies and their stellar and dust content through their observed photometry and spectral energy distributions, we modify the code in order to obtain the integrated absolute magnitude of the entire GC, summing up all stars' flux contributions in the system. We obtained also the integrated absolute magnitude of the system at different cluster radii (radii containing 1 per cent, 10 per cent, 50 per cent, 70 per cent, and 100 per cent of the total luminosity and at the observational core radius[2] R_c). In our study, we considered only the filters commonly used to observe GCs, that are: from Johnson–Cousins system U, B, V, R, I; from Sloan Digital Sky Survey (SDSS): u, g, r, i, z; from *HST* Wide Field and Planetary Camera 2 (WFCP2): F255W, F300W, F336W, F439W, F450W, F555W, F606W, F814W, F850LP; from *HST* Advanced Camera for Surveys (ACS) F435W, F474W, F555W, F606W, F625W, F775W, F814W, F850LP; from *HST* Wide Field Camera 3 (WFC3)-UVIS F218W, F225W, F275W, F336W, F390W, F438W, F475W, F555W, F606W, F775W, F814W, F850LP; from *HST* WFC3-IR F098M, F105W, F110W, F125W, F140W, F160W. Moreover, it is possible to shift the star's spectrum due to the Doppler effect according to its line of sight velocity or due to the redshift of the entire GC. For the purpose of this paper, we did not apply any shift in the calculation. In this proof of concept study, we did not consider any source of absorption or reddening in our calculation.

The core radius (for which we mean the observational core radius) and the CSB of each snapshot has been determined by applying a fit to the cumulative luminosity distribution (obtained from the snapshot) with the King (1962) approximation ($L(r) = \pi \cdot R_c \cdot \mathrm{CSB} \cdot \ln(1 + (r/R_c)^2)$, with $L(r)$ being the cumulative luminosity distribution at radius r, R_c the core radius, and CSB the central surface brightness). The core properties are obtained as cumulative contribution of each star inside the core radius.

Finally, we applied a best fit (quadratic polynomial for Standard and BHS models; sum of two exponential for IMBH models[3]) to the luminosity weighted VDP, obtained from the infinite projection of the snapshot (Mashchenko & Sills 2005). The velocity dispersion at different cluster radii has been determined by the value given by the best-fitting function at the desired radii (we consider the central velocity dispersion of the system to be the value obtained at 1 per cent light radius). A luminosity cut-off, for a star, of 5000 $L_\odot$[4] has been applied to the determination of GCs' properties (total luminosity, properties at different light radii), in order to reduce the fluctuation due the presence in the system of only a few very luminous stars. The VDPs obtained from only luminous stars could be very noisy and strong fluctuations are expected due to the presence of luminous

[1]For the comparison with MWGCs we used only 12 Gyr snapshots. In the next papers in the series, we will also use 6 and 9 Gyr snapshots for EGGCs.

[2]In this paper, we defined the observational core radius as the distance from the centre where the average surface brightness is half of the CSB, and the half-light radius (R_{hl}) as the distance from the centre of the cluster contains half of the full cluster luminosity, as described in King (1962).

[3]We used the best-fitting procedure present in PYTHON SCIPY library, *scipy.optimize.curve_fit*.

[4]Value calculated from the maximum apparent magnitude, reddening, and distance during observation of velocity dispersion in MWGCs (e.g, Carretta et al. 2009; Lane et al. 2011). See Baumgardt & Hilker (2018) and citation therein for more information.

stars (in particular in the central part of IMBH models). Applying the fitting procedure to the VDP is the simplest approach to avoid those fluctuations while keeping the shape of the VDP.

2.2 Model selection

Askar et al. (2017) showed that models from the MOCCA Survey Database are in relatively good agreement with the observational properties of Galactic GCs (Harris 1996, updated 2010). However, the final goal for our research is to compare our models with EGGCs. For this reason, we should consider a subsample of the data base which would mimic the observational limits and realistic properties of EGGCs.

The first limitation we imposed, is to consider only models that have $L > 2 \times 10^4\,L_\odot$ (or equivalently, the absolute M_V magnitude, $M_V < -6.5$), in order to mimic the observational limit for distant EGGCs (a nominal value of $L > 2 \times 10^4\,L_\odot$ was chosen, even if with *HST* observations is possible to go below this value). The sample of selected models actually coincides with models having the number of objects (i.e. stars and binaries in a cluster) at 12 Gyr $N > 10^5$ and the number of initial objects $N_0 > 10^5$. Indeed, for models with a high binary fraction (95 per cent of the total number of objects in the system) many binaries are dissolved during the very early cluster evolution, increasing the count of objects in the system. For this reason, both conditions on the minimum number of objects (initial and at 12 Gyr) are important.

The second limitation we imposed, is to restrict our analysis to models in which the fallback prescription (Belczynski et al. 2002) was used. Indeed, different prescriptions have been proposed to match the observed mass ranges and spin properties of stellar BHs, since the observations of gravitational waves with Laser Interferometer Gravitational-Wave Observatory (LIGO/Virgo). The most accepted scenario is the presence of mass fallback on the BHs during SN explosion (Belczynski et al. 2017). We decided to limit our subsample to models for which this prescription has been applied.

The strength and the importance of the tidal field (that is the 'external' field of host galaxy) is determined by the ratio between the tidal radius R_t and the half-mass radius R_h: models with higher R_t/R_h ratios experience less influence from the tidal field with respect to those with smaller ratios. For high values, the system is deeply inside its tidal field (i.e. all stars are deep inside the GC potential well), that would mean that the system will be able to freely expand before feeling the action of the tidal field. The system in this case is usually called 'tidally underfilling model'. Instead, when the system fills its Roche lobe entirely, the importance of the tidal field in the evolution of the system is very strong (from the very beginning), substantially increasing the number of escaped stars. This system is usually called 'tidally filling model'. So, in the case of a strong tidal field, and for a model that is tidally filling, the escape rate could be strong enough to dissolve the system in a time smaller than the Hubble time. Marks & Kroupa (2012) find a weak relation between the half-mass radius and the mass of newly formed star clusters ($R_h(pc) \propto (M/M_\odot)^{0.13}$), implying that at early stages, the clusters are very dense and strongly tidally underfilling. Recently, many theoretical (Marks & Kroupa 2012; Kruijssen 2014; Wang 2020) and observational (Webb, Sills & Harris 2013; Webb et al. 2016) works were published supporting the idea that initially clusters are born very concentrated and deeply tidally underfilling. As it will be discussed in the next section, we will consider only systems that were initially tidally underfilling.

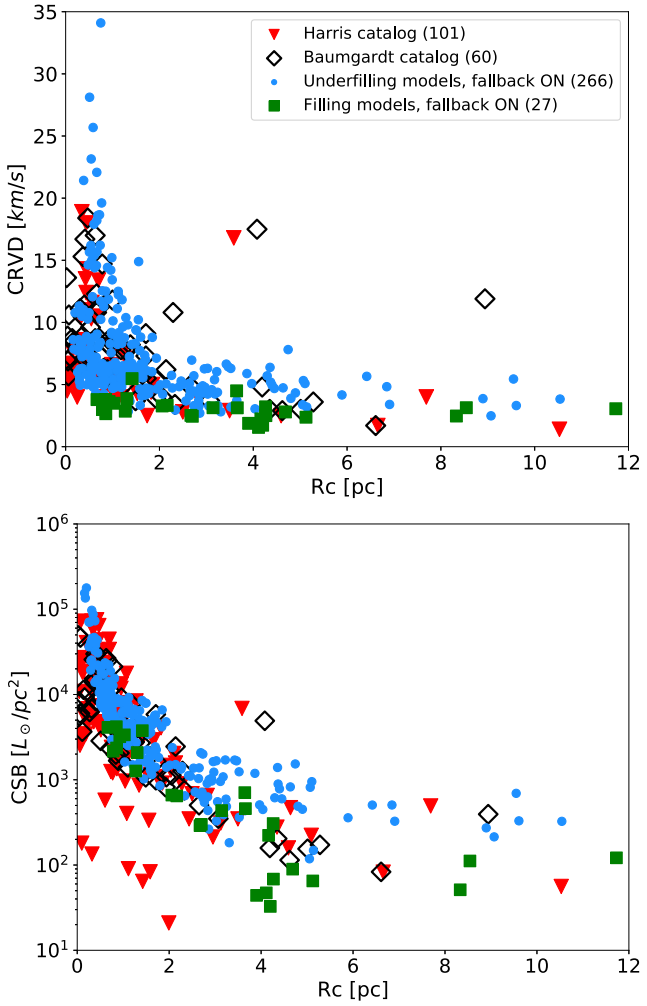

Figure 1. R_c versus CRVD (top) and CSB (bottom), for models at 12 Gyr with mass fallback prescription, tidally filling and underfilling models (blue circles and green squares, respectively). Red triangles are the Galactic GCs from Harris (1996, updated 2010) catalogue, and empty black diamonds from the Baumgardt catalogue (Baumgardt & Hilker 2018). For those two catalogues, only GCs with $M_V < -6.5$ are plotted. In parenthesis, the number of models for each catalogue.

3 RESULTS

3.1 Comparison with observed Galactic globular clusters

First, we want to show that our selected sub-samples are in agreement with observations of MWGCs and their properties. This would ensure us that our model selection is able to represent observed GCs, and we can apply it also to the EGGCs. We assume that MWGCS are similar to EGGCs and the formation scenario for old GCs is similar.

In Fig. 1, we compare the core radius (R_c) versus the CSB and central radial velocity dispersion (CRVD) respectively for our selected models with the Harris (1996, updated 2010) catalogue and Baumgardt (private communication for central surface brigthness, Baumgardt & Hilker 2018) catalogue. In Harris (1996, updated 2010) catalogue, for some GCs the central structural parameters have not been observationally determined; for this reason, we selected only GCs for which those quantities are present in the catalogue and therefore only such MWGCs are presented in figures in this paper. Moreover, in order to compare our models with the two catalogues,

we imposed an absolute magnitude limit $M_V < -6.5$ (as imposed on our subsample) on the observational data. The total number of models in our selected sample is 266 for tidally underfilling models, meanwhile the Harris (1996, updated 2010) catalogue has 101 and the Baumgardt catalogue has 60. As one can see from those two figures, the tidally filling models cannot reproduce the high CSB and CRVD, as observed in Galactic GCs, but can actually match low CSB MWGCs, which are systems having low mass ($< 2 \times 10^5\,M_\odot$) and low V absolute magnitude ($M_V \gtrsim -7$) in the considered subsample. Although we cannot exclude that some tidally filling models can reproduce properties of some low mass or close to disruption MWGCs, from the point of view of EGGCs such clusters will not be observable (or difficult to observe). Also the number of MWGCs which can be described by only tidally filling models is small, so if such models are not taken into account they will not spoil our statistic.Indeed, tidally filling clusters evolve much faster and lose much more stars than underfilling ones. So, at present time their number of stars is expected to be relatively small, that would mean a low CSB and star density, making them difficult to observe in EGGCs populations. The imposed cut-off for number of stars in our analysis may filter them out. For those reasons, we decided to exclude them from our sample and focus on underfilling models only.

Moreover, in Fig. 1, there are a few models with CRVD greater than 20 $\mathrm{km\,s^{-1}}$, values that are not present in the observational catalogue. Those models are connected with very massive IMBHs ($>10^4\,M_\odot$). Such high values for the IMBHs are obtained because in the simulation it is assumed 100 per cent accretion on to the BH; this is too optimistic of an assumption, so the real masses of IMBHs should be smaller than obtained in the MOCCA simulations. We decided to keep such models in our sample to show the properties of GCs which harbor such massive IMBHs. Since the number of such systems is small (only 6), this decision should not strongly influence our statistics.

The distribution of the central parameters (R_c, CSB, and CRVD) for the two catalogues and our selected models are shown in Fig. 2. In order to verify that such models are statistically in agreement with the two catalogues, we applied a two-sample Kolgomorov–Smirnov test (KS test) to those distributions. The KS test is used to compare two sample, quantifying the distance between the cumulative distribution functions, in order to verify the null hypothesis that the two samples are drawn from the same distribution. However, it is also possible to apply the alternative hypothesis, according to which the cumulative distribution of one sample is 'less' or 'greater' than the cumulative distribution of the other sample. In KS test terminology, a cumulative distribution that is 'greater' than one other means that its mean and median will be smaller than the mean and median of the other distribution (vice versa for 'smaller'). In a few words, applying this alternative hypothesis means that the two distributions have the same shape, but the mean values are shifted, one with respect to the other. We applied also the alternative hypothesis ('less' or 'greater') to our sample, and a threshold value of $p \geq 0.17$, meaning a significance of 2σ (instead, $p \geq 0.8$ would mean a significance of σ). Due to observational and systematic errors, it is possible that some values could be over- or underestimated in the observed samples: a shift between the observed and our distributions may be expected, so the alternative hypothesis should be tested too. The p-values for different hypotheses (alternative and null) and for the three parameters are showed in Table 1. The results of the KS test show that our sample has a similar distribution to the two observational catalogues, with small differences: the R_c of the two observational catalogues has a smaller mean radius compared to our sample; the Harris catalogue and our sample show a similar mean value for CSB, meanwhile our sample has a smaller mean CRVD when compared to Baumgardt catalogue. In Table 1, we also show the results of the KS test between the two observational catalogs. It is possible to see that the Harris (1996, updated 2010) catalog has smaller mean values compared to the Baumgardt & Hilker (2018) catalogue. Considering that the two catalogues are based on the same observational data, but two different approaches have been used (in the Harris 1996, updated 2010 catalogue, a fit of a King 1966 profile has been applied to the observations, meanwhile in the Baumgardt & Hilker 2018 catalogue a fit with N-body simulation has been applied), that differ from our method, some systematic shifts in the distribution (between the three samples) are expected. We should remember that in the Harris (1996, updated 2010) catalogue, for some collapsed GCs, it was arbitrarily assumed that the concentration parameter is equal to 2.5. Overall, those results show that our sample represents well the observed Galactic GCs; for this reason, as will be explained in detail in Section 4, we can make a first-order assumption that this will also be true for observed EGGCs.

3.2 Dynamical model selections

In the standard picture of the dynamical evolution of GCs, a GC would undergo a core collapse, unless a central source of energy can support the energy demand of the system. This supply is generally related to the energy released during the interaction of stars and binaries in the centre. After the early phase of SN explosions, some BHs can remain in the system (if the natal SN kick is not too high, if the gravitational potential is really deep, or if the SN explosion happened in a binary with some energy being absorbed by the orbit) and quickly segregate in the centre of the cluster, forming the so-called BHS. This subsystem is not entirely decoupled from the rest of the GC and its evolution is governed by the energy demands of the host GC (Breen & Heggie 2013a, b; Giersz et al. 2019). However, if the initial central density of the system is extremely high ($>10^8\,M_\odot\,\mathrm{pc^{-3}}$), the dynamical collision between massive BHs and runaway mergers of main-sequence (MS) stars and BHs in the central region increase strongly, leading to a possible formation of an IMBH in the first phase of the cluster evolution (time smaller than or roughly 1 Gyr; Fast scenario, Giersz et al. 2015). If the first condition is not met, but not all BHs have been expelled from the system and only a few BHs are left in the system at the time of the cluster core collapse, an IMBH can be still formed via multiple mergers or collisions of BHs and other objects during dynamical interactions (Slow scenario, Giersz et al. 2015). The dynamical evolution and properties of the GCs strongly depends on the presence of an IMBH (deep gravitational potential, kicking out all the massive BHs), or of a BHS, or the absence of both.

We dived our selected sample in three dynamical subsamples, according to the following:

(i) if an IMBH (BH with mass $> 500\,M_\odot$) is present in the system, it has been classified as *IMBH model*;

(ii) if the number of BH ($N_{\rm BH}$) present in the system is $\geq$50, it has been classified as *BHS model*; if $20 < N_{\rm BH} < 50$, we checked if the system is not experiencing the core collapse: if the system is in balanced evolution (Breen & Heggie 2013a, b), it has been also classified as *BHS model*;

(iii) if none of the previous conditions has been satisfied, the system has been classified as *Standard model*.

In the case of systems with $20 < N_{\rm BH} < 50$, we fit a third-order polynomial to the evolution of the 10 per cent Lagrangian radius of the system; if the time derivative of this quantity at 12

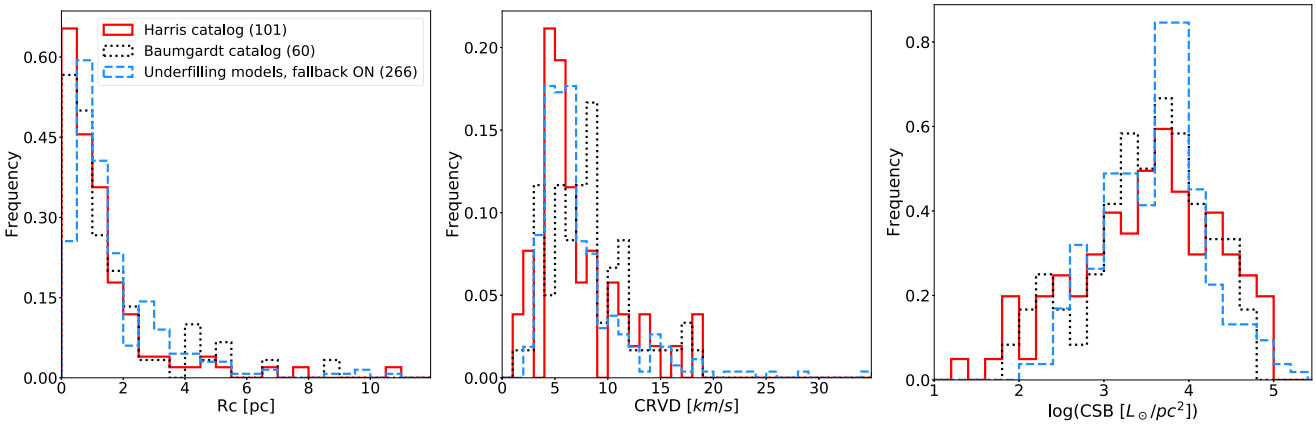

Figure 2. R_c (left), CRVD (centre), and CSB (right) histograms for our selected models (blue dashed), the observation of Galactic GCs from Harris (1996, updated 2010) catalogue (red solid) and the Baumgardt catalogue (Baumgardt & Hilker 2018, black dotted). In parenthesis, the number of models for each catalogue. The histograms have been normalized so that the area under the histogram will sum to 1.0. The bin sizes are 0.5 (R_c), 0.7 (CRVD), and 0.2 (CSB), respectively. *Legend:* HB: Harris–Baumgardt catalogues comparison; HM: Harris–MOCCA catalogues comparison; and HB: Baumgardt–MOCCA catalogues comparison.

and 13 Gyr is negative and less than -2.5×10^{-3} pc Gyr^{-1}, the system is considered in collapse, and classified as a Standard model, otherwise as a BHS model. The limit on the number of BHs was chosen by analysing many models by eye: we checked that systems having a number of BH greater than 50 were dynamically in balanced evolution, meanwhile this is not always true for a small number of BHs. In balanced evolution, the energy flow through the cluster half-mass radius equals the energy generated in the cluster core. In this case, the energy is provided by the energy produced in BHS by dynamical interactions of BH–BH binaries with other objects. As a results of those interaction, more and more BHs are kicked out from the system, and their number drops in time. In order to keep the required amount of energy production, the number of dynamical interactions has to increase, implying an increase of the central density. Finally, when the number of BHs is too small to generate the required amount of energy, the central part of the system enters the well-known core-collapse phase.

The choice of a minimum mass of 500 $M_\odot$ for a BH to be classified as IMBHs follows from the fact that for smaller masses the IMBH will still substantially move around in the central parts of the system (see Giersz et al. 2015), so their influence on the system structure will be smeared out and also the central structure will still be similar to that of a recently collapsed cluster.

The numbers of models for each submodel category are: IMBH – 104; BHS – 93; and Standard – 69. We would like to strongly emphasize that the relative number of models with different evolution types depends on the initial conditions chosen for the MOCCA simulations and should not be taken as a real number which can be confirmed by observations. Indeed, it is well known a strong degeneracy of final dynamical state (at 12 Gyr) and their global properties with respect to the initial conditions.

In Fig. 3, we show the position of such submodels in the R_c–CSB and R_c–CRVD planes. As expected, the BHS models have (on average) a large R_c value ($\gtrsim 2.0$ pc) and relatively low CRVD ($\lesssim 7.5$ km s^{-1}) and CSB ($\lesssim 10^4$ $L_\odot$ pc^{-2}), meanwhile systems with an IMBH show a small core (< 2.0 pc) and high values for the central parameters (CRVD can reach values of >12.0 km s^{-1} and CSB can reach values of $>10^4$ $L_\odot$ pc^{-2}). However, both submodels overlap with the Standard models in those two planes. This complicates the proper distinction between those systems from an observational point

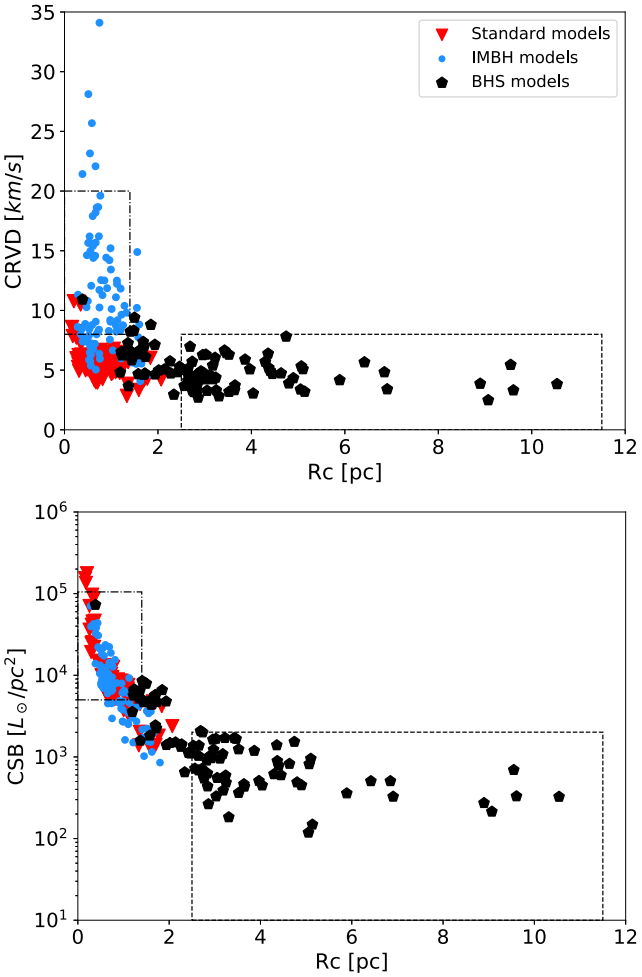

Figure 3. R_c versus CRVD (top) and CSB (below), for the three different dynamical models (red triangles for Standard, blue circles for IMBH, and black pentagons for BHS, respectively). The dashed lines represent the cut applied for 'large core radii' clusters ($R_c \geq 2.5$ pc, CRVD ≤ 7.5 km s^{-1}, and CSB $<2 \times 10^3$), meanwhile the dashed–dotted line represents the cut applied for 'small core radii' clusters ($R_c \leq 1.4$ pc, CRVD ≥ 8.0 km s^{-1}, and 5×10^3 <CSB<10^5).

of view: one can clearly see that such pairs of structural parameters are not enough for this purpose.

We applied some boundary conditions for observational cluster properties, in order to define two regions where only (or mostly) IMBH and BHS models are present, named 'small core radii clusters' and 'large core radii clusters', respectively. The 'small core radii clusters' (IMBH) models have:

(i) $R_c \leq 1.4$ pc;
(ii) $8.0 < \mathrm{CRVD} < 20.0\,\mathrm{km\,s^{-1}}$;
(iii) $5 \times 10^3 < \mathrm{CSB} < 10^5\,\mathrm{L_\odot\,pc^{-2}}$,

meanwhile 'large core radii clusters' (BHS) models have:

(i) $R_c \geq 2.5$ pc;
(ii) $\mathrm{CRVD} \leq 7.5\,\mathrm{km\,s^{-1}}$;
(iii) $\mathrm{CSB} < 2 \times 10^3\,\mathrm{L_\odot\,pc^{-2}}$.

With this selection criteria, the total number of 'large core radii clusters' model is 59, of which all are BHS models, with no IMBH and Standard models; on the other hand, the total number of 'small core radii clusters' model is 49, of which 43 are IMBH models, 5 Standard models and only 1 BHS model. It is important to underline that this number of models should not be taken as a real number, but strongly depends on the initial conditions chosen for the MOCCA simulations.

In Tables 2 and 3, we show the list of observed GCs that satisfied the conditions for 'small core radii' and 'large core radii' models respectively, from Harris catalogues. We consider only GCs for which all properties are available (that are R_c, CRVD, and CSB), since in the Harris catalogue not all system has a CRVD value and in the Baumgardt catalogue the CSB is not given for all models (private communication). We have considered only those clusters that have been selected in both catalogues (Harris and Baumgardt).

3.3 Comparison with previous works

In Fig. 4, we compared our selection of Galactic 'large core radii' systems (which correspond to BHS models), with the list of MWGCs reported in Askar et al. (2018) which could contain a BHS, and the list reported in Weatherford et al. (2019), considering only GCs that retain a number of BH $N_{\mathrm{BH}} > 50$. While in Askar et al. (2018), a shortlist of 29 Galactic GCs has been reported and the number of GCs shortlisted in Weatherford et al. (2019) with $N_{\mathrm{BH}} > 50$ includes 28 Galactic GCs, in the current work only three have been reported among the MWGCs. However, some of the GCs listed in Weatherford et al. (2019) with $N_{\mathrm{BH}} > 50$ are actually in the 'small core radii' models region. This is not completely surprising, since the author did not impose any constraint on the CSB and number of BH inside the GC. Also in Fig. 4, we compared our 'small core radii' clusters (that correspond mostly to IMBH), with the list of GCs reported in Arca Sedda, Askar & Giersz (2019). In their work, 35 observed Galactic GCs are likely to harbour an IMBH, meanwhile in our work only 15 do.

The different reported number could be explained by the differences in model selection used by the different groups. Askar et al. (2018) and Arca Sedda et al. (2019) also used the MOCCA Survey Database results to identify BHS and IMBH models, respectively, but with different selection criteria. The authors in Askar et al. (2018) selected models according to their CSB and the observed present-day half-mass relaxation time. In Arca Sedda et al. (2019), the authors labelled Galactic GCs as IMBH (or BHS) according to how many MOCCA models (among the 10 closest in 6D observational parameter space) contain an IMBH (or a BHS respectively). For this purpose, they used as properties the visual and bolometric total luminosity, half-mass and core radii, Galactocentric distance, and average and CSB. We would like to underline that in both those two works, the authors used all of the models from the MOCCA Survey Database, including those models with no mass fallback prescription and tidally filling models (which we excluded, as explained in Section 2.2). Instead, in Weatherford et al. (2019), the authors correlate the number of BHs in the system with the mass segregation parameter Δ, obtained from the 2D-projected snapshots of models presented in the CMC Cluster Catalog (Kremer et al. 2020). They did not use any other parameters to distinguish between IMBH, Standard, and BHS models. As will be shown in Section 3.5, at least three observational parameters can guarantee a relatively solid distinction between different cluster evolution histories.

Moreover, the strong and conservative limitations that have been used in the current work influence the reported number of MWGCs harbouring an IMBH or a BHS.

Indeed, we have considered only observed GCs with $M_V < -6.5$, for which all properties are available, and with a conservative choice of a minimum R_c of 2.5 pc. The reason for this choice is to consider two regions of the GCs' parameter space (R_c, CRVD, and CSB) that would mostly contain the two dynamical models of interest (IMBH and BHS), reducing as much as possible the region where those two could overlap with Standard models. Moreover, we want to use parameters and regions that would be relatively easy to define (and to observe) for EGGCs, which are the main target of our project. Additionally, in Askar et al. (2018, see also Arca Sedda et al. 2018), the limitations are less conservative. The authors considered all clusters with $\mathrm{CSB} < 10^4\,\mathrm{L_\odot\,pc^{-2}}$ and observed present-day half-mass relaxation times < 0.9 Gyr. This is clearly visible in Fig. 4 (on the left-hand side): if we were to consider clusters with radius ≥ 2.0 pc, regardless of whether CRVD information is available or not, the number of 'large core radii' models would increase up to $\sim$17. Similarly, a less conservative limitation has been applied in Arca Sedda et al. (2019). In this case, the main difference is the observational limit we imposed on our models ($M_V < -6.5$): by considering only those that satisfied this limit, their number of shortlisted GCs would decrease to 17. If we would consider clusters independently of all information being available, the number of GCs that we shortlisted as possibly harbouring an IMBH would increase up to $\sim$30. In a photometric and spectroscopic study, Lützgendorf et al. (2013) listed a sample of 13 IMBH MWGC candidates, a similar number reported in this paper. In Table 2, we also report the cluster listed in that work.

Overall, our model selection of 'small' and 'large core radii cluters' is in rough agreement with the results of previous work. However, the definition of 'small' and 'large core radii' clusters could be useful, from an observational point of view, for the identification and classification of the dynamical state of real GCs, knowing only the global properties of the system.

3.4 Colour distribution

A well-known property of observed Galactic and EGGCs is the bimodality (or sometimes even multimodality) in colour distribution. Even if it is up for debate whether or not it is universal features of GCs, it seems to be observed in most of the GC populations around early-type galaxies. This feature has been correlated with a bimodality (or multimodality respectively) in metallicity.

We tested, for fixed metallicities, the $V-I$ colour distribution for our sample of models. In Fig. 5, we show the $V-I$ colour distribution for models with solar metallicity ($Z = 0.02$, corresponding to

Table 2. Observational properties from the Harris (1996, updated 2010) catalogue (name, R_c, and half-light radius in parsec, CRVD in km s^{-1}, and CSB in L$_\odot$ pc^{-2}) for observed Galactic GC labelled as 'small core radii' in this work, that are likely to host an IMBH. In bold, the clusters that have been reported also in Arca Sedda et al. (2019), in bold italic the clusters that have been reported also in Lützgendorf et al. (2013).

Name	R_c (pc)	R_{hl} (pc)	CRVD $\pm$ $\delta_{\rm CRVD}$ (km s^{-1})	CSB (L$_\odot$ pc^{-2})
NGC 104	0.47	4.15	11.0 $\pm$ 0.3	64394.67
NGC 1851	**0.32**	**1.79**	10.4 $\pm$ 0.5	**72585.49**
NGC 2808	0.70	2.23	13.4 $\pm$ 1.2	33794.80
NGC 5286	*0.95*	*2.48*	*8.1 $\pm$ 1.0*	*11826.34*
NGC 5824	0.56	4.20	11.6 $\pm$ 0.5	30821.20
NGC 6093	**0.43**	**1.77**	12.4 $\pm$ 0.6	**32873.81**
NGC 6266	0.43	1.82	14.3 $\pm$ 0.4	33177.97
NGC 6388	0.34	1.50	18.9 $\pm$ 0.8	58190.21
NGC 6441	0.44	1.92	18.0 $\pm$ 0.2	41768.58
NGC 6541	0.39	2.31	8.2 $\pm$ 2.1	24257.73
NGC 6626	0.38	3.15	8.6 $\pm$ 1.3	17899.87
NGC 6715	0.69	6.32	10.5 $\pm$ 0.3	44550.22
NGC 6864	0.55	2.80	10.3 $\pm$ 1.5	22534.59
NGC 7078	0.42	3.02	13.5 $\pm$ 0.9	75309.51
NGC 7089	1.07	3.55	8.2 $\pm$ 0.6	17735.77

Table 3. Observational properties from Harris (1996, updated 2010) catalogue (name, R_c, and half-light radius in parsec, CRVD in km s^{-1}, and CSB in L$_\odot$ pc^{-2}) for observed Galactic GC labelled as 'large core radii' in this work, that are likely to host a BHS. In bold, the clusters that have been reported also in Askar et al. (2018), and in bold italic, the clusters that have been reported also in Weatherford et al. (2019).

Name	R_c (pc)	R_{hl} (pc)	CRVD $\pm$ $\delta_{\rm CRVD}$ (km s^{-1})	CSB (L$_\odot$ pc^{-2})
NGC 288	*3.49*	*5.77*	*2.9 $\pm$ 0.3*	*347.42*
IC4499	**4.59**	**9.35**	2.5 $\pm$ 0.5	**158.80**
NGC 6809	*2.83*	*4.44*	*4.0 $\pm$ 0.3*	*655.92*

[Fe/H] = 0.0; number of models: 45) and for subsolar metallicities (Z = 0.001, corresponding to [Fe/H] = −1.3, number of models: 137; Z = 0.005 and 0.006, corresponding to [Fe/H] = −0.55 and −0.6, respectively, number of models: 67). As can be seen from the figure, the distribution for each metallicity is unimodal, but the spread in colour can be substantial (of the order of ∼ 0.2 mag for subsolar metallicity, colour spread that would correspond to a spread in metallicity of [Fe/H] ∼ 0.6[5]), in agreement with the observational distribution (Larsen et al. 2001). From this figure it is also possible to note some signs of a slightly different spread in the colour, for different dynamical states, at fixed metallicity: this could imply that the internal dynamical evolution and state of GCs could influence the colour distribution. Finally, the value of this spread is comparable to the spread due to a small difference in metallicities: the colour spread for submetallicities Z = 0.001 and 0.006 is of the order ∼ 0.2 dex. However, this is difficult to confirm, since the number of models is not big enough to be statically strong and further studies are needed. Indeed, MOCCA Survey Database were aimed to reproduce MWGCs, resulting with metallicities similar to the observe MWGCs. It is important to underline here that in order to properly reproduce the observed EGGC colour distribution, a better covering of metallicities would be needed.

The importance of the spread in colour distribution for models at fixed metallicity could be explained by the interplay of different initial conditions and different dynamical history. Initial concentration and initial binary fraction are the main properties that drive the dynamical evolution of the system (core collapse, disruption, etc.), since they mostly influence the interaction and collision rate of stars: lower or higher numbers of stars could be removed, depending on the density and concentration of the system. The general fate of the system has been explained in Section 3.2, which depends on the initial conditions. This could be even enhanced by the presence of an IMBH (and depending on the mass of the IMBH), by a strong tidal field, or during core collapse (in Standard models, e.g.). Finally, the global GC evolution does not strongly depend on its metallicity, indeed the difference in the observed r_{hl} for blue or red GCs could be explained by a different number of BHs in the system (Downing 2012), or by metallicity-related stellar evolution effects (Sippel et al. 2012).

In Fig. 6, we show the $U - I$ colour at different radii (central, core, and R_{hl}) versus CRVD. It is possible to note that the models are barely distinguishable when considering the colour at R_{hl}, and the differentiation is getting better for smaller radii. However, it is not possible to distinguish properly the three dynamical models only considering two properties of the system, even if those are the central properties. In order to better separate the different dynamical models, more than two (central) properties of the system are needed.

3.5 3D space parameters

As was shown in the previous sections, considering only two global GC properties is not enough to divide the dynamical models into

[5]We used the calibration in Kissler-Patig et al. (1998), as was done in Larsen et al. (2001).

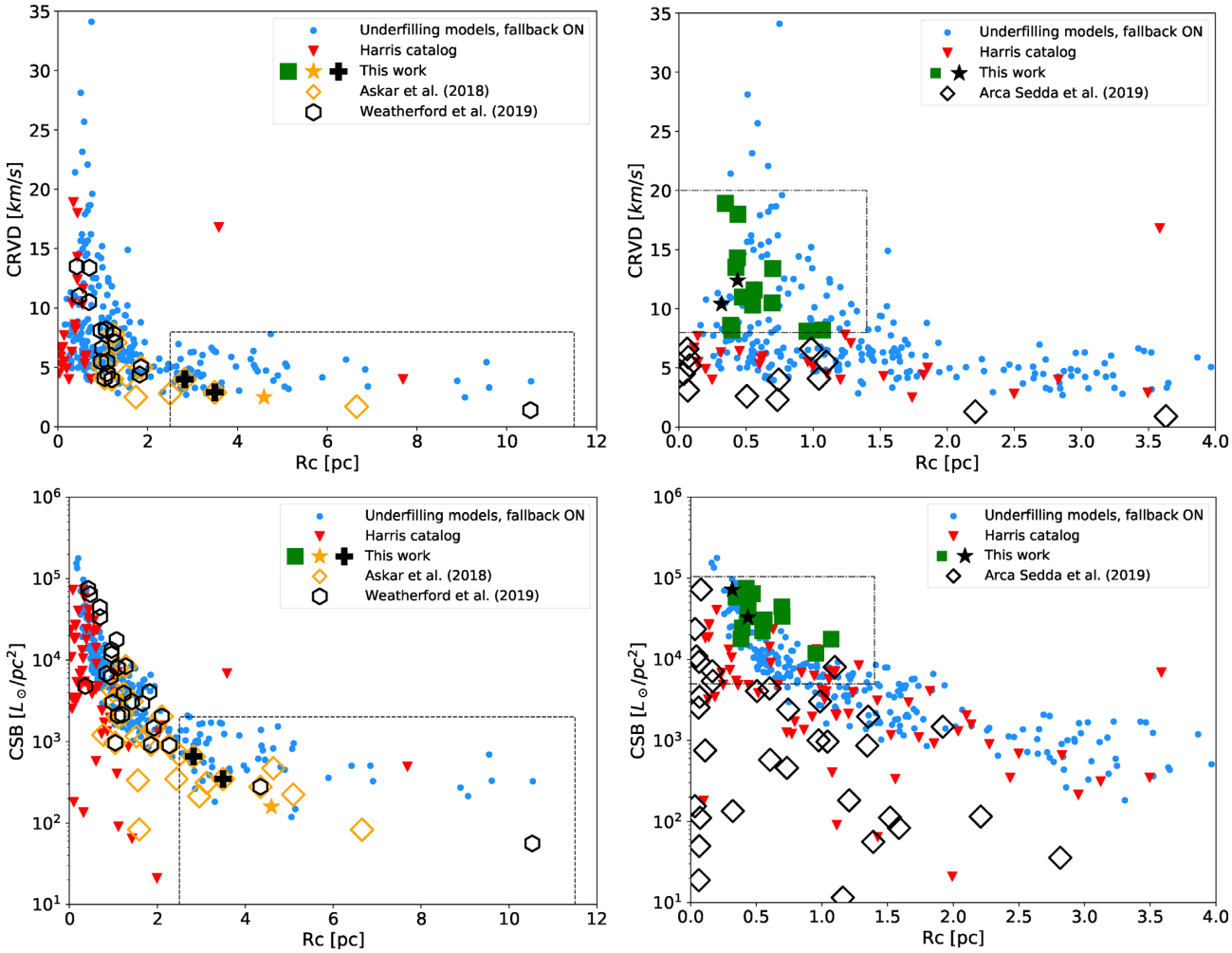

Figure 4. Same as Fig. 3, on the left for 'large core radii' models and on the right for 'small core radii' models, respectively. The models reported in this paper are shown with green squares. Models from Askar et al. (2018) and Weatherford et al. (2019) are shown in empty orange diamonds and in black hexagons, respectively (on the left) and models from Arca Sedda et al. (2019) are shown in empty black diamonds (on the right). Models that have been reported in this paper and in different works also are shown with stars (orange from Askar et al. 2018 and black from Arca Sedda et al. (2019), respectively) and with black crosses from Weatherford et al. (2019). In the upper left plot, all the models reported in this paper coincides with the ones reported in other works, so no green squares are visible. We expanded the region between $0.0 < R_c < 4.0$ pc for the figures in the right, in order to better distinguish between different points.

three different regions of the parameter space. In this section, we will discuss how this is possible in 3D space. To make the comparison with observations as easy as possible, we will try to use properties which can be in principle observed now or in future observation campaigns. To remind the reader, in this paper the central properties have been defined as the values obtained at 1 per cent light radius (the mean value in our selected models is 0.29 pc, ranging from 0.007 up to 1.12 pc), meanwhile the core properties are obtained as the cumulative contribution of each star inside the R_c.

Considering R_c, the ratio of radial velocity dispersion at R_{hl} and the CRVD (RRVD), and CSB, one can see that the three dynamical models are grouped in different regions of the space. This is clearly visible in Fig. 7. The BHS models are mostly concentrated in large R_c ($\gtrsim 2.0$ pc), relatively small CSB ($\lesssim 3.0\,L_\odot\,pc^{-2}$) with RRVD $\lesssim$ 0.9; IMBH models are mostly concentrated in small R_c ($\lesssim 2.0$ pc), CSB $\gtrsim 3.5\,L_\odot\,pc^{-2}$ and small RRVD ($\lesssim 0.9$); and Standard models, instead, have small value of R_c ($\lesssim 2.0$ pc), CSB $\gtrsim 3.0\,L_\odot\,pc^{-2}$ and high RRVD ($\sim$0.9).

In Fig. 8, we show the same 3D plot, but we considered instead the R_{hl}, the mean surface brightness, and the RRVD. The mean surface brightness is defined as the total luminosity of the system, divided by the area inside R_{hl}. Comparing Fig. 8 with Fig. 7, we can see that the properties at R_{hl} are not as good as the central properties for distinguish among the dynamical models, but still good enough to roughly separate the models.

In Fig. 9, we considered the central $U - I$ colour, the central V magnitude, and the RRVD. It is possible to note that the central colour and central magnitude can give a good distinction among dynamical models just as well. The same is true if we consider the central $B - V$ colour, the $U - I$ colour at R_c and the RRVD, as one can see in Fig. 10.

For each of these 3D plots, we can divide the space in three regions, that would include as many models as possible of only one dynamical state, with the less contamination from others. The borders and the number of models in each region are listed in Table 4. The division between the different regions has been chosen by eye. In Figs 7–10, we showed the boundaries for the three different regions. When considering the 2D projections for each figure, it is not possible to properly separate the three dynamical models in three distinct regions without the presence of dynamical contaminants for any of

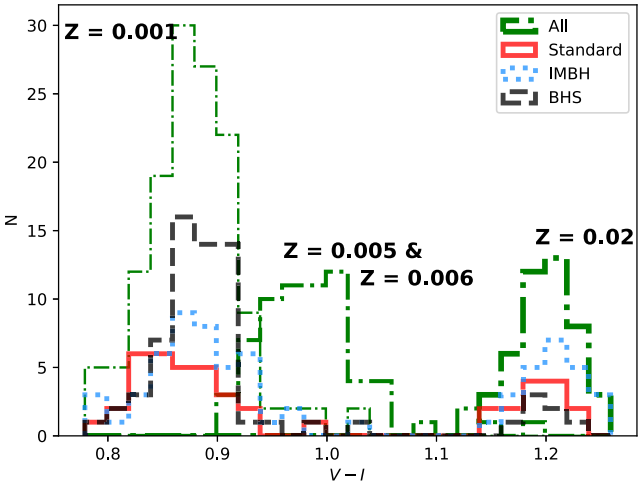

Figure 5. $V - I$ colour distribution for models with solar metallicity $Z = 0.02$ ([Fe/H] $= 0.0$) and subsolar metallicities $Z = 0.001$ ([Fe/H] $= -1.3$), $Z = 0.005$ ([Fe/H] $= -0.55$), $Z = 0.006$ ([Fe/H] $= -0.6$). The corresponding metallicity for each peak is written to the side. For $Z = 0.02$ and 0.001 metallicities, the distribution for different dynamical models is also reported, meanwhile for $Z = 0.005$ and 0.006 metallicities only the total distributions have been reported. For better visualization, different total distributions thickness of the lines corresponds to different metallicities.

the figures, although encouraging results can be noticed (e.g. the 2D projections in Fig. 7) for the identification of IMBH and/or BHS clusters in the tails of property distributions. However, in the 3D plots such contaminants are relatively small and they will not strongly affect the statistical distinctions between different GC evolutionary models.

The best combination of properties seem to be R_c, CSB and RRVD, or $(B - V)_{\rm central}$, $(U - I)_{\rm core}$ and RRVD. This could be useful from an observational point of view: when the structural parameters of the system (such as R_c or CSB) are not possible to determine, it is still possible to distinguish the different dynamical models using the central colours and magnitudes (if they can be observed). However, it is generally easier to determine and to observe properties at R_{hl}; even if the properties at this radius are not as good as the central values, they are still good enough to differentiate the dynamical models, and so they could be easier to verify.

4 DISCUSSION

EGGCs associated with different types of galaxies experience the effects of environments which differ from those experienced by MWGCs. They evolve in different gravitational potential structures and are influenced by the different tidal fields of their host galaxies. However, currently the limitations on computing power and on our knowledge of galaxy and GC systems formation and evolution, prevent the scientific community to simulate a GC system with full realistic physical conditions for every galaxy. Our attempt here is thus to use the MOCCA models as our knowledge base, to populate other galaxies. To infer correct predictions however we have to proceed in steps.

The first step is to extend the MOCCA models which have circular orbits around MW to eccentric ones. It is well known that the rate of star cluster evolution depends on the half-mass radius and cluster mass (half-mass relaxation time). In turn, the cluster mass depends on the strength of the tidal field and the rate of mass loss. As was shown by Cai et al. (2016), the long-term evolution of a star cluster

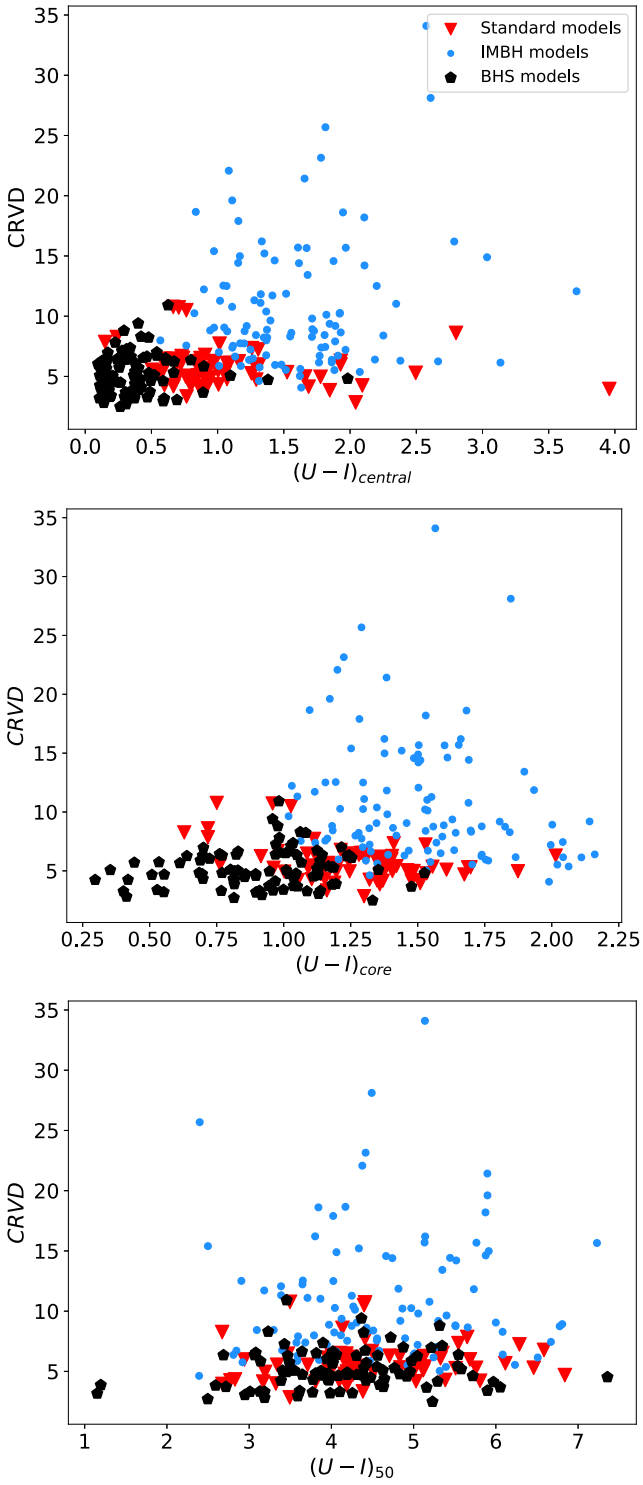

Figure 6. Central $U - I$ colour (top), $U - I$ colour at R_c (middle), and at R_{hl} (bottom) versus CRVD, respectively, for different dynamical models. The distinction among different dynamical models is the best for the central value colour, and it gets worse for larger radii.

on an eccentric orbit around its parent galaxy can be approximated by the evolution of cluster on a particular circular orbit. The second step involves placing the MOCCA models in different tidal fields in such a way that the evolution of clusters in other galaxies can be represented by MOCCA models. Knowing the galaxy mass distribution, we can

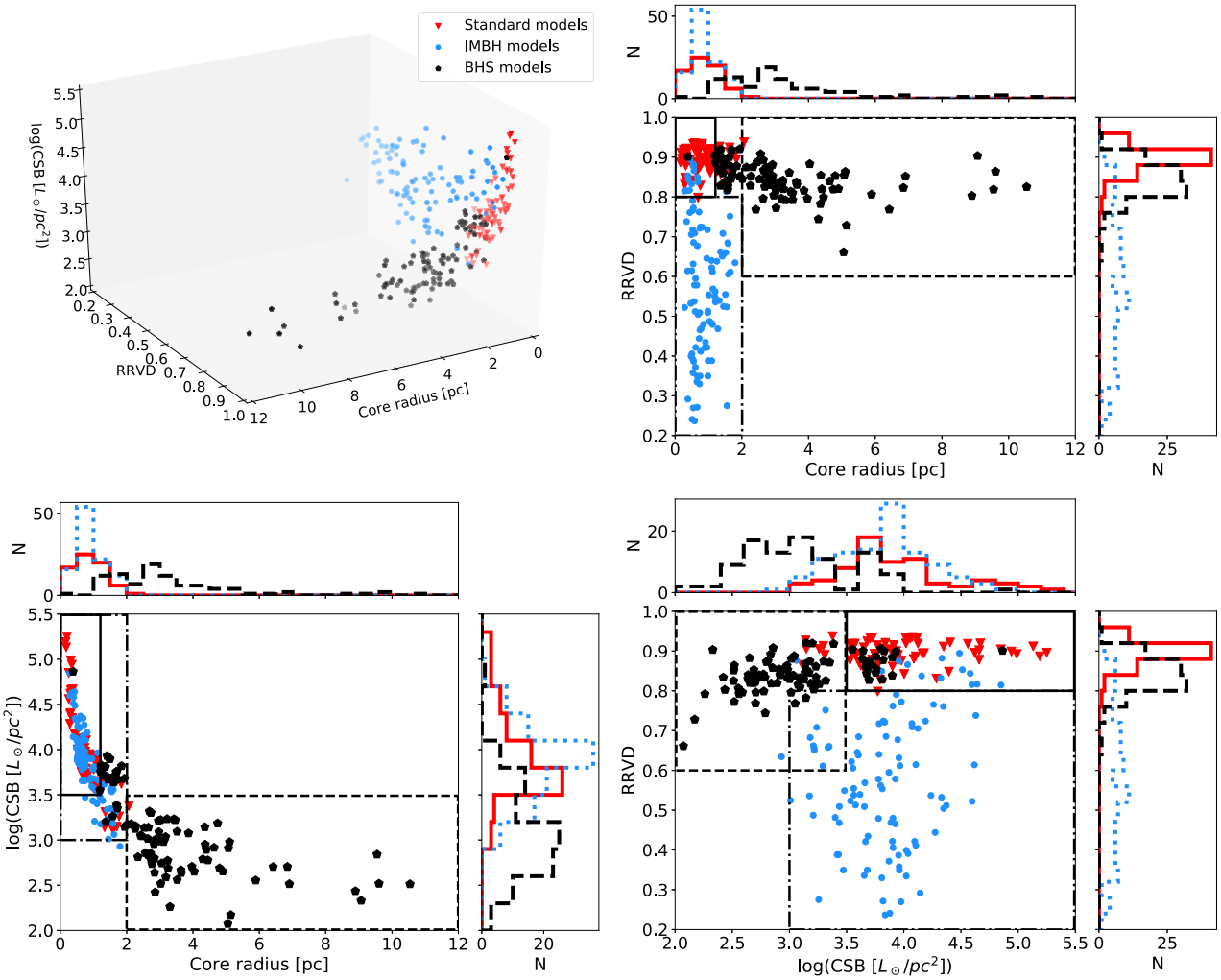

Figure 7. 3D plot of our selected models, showing the R_c, the RRVD and the CSB, for three dynamical models. On the side, the projection on three planes, with related histograms (red solid for Standard, blue dashed for IMBH and black dotted for BHS, respectively). Using three parameters it is possible to distinguish among different dynamical models. The continue line represents the border for the Region I, the dashed–dotted line for Region II, and the dotted line Region III, respectively; see the text for more details.

put the MOCCA model at such a galactocentric distance, on a circular orbit, that the GC tidal radius for the MW and the other galaxy are the same. Then using the first step, we can populate GCs around other galaxies by putting them on eccentric orbits and randomly picking their position along the orbit. In this way, we can roughly assume that the long-term GC evolution will be, to first order, represented by MOCCA models. The detailed description on the implementation of these two steps will be given in the next paper in the series.

In order to support our claim that MOCCA models can be used, at least as a first approximation, to populate other galaxies, we can make one further observation about GC models for the MW. Despite very poor knowledge about GC formation in the MW and the number and properties of GCs caught by the MW during mergers with other galaxies, it was shown by Askar et al. (2017) and in Sections 3.1 and 3.3 that the MOCCA models recover most observational parameters of MWGCs very well. This suggests that the initial phases of GC evolution during the MW formation and mergers with other galaxies (the first 1–2 Gyr) do not influence strongly their long-term evolution and present observational properties. If so, as a first approximation, we can extend this argument to GCs around other galaxies. Additionally, even if the MOCCA models would not be able to reproduce the entire population of EGGCs, it would still be possible to reproduce a subsample of EGGCs using those models, for example, by excluding GCs which are close to the galactic centre and experience strong and quickly changing tidal fields. It was shown by Madrid et al. (2017) that MOCCA models well represent the mass loss from GCs moving in the real MW gravitational potential provided their Galactocentric distances are larger than about 2–3 kpc. So, by restricting the sample of EGGCs to GC with larger galactocentric distances where the gravitational potential is relatively smooth, we can assume that the MOCCA models will better represent real GCs.

In this work, we showed that different types of observational cluster parameters connected with the central properties are needed to distinguish with more confidence between different cluster dynamical evolutions. In particular, as showed in Section 3.5, a minimum of three parameters is necessary (two parameters are not enough, see

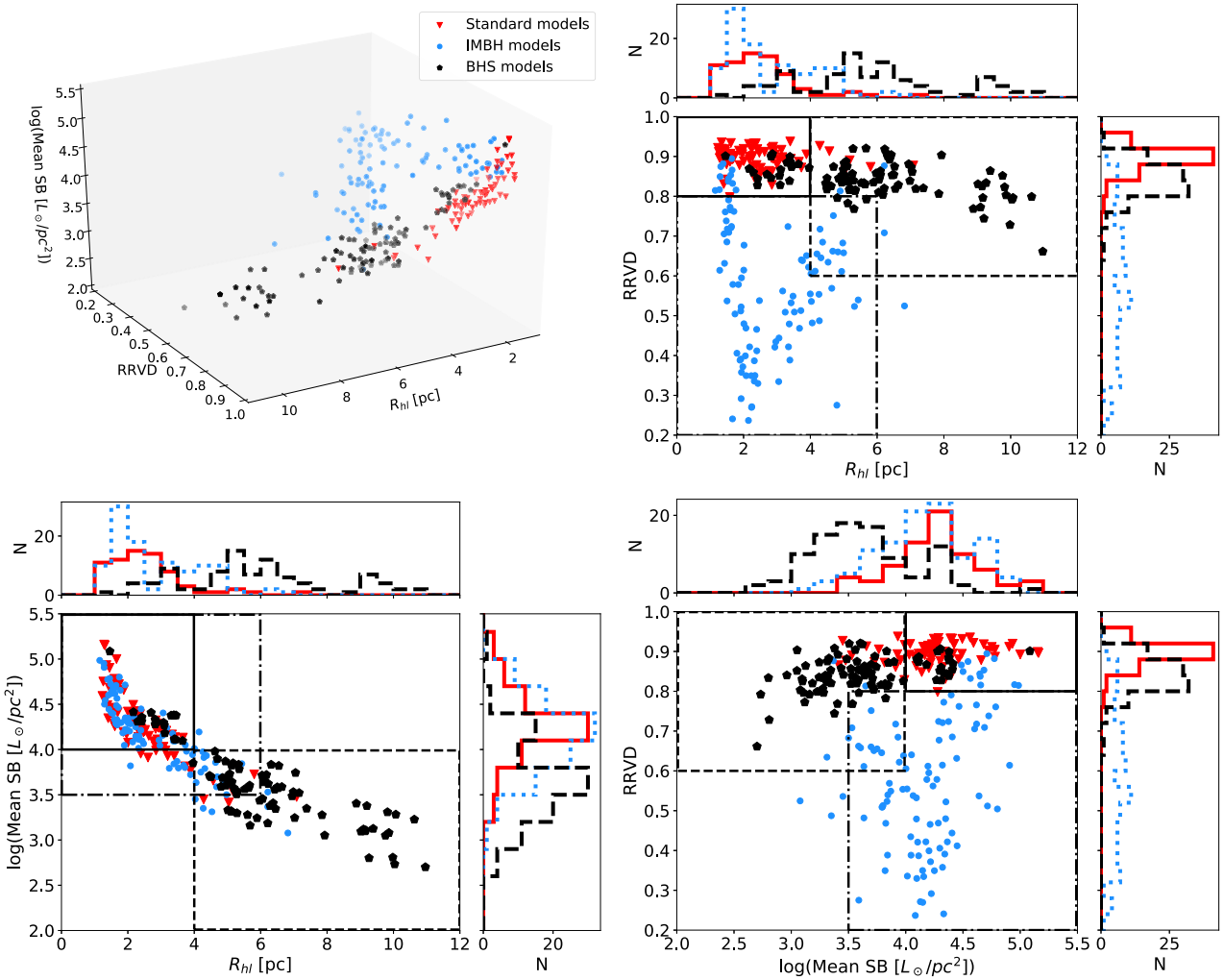

Figure 8. Same as in 7, but the R_{hl}, the mean surface brightness and the RRVD has been showed.

Fig. 6). This could be explained by the nature and structure of the systems due to their dynamical histories.

Indeed, it is expected that the influence of the IMBH would change the central properties of the GC: due to the dee per central potential, the system is expected to be more concentrated (small R_c), having a high CRVD (RRVD <0.8) and a high CSB, CSB> 10^3 $L_\odot$ pc^{-2}.

The central part of a BHS model is dominated by the presence of BHs. This implies that the observed R_c for such a system is expected to be larger (it is measured considering only luminous stars). The presence of a BHS in the central part of the system would imply a relatively small CSB, since the core of the system is dominated by the not luminous BHs. However, a strong gradient in velocity dispersion is not expected (implying an RRVD ∼0.9), since we have considered BHS models with systems that are in balanced evolution: indeed, the BHS is not detached from the whole system (Breen & Heggie 2013b) and the R_c is not strongly different from the half-mass radius.

The Standard models, finally, are models expected to be approaching core collapse or in the post-collapse phase. This means a small R_c and relatively large R_h/R_c ratio (R_c < 2.0 pc and CSB> 10^3 $L_\odot$ pc^{-2}) and RRVD is ∼0.9 (or smaller).

Regarding the different central colour, the BHS models show a bluer central region than the Standard and IMBH ones. This is again explained by a different dynamical history: the interactions of massive stars with IMBH would imply the removal of the former, so that mostly red stars (giant and low mass MS stars) would survive in the central part of the system. On the other hand, this is not strictly true for Standard and BHS models, where a higher number of MS stars are expected in the central part. Moreover, as discussed before, the observed core and central radius for BHS is expected to be larger than for Standard models, so the number of stars in the central part should be higher for the former. This is evident in Fig. 11, where we show the ratio of the total number of MS and red giant (RG) stars inside the central region and the R_c, for the 3D snapshots and the projected 2D snapshots. The mean number of MS and RG stars inside the considered regions, for different dynamical models, are shown in Table 5. It is clear that the central region of IMBH models contains a smaller mean number of MS stars compared to the mean number of RG stars, but the Standard and BHS models have on average an higher number of MS compared to the RG stars.

As shown in Fig. 6, the CRVD is already a powerful tool to distinguish IMBH models. However, the RRVD gives the best separation only among the IMBH models and the two other dynamical ones. It actually enhances the difference in kinematics between the central part and the R_{hl}, with the former more important in IMBH models, due to the deep central potential. The similar value and spread of RRVD for BHS and Standard, but a different one for IMBH, could mean

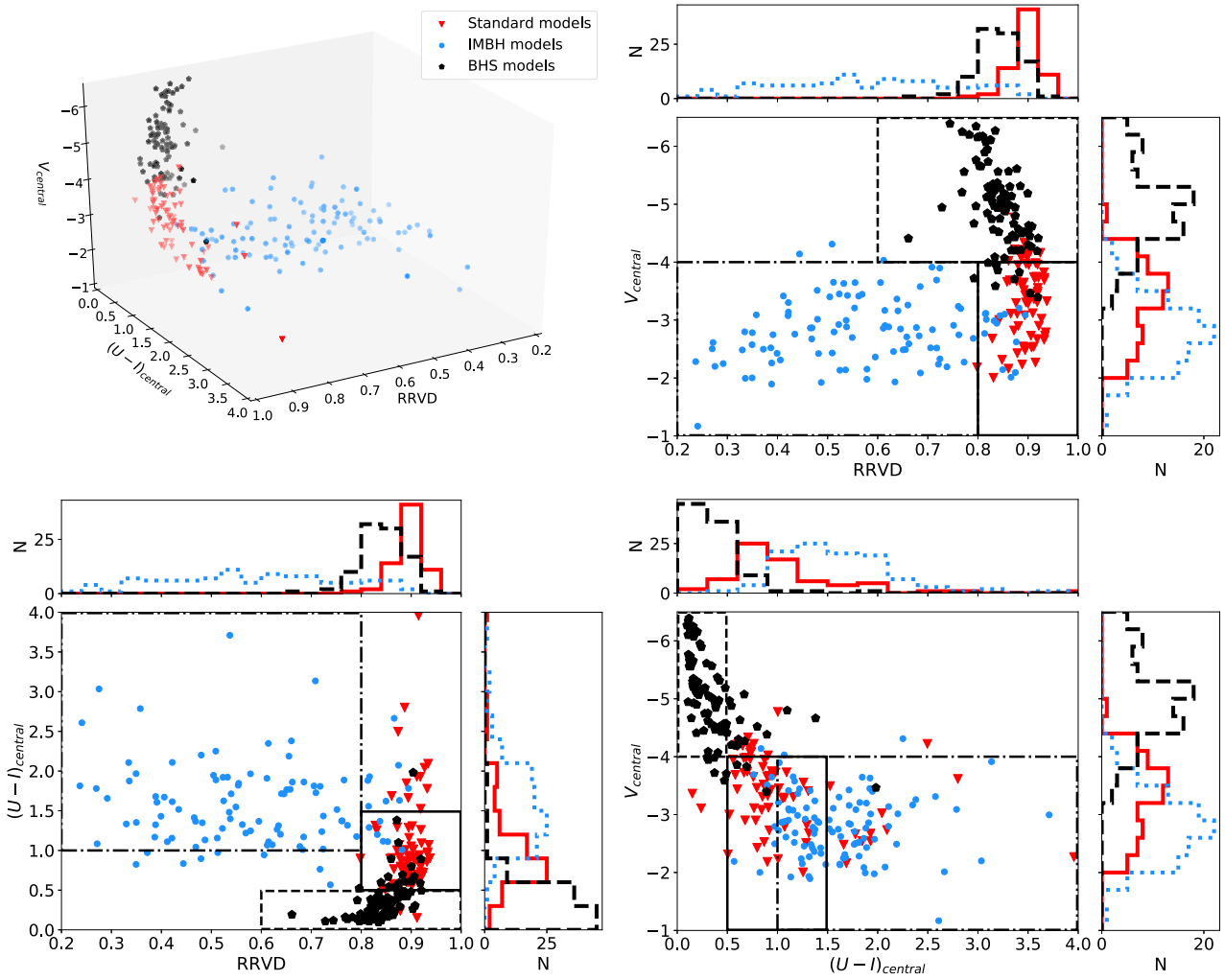

Figure 9. Same as in 7, but the central $U - I$ colour, the central V magnitude, and the RRVD has been showed.

that they belong to two different dynamical families: the presence of an IMBH and the deep central potential would lead to a completely different history and structure of the system. Meanwhile, BHS and Standard models have a similar evolutionary history, driven mostly by binary energy generation leading to a bigger and smaller core size (because BHs generate more energy than stars). Meanwhile for IMBH the evolutionary history has been driven by dynamical interactions with the IMBH.

The best distinctions among the dynamical models are achieved when considering the central region properties (those being R_c, CRVD, CSB, and central colours). Even if this is not prohibitive to observe for MWGCs, it could be challenging for EGGCs. Indeed, the mean value for R_c in our selected models is 1.72 pc (ranging from 0.16 up to 10.5 pc), for R_{hl} is 3.8 pc (ranging from 0.9 up to 10.7 pc), and for the 10 per cent light radius 1.07 pc (ranging from 0.13 up to 3.78 pc).

If we consider EGGCs in the Local Group,[6] the aperture size of the Large Magellanic Cloud (LMC) for the mean value of R_c is 7.09 arcsec (from 0.66 up to 43.31 arcsec), of R_{hl} is 15.67 arcsec (from 3.71 up to 44.14 arcsec), and of the 10 per cent light radius is 4.41 (from 0.54 up to 15.59 arcsec). The aperture size of the Andromeda galaxy distance, for the mean value of R_c is 0.46 arcsec (from 0.04 up to 2.81 arcsec), of R_{hl} is 1.02 arcsec (from 0.24 up to 2.87 arcsec), and of the 10 per cent light radius is 0.28 arcsec (from 0.03 up to 1.01 arcsec). Instead, if we consider EGGCs in the Virgo cluster, the aperture size for the mean value of R_c is 0.02 arcsec (from 0.002 up to 0.13 arcsec), of R_{hl} is 0.04 arcsec (from 0.01 up to 0.13 arcsec), and of the 10 per cent light radius is 0.01 arcsec (from 0.002 up to 0.05 arcsec); similar values are obtained for the Fornax cluster. The *HST* has a spatial resolution of 0.04–0.05 arcsec (so we could definitely observe the LMC, but some difficulties would arise for the 10 per cent light radius for some GCs, since the limit resolution at Fornax cluster can go down to 1.5 pc); the Very Large Telescope array (VLT) telescope (Narrow Field Mode of MUSE, e.g. has spatial resolution of 0.055–0.08 arcsec), instead, has a spatial resolution of 0.05 arcsec, reaching a value of 0.002 arcsec when all the telescopes are combined (possible up to the Virgo and Fornax clusters distance, but maybe not for the 10 per cent light radius where we are at the extreme).

In this preliminary work, we showed that our approach is working well for MWGCs. The results shown are in good agreement with

[6]The distance for the LMC is assumed to be 50 kpc, for the Andromeda galaxy 770 kpc, for the Virgo Cluster 16.5 Mpc, and for the Fornax cluster 19 Mpc.

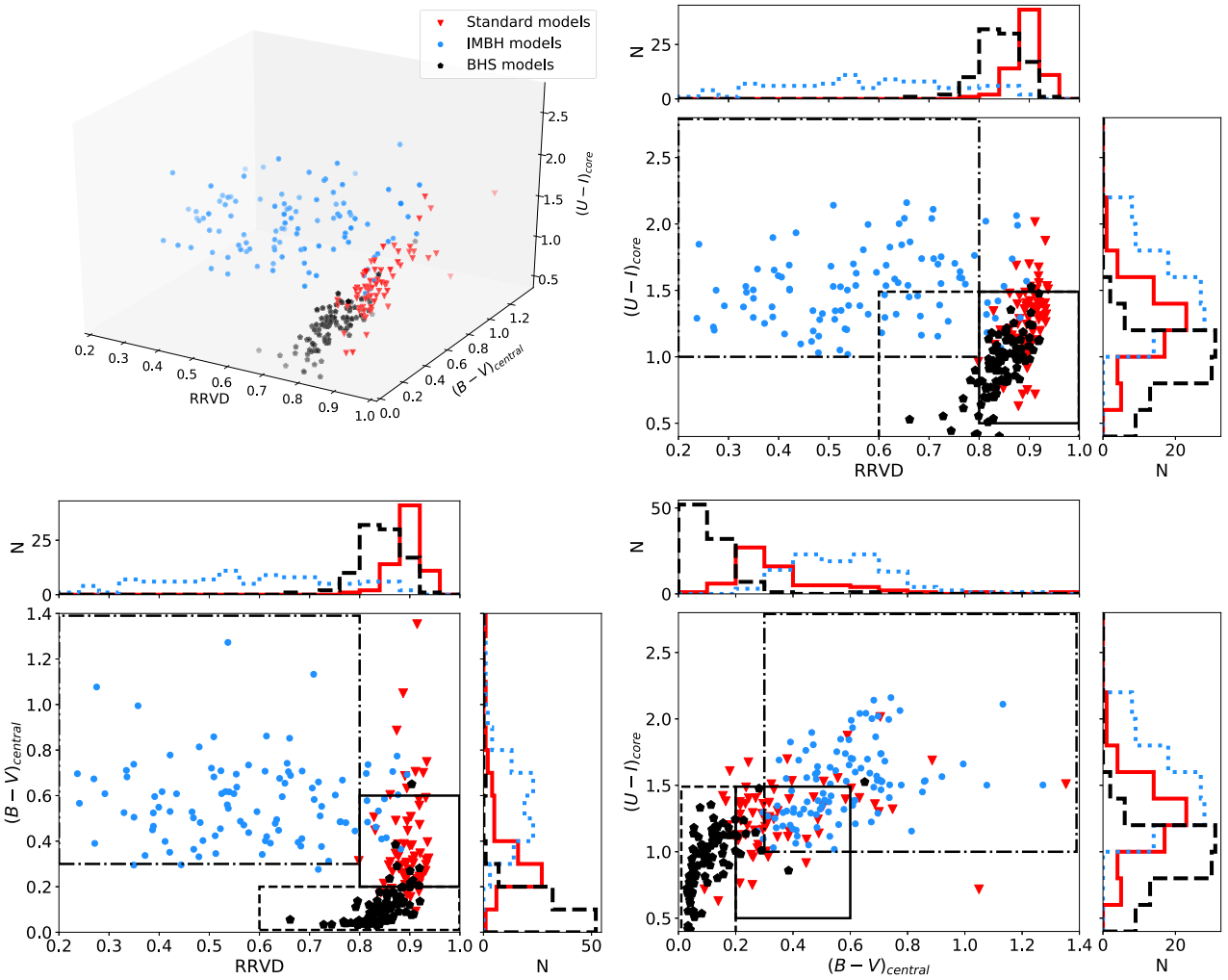

Figure 10. Same as in 7, but the central $B - V$ colour, the $U - I$ colour at R_c, and the RRVD have been showed.

observations, and with the results of previous works. Moreover, in the MWGCs sample, no circular orbits have been observed, and the assumption of a constant and smooth gravitational potential does not hold. Nevertheless, our selected models can still reproduce the overall properties of MWGCs. Taking this in consideration, and assuming that MWGCs' and EGGCs' formation processes are similar, we are can assume that our approach could also work for EGGCs, at least as a first approximation. Distinguishing between different evolutionary dynamical tracks for EGGCs could be also useful to better estimate the BH–BH merger rate, the number of exotic binaries in the local Universe (cataclysmic variable stars, X-ray binaries, etc.), the number of tidal disruption events around an IMBH, or the expected number of IMBH in a nuclear star cluster. In order to distinguish the type of cluster evolution, in the near future photometric (in different bands) and spectroscopic observations of the central properties of GCs would be needed. As shown, this may be possible for GCs in the Local Group, where the resolution needed to resolve the central part of the system could also be approachable given current technologies. If the central properties would actually be inaccessible with the current (or future) technologies, determining the 'average' properties at R_{hl} would be more realizable, even with current telescopes. Indeed, the 'average' properties give an overall acceptable result, roughly dividing the different dynamical models.

5 SUMMARY AND FUTURE WORK

In this work, we used models from the MOCCA Survey Database (Askar et al. 2017). We limit ourselves to a subsample of models that would mimic the observational limitations and realistic properties for EGGCs, which are models having current luminosity $>2 \times 10^4\,L_\odot$, with a mass fallback prescription and which were initially tidally underfilling. For each model, we projected the 12 Gyr snapshot, in order to determine the observed structural parameter (such as R_c, CSB, and CRVD). The models have been divided accordingly by their dynamical state at 12 Gyr, that is if an IMBH, a BHS, or neither are present in the system.

Our main results can be summarized as follows:

(i) in Sections 3.1 and 3.3, we showed that, overall, our subsample reproduces the observed properties of MWGCs, while being in rough agreement with the results of previous considered works (Askar et al. 2018; Weatherford et al. 2019; Arca Sedda et al. 2019);

Table 4. The definitions for the three different regions for each 3D space defined in this work. The first column names the three parameters that have been used; the second column shows the regions in which it has been divided; and the third column indicates the border of each region. In the fourth column, the number of dynamical models in each region are reported, respectively; in parenthesis the percentage of the model in the particular region compared to the total number of considered models (266) is reported too. In bold, the model type which dominate in each region.

Parameters	Region	Borders	Number of models
R_c, RRVD, CSB	I	$R_c \leq 1.2\,\mathrm{pc}$	**Standard: 57 (21.4)**
		$0.8 <$ RRVD < 1.0	IMBH: 12 (4.5)
		CSB $\geq 10^{3.5}\,\mathrm{L}_\odot\,\mathrm{pc}^{-2}$	BHS: 2 (0.75)
	II	$R_c \leq 2.0\,\mathrm{pc}$	Standard: 1 (0.4)
		RRVD < 0.8	**IMBH: 89 (33.4)**
		CSB $> 10^{3.0}\,\mathrm{L}_\odot\,\mathrm{pc}^{-2}$	BHS: 0 (0.0)
	III	$R_c > 2.0\,\mathrm{pc}$	Standard: 1 (0.4)
		RRVD < 1.0	IMBH: 0 (0.0)
		CSB $< 10^{3.5}\,\mathrm{L}_\odot\,\mathrm{pc}^{-2}$	**BHS: 67 (25.2)**
R_{hl}, RRVD, Mean SB	I	$R_{hl} < 4.0\,\mathrm{pc}$	**Standard: 54 (20.3)**
		$0.8 <$ RRVD < 1.0	IMBH: 12 (4.5)
		Mean SB $> 10^4\,\mathrm{L}_\odot\,\mathrm{pc}^{-2}$	BHS: 19 (7.1)
	II	$R_{hl} < 6.0\,\mathrm{pc}$	Standard: 1 (0.4)
		RRVD < 0.8	**IMBH: 85 (31.9)**
		Mean SB $\geq 10^{3.5}\,\mathrm{L}_\odot\,\mathrm{pc}^{-2}$	BHS: 3 (1.1)
	III	$R_{hl} > 4.0\,\mathrm{pc}$	Standard: 5 (1.9)
		RRVD < 1.0	IMBH: 17 (6.4)
		Mean SB $< 10^4\,\mathrm{L}_\odot\,\mathrm{pc}^{-2}$	**BHS: 73 (27.4)**
$(U-I)_{\mathrm{central}}$, RRVD, V_{central}	I	$0.5 < (U-I)_{\mathrm{central}} < 1.5$	**Standard: 44 (16.5)**
		$0.8 <$ RRVD < 1.0	IMBH: 6 (2.2)
		$V_{\mathrm{central}} > -4.0$	BHS: 3 (1.1)
	II	$(U-I)_{\mathrm{central}} > 1.0$	Standard: 0 (0.0)
		RRVD < 0.8	**IMBH: 80 (30.1)**
		$V_{\mathrm{central}} > -4.0$	BHS: 0 (0.0)
	III	$(U-I)_{\mathrm{central}} < 0.5$	Standard: 0 (0.0)
		RRVD < 1.0	IMBH: 0 (0.0)
		$V_{\mathrm{central}} < -4.0$	**BHS: 69 (25.9)**
$(B-V)_{\mathrm{central}}$, RRVD, $(U-I)_{\mathrm{core}}$	I	$0.2 < (B-V)_{\mathrm{central}} < 0.6$	**Standard: 45 (16.9)**
		$0.8 <$ RRVD < 1.0	IMBH: 7 (2.6)
		$0.5 < (U-I)_{\mathrm{core}} < 1.5$	BHS: 8 (3.0)
	II	$(B-V)_{\mathrm{central}} > 0.3$	Standard: 0 (0.0)
		RRVD < 0.8	**IMBH: 87 (32.7)**
		$(U-I)_{\mathrm{core}} > 1.0$	BHS: 0 (0.0)
	III	$(B-V)_{\mathrm{central}} < 0.2$	Standard: 4 (1.5)
		RRVD < 1.0	IMBH: 0 (0.0)
		$(U-I)_{\mathrm{core}} < 1.5$	**BHS: 81 (30.4)**

(ii) the significance of dynamical history in colour distribution could be important for the spread in metallicity but, due to the small number of our statistics, further study is needed (Section 3.4);

(iii) in Section 3.5, we established that in order to differentiate between the three dynamical models, at least three observational parameters are needed. The best choice would be the central properties; however, a good result is obtained also from the properties at R_{hl}, which may be easier to observe in EGGCs (R_{hl}, Mean SB, and RRVD).

Photometric and spectroscopic studies, in the central part or at R_{hl} of EGGCs, are necessary to distinguish the type of cluster evolution. Current technologies could be limiting the distance of possible observations, however it could be not so prohibitive in the Local Group. Even if the number of systems is not so high, combining those observation with those from MWGC, it would be possible to check and verify the correlations between the global properties of the GCs and their internal dynamical state.

The next step in our work plan is to populate GCs around an external galaxy. The distribution of position in the galactic surroundings, age, metallicity (and other GC's properties) will be selected according to the observed distribution. Those properties depend on the host galaxy's type, mass, size, and luminosity, as well as the number of GCs surrounding the host galaxy. We will adopt the procedure used in this paper to simulate the EGGC population, using models from the MOCCA Survey Database. For each GC's properties expected from the distribution, we will consider the model in our data base that will best match them. In this way, we will obtain a simulated external galaxy and its GC population, as in real galaxies. Finally, we will recreate a mock observation and we will apply our methodology to this simulated EGGC population, in order to mimic real observations as much as possible and compare them with observations in the Local Group and nearby clusters of galaxies. For this purpose, an expansion of the MOCCA Survey Database could be useful, in particular to better represent the low metallicities of GCs in the early stage of the Universe.

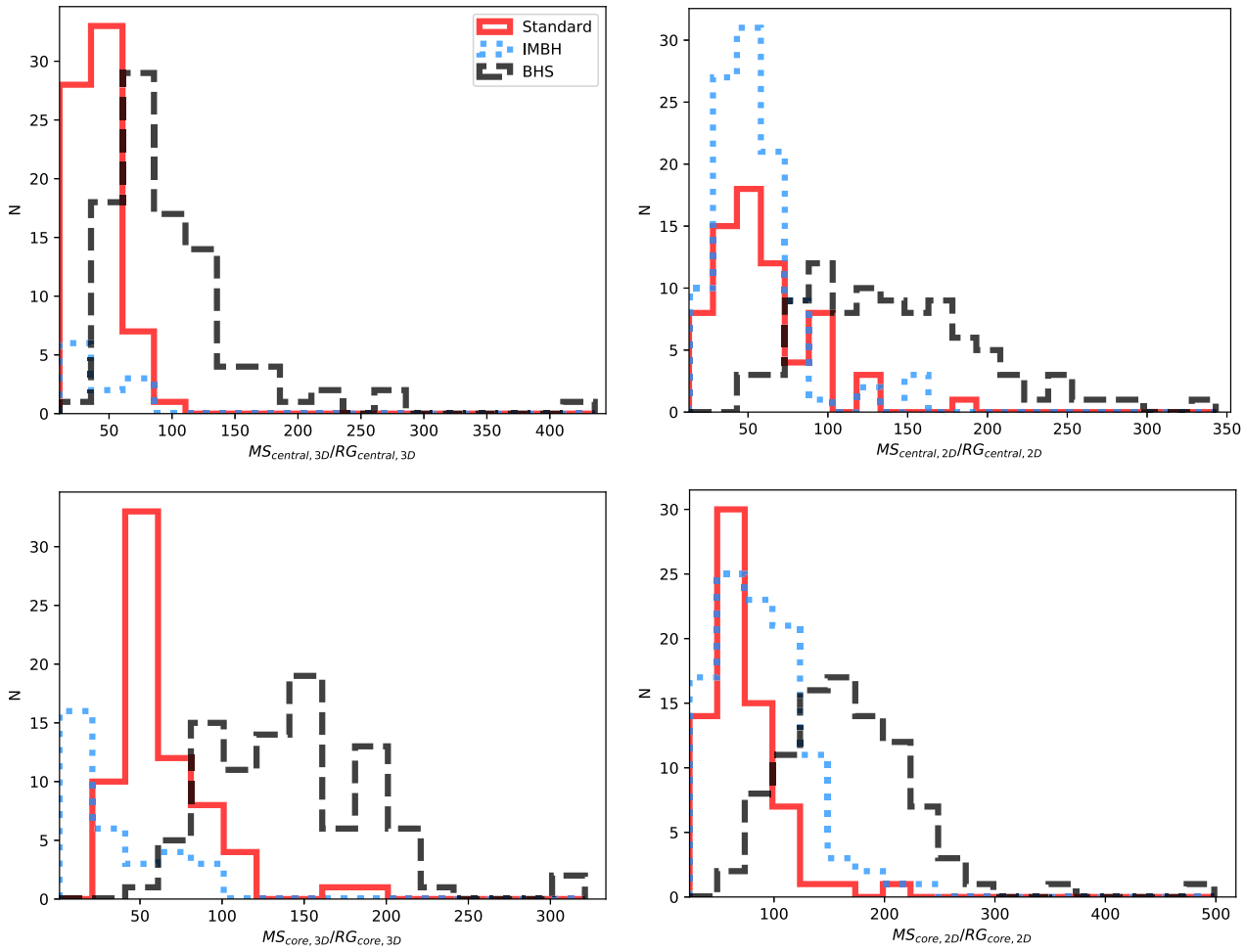

Figure 11. The ratio of the total number of MS and RG stars inside the central region and at R_c for the 3D snapshot (on the left, top, and below, respectively) and for the 2D projected snapshot (on the right, top, and below, respectively) histograms. Standard models are shown in the solid red lines, IMBH are shown in the blue dashed lines, and BHS are shown in the black dotted lines. The IMBH models show a small ratio, meanwhile, for BHS the distribution is extended to higher values.

Table 5. Mean value for the number of MS and RG stars, in the 3D snapshot and in the 2D projected snapshot, for different dynamical models. The second column names the region considered, and the third column the type of star. The fourth, the fifth, and the sixth names the mean value for Standard, IMBH, and BHS models, respectively. The mean value for each region and for each star type is calculated as the sum over all specific dynamical models, divided by the total number of models (Standard – 69; IMBH – 104; and BHS – 93).

	Region	Star type	Standard	IMBH	BHS
3D	Central	MS	2200	94	2208
		RG	60	3	29
	Core	MS	39715	870	92062
		RG	620	19	666
2D	Central	MS	1624	1201	4325
		RG	29	23	31
	Core	MS	26870	25963	111870
		RG	379	295	637

ACKNOWLEDGEMENTS

MG and AL were partially supported by the Polish National Science Center (NCN) through the grant UMO-2016/23/B/ST9/02732. The authors would like to express their gratitude to E. Peng: his support and encouragement were invaluable. We thank the referee Jarrod Hurley for his review and highly appreciate the comments and suggestions, which significantly contributed to improving the quality of the publication. This manuscript was edited for English language by D. Abarca. AL would like to offer his special thanks and deepest gratitude to V. S. Iorio, a friend and a mentor. Without her encouragement and counseling, all this would not have materialized ever.

DATA AVAILABILITY

The data underlying this article can be obtained upon request to Agostino Leveque (agostino@camk.edu.pl) or Mirek Giersz (mig@camk.edu.pl) and after agreeing to the terms of the MOCCA License. The license can be found in https://moccacode.net/license/.

REFERENCES

Arca Sedda M., Askar A., Giersz M., 2018, MNRAS, 479, 4652
Arca Sedda M., Askar A., Giersz M., 2019, preprint (arXiv:1905.00902)
Ashman K. M., Zepf S. E., 1992, ApJ, 384, 50

Askar A., Szkudlarek M., Gondek-Rosińska D., Giersz M., Bulik T., 2017, MNRAS, 464, L36
Askar A., Arca Sedda M., Giersz M., 2018, MNRAS, 478, 1844
Askar A., Askar A., Pasquato M., Giersz M., 2019, MNRAS, 485, 5345
Bajkova A. T., Carraro G., Korchagin V. I., Budanova N. O., Bobylev V. V., 2020, ApJ, 895, 69
Baumgardt H., Hilker M., 2018, MNRAS, 478, 1520
Beasley M. A., 2020, in Kabáth P., Jones D., Skarka M., eds, Reviews in Frontiers of Modern Astrophysics; From Space Debris to Cosmology. Springer International Publishing, Cham, p. 245
Belczynski K. et al., 2017, A&A, 636, A104
Belczynski K., Kalogera V., Bulik T., 2002, ApJ, 572, 407
Breen P. G., Heggie D. C., 2013a, MNRAS, 432, 2779
Breen P. G., Heggie D. C., 2013b, MNRAS, 436, 584
Brodie J. P., Strader J., 2006, ARA&A, 44, 193
Cai M. X., Gieles M., Heggie D. C., Varri A. L., 2016, MNRAS, 455, 596
Cantiello M. et al., 2018, A&A, 611, A93
Cantiello M. et al., 2020, A&A, 639, 136
Cantiello M., Blakeslee J. P., 2007, ApJ, 669, 982
Carretta E., Bragaglia A., Gratton R., Lucatello S., 2009, A&A, 505, 139
Conroy C., Gunn J. E., 2010, ApJ, 712, 833
Conroy C., Gunn J. E., White M., 2009, ApJ, 699, 486
Côté P. et al., 2004, ApJS, 153, 223
Côté P., Marzke R. O., West M. J., 1998, ApJ, 501, 554
D'Abrusco R. et al., 2016, ApJ, 819, L31
Downing J. M. B., 2012, MNRAS, 425, 2234
Forbes D. A., Brodie J. P., Grillmair C. J., 1997, AJ, 113, 1652
Fregeau J. M., Cheung P., Portegies Zwart S. F., Rasio F. A., 2004, MNRAS, 352, 1
Fukushige T., Heggie D. C., 2000, MNRAS, 318, 753
Gaia Collaboration et al., 2018, A&A, 616, A12
Giersz M., Heggie D. C., Hurley J. R., Hypki A., 2013, MNRAS, 431, 2184
Giersz M., Leigh N., Hypki A., Lützgendorf N., Askar A., 2015, MNRAS, 454, 3150
Giersz M., Askar A., Wang L., Hypki A., Leveque A., Spurzem R., 2019, MNRAS, 487, 2412
Harris W. E., 1996, AJ, 112, 1487
Harris G. L. H., Harris W. E., Poole G. B., 1999, AJ, 117, 855
Hénon M. H., 1971, Ap&SS, 14, 151
Hobbs G., Lorimer D. R., Lyne A. G., Kramer M., 2005, MNRAS, 360, 974
Hurley J. R., Pols O. R., Tout C. A., 2000, MNRAS, 315, 543
Hurley J. R., Tout C. A., Pols O. R., 2002, MNRAS, 329, 897
Hypki A., Giersz M., 2013, MNRAS, 429, 1221
Jeans J. H., 1919, MNRAS, 79, 408
Jordán A. et al., 2005, ApJ, 634, 1002
King I., 1962, AJ, 67, 471
King I. R., 1966, AJ, 71, 276
Kissler-Patig M., Brodie J. P., Schroder L. L., Forbes D. A., Grillmair C. J., Huchra J. P., 1998, AJ, 115, 105
Kremer K. et al., 2020, ApJS, 247, 48
Kroupa P., 1995, MNRAS, 277, 1522
Kroupa P., 2001, MNRAS, 322, 231
Kruijssen J. M. D., 2014, Class. Quantum Gravity, 31, 244006
Kundu A., Whitmore B. C., 2001, AJ, 121, 2950
Lane R. R., Kiss L. L., Lewis G. F., Ibata R. A., Siebert A., Bedding T. R., Székely P., Szabó G. M., 2011, A&A, 530, A31
Larsen S. S., Brodie J. P., Huchra J. P., Forbes D. A., Grillmair C. J., 2001, AJ, 121, 2974
Lützgendorf N. et al., 2013, A&A, 552, A49
Madrid J. P., Leigh N. W. C., Hurley J. R., Giersz M., 2017, MNRAS, 470, 1729
Marks M., Kroupa P., 2012, A&A, 543, A8
Mashchenko S., Sills A., 2005, ApJ, 619, 243
Ostrov P., Geisler D., Forte J. C., 1993, AJ, 105, 1762
Paolillo M., Puzia T. H., Goudfrooij P., Zepf S. E., Maccarone T. J., Kundu A., Fabbiano G., Angelini L., 2011, ApJ, 736, 90
Peng E. W. et al., 2006, ApJ, 639, 95
Peng E. W. et al., 2008, ApJ, 681, 197
Puzia T. H., Paolillo M., Goudfrooij P., Maccarone T. J., Fabbiano G., Angelini L., 2014, ApJ, 786, 78
Renaud F., 2020, in Bragaglia A., Davies M., Sills A., Vesperini E., eds, Star Clusters: From the Milky Way to the Early Universe. Proc. IAU, Vol. 351, p. 40
Rossi L. J., Bekki K., Hurley J. R., 2016, MNRAS, 462, 2861
Shukirgaliyev B., Parmentier G., Berczik P., Just A., 2019, MNRAS, 486, 1045
Sippel A. C., Hurley J. R., Madrid J. P., Harris W. E., 2012, MNRAS, 427, 167
Stodolkiewicz J. S., 1982, Acta Astron., 32, 63
Stodolkiewicz J. S., 1986, Acta Astron., 36, 19
Trujillo-Gomez S., Kruijssen J. M. D., Reina-Campos M., Pfeffer J. L., Keller B. W., Crain R. A., Bastian N., Hughes M. E., 2020, preprint (arXiv:2005.02401)
Wang L., 2020, MNRAS, 491, 2413
Weatherford N. C., Chatterjee S., Kremer K., Rasio F. A., 2019, ApJ, 898, 162
Webb J. J., Sills A., Harris W. E., 2013, ApJ, 779, 94
Webb J. J., Sills A., Harris W. E., Gómez M., Paolillo M., Woodley K. A., Puzia T. H., 2016, MNRAS, 460, 2129
Zepf S. E., Ashman K. M., 1993, MNRAS, 264, 611

This paper has been typeset from a TEX/LATEX file prepared by the author.

Chapter 3

Paper II - Milky Way and Andromeda

Monthly Notices of the ROYAL ASTRONOMICAL SOCIETY

MNRAS **514,** 5751–5766 (2022) https://doi.org/10.1093/mnras/stac1694
Advance Access publication 2022 June 17

MOCCA-survey data base: extra galactic globular clusters – II. Milky Way and Andromeda

A. Leveque [1]★ M. Giersz [1] M. Arca-Sedda [2] and Abbas Askar [3]

[1]*Nicolaus Copernicus Astronomical Center, Polish Academy of Sciences, ul. Bartycka 18, PL-00-716 Warsaw, Poland*
[2]*Astronomisches Rechen-Institut, Zentrum für Astronomie der Universit ät Heidelberg, Mönchhofstr. 12-14, D-69120 Heidelberg, German*
[3]*Observatory, Department of Astronomy, and Theoretical Physics, Lund University, Box 43, SE-221 00 Lund, Sweden*

Accepted 2022 June 13. Received 2022 June 8; in original form 2022 April 12

ABSTRACT

A comprehensive study of the co-evolution of globular cluster systems (GCS) in galaxies requires the ability to model both the large-scale dynamics (0.01–10 kpc) regulating their orbital evolution, and the small-scale dynamics (sub-pc – au) regulating the internal dynamics of each globular cluster (GC). In this work, we present a novel method that combine semi-analytic models of GCS with fully self-consistent Monte Carlo models to simultaneously evolve large GCSs. We use the population synthesis code MASinGa and the MOCCA-Survey Database I to create synthetic GC populations aimed at representing the observed features of GCs in the Milky Way (MW) and Andromeda (M31). Our procedure enables us to recover the spatial and mass distribution of GCs in such galaxies, and to constrain the amount of mass that GCs left either in the halo as dispersed debris, or in the galactic centre, where they can contribute to the formation of a nuclear star cluster (NSC) and can bring stellar and possibly intermediate mass black holes there. The final masses reported by our simulations are of a few order of magnitudes smaller than the observed values. These differences show that mass build-up of an NSC and central BHs in galaxies like MW and M31 cannot be solely explained by the infalling GC scenario. This build-up is likely to depend on the interplay between interactions and mergers of infalling GCs and gas. The latter can contribute to both *in situ* star formation in the NSC and growth of the central BH.

Key words: galaxies: star clusters: general.

1 INTRODUCTION

The advent of the *HST* and large ground-based telescopes (e.g. E-ELT, SALT, and LSST) increased significantly the level of detail of globular cluster (GC) observations (see Larsen et al. 2001; Côté et al. 2004; Brodie & Strader 2006; Peng et al. 2006, 2008; Kruijssen 2014; Renaud 2020; references therein). One crucial discovery has been the bimodality of GCs in the colour distribution, indicating two subpopulations of GCs around the host galaxy, with one peak shifted towards blue, indicating a metal-poor population, and the other red, indicating a metal-rich population. This feature seems to be common in all types of galaxies (Ostrov, Geisler & Forte 1993; Zepf & Ashman 1993; Kundu & Whitmore 2001; Larsen et al. 2001; Harris et al. 2006; Cantiello & Blakeslee 2007). The two blue and red peak locations differ from galaxy to galaxy. However, the $V-I$ colour distribution for bright early-type galaxies (like NGC 1023, NGC 3384, NGC 4472 for example) usually shows a blue peak at $V-I=0.95\pm0.02$, corresponding to [Fe/H] ~ -1.5 and a red peak at $V-I=1.18\pm0.04$, corresponding to [Fe/H] ~ -0.5 (Larsen et al. 2001). Despite different scenarios having been suggested to explain the observed colour distribution (Ashman & Zepf 1992; Forbes, Brodie & Grillmair 1997; Côté, Marzke & West 1998), no consensus has been reached. In the hierarchical scenario, among others, the metal-rich GCs would be created *in situ*, with the metal-poor GCs accreted from lower mass galaxies to more massive galaxies (Forbes et al. 1997; Harris, Harris & Poole 1999; D'Abrusco et al. 2016; Cantiello et al. 2018, 2020). Instead, at least two star formation events in the histories of such galaxies has to be invoked to generate such a bimodality, which can be triggered by major mergers (Ashman & Zepf 1992) or occur in isolation (Forbes et al. 1997).

As suggested by Harris, Harris & Alessi (2013), the total number (or mass) in GCS in a galaxy seems to ubiquitously increase with the host galaxy mass, or luminosity. The authors found that the low and very high luminosity galaxies show a larger number of surrounding GCs, and explain these results as an interplay of radiative feedback and gas ejection during the star formation events. To compare the richness of GCs (i.e. the number of GCs per each galaxy) for different galaxy types, Zepf & Ashman (1993) introduced the quantity T as the number of GCs per $10^9\,M_\odot$ of galaxy stellar mass. Considering the metal-poor and the metal-rich populations separately, it would be possible to place more stringent constraints on the star formation histories of galaxies (Kissler-Patig et al. 1997; Forbes, Brodie & Larsen 2001). In fact, $T_{\rm red}$ is expected to be significantly smaller for early elliptical galaxies compared to elliptical galaxies, given that they are expected to be formed through violent and gas-rich mergers with metal-rich GCs being formed within (Brodie & Strader 2006). Instead, in the high-density environment, collapses are expected to form metal-poor GCs first, meaning that $T_{\rm blue}$ is expected to be larger in hierarchical structure formation (Rhode, Zepf & Santos 2005).

Modelling the evolution of GC populations requires, on one hand, the ability to describe how the galactic field affects the GC evolution in terms of tidal mass-loss, shocks, dynamical friction and, on the other hand, the capability to closely follow GC internal

★ E-mail: agostino@camk.edu.pl

dynamics, which regulates the GC mass loss, stellar population, compact remnants. Indeed, the GCs properties are outlined by the internal dynamical processes and by their host galaxy's evolutionary history (Grudić et al. 2022; Rodriguez et al. 2022). In this work, we present a novel approach that combines the MASinGa semi-analytic tool with the MOCCA-Survey Database I. MASinGa is a semi-analytic tool that performs population synthesis of GCs. These are evolved via a set of analytical fitting formulae describing the GC orbital evolution. MASinGa basics scheme was presented in Arca-Sedda & Capuzzo-Dolcetta (2014b) and further improved in our companion paper (Arca-Sedda in preparation). The MOCCA-Survey Database I contains realistic GC models performed with MOCCA, a Monte Carlo code that follows the long-term dynamical evolution of spherically symmetric stellar clusters, based on Hénon's Monte Carlo method (and references therein for details about MOCCA code Hénon 1971; Stodolkiewicz 1982, 1986; Giersz et al. 2013), together with stellar and binary evolution and strong interactions. In this paper, we use MASinGa and MOCCA to create synthetic GC populations for the Milky Way (MW) and Andromeda (M31). We compare simulations with data from the Harris catalogue (updated 2010 Harris 1996) and Baumgardt catalogue (Baumgardt & Hilker 2018) for MW, and from the Revised Bologna Catalogue (RBC; Galleti et al. 2004; Galleti et al. 2006; Galleti et al. 2014) for M31, respectively.

The paper is organized as follows. In Section 2, we provide the details of the methodology and the physical recipes adopted in our tool, together with the extension introduced by this paper. In Section 3, we describe the initial conditions used to reproduce the MW and M31 GC populations, with the obtained results presented in Section 4. Finally, in Section 5, we provide our final conclusions and describe our future work. In the Appendix, we show the results for M31's GC population derived from an analytical fit to the observed galaxy's rotation curve.

2 METHOD

In this section, we briefly discuss the main features of MASinGa and the MOCCA Survey Database I.

The GC populations have been simulated using the MASinGa software (Arca-Sedda in preparation). The semi-analytic modelling used in MASinGa has been used previously to carry out GC infall scenario studies (Arca-Sedda & Capuzzo-Dolcetta 2014a; Arca-Sedda et al. 2015). The GC infall scenario has been discussed as a process for the formation of a compact nucleus in the centre of a galaxy (Tremaine, Ostriker & Spitzer 1975; Capuzzo-Dolcetta 1993; Arca-Sedda & Capuzzo-Dolcetta 2014a). Similarly, infalling GCs can merge in the galactic centre, enhancing the TDE event rate (Arca-Sedda et al. 2015) and contributing to the mass evolution of the super massive BHs (SMBHs).

2.1 MASinGa code

MASinGa (Modelling Astrophysical Systems In GAlaxies) enables the initialization of a GC system for a given set of galaxy parameters. For each GC in the sample, MASinGa simulates the orbital evolution taking into account the galactic tidal field and shocks, which contribute to the cluster disintegration, dynamical friction, which drags the cluster toward the galactic centre, and internal relaxation, which regulates the cluster mass-loss and expansion/contraction. MASinGa offers a wide series of choices for the galaxy parameters, the GC mass and spatial distribution, the total mass in GCs of a galaxy. An early version of MASinGa has been used to model the formation of NCSs via orbital segregation and merger of massive star clusters, a mechanism known as dry-merger.

In the following, we describe the main features of MASinGa and the parameter chosen in this work. More details about the code are discussed in our companion paper (Arca-Sedda in preparation).

2.1.1 *Galaxy density model and GC initial conditions*

In MASinGa, galaxies are modelled through the Dehnen (1993) family of potential density pairs, characterized by a spherically symmetric density profile in the form:

$$\rho_G(r) = \frac{(3-\gamma)M_g}{4\pi r_g^3}\left(\frac{r}{r_g}\right)^{-\gamma}\left(1+\frac{r}{r_g}\right)^{\gamma-4},$$

where M_g is the galaxy total mass in $M_\odot$, r_g is the galaxy length scale in kpc, and γ is the density profile slope. Hereafter, we identify with $M_g(r)$ the galaxy mass enclosed within a galactocentric distance r. The advantage of the Dehnen density profile is the simple analytic form and the flexibility to generate different galaxy density profile distributions, determined by only two parameters r_g and γ. The galaxy profile can be more or less cuspidal with the adjustment of those two parameters.

MASinGa offers several choices to initialize galactic star cluster systems in terms of cluster mass function, radial distribution, or formation time. In our models, each GC is characterized by its galactocentric distance $R_{\rm GC}$, its mass $M_{\rm GC}$, the eccentricity of the orbit $E_{\rm GC}$, and the half mass radius $r_{h,\,\rm GC}$.

For our purposes, in this work we assume that the GC population is initially distributed across the galaxy following the density distribution of the host galaxy, with the GCs' total mass population being a fraction of the total galaxy mass, i.e. $\rho_{\rm GCS}(r) = \alpha \cdot \rho_G(r)$. This implies that the total GC mass within any concentric radial annulus should be proportional to the total galaxy mass within the same radial annulus, with the total number of GCs within each radial bins set by the total GC mass inside the radial bin and the initial mass function (GCIMF). The GC masses $M_{\rm GC}$ are selected randomly from the GCIMF. The orbital eccentricities $E_{\rm GC}$ have been randomly picked from a thermal distribution. Finally, the $R_{\rm GC}$ have been chosen randomly within the radial bins in which the galaxy density profile has been divided. This method ensures that in our initial model the density profile of the galaxy and the GC system share the same functional form.

2.1.2 *Globular cluster dynamical evolution*

The interplay between the internal dynamics, the galactic tidal field, and the dynamical friction dictates the evolution and the survival of the GCs. Meanwhile the GCs internal evolution is driven by the stellar evolution and the relaxation process, the galactic tidal dissolution is driven by the change of the galactic gravitational field in which the GC moves. The presence of a tidal field influences the half-mass radius relaxation time-scale and the system mass-loss, with a GC in a strong tidal field dissolving faster than an isolated GC. For a GC in a circular orbit and in a point-mass galaxy potential, the GC experiences a static tidal field. Internal evolution is dominated by stellar evolution, which regulates mass-loss in the first $\sim$10$-$100 Myr, while external evolution is regulated by the galaxy tidal field, which drives the cluster dissolution, and dynamical friction, which drags GCs towards the host galaxy centre (Tremaine et al. 1975; Capuzzo-Dolcetta 1993; Antonini et al. 2012; Arca-Sedda & Capuzzo-Dolcetta 2014a). The GC dissolution can also be boosted by interactions with the galactic central regions and structural elements, like a bulge or stellar disc. These strong interactions are usually referred to as bulge and disc shocks. Based on the efficiency of the energy transferred during these phases, the dissolution can be

catastrophic or diffusive, with the GCs disrupted in shorter or on longer time-scales, respectively. If the galactic local density would be larger than the GCs' densities, the interaction between the GC and the galaxy could be catastrophic, resulting in the GC's dissolution.

As mentioned above, the dynamical friction drags the GCs towards the galactic centre, where they can contribute to the formation of a NSC (Tremaine et al. 1975). In previous studies, Arca-Sedda & Capuzzo-Dolcetta (2014b) and Arca-Sedda et al. (2015) exploited *N*-body simulations of Dehnen galaxy models to derive a fitting formula for the dynamical friction time-scale $\tau_{\rm df}$ in the form:

$$\tau_{df} = 0.3 \cdot g(E_{\rm GC}, \gamma) \cdot \left(\frac{r_g}{1\,{\rm kpc}}\right)^{3/2} \left(\frac{M_g}{10^{11}\,{\rm M}_\odot}\right)^{1/2} \cdot \cdot \left(\frac{M_{\rm GC}}{M_g}\right)^{-0.67} \left(\frac{R_{\rm GC}}{r_g}\right)^{1.76}, \quad (1)$$

with r_g in kpc and M_g is the total galaxy mass in $M_\odot$, $M_{\rm GC}$ is the GC mass, and $R_{\rm GC}$ is its galactocentric position. The function $g(e, \gamma)$ is a dimensionless function given by

$$g(e, \gamma) = (2 - \gamma)\left[a_1\left(\frac{1}{(2-\gamma)^{a_2}} + a_3\right)(1 - e) + e\right], \quad (2)$$

with $a_1 = 2.63 \pm 0.17$, $a_2 = 2.26 \pm 0.08$, and $a_3 = 0.9 \pm 0.1$ (Arca-Sedda et al. 2015).

The importance of these three factors (internal dynamics, static and dynamical tides, and dynamical friction) is established by their respective time-scales. The long-term time-scale of internal dynamics is connected to the half-mass radius relaxation time-scale. If the dynamical friction time-scale is smaller than the GCs' age and the dissolution time-scale, the GCs would dissolve, possibly polluting the galactic halo. On the other hand, if the dissolution time-scale (connected with interplay between the relaxation process and tides) is smaller than the dynamical friction time-scale, the GCs would be dissolved before merging into galaxy centre. In MASinGa, the star cluster orbital evolution is performed taking into account the orbital segregation driven by dynamical friction, the tidal dissolution driven by internal dynamics, the galactic tidal field, and the close orbital passages around the galactic bulge and across the galactic disc. Moreover, to take into account the mass-loss triggered by these disruptive mechanisms, in MASinGa we assume that the GC mass evolution follows an exponential form, $M_{\rm GC}(t) \propto \exp(-t/t_d)$ (Hénon 1961), where t_d is the smallest disruption time-scale among internal evolution, bulge and disc shocks, galactic field.

The galactocentric position time evolution is described by the dynamical friction time-scale evolution. In fact, the actual galactocentric position $r(t)$ at each time t is given by

$$\tau_{df}(r_0) - \tau_{df}(r) = t,$$

with r_0 being the initial galactocentric position and τ_{df} the dynamical friction time-scale, described by equation (1) (Arca-Sedda et al. 2015). Substituting the value for τ_{df}, it is possible to determine the galactocentric position at time t. Finally, the eccentricity time evolution is described as $E_{\rm GC}(t) = E_{\rm GC}(t = 0) \cdot \exp(-t/\alpha)$, with $\alpha = g(0, \gamma)/(g(E_{\rm GC}, \gamma) \cdot \tau_{df})$ as the orbit circularization time-scale due to dynamical friction, and $g(e, \gamma)$ as described in equation (2). This choice ensures that the orbit circularizes as the GC approaches the centre, as is expected from dynamical friction (Colpi, Mayer & Governato 1999).

In this work, we assume that all GC form at redshift $z = 4$, thus MASinGa evolves GC orbit either down to $z = 0$, up to the cluster dissolution, or until the cluster orbit reaches the inner 10 pc, i.e. twice the observed half light radius of the MW NSC (Chatzopoulos et al. 2015). Also, models that were dissolved at distances within twice the chosen NSC radius (that is, within 20 pc) were considered as accreted to the NSC. Indeed, the dissolved GC would be gravitationally bound to the NSC and hence accreted. The possibility to follow GC dynamics down to the inner few pc of the galaxy enables us to place constraints on the possible formation of an NSC. To test the uncertainties in our models, we varied the maximum distance below which a GC is considered accreted into the NSC, finding not significant changes in the range of 10−50 pc. Finally, a GC was considered disrupted if the local galactic density is greater than the GC half-mass radius density, or when the actual mass is smaller than 5 per cent its initial value.

2.2 Updated GC internal dynamics recipes

Semi-analytic tools like MASinGa offers the unique advantage of a risible computational load, thus allowing the realization of hundreds galaxy models within a few hours. None the less, the simplistic approach behind this type of tools misses the great level of detail attainable with direct *N*-body and Monte Carlo codes, whose computational costs made, however, impossible any population studies. MASinGa is conceived and devised to efficiently exploit the advantages of both semi-analytic and *N*-body methods. In fact, MASinGa can be interfaced with cluster simulation catalogues to provide a comprehensive view of internal and external GC evolution. In this work, we devise an interface to couple MASinGa with the MOCCA-Survey Database I, as explained in the following.

The Monte Carlo methods are known to be fast and reliable, with results comparable with the NBODY ones (Wang et al. 2016; Kamlah et al. 2021) and MW GC properties (Leveque, Giersz & Paolillo 2021; Leveque et al. 2022). The models from the MOCCA-Survey Database I (Askar et al. 2017) have been used in this work. In order to couple the MASinGa results with the MOCCA-Survey Database I model, an update for the internal dynamical evolution has been applied to the MASinGa analytical equations. Better estimations of mass-loss, tidal field, and half-mass radius have been introduced in this work, together with the creation of the MASinGa-MOCCA model connection.

The tidal radius and half-mass radius evolution play an important role in the GC mass-loss. More compact clusters (that is, with small half-mass radius versus tidal radius ratio) would remove less objects (stars or binaries) from the system, and therefore loose less mass compared to less compact clusters. MOCCA-Survey Database I models take into account the realistic evolution of star clusters and do show a different mass-loss evolution for tidally filling and underfilling models. To better represent the mass loss for MASinGa models at 12 Gyr, and to compare GC models from MASinGa with the ones from MOCCA Database I, a better constraint for mass loss (and hence half-mass radius and tidal radius) evolution was needed.

In MASinGa, the initial tidal radius $r_{\rm tidal}$ is determined from the galactocentric distance R_C. Supposing a circular orbit, the given $r_{\rm tidal}$ in the external galaxy is calculated according to the equation:

$$R_C: \qquad r_{\rm tidal} = R_C \cdot \sqrt[3]{\frac{M_{\rm GC}}{3M_g(R_C)}}, \quad (3)$$

with $M_g(R)$ as the galaxy's mass at position R. The galaxy's mass at each position can be determined by the galaxy's rotational curve or from the Dehnen model mass profile.

The initial half-mass radius for MASinGa models are determined by the Marks & Kroupa (2012) relationship. In order to reproduce

the observed scatter, the initial half-mass radius value has been increased by a multiplicative factor, chosen randomly from a uniform distribution between 1 and 15. A minimum and a maximum value for $r_{h,\,\mathrm{GC}}$ of 0.2 and 7 pc was set, respectively. An additional limitation has been imposed on $r_{h,\,\mathrm{GC}}$, so that its value cannot be larger than 0.3 r_{tidal}. In fact, for a cluster with an initial spatial distribution described by a tidally underfilling King model (King 1966) with $W_0 = 6.0$, the half-mass radius is around 10 times smaller than the initial r_{tidal}.

The evolution of the tidal radius at each time t_i takes into consideration the mass-loss of the system,

$$r_{\mathrm{tidal}}(t_i) = r_{\mathrm{tidal}}(t_0) \cdot \sqrt[3]{M_{\mathrm{GC}}(t_{i-1})/M_{\mathrm{GC}}(t_0)},$$

with $M_{\mathrm{GC}}(t_0)$ being the initial GC mass, $t_0 = 0$ and $t_i > t_{i-1}$. Instead, the evolution of the half mass radius followed equation 1 from Giersz & Heggie (1996),

$$r_{h,\mathrm{GC}}(t_i) = r_{h,\mathrm{GC}}(t_0) \cdot b \cdot (t_i - T_0)^{(2+\nu)/3}$$

The values for b, T_0, and ν have been obtained by fitting the formula to the half-mass radius evolution to all the models used in Paper I (Leveque et al. 2021). The mean values are: $b = 0.787 \pm 0.124\ pc/Myr$, $\nu = -1.467 \pm 0.545$, $T_0 = -13.48 \pm 4.56$ Myr. The models used for our estimation are only models that survived 12 Gyr of evolution. This means that the reported values are biased for the surviving clusters only.

Finally, the mass evolution is determined by the Spitzer formula (Spitzer 1987), so that

$$M_{\mathrm{GC}}(t_i) = M_{\mathrm{GC}}(t_0) \cdot e^{-t_c/t_i},$$

with $t_c = t_{\mathrm{relax}}/\xi$ and t_{relax} is the initial *Spitzer* relaxation time (Spitzer 1987). The value of ξ is determined by whether the model is isolated or not at each time-step t; that is,

$$\xi = 8.5 \times 10^{-3} \quad if\ r_{h,\mathrm{GC}}(t_i)/r_{\mathrm{tidal}}(t_i) \leq 0.1,$$
$$\xi = 4.5 \times 10^{-2} \quad if\ r_{h,\mathrm{GC}}(t_i)/r_{\mathrm{tidal}}(t_i) > 0.1.$$

For an initially tidally filling King cluster (King 1966) with $W_0 = 6.0$, the initial half-mass radius is 10 times smaller than the initial tidal radius. This value has been chosen as a limiting value to describe an isolated and non-isolated cluster in our simulation. The MOCCA-Survey Database I models used in this study were mostly tidally underfilling models, with $r_{h,\,\mathrm{GC}}(0)/r_{\mathrm{tidal}}(0) = 0.02$ and 0.04. So it seems that the mass-loss from the cluster can be described, for a considerable fraction of its evolution, as for an isolated cluster. The assumption about mass-loss according to *Spitzer*'s recipe for isolated clusters is a reasonable first-order approximation. However, due to the mass-loss connected with stellar evolution and binary energy generation, the cluster will expand and eventually will become tidally filling (after a relatively long time, depending on the degree of underfilling). In that case, the mass-loss is governed by the galactic tidal field. This rather rough treatment should provide an approximate evolution of the mass loss from the cluster and also provide the evolution of the tidal radius.

2.3 MASinGa-MOCCA connection

At the end of the MASinGa evolution, the MASinGa results are coupled with the models from the MOCCA-Survey Database I. To better reproduce the observed properties of the studied GC populations, a model subset from the MOCCA-Survey Database I was chosen, with the selection procedure described in Section 3.2. Using the subset of models from MOCCA-Survey Database I, a library of MOCCA models has been generated – the MOCCA-Library models. The MOCCA-Library consists of MOCCA-Survey Database I model representations with different orbital properties and orbital positions in the studied galaxy's gravitational field. Models from the MOCCA-Library were picked to populate the studied galaxies, and used to provide detailed GC observational properties.

2.3.1 *MOCCA models in a different tidal field*

In order to determine the galactocentric position in the studied galaxy gravitational potential, a few steps have been taken. First of all, the tidal radius and galactocentric distance for a circular orbit in the studied galaxy potential has been determined. The MOCCA-Survey Database I models were assumed to move on a circular orbit at Galactocentric distances between 1 and 50 kpc in the Galaxy. The Galactic potential was modelled as a simple point-mass, taking as the central mass the value of the galaxy mass enclosed within the GC's orbital radius. The GC's rotation velocity was set to 220 km s^{-1} over the whole range of galactocentric distances. Knowing the tidal radius for the MOCCA model and the density/potential distribution for the simulated galaxy, it is possible from equation (3) to determine the correct galactocentric distance R_C for a circular orbit in an external galaxy, for a given tidal radius r_{tidal} and GCs mass M_{GC}.

Cai et al. (2016) exploited *N*-Body simulations to establish the evolution of GCs on circular and eccentric orbits. The authors established the apocentric distance for the eccentric orbit that has a lifetime similar to a cluster with the same mass on a circular orbit. Therefore, for each GC eccentric orbit, it is always possible to find a circular orbit on which the GC will experience an equivalent mass loss. Fitting the data shown in their Fig. 6, it is possible to find the apocenter distance R_{apo}, scaled to R_C, for an eccentric orbit with an initial orbital eccentricity E_{GC} as

$$\frac{R_{\mathrm{apo}}}{R_C} = (1 - 0.71 \cdot E_{\mathrm{GC}})^{-5/3}. \quad (4)$$

The pericenter distance is then determined as $R_{\mathrm{peri}} = 2.0 \cdot a - R_{\mathrm{apo}}$, with a as the semimajor axis of the orbit. Using Kepler's third law, we found the GC orbital period P, and then computed the mean anomaly ϵ,

$$\epsilon = \frac{2\pi \cdot (t - T)}{P},$$

with T being the periastron passage time and t the current time. The term $(t - T)$ has been randomly picked between 0 and P. Successively, the eccentric anomaly E has been determined solving the Kepler equation, $\epsilon = E - E_{\mathrm{GC}} \cdot \sin(E)$. Knowing the relation between the eccentricity and the true anomalies μ,

$$\tan\left(\frac{\mu}{2}\right) = \sqrt{\frac{1+e}{1-e}} \tan\left(\frac{E}{2}\right),$$

the galactocentric position R_{GC} has been determined as

$$R_{\mathrm{GC}} = \frac{a \cdot (1 - e^2)}{1 + e \cdot \cos(\mu)}.$$

This simplistic procedure does provide a reasonable first-order approximation for the GC's galactocentric distance distribution. As for the observed GC populations in external galaxies, the actual orbit and actual galactocentric distances are unknown. For this reason, the GC's galactocentric distance R_{GC} has been chosen randomly within the orbit apocentre and pericentre.

2.3.2 *MOCCA-Library model generation and selection*

For each model in the selected subset, 30 eccentricities have been selected. Each eccentricity identifies an orbital representation in the studied galaxy (see equation 4). The MOCCA-Library eccentricity E_{GC} has been randomly chosen from the thermal distribution. For each orbital representation, R_{GC} has been sampled 30 times within the orbit apsis as described above,[1] giving a total of 900 representations of each unique MOCCA-Survey Database I model in the MOCCA-Library. This procedure allows us to populate the same model in different regions of the galactic field (that is, different galactocentric radial bins), and with different orbital eccentricities.

For a fixed galaxy model, the dynamical friction time-scale and the galaxy-GC interactions are functions of position and eccentricity only, as shown in equation (1). Therefore, the family of different representations in the studied galaxy implies a variety of dynamical interactions with the galactic potential field for each MOCCA-Survey Database I model. These model representations have similar mass loss as simulated in the MOCCA-Survey Database I model. In fact, a shorter dynamical friction time-scale would grab the GCs closer to the galactic centre, and eventually disrupt them due to the high galactic density or even lead to accretion into the galactic centre. Finally, models from the MOCCA-Library are defined as unique when they represent different MOCCA models. Indeed, for different unique models the internal dynamical evolution is diverse – for example, mass-loss, half-mass radius, and compact-object composition. The different representations of one unique model in the MOCCA-Library result in a similar internal dynamical evolution, but with an important diversity in external dynamical evolution.

MOCCA models which lasted up to 12 Gyr were used in our simulations. In order to preserve the initial number of GCs and the number of surviving GCs, the number of GCs for the MOCCA populations are set equal to the number of MASinGa models that at 12 Gyr survived the internal dynamical evolution, independent of whether they were disrupted because of external interactions with the galaxy or sunk to the galactic centre.

This means that each MASinGa model has to be mapped to a MOCCA-Library model representation, taking into account its initial position and initial mass. To simplify the model selection procedure and reduce the number of repetitions of unique MOCCA Database models, the MOCCA-Library population has been divided into a 2D matrix grid, according to the GCs' initial galactocentric distance and initial mass bins. For each MASinGa model, only one representation for each unique MOCCA model was randomly selected within each matrix cell: the same initial galactocentric bin from the MASinGa model has been used to select the matrix cell, meanwhile the initial mass bin was selected randomly from the GCIMF cumulative distribution. Finally, one model representation from the selected model representations has been randomly chosen to represent the considered MASinGa model and successively removed from the MOCCA-Library.[2] It is expected that multiple instances

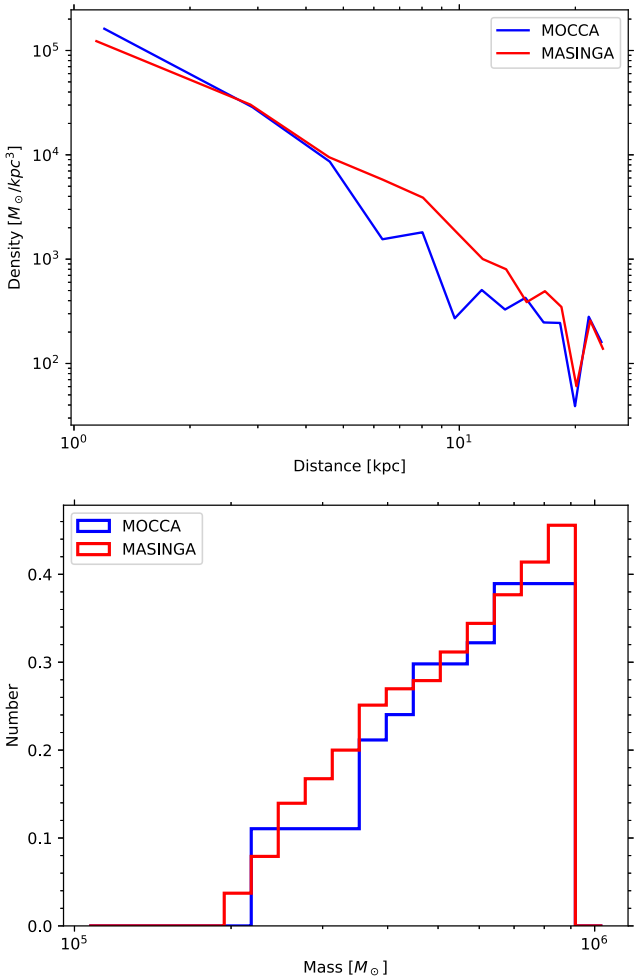

Figure 1. Initial density distribution (top) and GCIMF cumulative distribution (bottom) for a randomly selected model for MOCCA (blue) and MASinGa (red) for the MW representation. Similar results have been obtained for the M31 representation.

(even thousands) of MOCCA representations populate each mass and galactocentric position bin, implying multiple repetitions of the same unique MOCCA models. This procedure has been necessary to reduce the bias to over-reproduce the MASinGa models with few unique MOCCA models.

The GCIMF has been divided into only a few mass groups with different bin sizes, in order to contain at least one model from the MOCCA-Survey Database I. Indeed, as it will be explained in Section 3.2, the initial masses in the MOCCA-Survey Database I are not continuous. Instead, the GCIMF cumulative distribution has been normalized to the initial MASinGa models mass distribution. This whole procedure will assure that the galaxy density distribution together with the GCIMF distribution will reproduce the initial conditions in the MASinGa population.

In Fig. 1, we report the comparison between the MASinGa and MOCCA initial GCs density distribution and their GCIMF cumulative distribution. The GC density distribution in MASinGa follows the galaxy density distribution function, and the MOCCA-Library density distribution is comparable with the MASinGa one. Similarly, the GCIMF cumulative distribution inferred from the MOCCA-Library is in good agreement with the MASinGa distri-

[1] In a proper GC orbit representation, the orbit should be sampled with higher probability close to the pericenter and apocenter where the radial velocity is smallest.

[2] Being N_1, N_2, etc., the total number of MOCCA-Library model representations in each cell and N_1', N_2', etc., the number of representations of unique models in each cell, only one model has been chosen among the representation ones N_1', N_2', etc. Whenever a representation model has been chosen to represent a MASinGa model, it has been removed from the MOCCA-Library. This means that the new number of model representations and unique models in the corresponding cell would be $N_i - 1$ and $N_i' - 1$, respectively.

bution, taking into consideration the discontinuity in the initial mass in the MOCCA-Survey Database I models.

2.3.3 *MOCCA-Library model evolution*

The connection with the MASinGa code is necessary to describe the GCs' dynamical friction and the interactions with the galaxy evolution with the internal properties for the MOCCA models being already known. Once the MOCCA-Library models have been connected with the MASinGa GC population, the selected models were evolved. The actual mass, half-mass radius, and internal objects' property values from the MOCCA-Survey Database I were used to determine their evolution within MASinGa. Instead, the galactocentric distance and eccentricity evolution are determined using the equations adopted in MASinGa, as described in Section 2.2. Finally, the same condition for sinking to the NSC used for MASinGa models were applied to the chosen MOCCA-Library models – that is models have been considered accreted to the NSC if their galactocentric position is smaller than the NSC radius. Also, the models were considered as disrupted if the local galactic density was found to be greater than the GC half-mass radius density.

3 INITIAL CONDITIONS

3.1 Observed GC populations for MW and M31

The results from our simulations have been compared with the observational data from the Harris catalogue (updated 2010 Harris 1996) and Baumgardt catalogue (Baumgardt & Hilker 2018) for the MW, and from Revised Bologna Catalogue (RBC; Galleti et al. 2004; Galleti et al. 2006; Galleti et al. 2014) for M31.

The Harris catalogue contains the basic parameters for the 157 classified GCs observed in the MW galaxy. Meanwhile, the structural parameters for the 112 MW GCs are reported in the Baumgardt catalogue. The RBC contains the 231 confirmed M31 GCs and their positions, photometry, velocities, structural parameters, metallicities, and lick indexes. The complete catalogue also contains information about non-GC objects (such as galaxies or GC candidates). In this work, we selected only objects in the catalogue that are confirmed GCs.

Additionally, for the M31 GC population, the observed V magnitude has been transformed to the absolute $V_{\rm abs}$, using a distance of M31 from the Sun of 783.43 kpc and $E(V-B)=0.11$, as reported in Galleti et al. (2004, 2006).The galactocentric distances have been determined as the distance between the position in the sky of each GC and the M31 centre (RAJ2000 = 00 42 44.330, DECJ2000 = +41 16 07.50).

The total mass for each GC in the Harris catalogue and in the RBC was estimated using a mass-to-light ratio $M/L_V = 1.83$ (Baumgardt, Sollima & Hilker 2020), with L_V as the absolute V luminosity expressed in units of $L_\odot$ and M in units of $M_\odot$. The dispersion around the M/L_V mean found in Baumgardt et al. (2020) of 0.24 was used to determine the mass error for each GC. The determined GC masses range between $1\times10^4-2\times10^6$ and $5\times10^4-3\times10^6$, for MW and M31, respectively.

As seen in most of the observed galaxies, the largest parts of the GC populations are located within a few kpc from the galactocentric centre. Furthermore, due to observational limits and errors, detecting and confirming GCs that would belong to external galaxies' GC populations at larger distances from the galactic centre can be challenging. Indeed, the number of confirmed GCs in the RBC catalogue are distributed within 17 kpc from the galactic centre. For this reason, we limited our study to GCs within 17 kpc from the galactic centre.

The derived structural parameters (such as half-light radius, core radius, etc.) for M31 have been derived by fitting to the surface brightness profile of the observed GCs. The derived parameter uncertainties are enhanced for smaller GC surface brightness profiles. In order to reduce the uncertainties of the half-light radius, we have considered only the observed M31 GCs with half-light radius surface brightnesses (defined as L_V/r_h^2, with L_V being the total V luminosity and r_h the half-light radius) greater than $4000\,L_\odot/pc^2$. This value was set arbitrarily, but with the aim of keeping a large fraction of the observed GCs. Indeed, $\sim$ 95 per cent of the M31 GC population has a half-light radius surface brightness greater than this value.

3.2 MOCCA-Survey Database I model selection

The MOCCA-Survey Database (Askar et al. 2017) consists of nearly 2000 real star cluster models that span a wide range of initial conditions, provided in table 1 in Askar et al. (2017). For half of the simulated models, supernovae (SNe) natal kick velocities for neutron stars (NSs) and BHs are assigned according to a Maxwellian distribution, with a velocity dispersion of $265\,km\,s^{-1}$ (Hobbs et al. 2005). In the remaining cases, BH natal kicks were modified according to the mass fallback procedure described by Belczynski, Kalogera & Bulik (2002). Metallicities of the models were selected as follows: $Z = 0.0002$, 0.001, 0.005, 0.006, 0.02. All models were characterized by a Kroupa (2001) IMF, with minimum and maximum initial stellar masses of 0.08 and $150\,M_\odot$, respectively. The GC models were described by the King (1966) profile with central concentration parameter values $W_0 = 3$, 6, 9. They had tidal radii ($r_{\rm tidal}$) equal to 30, 60, or 120 pc, and were either tidally filling or had ratios between $r_{\rm tidal}$ and the half-mass radius (r_h) equal to 25 or 50. The primordial binary fractions were chosen to be 5 per cent, 10 per cent, 30 per cent, or 95 per cent. Models characterized by an initial binary fraction equal to or lower than 30 per cent had their initial binary eccentricities selected according to a thermal distribution Jeans (1919), with mass ratios and logarithms of the semimajor axes according to uniform distributions. For models containing a larger binary fraction, the initial binary properties were instead selected according to the distribution described by Kroupa (1995), via so-called eigen-evolution and mass feeding algorithms. The models consist of 4×10^4, 1×10^5, 4×10^5, 7×10^5, 1.2×10^6 objects (stars and binaries). As shown by Askar et al. (2017) and Leveque et al. (2021), the MOCCA models reproduce observational properties of Milky Way GCs relatively well.

3.3 MASinGa initial conditions

Dynamical friction is an important process for the GC galactocentric distance evolution. As shown in Arca-Sedda & Capuzzo-Dolcetta (2014b) and equation (1), it strongly depends on the galaxy mass M_g, typical radius r_g, and slope of the matter density γ. In Dehnen models (Dehnen 1993), these quantities can be used to calculate the rotation curve, given in the form:

$$v_c^2(R) = G\cdot M_g\cdot\frac{R^{2-\gamma}}{(R+r_g)^{3-\gamma}},$$

with R being the galactocentric distance and G the gravitational constant.

We fit the equation above to tailor our model to the MW and M31 rotation curves, finding the best fit parameters to the observed

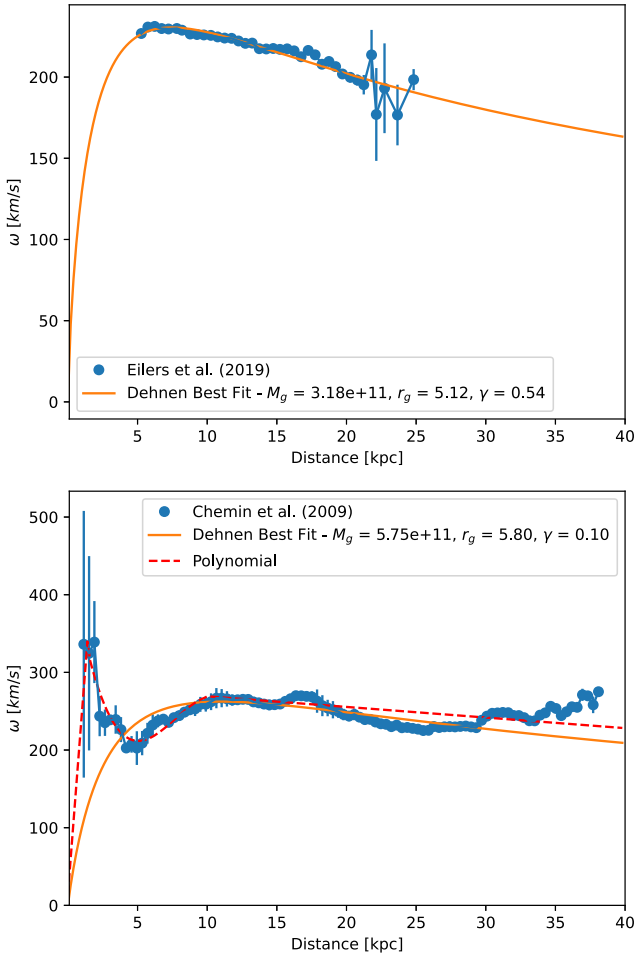

Figure 2. Rotational curve fitting for MW (top) and M31 (bottom). In the figure label, the Dehnen best-fitting parameters are reported.

MW rotational curve (Eilers et al. 2019) are $M_g = 3.18 \times 10^{11}\,\mathrm{M}_\odot$, $r_g = 5.12$ kpc, $\gamma = 0.54$. Similarly, the best fit to the observed M31 rotational curve (Chemin, Carignan & Foster 2009) gives $M_g = 5.75 \times 10^{11}\,\mathrm{M}_\odot$, $r_g = 5.8$ kpc, $\gamma = 0.1$. The best fit, together with the observational rotational curves are showed in Fig. 2 with the top and bottom panels corresponding to the MW and M31, respectively. The Dehnen density profile cannot reproduce the observed increase of the observed rotational velocity in the central region of M31 (∼5 kpc), implying a mass underestimation in that zone of the galaxy and, as will be also discussed in the Appendix, an underestimation in the number of infalling GCs in the central region, the NSC mass growth, and the mass evolution of the infalling intermediate-mass BHs (IMBHs) in the NSC. To better understand the importance of the underestimation of the GCs infall, a polynomial fit was applied to the M31 rotational curve to reproduce the central density increase in the observed rotational curve. In particular, the polynomial curve was divided into three regions to better reproduce the observed curve: a linear fit between 0 and 1.5 kpc, a cubic fit between 1.5, and 10 kpc and a linear fit between 10 and 20 kpc. In this model, the polynomial curve fit has been used to determine the mass and the density profile of the simulated M31 galaxy. Instead, the Dehnen best-fitting model parameters for M31 rotational curve have been used to determine the dynamical friction time-scales, as described in equation (1).

The initial mass function for GCs is set to be a power-law dN/dm $= b \cdot m^{-\alpha}$ with a slope of $\alpha = 2$ (Lada & Lada 1991; Kroupa 2001). The GC's total mass population is expected to be a fraction of the total galaxy mass, that is $M_{\mathrm{GCS}} = \beta M_g$. The β parameter can be estimated from the observed GC masses. Webb & Leigh (2015) found that the initial GC mass was ∼5 times larger than the actual observed values. This results is in agreement with the values reported in the MOCCA Database I, with a mean mass ratio at the initial time and at 12 Gyr being 4.2. Using this result, we determined the initial minimum and maximum masses for the observed GCs in MW and M31, being $M_{\mathrm{min}} = 4.2 \times 5 \times 10^4 \sim 2.1 \times 10^5\,\mathrm{M}_\odot$ and $M_{\mathrm{max}} = 4.2 \times 3 \times 10^6 \sim 1 \times 10^7\,\mathrm{M}_\odot$, respectively. The considered observed GC populations (located within 17 kpc from the galactic centre) have total masses of $M_{GCS,17} \sim 3 \times 10^7\,\mathrm{M}_\odot$ and $\sim 1 \times 10^8\,\mathrm{M}_\odot$, for MW and M31, respectively. The total galactic mass included within 17 kpc is obtained from the best fit to the rotational curve, giving $M_{g,17} \sim 10^{11}\,\mathrm{M}_\odot$ and $\sim 2.5 \times 10^{11}\,\mathrm{M}_\odot$, for MW and M31, respectively. For the observed GC populations in MW and M31 we obtained a value of $\beta = M_{\mathrm{GCS},\,17}/M_{g,\,17} \sim 10^{-3}$ for both MW and M31.

However, the β parameter used in our simulations has to be adjusted. In fact, the maximum MOCCA initial mass is $1.1 \times 10^6\,\mathrm{M}_\odot$, much smaller than the initial mass seen in the observations ($M_{\mathrm{max}} = 1 \times 10^7\,\mathrm{M}_\odot$). As expressed previously, the minimum mass is set to reproduce a minimum mass at 12 Gyr of 5×10^4, implying an initial mass of 2×10^5. The total GC mass simulated from the MOCCA models would be

$$b \cdot \int_{2\times10^5\,\mathrm{M}_\odot}^{1.1\times10^6\,\mathrm{M}_\odot} m^{1-\alpha}\mathrm{d}m = M_{\mathrm{GC,MOCCA}} = \beta_{\mathrm{MOCCA}} M_g$$

To properly scale the total mass population, an appropriate value of β_{MOCCA} has been calculated as

$$\beta_{\mathrm{MOCCA}} = \beta \cdot \frac{\int_{2\times10^5\,\mathrm{M}_\odot}^{1.1\times10^6\,\mathrm{M}_\odot} m^{1-\alpha}\mathrm{d}m}{\int_{M_{\mathrm{min}}}^{M_{\mathrm{max}}} m^{1-\alpha}\mathrm{d}m}. \quad (5)$$

A value of $\sim 10^{-4}$ is obtained, and specifically a value of 2.0×10^{-4} and 3.0×10^{-4} has been used to determine the total GC population masses within 17 kpc during the MASinGa initial conditions for MW and M31, respectively.

4 RESULTS

To filter out statistical fluctuations we create 100 galaxy models for MW and M31, all formed 12 Gyr ago and evolved until present day as described above. We considered the mean values obtained from those GC populations to better obtain a more robust statistical representation of the models.

4.1 Comparison with observations

In this paper, we introduced the machinery that will be used in the following works to populate in an automatic way the GC populations of thousands of galaxies in the local universe. In order to reproduce the observed properties of the external galaxies, limitations in the simulated models (such as masses and galactocentric distances) are applied. In particular, in this work we restrict the selected models from the MOCCA-Survey Database I to generate the MOCCA-Library used in MASinGa to those in which the fallback prescription (Belczynski et al. 2002) was used. In order to generate, the initial conditions to be as generic as possible and following the observational mass at 12 Gyr, models with masses at 12 Gyr larger than $5 \times 10^4\,\mathrm{M}_\odot$ have been selected to reproduce both MW and M31 GC populations. Similarly, we have considered MOCCA models with half-light radius surface brightnesses greater than 4000 $\mathrm{L}_\odot/\mathrm{pc}^2$.

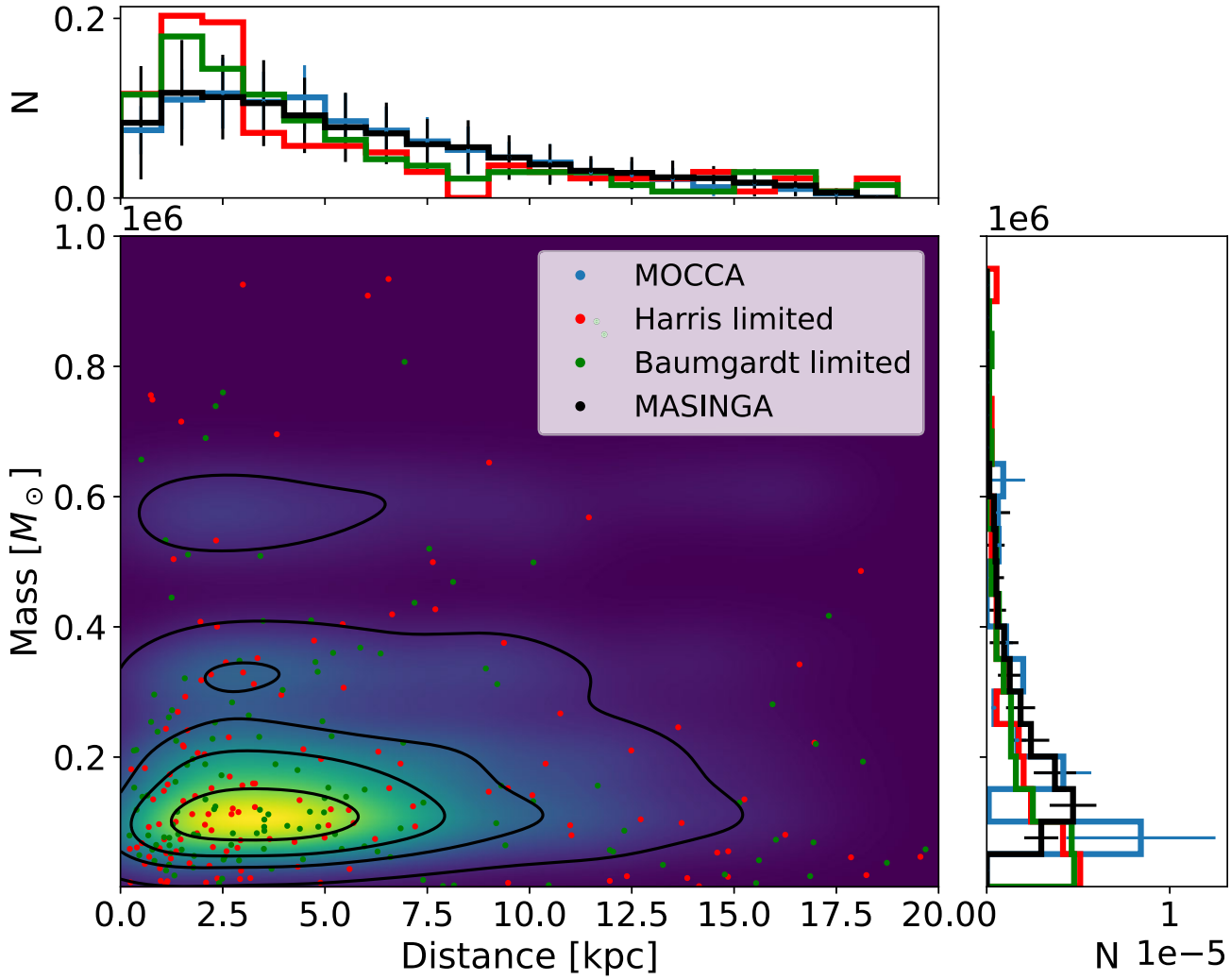

Figure 3. Density map for the galactocentric position and final mass for the MOCCA population for MW. The contours include the 80, 50, 30, and 10 per cent levels of population. The Harris and Baumgardt catalogues are reported in red and in green, respectively. On the side, the normalized histogram showing the distributions of each population is reported, with the error bars showing the standard deviations for the simulated models. In blue and black lines, the histogram for MOCCA and MASinGa models are shown, respectively.

As output from the MASinGa code, the 3D galactocentric distance for each GC is given. On the other hand, the observed distances for MW and M31 are projected distance in the sky plane. To compare our models and observations, we project MASinGa cluster position on to the plane of the sky.

In Figs 3 and 4, the density map for the final galactocentric position and final mass for the MOCCA population for MW and M31, respectively, has been reported. The colour map shows the density map for our models, and the contours include the 80, 50, 30, and 10 per cent levels of population. In black we reported the results from MASinGa, while in red, we reported the properties of MW and M31 GCs retrieved from the Harris and RBC catalogue, respectively. For MW, the observed properties from the Baumgardt catalogue are reported in green. The regions containing most of the populations are presented with brighter colour. The comparison shows that our models represent decently well the galactocentic distance and mass distribution of MW and M31 clusters. As expected, most of the GC populations are localized at smaller galactocentric distances, with a decreasing number of GCs at larger galactocentric positions. The overall spatial distributions obtained from our models are in relatively good agreement with the observed ones. However, our models exhibit a lower number of clusters within 5 kpc compared to observations. As it will be discussed in Section 5, these differences can be due to the bimodal nature of the observed GC populations, which has not been simulated in our models. Finally, both observed and simulated GCs have mostly masses in the range 10^5 and 3×10^5 $M_\odot$, with a small percentage having large masses ($> 5 \times 10^5$ $M_\odot$). Our simulated populations show a mass distribution in relatively good agreement with the observed ones. The peaks seen in the simulated distributions are connected to the mass distribution in the MOCCA models.

In Madrid et al. (2017), the authors studied the mass loss and evaporation rate of GCs in a strong Galactic tidal field, as a function of time and galactocentric distance. Their N-body simulations were compared to the MOCCA models. The authors found that the mass loss in the inner Galactic region can be enhanced. The MOCCA models were comparable with N-body simulation evolution for Galactocentric distances down to few kpc. Given that, the MOCCA models have been simulated for a constant rotational velocity and from the observed rotational curve, it is possible to see an almost

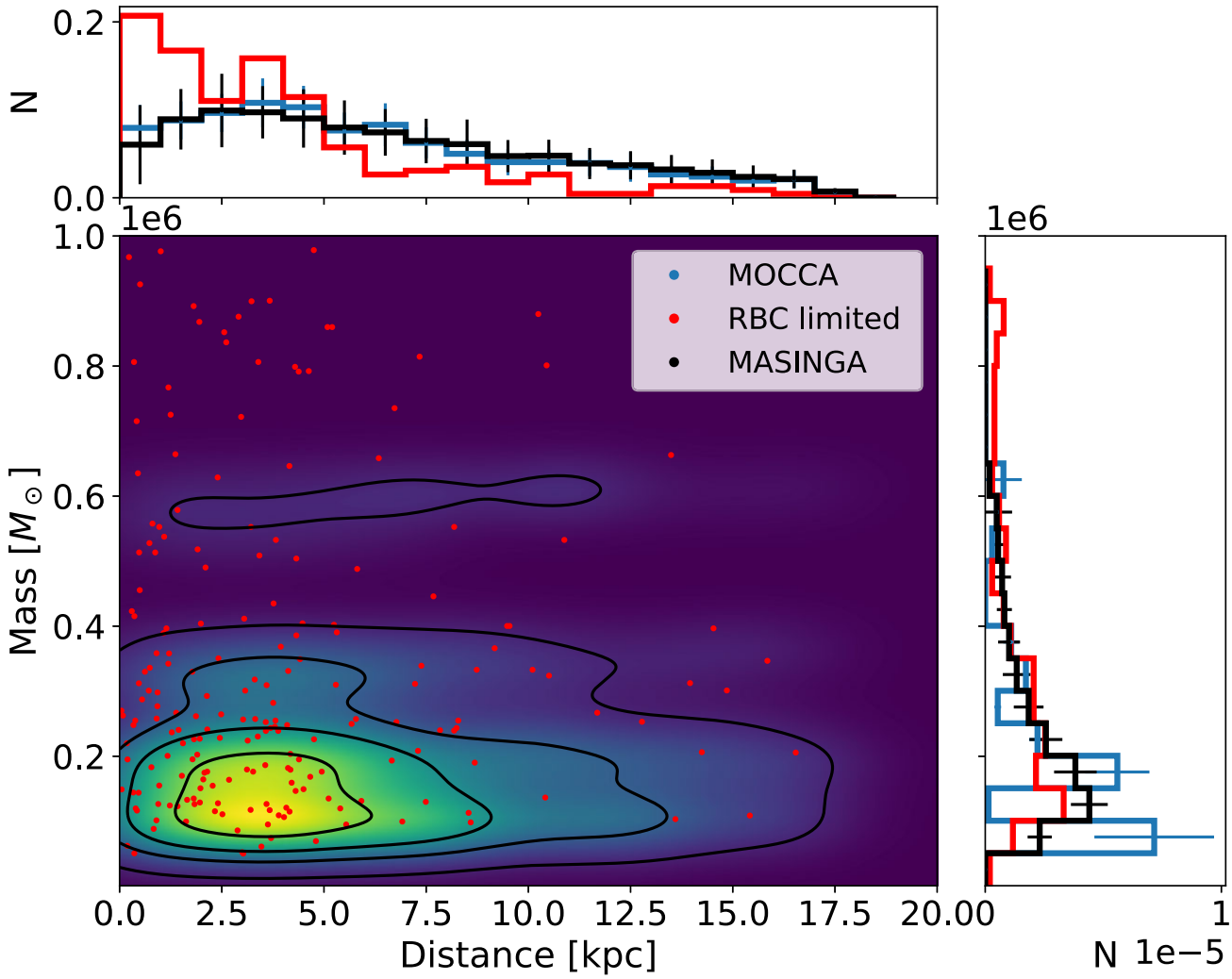

Figure 4. Density map for the galactocentric position and final mass for the MOCCA population for M31. The contours include the 80, 50, 30 and 10 per cent levels of population, respectively. The RBC catalogue is reported in red. On the side, the normalized histogram showing the distributions of each population is reported, with the error bars showing the standard deviations for the simulated models. In blue and black lines, the histogram for MOCCA and MASinGa models are shown, respectively.

constant rotational velocity in the galacatocentric distance between ∼5 and 20 kpc. Because of the point-mass approximation used in the simulations, it is expected that MOCCA models would not reproduce the mass loss of GCs at smaller distances. In order to not limit too strongly the comparison sample, the post-processing investigation and the statistical determination of GC populations' properties have been carried out for the region between 2 and 17 kpc.

One possible source of bias in our models owes to the fact that the number of MOCCA models is finite, thus it can happen that a MOCCA GC is used multiple times to replace MASinGa clusters. The repetition of the same unique model can misrepresent the structural GC parameter distribution, biasing the simulated distribution towards the unique models' properties that were randomly chosen the most. To avoid such kind of bias, when determining the radial distribution of each properties, only one unique model within each radial bin was considered. For each property, the mean value of each population's measurements has been determined together with the standard deviation.

The mass distribution profiles of GC populations are reported in Fig. 5 for MW and M31. The GC populations have been divided into 20 galactocentric radial bins, and the mass distribution has been determined as the total mass within the galactocentric distance bin. As it is possible to note, the GC's population is mostly concentrated within 5 kpc from the galaxy centre. Also, the simulated distribution falls within the error limits of the observed distribution. However, a central steep increase is seen in the observational data, meanwhile our results do not show such prominent growth in comparison. As mentioned before, this difference can be due to the insufficiency of the MOCCA model to represent the region within 5 kpc from the galactic centre. On the other hand, the simulated mean mass within the galactocentric distance bin distributions is comparable with observations at all galactocentric distance bins for both MW and M31 with a constant value for different radial bins, as shown in Fig. 6. These results gave additional evidence that the GCs' spatial density profiles obtained by our simulations follow a similar profile to the observed GCs in the MW and M31. Finally, the spikes in the observational profiles are caused by the small number of GCs found within the radial bin.

The mean half-light radius distributions are properly reproduced, for both MW and M31, as it is possible to see in Fig. 7. Most of the

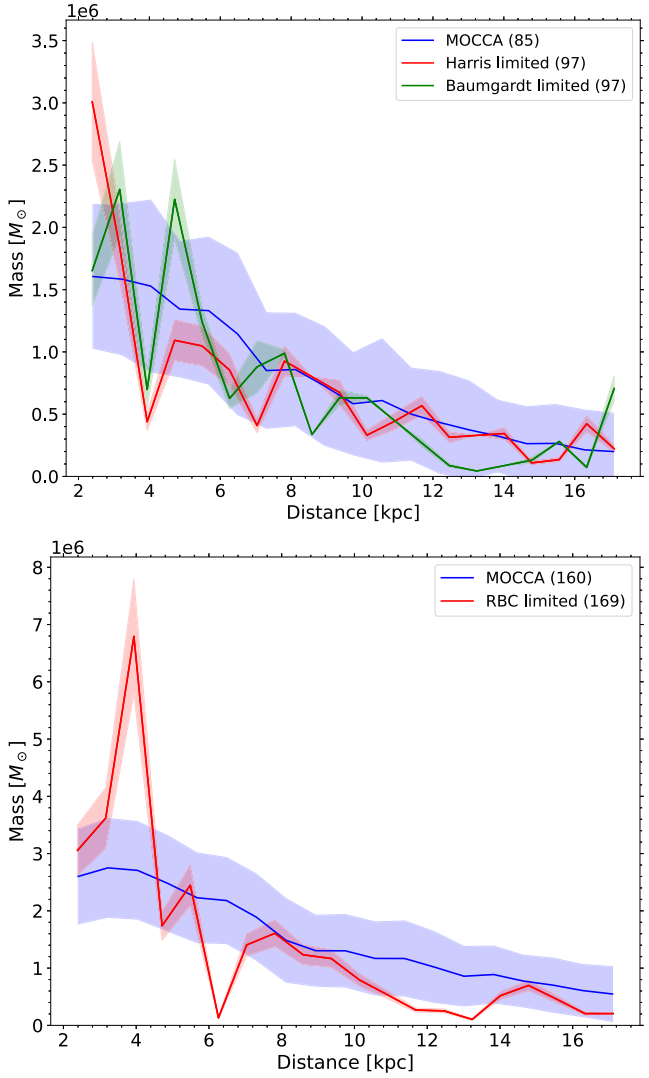

Figure 5. Mass distribution for the MOCCA population and the observed population for MW (top) and M31 (bottom) respectively. The shadow regions represent the standard deviations of the error for both the observed and the simulated GC populations. The mean number of surviving GCs are reported for MOCCA models, and the number of observed GCs are reported in parenthesis.

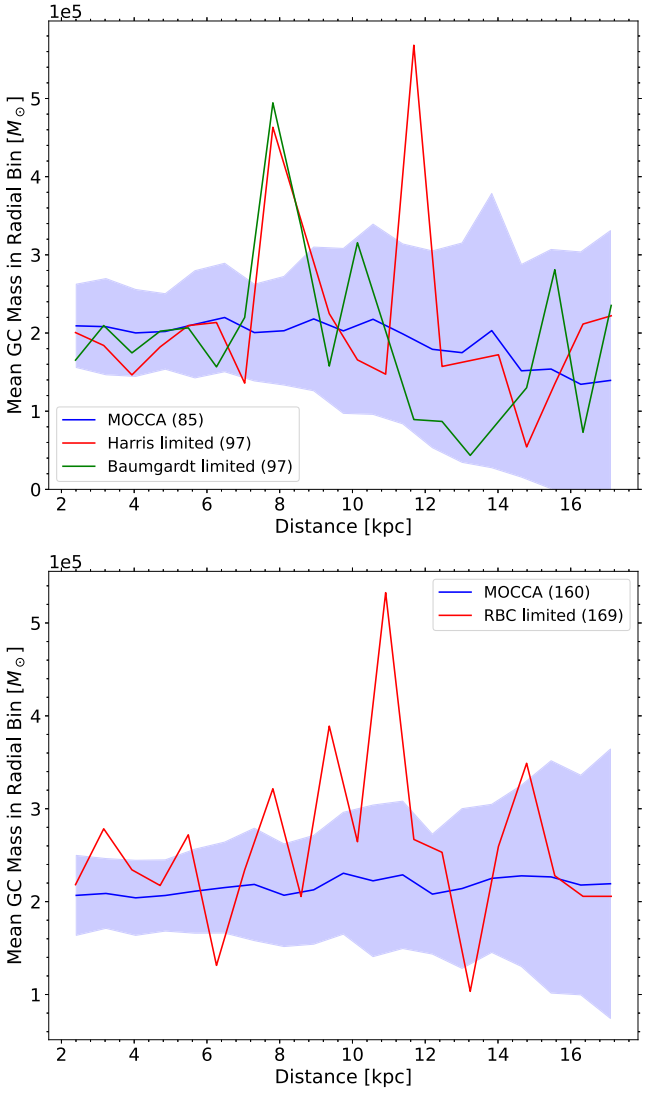

Figure 6. Mean mass distribution for the MOCCA population and the observed population for MW (top) and M31 (bottom), respectively. The shadow regions represent the standard deviations of the error for the simulated GC populations. The mean number of surviving GCs are reported for MOCCA models, and the number of observed GCs are reported in parenthesis.

GC populations show a small half-light radius, with a peak around 2 pc for both MW and M31. As shown above, the GC populations are concentrated mostly in the central region of the galaxy, where the tidal field is stronger compared to the outer regions. The half-mass radius is expected to expand until the tidal field starts to control the system evolution. From that point the half-mass radius evolution would be regulated mainly by tidal mass loss. Additionally, at smaller galactocentric distances, the galactic density is higher, meaning a higher chance to be disrupted during close passages to the galactic centre compared to the GCs in the outermost regions. Large GCs (with half-light radius greater than 8 pc) are not reproduced in our simulations, in contrast with the observed GCs in the MW. This is a consequence of the model selection described in Section 3, due to the half-light radius surface brightness limitation imposed on the MOCCA models.

In order to verify that our results are statistically in agreement with the observed properties, we applied a two-sample Kolgomorov–Smirnov test (KS test) to those distributions. The KS test is used to compare two samples, quantifying the distance between the cumulative distribution functions, in order to verify the null hypothesis that the two samples are drawn from the same distribution. However, it is also possible to apply the alternative hypothesis, according to which the cumulative distribution of one sample is 'less' or 'greater' than the cumulative distribution of the other sample. In KS test terminology, a cumulative distribution that is 'greater' than one other means that its mean and median will be smaller than the mean and median of the other distribution (vice-versa for 'smaller'). In fewer words, applying this alternative hypothesis means that the two distributions have the same shape, but the mean values are shifted, one with respect to the other. We applied also the alternative hypothesis ('less' or 'greater') to our sample, and a threshold value of $p \geq 0.05$. The best p-values and hypotheses (alternative and null) for the three comparison are showed in Table 1. The reported best hypothesis indicate if our sample has a smaller mean (reported as 'Greater') or greater mean (reported as 'Less') compared to the observed samples.

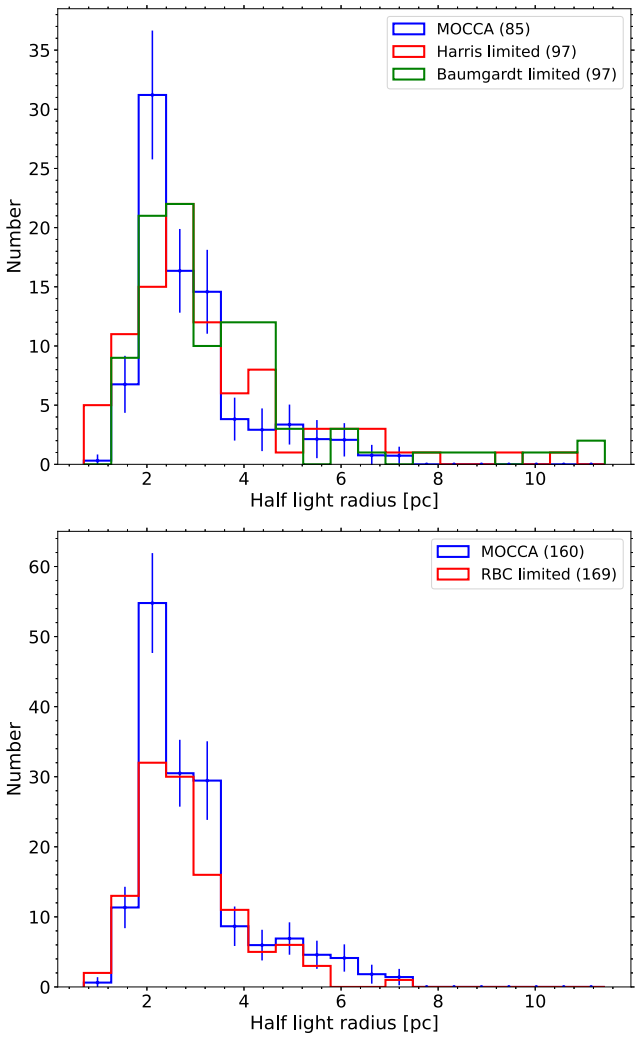

Figure 7. Half-light radius distribution for the MOCCA population and the observed population for MW (top) and M31 (bottom), respectively. The mean number of surviving GC are reported for MOCCA models, and the number of observed GCs are reported in parenthesis.

The results in Table 1 show that our results are consistent with the observational data with a significance between σ ($p \geq 0.8$) and 2σ ($p \geq 0.17$), with the only exception being the mass distribution for the Baumgardt catalogue comparison, with the best p-value close to the threshold acceptance criteria. The discrepancies seen for the Baumgardt catalogue comparison are connected to the spikes in the observational profiles, as explained before.

4.2 NSC and central massive BH evolution

In our simulations, models with galactocentric distances smaller than 10 pc were considered as accreted into the NSC. Since the internal dynamics have been followed for the MOCCA Database model, it is possible to determine the mass of the IMBHs (if present in the cluster) that have also been accreted into the NSC for the MOCCA results. In our models, the SMBH mass build-up is driven by the build-up and merger of the IMBH hosted by the infallen GCs. The IMBH mass is not determined in the MASinGa code, and for this reason the SMBH mass was not estimated. This calculation involves all the models reproduced during the simulations, not only the ones above 2 kpc as done in the post-processing procedure. Also, during our simulations, only GCs with initial distance of 2.5 kpc merged at the centre of the galaxy.

The NSC and SMBH masses from observations, MOCCA, and MASinGa are shown in Tables 2 and 3, together with the number and the mean mass of surviving GCs and the number and the total mass of IMBH sunk in the NSC. The observed mass of the NSC in the MW has a value of $1.8 \pm 0.3 \times 10^7$ $M_\odot$ (with an half-light radius of 4 pc) (Chatzopoulos et al. 2015), meanwhile the SMBH at the centre of the MW is $4.23 \pm 0.14 \times 10^6$ $M_\odot$ (Chatzopoulos et al. 2015). Similarly, the NSC mass in M31 is $3.5 \pm 0.8 \times 10^7$ $M_\odot$ (Lauer et al. 1993; Kormendy & Ho 2013; Georgiev et al. 2016) (with an half-light radius of ∼12 pc (Peng 2002; Neumayer, Seth & Böker 2020), meanwhile the M31 SMBH has a mass of $\sim 1.1 - 2.3 \times 10^8$ $M_\odot$ (Bender et al. 2005). The NSC mass obtained in our simulations is smaller than the observed one by one order of magnitude. Similarly to the NSC mass, the total built-up mass for the SMBHs is on the order of $\sim 10^4$ $M_\odot$, much smaller than the observed SMBH masses. The authors in Takekawa et al. (2021) reported 5 IMBH candidates in the centre of the MW, each of them having a mass $\gtrsim 10^4$ $M_\odot$. In our simulations, the mean number of accreted IMBHs is in mean ∼1−5 for MW and ∼1−3 for M31. Finally, the number of survived clusters in MOCCA is 86 ± 5 and 164 ± 7 for MW and M31, respectively. These values are smaller than the observed number of cluster in MW and M31. The mean masses of surviving GCs in our simulations are in relatively well agreement with the observations.

As previously said, the MOCCA-Survey Database I does not reproduce properly GCs in the central region of the galaxy, influencing the final number and mass of GCs that would be accreted to the NSC or to the SMBH. In Fig. 8, we report the evolution in time for the number of GCs survived and sunk to the NSC, reporting also the number of sunk models hosting an IMBH. On average, around 10 per cent for the MW and 5 per cent for M31 of the total initial GC populations sank into the NSC during the simulations, with only a very small percentage (∼ 1 per cent) of models hosting an IMBH that sank into the NSC. The self-consistency of IMBHs in GCs and their accretion on to the NSC in our models are improvements with regard to previous works. These values do not change even when the galaxy's density in the central regions (<100 pc) was increased

Table 1. Best results of *p*-values from the Kolgomorov–Smirnov test between our simulations and the observed properties, and the corresponding hypotheses for mass distribution (left), mean mass distribution (centre), and half-light radius (right).9

	Mass distribution		Mean mass distribution		Half-light radius	
Catalogue	*p*-value	Hypothesis	*p*-value	Hypothesis	*p*-value	Hypothesis
Harris	0.82	Greater	0.17	Less	0.95	Less
Baumgardt	0.17	Two-sided	0.08	Two-sided	0.81	Greater
RBC	0.64	Greater	0.64	Less	0.95	Greater

Table 2. The number and the mean masses of survived GC, the NSC accreted mass, the number and the total mass of IMBHs accreted to the NSC and the observed SMBH mass from observations, MOCCA and MASinGa for MW. The mass values are in solar units. The values from the Harris catalogue have been used to determine the properties of the survived GCs.

Model	Number of GCs	Mean GC mass	NSC accreted mass	Number of IMBH in NSC	Total IMBH mass in NSC	Observed SMBH in NSC
Observations	156	$2.1 \pm 2.9 \times 10^5$	$1.8 \pm 0.3 \times 10^7$	5	$\gtrsim 5 \times 10^4$	$4.2 \pm 0.1 \times 10^6$
MOCCA	86 ± 5	$2.1 \pm 1.5 \times 10^5$	$3.4 \pm 1.0 \times 10^6$	3 ± 2	$3.6 \pm 2.7 \times 10^4$	–
MASinGa	120 ± 6	$2.2 \pm 1.3 \times 10^5$	$3.3 \pm 0.9 \times 10^6$	–	–	–

Table 3. The number and the mean masses of survived GC, the NSC accreted mass, the number and the total mass of IMBHs accreted to the NSC and the observed SMBH mass from observations, MOCCA and MASinGa for M31. The mass values are in solar units.

Model	Number of GCs	Mean GC mass	NSC accreted mass	Number of IMBH in NSC	Total IMBH mass in NSC	Observed SMBH in NSC
Observations	231	$4.7 \pm 2.0 \times 10^5$	$3.5 \pm 0.7 \times 10^7$	–	–	$\sim 1.1 - 2.3 \times 10^8$
MOCCA	164 ± 7	$2.1 \pm 1.4 \times 10^5$	$3.3 \pm 1.2 \times 10^6$	2 ± 1	$2.7 \pm 2.0 \times 10^6$	–
MASinGa	231 ± 11	$2.3 \pm 1.3 \times 10^5$	$3.1 \pm 1.0 \times 10^6$	–	–	–

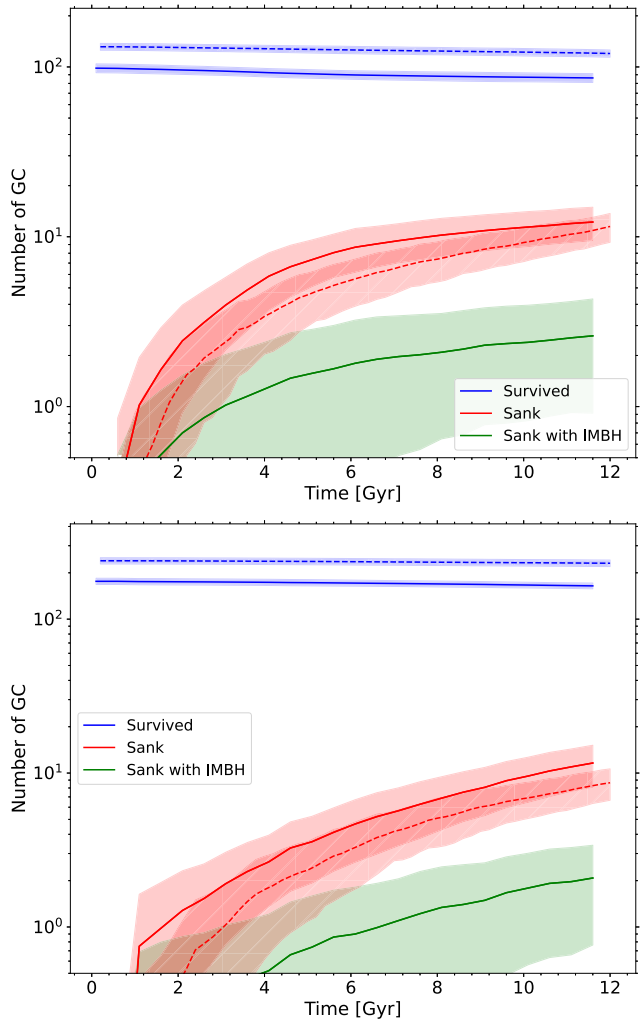

Figure 8. Time evolution of the mean number of GCs that survived (blue), that sank to the galactic centre (red), and that sank to the galactic centre hosting an IMBH (green) for MW (top) and M31 (bottom), respectively. The shadow region represents the standard deviation errors. The MOCCA and the MASinGa results are shown in solid and dashed lines, respectively.

to 10 times the actual galaxy's density. This simulated over-density would resemble the presence of a primordial NSC. Moreover, the rate of infalling GCs in the galaxy centre is constant in time (apart from an important increase in the initial time) for M31 with a value of $3.2 \pm 1.2 \times 10^5\ M_\odot\ Gyr^{-1}$, meanwhile for the MW it was important in the first Gyr and it became less and less important at later times, with a value at 12 Gyr of $1.03 \pm 0.8 \times 10^5\ M_\odot\ Gyr^{-1}$.

5 DISCUSSION

The model evolution recipe used in MASinGa has been carried out with a few simplifications for the half-mass radius, the tidal radius and the mass evolution. With simplistic physical assumptions, the equations used to describe their evolution have been determined. The galaxy density profile has been described by a Dehnen model (Dehnen 1993), with the assumption that the initial density profile for the galaxy is similar to the currently observed ones.

The properties of our simulated GC populations are in agreement with the observed properties for both the MW and M31, despite the simplifying assumptions and limitations of our models. Our simulations show a large-density distribution of models in the central region of the galaxy (<5 kpc), with a decreasing density at larger galactocentric distances. A similar trend is seen in the observed population. Therefore, it is expected that the GC populations would be composed mostly of compact GCs, with half-light radii on the order of few pc, as seen in both observations and simulations. Indeed, the interplay of a smaller tidal radius and larger galaxy density, would not allow the GCs to expand substantially since they would be disrupted by interaction events with the galaxy. To quantify the quality of our results, a two-sample Kolgomorov–Smirnov test was applied to the observed and simulated distributions, for different alternative hypotheses. The results show that the simulated and observed distributions likely come from the same distribution, with a significance between σ and 2σ.

The models from the MOCCA Database I have been used to reproduce the MW and M31 GC populations. A non-uniform initial mass distribution in the MOCCA Dabase I models could put some limitations on the reproduction of the initial GCIMF and observed final masses. Moreover, as reported in Madrid et al. (2017), the MOCCA results were able to reproduce the *N*-body simulations for Galactocentric distance down to few kpc. Considering also an underestimation of galaxy density and mass in the central region due

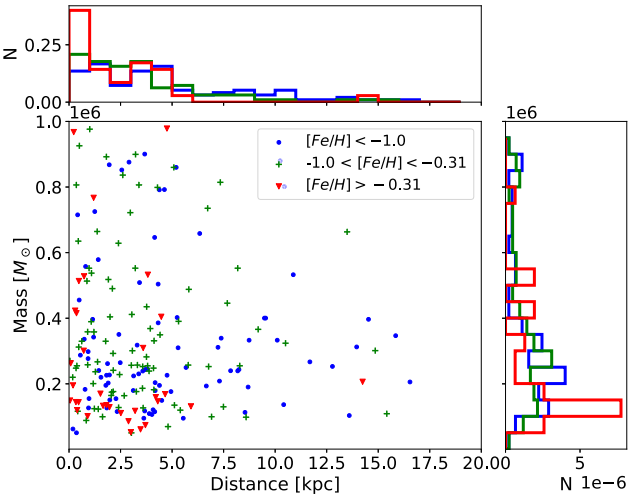

Figure 9. Observed masses versus the projected position for the M31 GCs, for different metallicities. In red, in green, and in blue the metal-rich, the intermediate metallicity, and metal-poor GCs are shown, respectively. On the side, the normalized histogram showing the distribution of each population is reported.

to the limitations of the Dehnen model, the number and the evolution of GCs in the central regions could have been underestimated.

One additional source of differences seen in our simulations and the observed GC populations can be the bimodal nature of GCs. It is known that both the MW and M31 present two GCs populations: a blue, metal-poor one and a red, metal-rich one. Generally, the metal-rich red clusters are expected to form during the gas-rich mergers during minor galaxies mergers. On the other hand, the blue GCs would be formed in the progenitor galaxies. For this reason, it is expected that the metal-rich GCs would be mostly centrally concentrated, and the metal-poor ones more spatially redistributed during the galaxies' collisions (Renaud, Agertz & Gieles 2017). This is indeed observed in both MW and M31 populations, as is possible to see in Fig. 9. The figure shows the observed mass and projected positions for GCs in M31 for different metallicities. The GCs have been divided into three groups depending on their metallicities: metal-poor ones with [Fe/H] < -1.0, metal-rich with [Fe/H] > -0.31 and intermediate metallicity GCs with $-1.0 <$ [Fe/H] < -0.31. The observed over-density in the central regions is actually predominated by the presence of metal-rich and intermediate metallicity GCs, even though the metal-rich GCs represent a small percentage of the total population. Similar results are obtained for the MW GC population. On the other hand, our simulations assumed that all GCs were generated simultaneously at the initial times. This means that our models do not take into account the presence of different GC populations.

The number of infalling GCs seems to be a small percentage of the total GC population, being around 10 per cent and 5 per cent for the MW and M31, respectively, with an even smaller percentage for infalling GCs hosting an IMBH ($\sim$ 1 per cent). The rate of infalling events seems to be constant for the M31 model evolution, with a small peak in the initial times, whereas the event rate for the MW seems to be more important at later times. As mentioned earlier, the central galactic region is not properly reproduced by the MOCCA models.

On the other hand, as shown in the Appendix, the polynomial fit to the rotational curve improves the estimated galaxy mass in the central region, as seen in observations. Meanwhile, its overall GC population's properties are not different from the Dehen density fit model with a larger number of infalling GCs having been observed together with a larger NSC and SMBH masses. The NSC and SMBH do show larger final build-up masses in the polynomial fit model compared to the rotational curve. However, the final masses are still importantly smaller than the observed values, meaning that the final NSC and SMBH masses are not strongly influenced by a better representation of the galaxy density in the central region. Given the flexibility that the Dehnen model allows, it will be possible to populate GCs around a larger number of external galaxies easily and automatically using the Dehnen family models. As shown the galaxy density profile represented by a Dehnen model can actually reproduce adequately the observed GCs population properties.

The formation mechanics of NSCs is still an open topic, with two main mechanics principally considered: the *in situ* formation, and the GC infall and merging with the galactic centre. In the *in situ* formation scenario, the pristine gas would fall into the galactic centre and boost an intense burst of star formation (Loose, Kruegel & Tutukov 1982; Milosavljević & Merritt 2001; Bekki 2007; Neumayer et al. 2011). In the second scenario, the dynamical friction would slowly spiral the GCs inwards, and eventually they would be accreted in the galaxy centre (Tremaine et al. 1975; Capuzzo-Dolcetta 1993; Capuzzo-Dolcetta & Mastrobuono-Battisti 2009; Arca-Sedda & Capuzzo-Dolcetta 2014b). Finally, Guillard, Emsellem & Renaud (2016) showed that the interplay of those two mechanics may explain the formation and evolution of NSC, with a massive star cluster formed in the disc of the galaxy, migrating to the centre and increasing its mass through interactions with other star clusters and substructures. The final NSC mass from our simulations is roughly 10 per cent of the observed NSC mass in both MW and M31, meaning that the mechanics for the NSC build-up mass is driven not only by the infalling scenario, but by the initial accreted mass and mergers with the fallen GCs operating together (Urry & Padovani 1995; van den Bosch et al. 2012; Emsellem 2013; Kormendy & Ho 2013).

Single SMBHs are often hosted at the centres of galaxies, with masses ranging 10^6-10^{10} $M_\odot$. For galaxies with masses between 10^{10} and 10^{11} $M_\odot$ the co-existence of a SMBH and NSC is observed (Seth et al. 2008; Leigh, Böker & Knigge 2012; Scott & Graham 2013). Galaxies with masses below 10^{10} or above 10^{11} $M_\odot$ are dominated by the presence of either an NSC or an SMBH, respectively. The observed scaling relations between the host galaxy, the NSC and the SMBH suggests a continuous sequence of NSC- and SMBH-dominated galaxies (Bekki & Graham 2010). The main proposed scenario to explain the formation of SMBHs is the formation and the merger of massive stellar remnants which sink into the galaxy centres (Quinlan & Shapiro 1990; Ebisuzaki et al. 2001; Volonteri & Rees 2005). One other possible formation scenario of an SMBH is the collapse of supermassive primordial gas and the evolution the supermassive object which forms as a result (Haehnelt & Rees 1993; Gnedin 2001; Bromm & Loeb 2003).

Recent works show that the *in situ* gas growth and mergers of young stellar cluster that formed nearby in the Galactic centre can contribute importantly to the NSC and SMBH mass growth. Using direct *N*-body simulations to reproduce the merge of stellar clusters and using a very simplified growth model for the SMBH and NSC masses, the authors in Askar, Davies & Church (2021a, b) found that for galaxies like the MW (with stellar masses close to 10^{10} and 10^{11} $M_\odot$), the gas growth can be very important in increasing both the NSC mass and as well as the SMBH mass. Also, about 10–15 per cent of the stars that compose the mass of the NSC in the MW are actually old metal-poor stars, with abundances that are similar to the ones observed in the GCs (Arca Sedda et al. 2020; Do et al. 2020). These

results are in agreement with the value reported in this paper, with around 10 per cent of the NSC mass being explained by the dry merger scenario. In fact, we applied the procedure described in Askar et al. (2021a, b) to our MW and M31 results. We assumed that the IMBH delivered to the NSC may accrete the gas in the central region of the galaxy before the delivery of a next IMBH, with a 10 per cent of Eddington accretion rate during this phase. This means that the IMBH mass would double in a time-scale of ∼300 Myr, and in our calculation, a random value between 250 and 350 Myr was used. We applied this calculation only if the IMBH was delivered before 4.5 Gyr. Finally, not all the gas present in the galactic centre could be accreted in the SMBH. The remaining gas can contribute to the *in situ* star formation in the NSC, and eventually induce the NSC mass growth. The contribution of this star formation event is related to the final SMBH mass, and it was randomly chosen between 0.8 and 3 for MW and 0.8 and 1.5 for M31, respectively. Using these simple and ad hoc prescriptions, we applied this procedure to all the 100 representation of GC population for both MW and M31, finding that the SMBH and the NSC final masses were growing by few order of magnitudes, with values comparable to the observations. A more detailed study will be performed in the future works.

6 CONCLUSION

In this paper, we introduced the machinery that will be used in the next works to populate the local Universe galaxies GC populations with the MOCCA models. The reproduction of the MW and M31 GC populations has been carried out using the semi-analytic modelling code MASinGa (Arca-Sedda in preparation). The MASinGa code has been updated and extended, with the internal dynamical evolution described by the MOCCA-Survey I Database models instead of the analytic approximations.

The MW and M31 have been populated with 100 GC population representations, evolving them up to 12 Gyr. The mean properties obtained from these representation have been compared to the observed GC populations' proprieties. The results shown are in agreement with the observed properties for both the MW's and M31's GC populations. Similarly, the NSC and SMBH masses found in our models are in agreement with the dry merger scenario.

Summarizing our main results:

(i) The spatial distributions for the MW's and M31's GC populations have been reproduced, with a large amount of the population observed within a galactocentric distance of 5 kpc, as shown in Figs 3 and 4. The observed mass profile of the GC populations also shows an important increase in the central region of the galaxy, not reproduced by our simulations (see Fig. 5).

(ii) In the central galactic regions, the stronger tidal field and higher galactic density would constrain the GCs expansion and mass loss, implying that only dense and compacted GCs would survive the galaxy interactions. As a result, most of the GCs are relatively compact and have a half mass radius smaller than 4 pc, as shown in Fig. 7 for both observations and simulations, in the MW and M31.

(iii) The GCs' galactocentric distance evolution has been followed down to 10 pc, with GCs considered accreted to the NSC for smaller distances. The mass accretion rate in the galactic centre seems to be constant in time, with values of $\sim 1\text{–}3 \times 10^5\,M_\odot$ Gyr for both the MW and M31.

(iv) The SMBH mass build-up has been considered as the accretion of GCs hosting IMBHs that have fallen into the NSC during the simulation (see Tables 2 and 3). The final NSC and SMBH masses determined by our simulations are smaller than the observed values by few order of magnitudes. These differences do show that the NSC and SMBH mass build-up cannot be explained completely and only by infalling scenario model, and that the interplay of the formation on an initial accreted mass and the interactions and merges with infalling GCs is needed.

Our work lays the ground for a series of future explorations which will focus on the impact of galaxy-GC co-evolution on the formation of compact object binaries, IMBHS, and GW sources. We aim to constrain and determine not only the GCs' observational properties, evolutionary paths, and their compact object content (such as IMBH, BHS, BH–BH binaries, X-ray binaries), but also the NSC and the central SMBH mass build-up. The results from our simulations could be used to determine the BH–BH merger rate in the local Universe, together with the event rates of TDEs between the SMBH and the infalling GCs.

ACKNOWLEDGEMENTS

MG and AL were partially supported by the Polish National Science Center (NCN) through the grant UMO-2016/23/B/ST9/02732. MAS acknowledges financial support from the European Union's Horizon 2020 research and innovation programme under the Marie Sklodowska-Curie grant agreement no. 101025436 (project GRACE-BH, PI Manuel Arca Sedda). AA acknowledges support from the Swedish Research Council through the grant 2017-04217.

DATA AVAILABILITY

The data underlying this article will be shared on reasonable request to the corresponding author.

REFERENCES

Antonini F., Capuzzo-Dolcetta R., Mastrobuono-Battisti A., Merritt D., 2012, ApJ, 750, 111
Arca Sedda M., Gualandris A., Do T., Feldmeier-Krause A., Neumayer N., Erkal D., 2020, ApJ, 901, L29
Arca-Sedda M., Capuzzo-Dolcetta R., 2014a, MNRAS, 444, 3738
Arca-Sedda M., Capuzzo-Dolcetta R., 2014b, ApJ, 785, 51
Arca-Sedda M., Capuzzo-Dolcetta R., Antonini F., Seth A., 2015, ApJ, 806, 220
Ashman K. M., Zepf S. E., 1992, ApJ, 384, 50
Askar A., Szkudlarek M., Gondek-Rosińska D., Giersz M., Bulik T., 2017, MNRAS, 464, L36
Askar A., Davies M. B., Church R. P., 2021a, MNRAS, 511, 2631
Askar A., Davies M. B., Church R. P., 2021b, MNRAS, 502, 2682
Baumgardt H., Hilker M., 2018, MNRAS, 478, 1520
Baumgardt H., Sollima A., Hilker M., 2020, PASA, 37, e046
Bekki K., 2007, PASA, 24, 77
Bekki K., Graham A. W., 2010, ApJ, 714, L313
Belczynski K., Kalogera V., Bulik T., 2002, ApJ, 572, 407
Bender R. et al., 2005, ApJ, 631, 280
Brodie J. P., Strader J., 2006, ARA&A, 44, 193
Bromm V., Loeb A., 2003, ApJ, 596, 34
Cai M. X., Gieles M., Heggie D. C., Varri A. L., 2016, MNRAS, 455, 596
Cantiello M. et al., 2018, A&A, 611, A93
Cantiello M. et al., 2020, A&A, 639, 136
Cantiello M., Blakeslee J. P., 2007, ApJ, 669, 982
Capuzzo-Dolcetta R., 1993, ApJ, 415, 616
Capuzzo-Dolcetta R., Mastrobuono-Battisti A., 2009, A&A, 507, 183
Chatzopoulos S., Fritz T. K., Gerhard O., Gillessen S., Wegg C., Genzel R., Pfuhl O., 2015, MNRAS, 447, 948
Chemin L., Carignan C., Foster T., 2009, ApJ, 705, 1395
Colpi M., Mayer L., Governato F., 1999, ApJ, 525, 720

Côté P. et al., 2004, ApJS, 153, 223
Côté P., Marzke R. O., West M. J., 1998, ApJ, 501, 554
D'Abrusco R. et al., 2016, ApJ, 819, L31
Dehnen W., 1993, MNRAS, 265, 250
Do T., David Martinez G., Kerzendorf W., Feldmeier-Krause A., Arca Sedda M., Neumayer N., Gualandris A., 2020, ApJ, 901, L28
Ebisuzaki T. et al., 2001, ApJ, 562, L19
Eilers A.-C., Hogg D. W., Rix H.-W., Ness M. K., 2019, ApJ, 871, 120
Emsellem E., 2013, MNRAS, 433, 1862
Forbes D. A., Brodie J. P., Grillmair C. J., 1997, AJ, 113, 1652
Forbes D. A., Brodie J. P., Larsen S. S., 2001, ApJ, 556, L83
Galleti S., Federici L., Bellazzini M., Fusi Pecci F., Macrina S., 2004, A&A, 416, 917
Galleti S., Federici L., Bellazzini M., Buzzoni A., Fusi Pecci F., 2006, A&A, 456, 985
Galleti S., Federici L., Bellazzini M., Fusi Pecci F., Macrina S., Buzzoni A., 2014, VizieR Online Data Catalog, p. 5143, V/143
Georgiev I. Y., Böker T., Leigh N., Lützgendorf N., Neumayer N., 2016, MNRAS, 457, 2122
Giersz M., Heggie D. C., 1996, MNRAS, 279, 1037
Giersz M., Heggie D. C., Hurley J. R., Hypki A., 2013, MNRAS, 431, 2184
Gnedin O. Y., 2001, Class. Quantum Gravity, 18, 3983
Grudić M. Y., Hafen Z., Rodriguez C. L., Guszejnov D., Lamberts A., Wetzel A., Boylan-Kolchin M., Faucher-Giguère C.-A., 2022, preprint (arXiv:2203.05732)
Guillard N., Emsellem E., Renaud F., 2016, MNRAS, 461, 3620
Haehnelt M. G., Rees M. J., 1993, MNRAS, 263, 168
Harris W. E., 1996, AJ, 112, 1487
Harris G. L. H., Harris W. E., Poole G. B., 1999, AJ, 117, 855
Harris W. E., Whitmore B. C., Karakla D., Okoń W., Baum W. A., Hanes D. A., Kavelaars J. J., 2006, ApJ, 636, 90
Harris W. E., Harris G. L. H., Alessi M., 2013, ApJ, 772, 82
Hénon M., 1961, Annales d'Astrophysique, 24, 369
Hénon M. H., 1971, Ap&SS, 14, 151
Hobbs G., Lorimer D. R., Lyne A. G., Kramer M., 2005, MNRAS, 360, 974
Jeans J. H., 1919, MNRAS, 79, 408
Kamlah A. W. H. et al., 2021, MNRAS, 511, 4060
King I. R., 1966, AJ, 71, 276
Kissler-Patig M., Kohle S., Hilker M., Richtler T., Infante L., Quintana H., 1997, A&A, 319, 470
Kormendy J., Ho L. C., 2013, preprint (arXiv:1308.6483)
Kroupa P., 1995, MNRAS, 277, 1522
Kroupa P., 2001, MNRAS, 322, 231
Kruijssen J. M. D., 2014, Class. Quantum Gravity, 31, 244006
Kundu A., Whitmore B. C., 2001, AJ, 121, 2950
Lada C. J., Lada E. A., 1991, in Janes K., ed., ASP Conf. Ser. Vol. 13, The Formation and Evolution of Star Clusters. Astron. Soc. Pac., San Francisco, p. 3
Larsen S. S., Brodie J. P., Huchra J. P., Forbes D. A., Grillmair C. J., 2001, AJ, 121, 2974
Lauer T. R. et al., 1993, AJ, 106, 1436
Leigh N., Böker T., Knigge C., 2012, MNRAS, 424, 2130
Leveque A., Giersz M., Paolillo M., 2021, MNRAS, 501, 5212
Leveque A., Giersz M., Banerjee S., Vesperini E., Hong J., Portegies Zwart S., 2022, preprint (arXiv:2206.03404)
Loose H. H., Kruegel E., Tutukov A., 1982, A&A, 105, 342
Madrid J. P., Leigh N. W. C., Hurley J. R., Giersz M., 2017, MNRAS, 470, 1729
Marks M., Kroupa P., 2012, A&A, 543, A8
Milosavljević M., Merritt D., 2001, ApJ, 563, 34
Neumayer N., Walcher C. J., Andersen D., Sánchez S. F., Böker T., Rix H.-W., 2011, MNRAS, 413, 1875
Neumayer N., Seth A., Böker T., 2020, A&AR, 28, 4
Ostrov P., Geisler D., Forte J. C., 1993, AJ, 105, 1762
Peng E. W. et al., 2006, ApJ, 639, 95
Peng E. W. et al., 2008, ApJ, 681, 197
Peng C. Y., 2002, AJ, 124, 294
Quinlan G. D., Shapiro S. L., 1990, ApJ, 356, 483
Renaud F., 2020, in Bragaglia A., Davies M., Sills A., Vesperini E., eds, IAU Symp. Vol. 351, IAU Symposium. Cambridge University Press, Cambridge, England, p. 40
Renaud F., Agertz O., Gieles M., 2017, MNRAS, 465, 3622
Rhode K. L., Zepf S. E., Santos M. R., 2005, ApJ, 630, L21
Rodriguez C. L., Hafen Z., Grudić M. Y., Lamberts A., Sharma K., Faucher-Giguère C.-A., Wetzel A., 2022, preprint (arXiv:2203.16547)
Scott N., Graham A. W., 2013, ApJ, 763, 76
Seth A., Agüeros M., Lee D., Basu-Zych A., 2008, ApJ, 678, 116
Spitzer L., 1987, Dynamical Evolution of Globular Clusters. Princeton University Press, Princeton, New Jersey
Stodolkiewicz J. S., 1982, AcA, 32, 63
Stodolkiewicz J. S., 1986, AcA, 36, 19
Takekawa S., Oka T., Iwata Y., Tsujimoto S., Nomura M., 2021, in Tsuboi M., Oka T., eds, Astronomical Society of the Pacific Conference Series Vol. 528, New Horizons in Galactic Center Astronomy and Beyond. Astronomical Society of the Pacific, San Francisco, CA, p. 149
Tremaine S. D., Ostriker J. P., Spitzer L. J., 1975, ApJ, 196, 407
Urry C. M., Padovani P., 1995, PASP, 107, 803
van den Bosch R. C. E., Gebhardt K., Gültekin K., van de Ven G., van der Wel A., Walsh J. L., 2012, Nature, 491, 729
Volonteri M., Rees M. J., 2005, ApJ, 633, 624
Wang L. et al., 2016, MNRAS, 458, 1450
Webb J. J., Leigh N. W. C., 2015, MNRAS, 453, 3278
Zepf S. E., Ashman K. M., 1993, MNRAS, 264, 611

APPENDIX: POLYNOMIAL FIT TO THE ROTATIONAL CURVE M31 RESULTS

As discussed in Section 3.3, the results shown so far are obtained from the Dehnen model fit for the observed rotational velocity curve. This fit, as shown in Fig. 2, does not properly reproduce the M31 central region rotational velocity. A polynomial curve was fitted to the observed rotational velocity, in order to better estimate the M31 central mass. The Dehnen best-fitting parameters were used to estimate the dynamical friction. Instead, the mass and density distribution, together with the GCs' density distributions are determined using the polynomial curve. In this way, the central GCs'

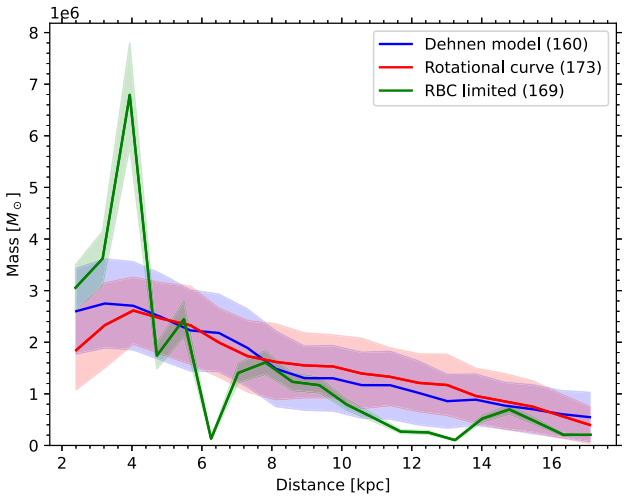

Figure A1. Mass distribution for the MOCCA population and the observed population for M31, from the models with the Dehnen model (blue) and the polynomial curve fit (red). The shadow regions represent the standard deviation error for both the observed and the simulated GC populations. The mean number of surviving GCs are reported for MOCCA models, and the number of observed GCs are reported in parenthesis.

Table A1. The number and the mean masses of survived GC, the NSC accreted mass, the number and the total mass of IMBHs accreted to the NSC and the observed SMBH mass from observations, MOCCA and MASinGa for the M31 polynomial fit result. The mass values are in solar units.

Model	Number of GCs	Mean GC mass	NSC accreted mass	Number of IMBH in NSC	Total IMBH mass in NSC	Observed SMBH in NSC
Observations	231	$4.7 \pm 5.0 \times 10^5$	$3.5 \pm 0.7 \times 10^7$	–	–	$\sim 1.1 - 2.3 \times 10^8$
MOCCA	177 ± 8	$1.8 \pm 1.4 \times 10^5$	$4.7 \pm 1.0 \times 10^6$	4 ± 2	$6.4 \pm 3.0 \times 10^6$	–
MASinGa	261 ± 11	$2.1 \pm 1.3 \times 10^5$	$2.2 \pm 0.9 \times 10^6$	–	–	–

density distributions are enhanced compared to the Dehnen model fit.

Even though the central region was more populated (with more GCs in number and in mass) in the initial condition, the overdensity of GCs in the central region seen in observations is still not reproduced. In Fig. A1, the mass distribution obtained with this model fit is shown, compared to the mass distribution obtained from the Dehnen model fit. The results do not differ much from the ones obtained from the Dehnen model fit only (see Fig. 5), indicating that the overdensity seen in observations is not only related to the not precise rotational curve fit and galaxy mass distribution in the central region. Similarly, the mean GC mass distribution and the half-light radius distribution show similar results to the Dehnen model fit. This means that the GC's surviving population's properties is not strongly affected by a better rotational curve model representation in the central region of the galaxy.

On the other hand, comparing the value reported in Table 3 and in Table A1, a larger NSC mass is obtained from a polynomial fit to the rotational curve compared to the Dehnen fit model, with the final SMBH mass being 2 times larger than the Dehnen fit model value. However, these values are still largely smaller than the observed values. Instead, a larger number of infalling GCs have been observed in the polynomial fit simulation. Overall, a better fit to the rotational curve velocity for M31 does not influence the surviving GC population properties. On the other hand, a slight increase of the NSC and SMBH masses is observed, but it is still not so important as to be comparable with observations. These results show that the Dehnen density model is adequate enough to describe the galaxy density profile.

This paper has been typeset from a TEX/LATEX file prepared by the author.

Chapter 4

Paper III - Globular Clusters Black Hole populations in Milky Way and Andromeda-like galaxies

Monthly Notices of the ROYAL ASTRONOMICAL SOCIETY

MNRAS **520,** 2593–2610 (2023) https://doi.org/10.1093/mnras/stad240
Advance Access publication 2023 January 23

MOCCA-Survey Database: extra galactic globular clusters – III. The population of black holes in Milky Way and Andromeda-like galaxies

A. Leveque [1]★ M. Giersz [1] Abbas Askar [2] M. Arca-Sedda [3] and A. Olejak [1]

[1]*Nicolaus Copernicus Astronomical Center, Polish Academy of Sciences, ul. Bartycka 18, PL-00-716 Warsaw, Poland*
[2]*Observatory, Department of Astronomy, and Theoretical Physics, Lund University, Box 43, SE-221 00 Lund, Sweden*
[3]*Department of physics and astronomy 'G.Galilei', University of Padua, Vicolo dell'Osservatorio 3, I-35122, Padua, Italy*

Accepted 2023 January 20. Received 2023 January 19; in original form 2022 August 29

ABSTRACT

This work investigates the black hole (BH) population of globular clusters (GCs) in Milky Way- and Andromeda-like galaxies. We combine the population synthesis code MASinGa and the MOCCA-Survey Database I to infer the properties of GCs harbouring a stellar-mass BH subsystem (BHS), an intermediate-mass BH (IMBH), or neither of those. We find that the typical number of GCs with a BHS, an IMBH, or none become comparable in the galactic outskirts, whilst the inner galactic regions are dominated by GCs without a significant dark component. We retrieve the properties of binary BHs (BBHs) that have either merged in the last 3 Gyr or survived in their parent cluster until present-day. We find that around 80 per cent of the merging BBHs form due to dynamical interactions while the remaining originate from evolution of primordial binaries. The inferred merger rate for both in-cluster and ejected mergers is 1.0–23 $\mathrm{yr}^{-1}\,\mathrm{Gpc}^{-3}$ in the local Universe, depending on the adopted assumptions. We find around 100–240 BBHs survive in GCs until present-day and are mostly concentrated in the inner few kpc of the galaxy. When compared with the field, GCs are at least two times more efficient in the formation of BHs and binaries containing at least one BH. Around 1000–3000 single BHs and 100–200 BBHs are transported into the galactic nucleus from infalling clusters over a time span of 12 Gyr. We estimate that the number of BHs and BBHs lurking in the star cluster to be about 1.4–2.2 $\times\ 10^4$ and 700–1100, respectively.

Key words: galaxies: star clusters: general.

1 INTRODUCTION

Numerous observational studies have found black holes (BHs) and accreting BHs candidates in Galactic and extra galactic globular clusters (GCs; Maccarone et al. 2007; Barnard & Kolb 2009; Roberts et al. 2012; Miller-Jones et al. 2015; Minniti et al. 2015; Bahramian et al. 2017; Dage et al. 2018). Radial velocity measurements of a binary system in NGC 3201 provide the strongest proof that a BH exists in a Galactic GC (Giesers et al. 2018, 2019). Additionally, both electromagnetic emission and dynamical mass measurements from kinematic observations of extragalactic GCs indicate the presence of a significant fraction of unseen mass, possibly stellar-mass BHs in binary systems and intermediate-mass BH (IMBH; Taylor et al. 2015; Dumont et al. 2022). Similarly, recent studies have also looked for indicators of the presence of BHs in GCs using numerical simulations of GC models containing sizable populations of BHs (Morscher et al. 2015; Arca-Sedda, Capuzzo-Dolcetta & Spera 2016; Askar, Arca Sedda & Giersz 2018; Arca Sedda, Askar & Giersz 2019; Weatherford et al. 2019).

Generally, the most massive GCs should form up to several thousands of BHs in the first few Myr of cluster evolution. The natal kicks that these BHs experience upon birth and the cluster's escape velocity have a substantial impact on how many of these BHs can be kept in the GCs, and it is crucially affected by the uncertain physics of stellar collapse (Belczynski, Kalogera & Bulik 2002; Belczynski et al. 2010; Fryer et al. 2012; Repetto, Igoshev & Nelemans 2017; O'Shaughnessy, Gerosa & Wysocki 2017). Retained BHs would segregate rapidly, populating the central regions of their host GC (Portegies Zwart & McMillan 2000, 2002a; Fregeau et al. 2004; Freitag, Gürkan & Rasio 2006; Arca-Sedda et al. 2016). The dynamics in the cluster central region is thus dominated by stellar-mass BHs, and can lead to different outcomes. One possibility is that dynamical interactions among the most massive BHs lead to their ejection, freeing the cluster centre from their dark content. Another possibility is that, despite dynamics, BHs form a subsystem dominating the innermost cluster region, or they merge among themselves or with other stars to build-up an IMBH. IMBHs have masses in the range 10^2–$10^5\ \mathrm{M}_\odot$ and they are considered as the link between the stellar-mass and supermassive BHs (Barack et al. 2019). Recent numerical studies (Breen & Heggie 2013a, b; Heggie & Giersz 2014; Banerjee 2018; Kremer et al. 2018, 2019; Webb et al. 2018) showed that the BHS is not entirely decoupled from the rest of the GC, and that the energy demands of the host GC would control the evolution of its BHS (Breen & Heggie 2013a, b). The presence of a massive BHS can be responsible for the cluster dissolution, due to the interplay of the strong energy produced from the BHS and tidal stripping (Giersz et al. 2019).

High stellar densities are required to form massive BHs such as IMBH, with a possible scenario of IMBH formation being repeated

★ E-mail: agostino@camk.edu.pl

collisions in the central regions of GCs (Portegies Zwart & McMillan 2002b; Portegies Zwart, Dewi & Maccarone 2004; Portegies Zwart & McMillan 2007; Giersz et al. 2015; Mapelli 2016). Indeed, IMBH can be form through multiple stellar mergers in binary system (see also Maliszewski et al. 2022; Di Carlo et al. 2021; González et al. 2021; Arca Sedda, Amaro Seoane & Chen 2021; Rizzuto et al. 2021, 2022). So far, there is still no conclusive evidence of IMBH presence in Galactic GCs, even though they are considered to potentially host an IMBH (Bash et al. 2008; Maccarone & Servillat 2008; Lanzoni et al. 2013; Lützgendorf et al. 2013; Kamann et al. 2014; Askar et al. 2017; Arca Sedda et al. 2019; Arca Sedda et al. 2020; Hong et al. 2020).

Multiple three-body interactions can cause the formation of BH–BH binaries (BBHs), which serve as a power supply for the cluster core. The continuous interactions between the BBHs and the other objects in the GC would harden the binaries, until they would be ejected from the cluster core or be merged, releasing gravitational waves (Portegies Zwart & McMillan 2000; Banerjee, Baumgardt & Kroupa 2010; Downing et al. 2010; Wang et al. 2016; Askar et al. 2017). Similarly, stars that interact with retained BHs are forced into wider orbits, causing the GC to expand and this can postpone core-collapse (Merritt et al. 2004; Mackey et al. 2008; Gieles et al. 2010; Wang et al. 2016; Kremer et al. 2019). The presence of a BHS or of an IMBH in the central region of a GC would importantly shape the structure of the host GC (Mackey et al. 2007; Zocchi 2015; Arca Sedda, Askar & Giersz 2018; Baumgardt, Sollima & Hilker 2020).

In this work, we extend the study of the GC populations for the MW and M31 exploited in our companion paper (Leveque et al. 2022b, hereafter Paper II). In previous papers in this series, we set-up the machinery that would be used to populate external galaxies with their GC populations by combining the results from the MOCCA-Survey Database I with the MASinGa semi-analytic tool. In this work, we would like to test for the first time our machinery against the GCs properties and their BH content simulated in our models for both MW and M31 populations. In particular, we compare the orbital properties of the MW GC population with the observed properties from the Bajkova catalogue (Bajkova & Bobylev 2021). Also, we aim to constrain the spatial distribution in the galactic halo of different GCs properties for different GC dynamical states comparing our results with previous studies (Lützgendorf et al. 2013; Askar et al. 2018; Arca Sedda et al. 2019; Weatherford et al. 2019). Then, we intend to determine the properties of the BBH mergers reported in our simulations and the inferred BBH merger rate (Banerjee 2022; Mapelli et al. 2022). Finally, we show the properties of BBHs present at 12 Gyr that could potentially be observed, and the number of BH and BH binaries that have been transported to the nuclear star cluster (NSC) by infalling star clusters. In Appendix A, we present the statistical tests of the studied populations.

2 METHOD

In this section, we will summarize the most important ingredients of our machinery. More details about all the physical assumptions are properly described in section 2 of Paper II.

The MASinGa (Modelling Astrophysical Systems In GAlaxies) programme has been used to model the GC populations (Arca-Sedda & Capuzzo-Dolcetta 2014a; Belczynski et al. 2018; Paper II; Arca-Sedda, in preparation). For each GC in the population, MASinGa simulates the orbital evolution while taking into consideration the galactic tidal field and shocks, which contribute to the cluster disintegration, dynamical friction, which pulls the cluster towards the galactic centre, and internal relaxation, which controls the cluster mass-loss and expansion/contraction.

The number of GCs and distributions of GC masses and galactocentric positions generated by MASinGa have been used to choose appropriate models from the MOCCA-Survey Database I (Askar et al. 2017) to reproduce the initial distributions (the details are provided in section 2.3 in Paper II). However, few steps have been taken in order to determine the galactocentric position of the MOCCA models in the gravitational potential of the studied galaxy. Indeed, the simple point-mass approximation for the Galactic potential was used to evolve the MOCCA models, with the central galaxy mass being contained inside the GC's orbital radius. The initial Galactocentric distance of a model in MOCCA-Survey Database I is defined by its initial mass and its tidal radius. Only a finite set of such values were considered (see table 1 in Askar et al. 2017), with no specific initial density profile being taken into account while modelling the MOCCA-Survey Database I models. A circular orbit at Galactocentric distances between 1 and 50 kpc were assumed, and the GC's rotation velocity was set to 220 km s^{-1} for the whole range of galactocentric distances. The correct galactocentric distance for a circular orbit in an external galaxy, for a given tidal radius $r_{\rm tidal}$ and GCs mass $M_{\rm GC}$ can be determined knowing the tidal radius for the MOCCA model and the density distribution of the simulated galaxy. From the results presented in Cai et al. (2016), it is possible to determine the galactocentric radius of a circular orbit on which a GC will experience an equivalent mass-loss if it were on an eccentric orbit. In particular, the apocenter distance $R_{\rm apo}$ for the eccentric orbit can be determined as $R_{\rm apo} = R_C \cdot (1-0.71 \cdot E_{\rm GC})^{-5/3}$ (Cai et al. 2016), with R_C the galactocentric distance for a circular orbit, and $E_{\rm GC}$ the initial orbital eccentricity, chosen from a thermal distribution. The initial galactocentric distance for a circular orbit R_C is known for the MOCCA models. Finally, the initial galactocentric position has been selected within the orbit apsis. For each MOCCA model, a total of 900 representations of each MOCCA-Survey Database I model were generated, with different initial orbital eccentricity and galactocentric distances – the MOCCA-Library. In this way, the same model could be populated with different orbital parameters and in different galactocentric distance regions. Each simulated cluster from the MOCCA-Survey Database I has a different internal dynamical evolution (such as mass-loss, half-mass radius, etc.). Consequently, the dynamical evolution of MOCCA-Library models that represent different MOCCA models are diverse. Hence, models from the MOCCA-Library are defined as unique when they represent different MOCCA models (more details are provided in Section 2.3.1 in Paper II).

Only MOCCA models that survived their internal dynamical evolution up to 12 Gyr were selected to represent the MASinGa GC models. Indeed, the initial galactocentric position for each MOCCA model was chosen within the same initial galactocentric radius bin of the representative MASinGa model. Instead, the initial mass was chosen randomly from the GC initial mass function (GCIMF) cumulative distribution (a power law $dN/dm = b \cdot m^{-\alpha}$ with a slope of $\alpha = 2$ function has been used as GCIMF), with lower and upper limits of 2×10^5 $M_\odot$ and 1.1×10^6 $M_\odot$, respectively. This mass range was set in order to reproduce the expected initial mass range for MW and M31, being of $\sim 10^5 - 10^7$. Indeed, the observed masses for the survived GCs located within 17 kpc from the galactic centre range between 10^4–2×10^6 $M_\odot$ and 5×10^4–3×10^6 $M_\odot$, for MW and M31, respectively.[1] According to Webb & Leigh (2015), the initial GC mass was ∼5 times greater than the actual observed values (more

[1]In this calculation, we did not take in consideration GCs with masses at 12 Gyr smaller than 10^4 $M_\odot$, as they would be closed to the cluster dissolution, and they would be hard to be observed in external galaxies.

Table 1. Initial conditions for the MW and M31 GC population simulated in MASinGa. $N_{\rm ini}$ and $M_{\rm GC,ini}$ represent the initial total number and initial total mass of the GC population, respectively.

Parameter	MW	M31
Galaxy density profile	Dehnen (1993)	Dehnen (1993)
M_g ($M_\odot$)	3.18×10^{11}	5.75×10^{11}
r_g (kpc)	5.12	5.8
γ	0.54	0.1
GCIMF function	Power law	Power law
GCIMF slope	2	2
GCIMF $M_{\rm min}$ ($M_\odot$)	2×10^5	2×10^5
GCIMF $M_{\rm max}$ ($M_\odot$)	1.1×10^6	1.1×10^6
$N_{\rm ini}$	132	245
$M_{\rm GC,ini}$ ($M_\odot$)	6.3×10^7	10^8

details are provided in section 3.3 of Paper II). On the other hand, the maximum mass in the GCIMF was chosen according to the maximum initial mass in the MOCCA models, being of 1.1×10^6 $M_\odot$.[2] The GCIMF cumulative distribution has been normalized to the initial MASinGa models mass distribution. Each model representation was successively removed from the MOCCA-Library, in order to avoid multiple instances of the same model to populate each mass and galactocentric position bin. Our procedure would guarantee that the total number of GCs in the population, the galaxy density distribution, and the GC IMF distribution for the MOCCA population would reproduce the initial conditions in the MASinGa population. Also, this procedure guaranteed an 85 per cent minimum coverage of not repeated unique MOCCA models for both MW and M31 populations. Finally, most of the selected MOCCA models has an initial pericenter distance within 4 kpc from the galactocentric centre, and an initial thermal distribution for the eccentricity. The models that has been delivered to the NSC have small pericenter distances (<0.5 kpc) and really eccentric orbits (>0.8). The galaxy density profile have been modelled with a Dehnen (1993) density profile family of the form:

$$\rho_G(r) = \frac{(3-\gamma)M_g}{4\pi r_g^3}\left(\frac{r}{r_g}\right)^{-\gamma}\left(1+\frac{r}{r_g}\right)^{\gamma-4},$$

where M_g is the galaxy total mass in $M_\odot$, r_g the galaxy length-scale in kpc, and γ the density profile slope. The Dehnen models parameters' values have been determined fitting the observational rotational curve (data from Eilers et al. 2019 and Chemin, Carignan & Foster 2009 for MW and M31, respectively) to the Dehnen rotational curve. The initial number of GCs in our models has been set by the total GC mass (defined as a fraction of the total galaxy mass) and the GCIMF. Even though the initial total number of GCs found in our simulations is much smaller compared to the observed total number of GC in both MW and M31, we found a similar number of initial GCs in our simulations and the observed one when we limit to GCs located within 17 kpc from the galactic centre. Also, we found that the number of surviving GCs in our models is similar to the observed number of GCs within the selected mass and distance range for both MW and M31. The initial conditions used in our simulations to reproduce the MW and M31 population are summarized in Table 1.

Successively, the MOCCA models selected with the prescription described above have been used to follow the internal and external dynamics evolution of the GC population. This allowed not only to follow the actual evolution for GC's mass, and half-mass radius but also to follow the evolution of the compact objects present in the system, together with the compact object binary evolution and their survival. On the other hand, the formulae adopted in MASinGa have been used to determine the galactocentric distance and eccentricity evolution.

It is important to underline that the stellar evolution prescription adopted in MOCCA models is outdated. The BH masses prescription used in MOCCA models follows the Belczynski et al. (2002) mass fallback formulae. In particular, proposed rapid and delayed supernova mechanisms (Fryer et al. 2012) were not implemented in stellar evolution prescriptions used in MOCCA-Survey Database I models. For this reason, the final BH masses are smaller compared to the observed values from GW detections (Abbott et al. 2021, 2022) and updated stellar and binary evolution prescriptions for BH progenitors (Kamlah et al. 2022). Also, the subsample of MOCCA models used to populate the studied galaxies have metallcities Z of 0.02, 0.006, 0.005, 0.001, and 0.0002 ($Z_\odot = 0.02$).

As mentioned in Paper II and in Madrid et al. (2017), the MOCCA results were able to recreate the N-body simulations for galactocentric distances down to a few kpc. For this reason, the region between 2 and 17 kpc has been the focus of the post-processing investigation and statistical analysis of GC populations' properties in Paper II. In a similar way, we also restricted our analysis in this work to GCs that were located in the same galactocentric zone.

3 RESULTS

For both MW and M31, 100 galaxy models were created, all formed 12 Gyr ago and evolved until the present day as in the prescription described in Paper II. To reduce statistical fluctuations and have a more robust statistical representation of the models, the average values obtained from the galaxy models and their GC population have been considered. The repeating of the same unique model might distort the structural GC parameter distribution, biassing the simulated distribution towards the attributes of the unique models that were randomly picked the most. To prevent such bias, when estimating the radial distribution of each property, only one unique model inside each radial bin was examined. The average value of each population's measurements, as well as the standard deviation, have been calculated for each attribute.

While in Paper II, we discussed and studied the global properties of the GC population reproduced by our machinery (such as mass spatial distribution, half-light radius distributions, etc.), in this work, we focus on studying the properties of the simulated GC population and their BH content.

3.1 Orbital properties in MW GC population

The orbital properties obtained in the MW GC population have been compared to the observed data from the Bajkova catalogue (Bajkova & Bobylev 2021). The Bajkova catalogue contains the orbital properties of 152 GCs in the MW, determined using the *Gaia* DR2 proper motions and the data from the Vasiliev (2019) and Massari, Koppelman & Helmi (2019) catalogues. The orbital properties have been determined considering an axisymmetric Galactic potential based on the Navarro–Frenk–White dark halo (Navarro, Frenk & White 1997).

In Fig. 1, we show the density map for the orbital eccentricity and pericenter distance for the population of MOCCA models in the case of the MW. The colour map shows the density map for our

[2]For an initial power-law GCIMF between $M_{\rm low} = 10^3$–10^4 $M_\odot$ and $M_{\rm up} = 10^7$ $M_\odot$, we would expect a total number of low-mass clusters ($M < 10^5$ $M_\odot$) being around 1500–200 for $M_{\rm low} = 10^3$ $M_\odot$ and 10^4 $M_\odot$, respectively, and a total mass of the GCs population around 2–3 $\times 10^8$ $M_\odot$.

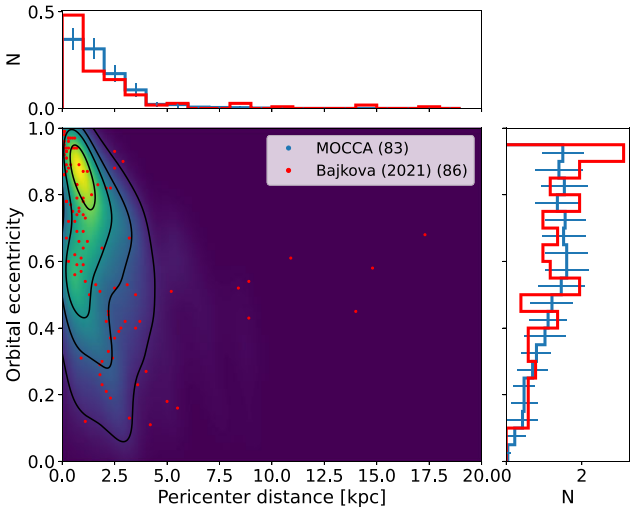

Figure 1. Density map for the orbital eccentricity and pericenter distance for the MOCCA population for MW. The contours include the 80, 50, 30, and 10 per cent levels of population. The Bajkova catalogue is reported in red. On the side, the normalized histogram showing the distributions of each population is reported (the area beneath the histogram has been set to 1), with the error bars showing the standard deviations for the simulated models. In brackets, the mean number of MW GCs simulated and the observed population number have been reported for MOCCA and Bajkova catalogue, respectively.

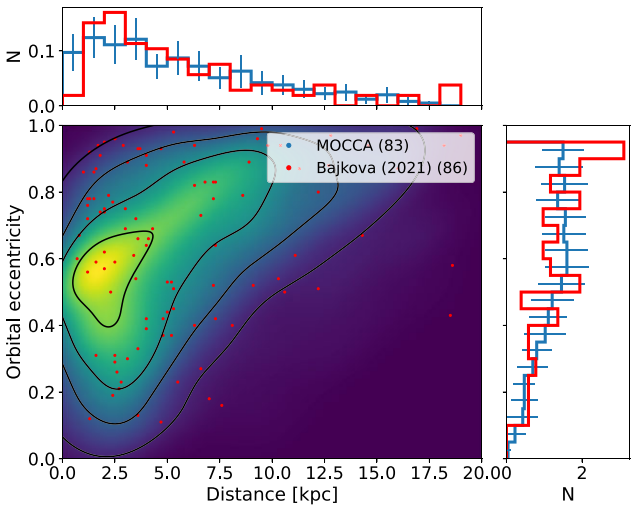

Figure 2. Density map for the orbital eccentricity and galactocentric distance for the MOCCA population for MW. The contours include the 80, 50, 30, and 10 per cent levels of population. The Bajkova catalogue is reported in red. On the side, the normalized histogram showing the distributions of each population is reported (the area beneath the histogram has been set to 1), with the error bars showing the standard deviations for the simulated models. In brackets, the mean number of MW GCs simulated and the observed population number have been reported for MOCCA and Bajkova catalogue, respectively.

models, and the contours include the 80, 50, 30, and 10 per cent levels of population. In red, we reported the properties retrieved from the Bajkova catalogue (Bajkova & Bobylev 2021). The regions containing most of the populations are presented with brighter colours. On the side, the histogram showing the distribution for each population is also reported, with the area below the histogram being set to 1. Similarly, in Figs 2 and 3 the density map for the projected galactocentric distance versus the eccentricity and for the circular orbit versus the GC mass are reported. The circular orbit of the observed GC has been determined using the results in Cai et al. (2016). The comparison shows that our sampled models are in reasonable agreement with the observed orbital properties of MW clusters. However, our models have smaller mean values compared to the observed ones (the statistical test results are reported in Appendix A). In our machinery, the GCs have been populated around a galaxy at first on a circular orbit, and successively modelled in elliptical orbits using the results from Cai et al. (2016). The circular orbit comparison, and more in general the kinematical findings shown so far provide additional confidence that our machinery can recreate real kinematical properties of MW GCs, and it may also be used to populate external galaxies.

3.2 Dynamical models

The presence of an IMBH, or of a BHS, or neither of them, has a significant impact on the dynamical history and characteristics of the GCs. Following the division described in Paper I (Leveque, Giersz & Paolillo 2021), we divided our chosen sample into three dynamical subsamples namely:

(i) If there is an IMBH (BH with mass greater than 500 $M_\odot$), the system has been classified as an IMBH model.

(ii) If the number of BH (N_{BH}) present in the system is $\geq$50, it has been classified as BHS model; if $20 < N_{BH} < 50$, we checked if the system is not experiencing the core collapse: if the system is in balanced evolution (Breen & Heggie 2013a, b), it has been also classified as BHS model.

(iii) A model that is not categorized as an IMBH nor as a BHS has been classified as a Standard model.

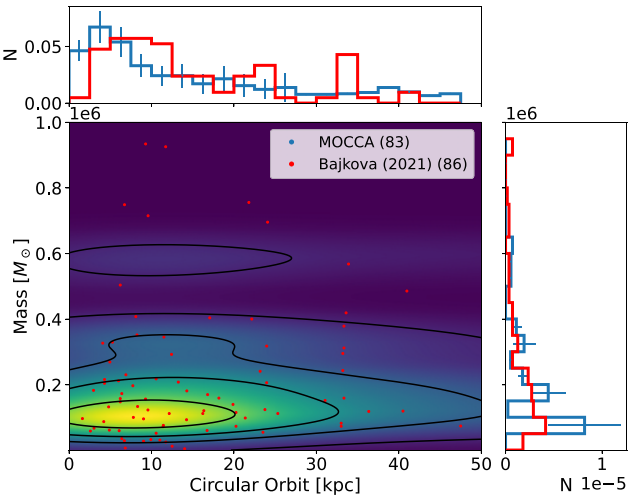

Figure 3. Density map for the circular orbit and the mass for the MOCCA population for MW. The contours include the 80, 50, 30, and 10 per cent levels of population. The Bajkova catalogue is reported in red. On the side, the normalized histogram showing the distributions of each population is reported (the area beneath the histogram has been set to 1), with the error bars showing the standard deviations for the simulated models. In brackets, the mean number of MW GCs simulated and the observed population number have been reported, for MOCCA and Bajkova catalogue, respectively.

Fig. 4 shows the binned radial distribution (total number of models in a given radial bin) of the different dynamical models considered in this study. The Standard model predominates in the central region

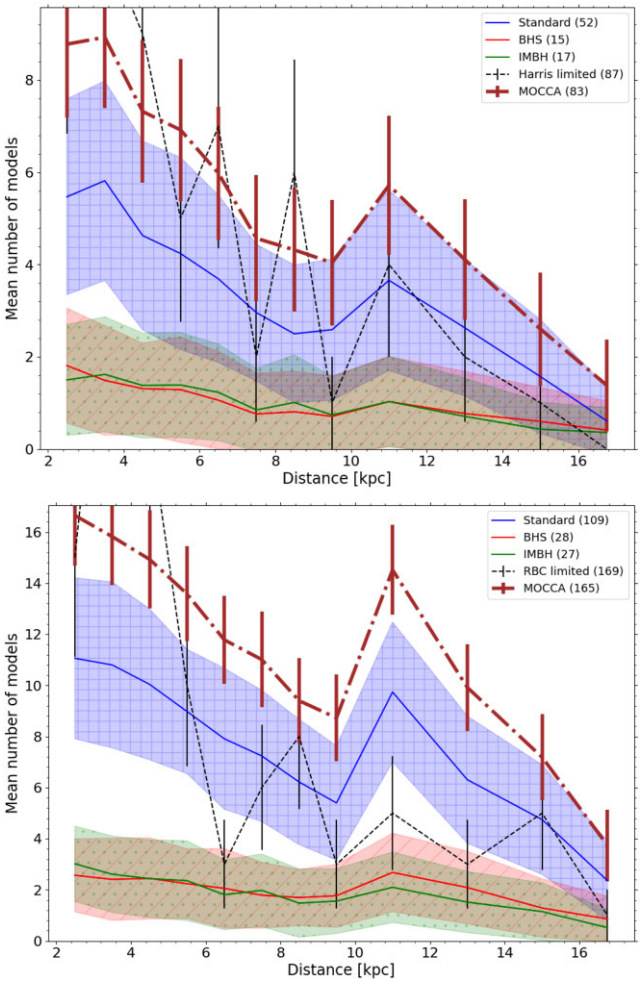

Figure 4. Spatial distribution for Standard (blue), BHS (red), and IMBH (green) models for MW (top) and M31 (bottom) for the MOCCA, respectively. The shaded regions represent the standard deviation for the simulated GC populations. The squared region, the oblique lines and the dots show the standard deviation for Standard, BHS and IMBH model, respectively. The mean number of GCs for each dynamical model are reported in brackets. In black dashed lines, we report the spatial distributions for the observed populations, while in thick brown dot–dashed line we report the spatial distribution for the entire simulated population.

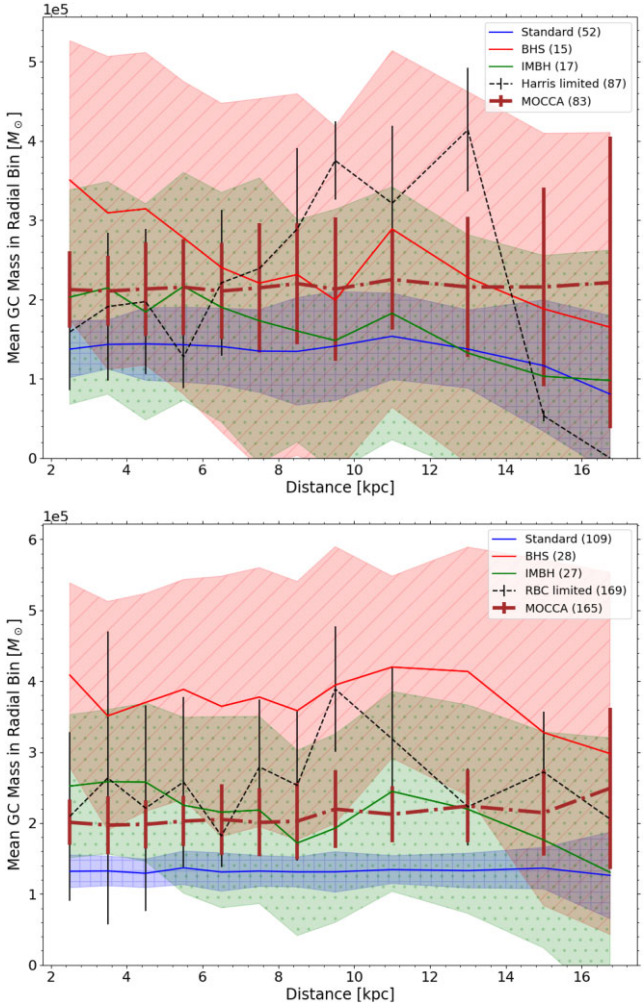

Figure 5. Mean mass distribution for Standard (blue), BHS (red), and IMBH (green) models for MW (top) and M31 (bottom) for the MOCCA, respectively. The shaded regions represent the standard deviation for the simulated GC populations. The squared region, the oblique lines and the dots show the standard deviation for Standard, BHS, and IMBH models, respectively. The mean number of GCs for each dynamical model are reported in brackets. In black dashed lines, we report the mean GC mass distributions for the observed populations, while in thick brown dot–dashed line we report the spatial distribution for the entire simulated population.

of the galactic halo; meanwhile the numbers of dynamical models for all the three dynamical subsamples seem to be comparable for distance >14 kpc. On the other hand, the BHS models show a higher mean mass distribution at all the galactocentric distances, and IMBH models show a slightly higher mean mass than the Standard models for small galactocentric distances (<6−10 kpc), as it is possible to see in Fig. 5. For comparison, the observed number distributions for the MW and M31 are reported in black dashed lines. For the MW population, results from the (Harris 1996, 2010) catalogue have been used, and for the M31 population the results from the Revised Bologna Catalogue (RBC; Galleti et al. 2004; Galleti et al. 2006; Galleti et al. 2014) have been used. For the observational catalogues we applied the same filtering condition carried out in Paper II, that is we limited to GCs within 17 kpc from the galactic center, and with half-light radius surface brightnesses (defined as L_V/r_h^2, with L_V being the total V luminosity and r_h the half-light radius) greater than 4000 $L_\odot$ pc^{-2}. The distributions reported by our models are comparable with the observed ones.

In Fig. 6, we show the radial distribution of the number fraction of BHS and IMBH models in each radial bin. The fraction number has been determined as the mean number of the dynamical models in the radial shell divided by the total number of models in the same shell. It can be seen that the number fraction of both IMBH and BHS models are similar and uniform.

In Fig. 7, we show the mean half-light radius distribution for the different dynamical models for both MW and M31. It is possible to see that for different galactocentric distances in both the MW and M31 populations the mean half light radius of the BHS models is larger compared to Standard and IMBH models, with IMBH models being more compact at larger galactocentric distances. For comparison, the observed number distributions for the MW and M31 are reported in black dashed lines. The observed distributions follow with relatively good agreement the distributions from our simulated models.

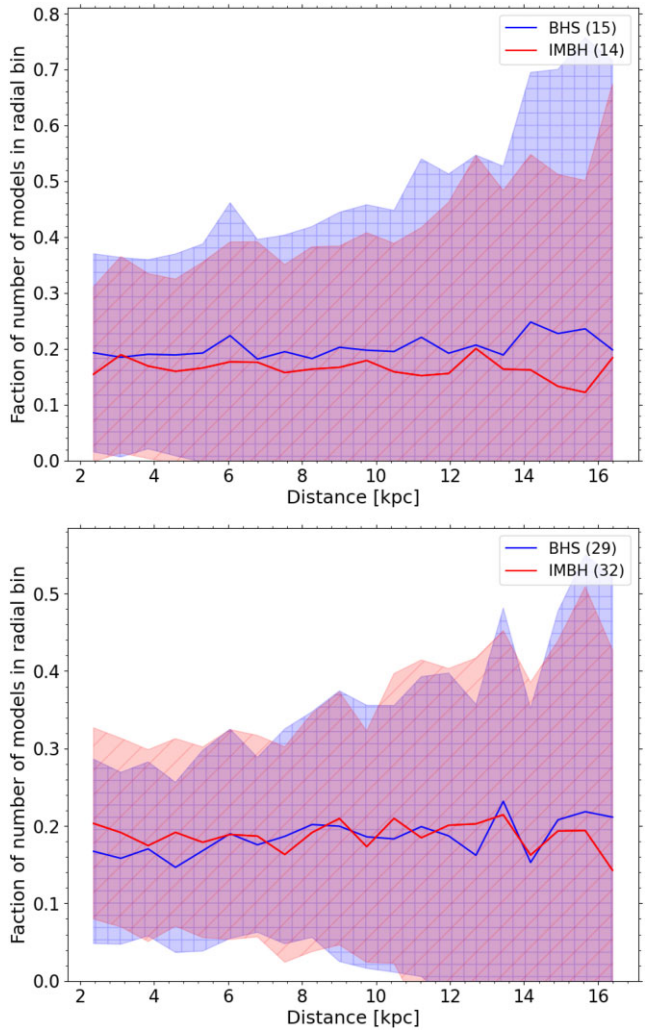

Figure 6. Spatial distribution for fraction of models in the radial bins for the BHS (blue) and IMBH (red) models for MW (top) and M31 (bottom) for the MOCCA population, respectively. The shaded regions represent the standard deviation for the simulated GC populations. The oblique lines and the dots show the standard deviation for BHS and IMBH models, respectively. The mean number of GCs for each dynamical model are reported in brackets.

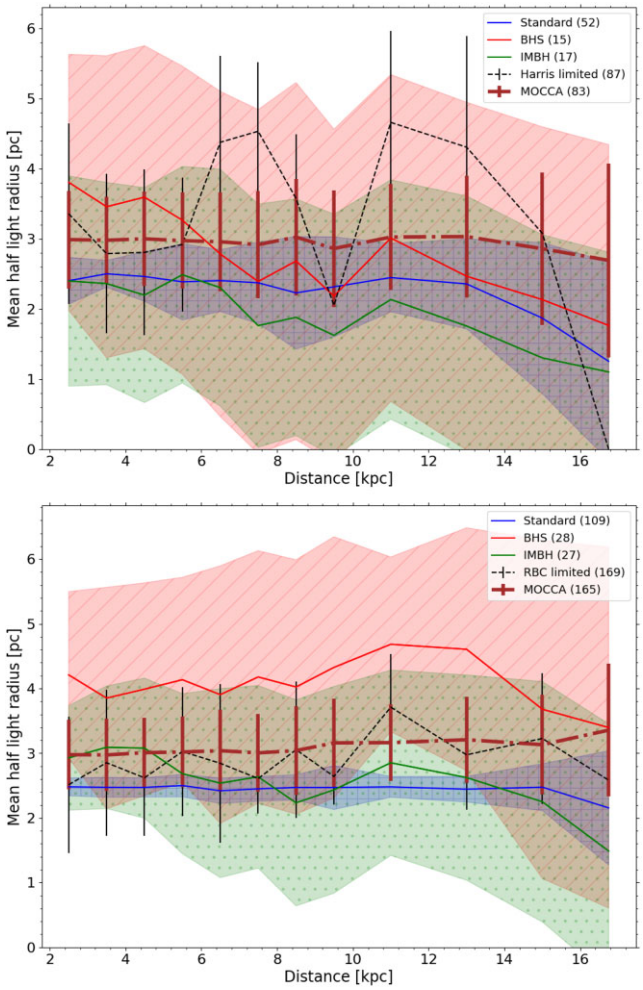

Figure 7. Mean half-light radius distribution for Standard (blue), BHS (red), and IMBH (green) models for MW (top) and M31 (bottom) for the MOCCA, respectively. The shaded regions represent the standard deviation for the simulated GC populations. The squared region, the oblique lines and the dots show the standard deviation for Standard, BHS, and IMBH models, respectively. The mean number of GCs for each dynamical model are reported in brackets. In black dashed lines, we report the mean half-light radius distributions for the observed populations, while in thick brown dot–dashed line we report the spatial distribution for the entire simulated population.

In Fig. 8, we show the mean total BH mass per GC distribution for the different dynamical models for both MW and M31. The total BH mass per GC is determined as the sum of all BH present in the GC. The mean total BH mass per GC in the IMBH models is visibly larger in the centre of the galactic halo compared to the outskirt (∼4−5 times larger). This behaviour is a consequence of the fact that in MOCCA models, the most massive IMBHs form in GCs that were born close to galactic centre. These GCs are initially more compact and dense (Giersz et al. 2015; Arca Sedda et al. 2019) and thus more conducive to forming IMBHs with respect to those in outskirt. However, this is not visible in the BHS model, where the differences in the total BH masses are negligible. Finally, the mean total BH mass in the Standard models is insignificant.

To summarize our results, Standard models are more numerous in the central region of the galactic halo, but they consist typically of low-mass and relatively compact GCs, with almost no BHs in the system. Meanwhile the IMBH models show similar global system structure to the Standard models (mean mass and half-light radius), the total BH mass for these models is dominated by the central IMBH. Instead, the BHS models are more massive than both the IMBH and Standard models, and do show a larger half-light radius for almost all galactocentric distances. As already discussed in Paper I, these distributions are correlated with the intrinsic properties of the GCs and their dynamical history, as it will be discussed more in Section 4. The statistical test results are reported in Appendix A.

3.3 Single and binary BH populations

The MOCCA-Survey Database I models followed the evolution of the internal dynamics of GCs and also their stellar content, including the BH counts and the BBHs properties.

3.3.1 Merging binary BH population

The number of BBHs that would merge in a time range within 12 and 12.5 Gyr and within 10 and 13 Gyr found in our results is presented

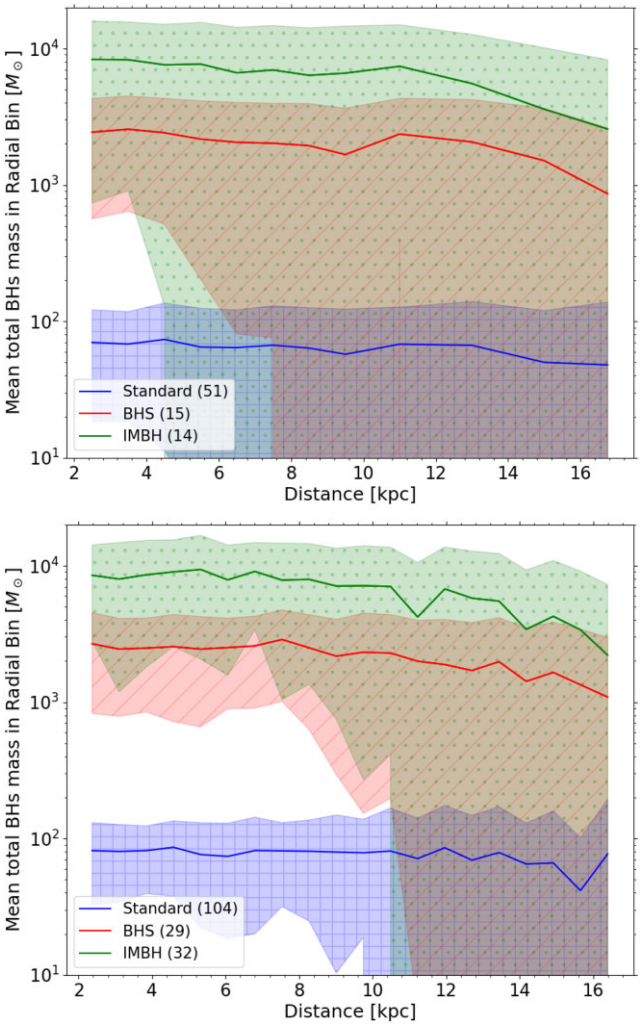

Figure 8. Mean total BH mass distribution for Standard (blue), BHS (red), and IMBH (green) models for MW (top) and M31 (bottom) for the MOCCA, respectively. The shaded regions represent the standard deviation for the simulated GC populations. The squared region, the oblique lines and the dots show the standard deviation for Standard, BHS, and IMBH models, respectively. The mean number of GCs for each dynamical model are reported in brackets.

in Table 2, together with the number of BBHs that would survive at 12 Gyr. These results consider all the BBH mergers that are generated in GCs, independently of whether the merger actually occurred within the GCs or the binary escaped the GC before merging. For this purpose, also BBHs present in GCs that have merged with the NSC due to dynamical friction are also taken into account. Instead, BBH mergers in dissolved clusters have been excluded from the analysis, together with the mergers between a stellar-mass BH and an IMBH. Considering only a time span within 12 and 12.5 Gyr, our results show that the estimated BBH merger rate expected in 10 yr is of the order of $\sim 7 \times 10^{-7}$ and $\sim 10^{-6}$ for MW and M31, respectively. Similar numbers of mergers can be obtained considering a larger time span between 10 and 13 Gyr. The latter time span is more in line with the GCs' age range in the MW and M31, that would vary between 10 and 13 Gyr. None the less, the number of BBH mergers would not differ much between the two time spans. These numbers are reported in Table 2, and they define the expected BBH merger rate if these populations would be continuously observed for 10 yr. The BBHs in GCs can be either primordial, that is the binary formed from the evolution of the two massive stars that were in a binary system in the initial GC model, or dynamically formed, that is the binary formed in the GC via dynamical processes during the GC evolution. The total number of primordial binaries that merged in the two time range considered are reported in Table 2 too.

In order to determine the merger rate for BBHs within 1 Gpc, we considered a cosmological cube of a side with a length of 1 Gpc. Supposing a constant density number of galaxies in the local Universe $\rho_{\rm galaxy}$, the BBH merger rate R in the studied cosmological cube can be determined as

$$R = (\rho_{\rm galaxy} \cdot V \cdot N_{\rm mergers})/\Delta T, \quad (1)$$

with V is the volume of the cosmological cube, and $N_{\rm mergers}$ is the number of mergers within the time interval $\Delta T = 3$ Gyr. For our study, two different galaxy densities have been used. The evolution of a cosmological cube with volume $V = 1.2 \times 10^6$ Mpc^3 and 1.8×10^{10} particles representing baryonic and dark matter was modelled in Illustris-1 simulation (Vogelsberger et al. 2014). To account for all the bounded galaxy systems present in the simulation at redshift $z = 0$, the total number of objects and with mass greater than 10^6 M$_\odot$ has been considered, implying a total galaxy density of $\rho_{\rm Illustris} = 0.2\,{\rm Mpc}^{-3}$. In the local Universe, only 2/3 of galaxies are spirals (Conselice et al. 2016), the total galaxy density for spiral galaxies in the Illustris simulation would be $\rho_{\rm Illustris} = 0.13\,{\rm Mpc}^{-3}$. Instead, Abadie et al. (2010) estimate the number of accessible Milky Way Equivalent Galaxies (MWEGs) and the extrapolated density of MWEGs in the space, being $\rho_{\rm MWEG} = 0.0116\,{\rm Mpc}^{-3}$. We find a merger rate of $R_{\rm Illustris} = 12.7\ (22.9)\ {\rm yr}^{-1}\ {\rm Gpc}^{-3}$ and $R_{\rm MWEG} = 1.0\ (1.8)\ {\rm yr}^{-1}\ {\rm Gpc}^{-3}$ in the two cases and for the MW (M31). These results are summarized in Table 3, and will be discussed with more details in Section 4.

The semimajor axis, eccentricity and mass ratio of the BBHs that would merge in the time range within 10 and 13 Gyr are reported in Fig. 9, together with the distribution of BBHs that merged in the GC or that escaped the host GC at the merging time. As it is possible to note, binaries with high eccentricity and small semimajor axes ($<$ 100 R$_\odot$) would merge in this time range. Also, most of the merged binaries have a high mass ratio, meaning that the mass difference of the two BHs are negligible. The mass ratio reproduced in our simulations differs from the value observed in LIGO/VIRGO BBH mergers. As mentioned already before, these differences are expected

Table 2. Number of BBHs present at 12 Gyr and merged for two different time ranges and their corresponding merger rate in 10 yr, for MW and M31, respectively. For the BBHs present at 12 Gyr, the total number of primordial binaries are reported in brackets, meanwhile for the merging BBHs, the total number of escaped mergers are reported in the brackets. The number of primordial binaries that merged in the two different time ranges are reported too.

Galaxy	Present at 12 Gyr	Merged		Merger rate in 10 yr		Primordial binaries merged	
		10–13 Gyr	12–12.5 Gyr	10–13 Gyr	12–12.5 Gyr	10–13 Gyr	12–12.5 Gyr
MW	120 ± 16 (6)	285 ± 34 (284)	30 ± 6 (6)	9.5×10^{-7}	6.0×10^{-7}	73 ± 13	4 ± 2
M31	235 ± 27 (13)	515 ± 50 (513)	53 ± 7 (7)	1.7×10^{-6}	1.1×10^{-6}	145 ± 21	5 ± 2

Table 3. The merger rate R for MW-like galaxies within a distance of 1 Gpc, using the galaxy density from Illustris and the interpolated density of MWEGs, for both MW and M31, respectively.

Galaxy	$R_{\rm Illustris}$ $(D = 1\,{\rm Gpc})$ $({\rm yr}^{-1})$	R_{MWEG} $(D = 1\,{\rm Gpc})$ $({\rm yr}^{-1})$
MW	12.7	1.0
M31	22.9	1.8

due to the outdated BH mass prescription used in the MOCCA-Survey Database I. Instead, the distribution properties of the merger BBHs for primordial and dynamically formed binaries are shown in Fig. 10. The dynamically formed binaries have more eccentric orbit compared to the primordial ones, and also have a larger mass ratio. Also, the semimajor axis for the dynamically formed binaries seems to be larger than the primordial binaries.

3.3.2 *Non-merging binary BHs*

The distributions for the total number and the mean number of BBHs at 12 Gyr at different galactocentric distances are shown in Fig. 11 for both MW and M31, respectively. The mean number of BBHs has been determined as the total number of BBHs in the radial bin divided by the total number of GCs in the same radial shell. Our results show that most of the BBHs are found in the central region of the galaxy. However, the mean number of BBHs per GC is constant for different galactocentric distances. Indeed, the p-values for the Kolgomorov–Smirnov test (KS test) comparing our results with a uniform distribution in galactocentric distances are 0.68 and 0.64 for MW and M31, respectively, both with the 'two-sample' alternative hypothesis. This implies that the mean number of BBHs per GC are uniformly distributed in galactocentric radius.

The mean number of non-merging BBHs found at 12 Gyr in our simulations is 120 ± 16 and 235 ± 27 for MW and M31, respectively. The normalized histograms (the area beneath the histograms have been set to 1) of the orbital eccentricity, mass ratio and semimajor axis of the BBHs at 12 Gyr are reported in Figs 12 and 13 for MW and M31, respectively. The orbital eccentricity of the BBHs are mostly concentrated in two regions: extremely eccentric (∼1.0) and almost circular (∼0.2), whereas the semimajor axis of the binaries are relatively compact with a mean value of $\sim 50\ {\rm R}_{\odot}$). On the other

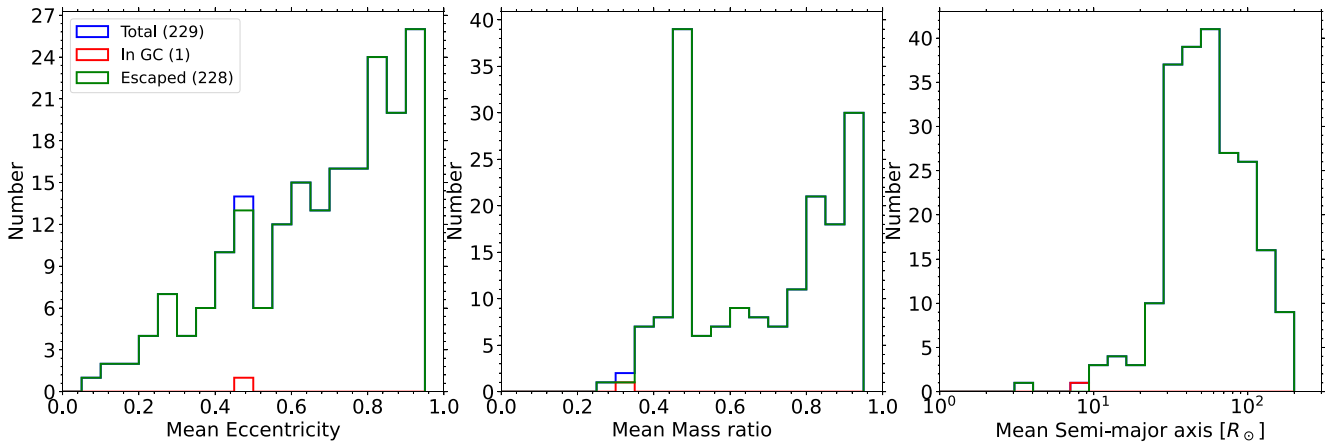

Figure 9. Semimajor axis (left), orbital eccentricity (middle), and mass ratio (left) histograms for the BBHs that would merge in the time range between 10 and 13 Gyr in the MW population. The distribution for the BBHs that would merge in the GC or that escaped the GC when merged are reported. In brackets, the number of each sample has been reported.

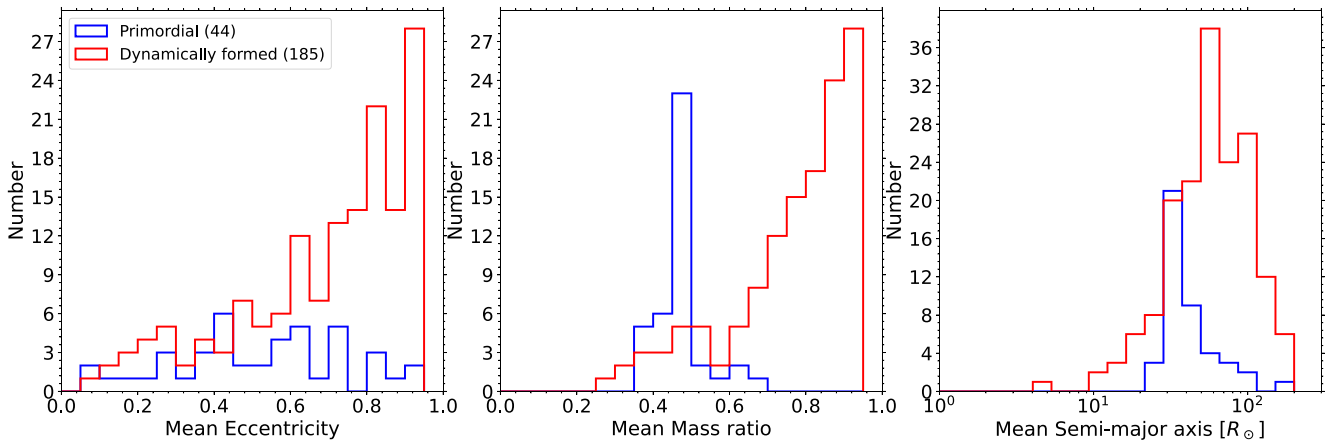

Figure 10. Semimajor axis (left), orbital eccentricity (middle), and mass ratio (left) histograms for the BBHs that would merge in the time range between 10 and 13 Gyr in the MW population. The distribution for primordial and dynamically formed BBHs that would merge are reported. In brackets, the number of each sample has been reported.

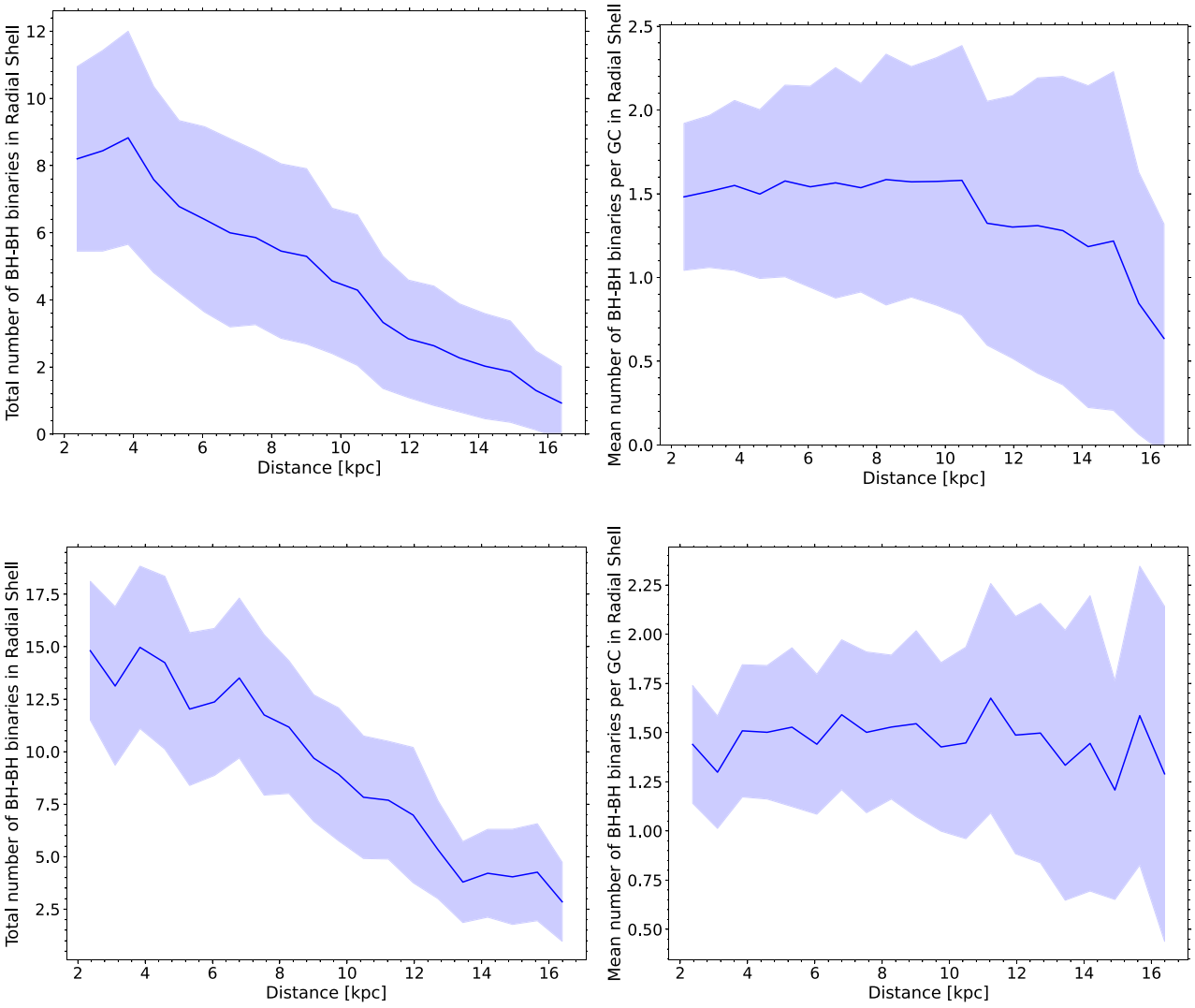

Figure 11. Total number (left) and mean number (right) of non-merging BBH distribution for MW (top) and M31 (bottom) for the MOCCA, respectively. The shaded regions represent the standard deviation for both the observed and the simulated GC populations.

hand, the mass ratio of the binaries is mostly concentrated in the region between 0.8 and 1. In the histograms, the distribution for different galactocentric distance shells are reported too. As it is possible to see, the orbital eccentricity of BBHs is more extended to circular orbit at larger galactocentric distances, with large part of the population having a more thermal orbital eccentricity (>0.6) in the central galactic regions. Similarly, the mass ratio and the orbital semimajor axis at larger galactocentric distances seem to be more extended towards small values (<0.6) and larger values ($> 10^2\,R_\odot$), respectively. Instead, for smaller galactocentric distances, the mass ratio peaks for larger values (>0.8), with the semimajor axis peaking at smaller values ($< 10^2\,R_\odot$).

The spatial distribution for the semimajor axis, eccentricity and mass ratios are showed in Fig. 14 for the MW BBHs present at 12 Gyr. We found that the distributions are a statistically decreasing function with galactocentric distance (the statistical test results are reported in Appendix A). These results show that close BBHs might be found in the central region of the galactic halo, where they are also more numerous. Also, this implies that it might be expected that the number of BBH mergers are more likely to be observed at smaller galactocentric distances.

3.3.3 BH delivered to the NSC

The evolution of the total number of BHs delivered to the NSC are reported in Fig. 15. It can be seen that a significant number of BHs and BBHs have been delivered to the NSC by GCs within a few Gyr after their formation (∼ 30 per cent of the total number of BHs are delivered in the first 2 Gyr). A slow increase in these numbers is seen at later times. The total number of binaries delivered to the NSC is ∼ 5 per cent of the total BH population that were delivered to the NSC. The mean total number of BH delivered to the NSC are ∼3000 and ∼1000 for MW and M31, respectively, of which ∼100 and ∼60 are BBHs for MW and M31, respectively.

For an initial power-law GCIMF between $M_{\rm low} = 10^3$–$10^4\,M_\odot$ and $M_{up} = 10^7\,M_\odot$, the initial total number of GCs in the population would be 10 to 5 times larger, respectively, and a total mass of the GCs population ∼6−5 times larger. Because of the fast cluster dissolution time for low-mass clusters at small galactocentric distances (Gnedin & Ostriker 1997; Arca-Sedda & Capuzzo-Dolcetta 2014b; Rodriguez et al. 2022), we would expect that the number of GCs delivered to the NSC due to dynamical friction would be 3–4 times larger only, with the total mass of roughly one order of

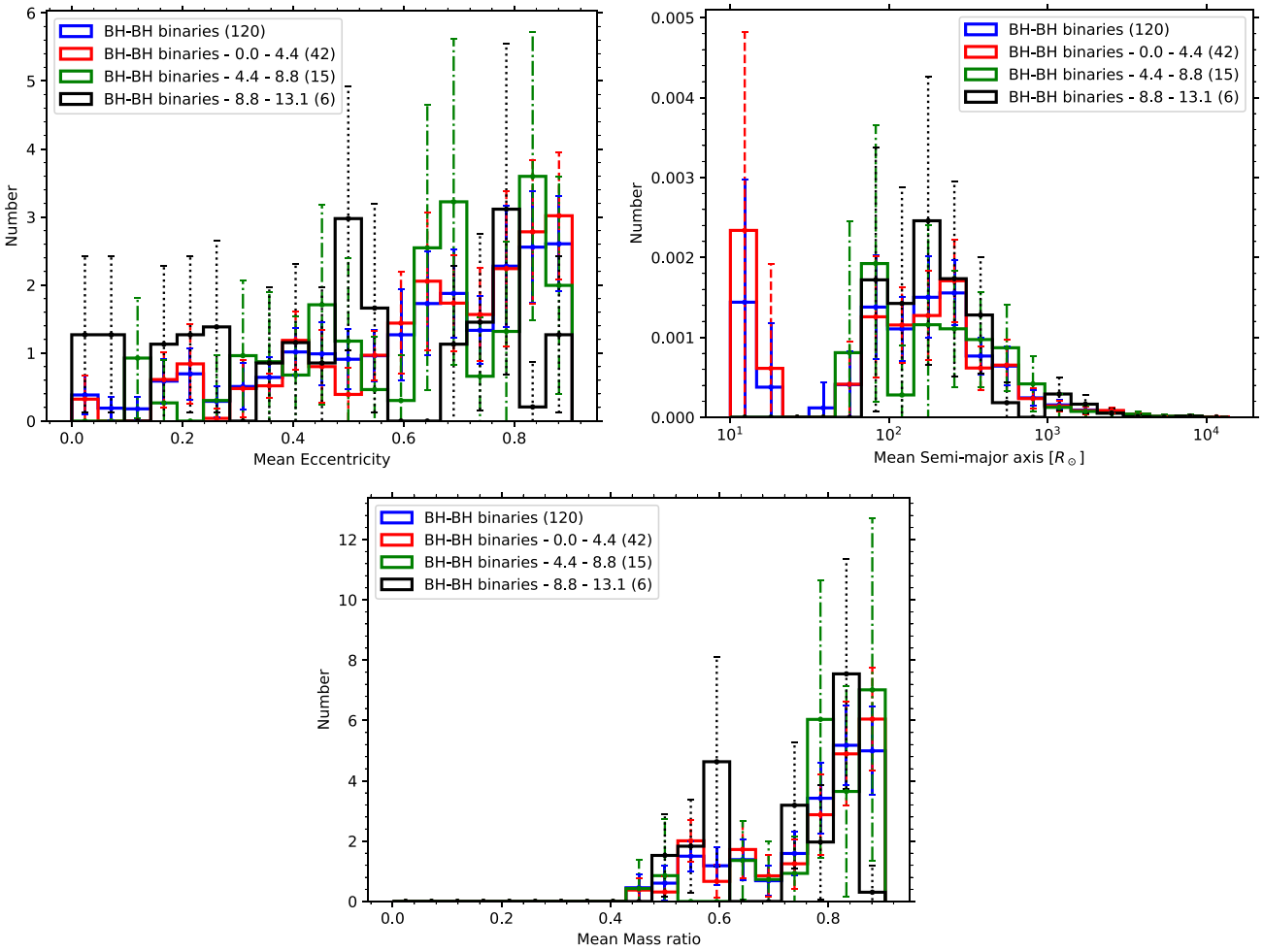

Figure 12. Orbital eccentricity (top-left), semimajor axis (top-right), and mass ratio (bottom) histograms for the BBHs that are present at 12 Gyr in the MW population. The distribution for all BBHs (blue), and for different galactocentric distance shells are reported. The mean number of BBHs for each population is reported in brackets. The area beneath the histograms have been set to 1.

magnitude larger. This will imply that the number of BHs and BBHs delivered to the NSC of few times larger only.

4 DISCUSSION

The kinematic comparison with the MW GC population in the Bajkova catalogue (Bajkova & Bobylev 2021) shows that the GC population simulated in our models represent decently the observed kinematic properties. To model the Galactic potential, the MOCCA models were simulated using a point mass approximation and GCs were assumed to move on a circular orbit. From Fig. 3 it is possible to note that the orbital approximations deployed in the MOCCA models is in relatively good agreement with the observational data in the MW GC population, within the simulated mass range. This is a crucial and important result for our models: indeed, the GCs in our machinery were initially placed in a circular orbit around the external galaxy and then they were modelled in elliptical orbits, given the findings in Cai et al. (2016). None the less, despite the limitations that this assumption would imply, the distribution of the observed GC mass and their circular orbits are in agreement with our simulations.

The distribution of the mean GC mass for different dynamical models is similar between the MW and M31 population. The BHS models tend to be more massive than the Standard and IMBH models, and the IMBH models being more massive than the Standard ones. These results would suggest that the most massive GCs might contain a BHS in their center. Similarly, some correlation between the BHS mass and the galactocentric distance might exist, with more massive BHS GCs seen at small galactocentric distances.

As already shown in Paper I, the BHS models are expected to have a larger half light radius since the central energy generation (controlled by the BHs) is much stronger compared to the other systems, implying a more expanded system. On the other hand, it is expected that the influence of the IMBH would change the central properties of the GC: due to the dee per central potential, the system is expected to be more concentrated, implying a smaller half light radius. This is indeed seen in our simulations for different galactocentric distances in the both MW and M31 populations: the mean half light radius of the BHS models is larger than the Standard and IMBH models, with IMBH models being more compact at larger galactocentric distances. In comparison with the results shown in Paper I, the results shown in this work also take into consideration the interaction between the GC and the host galaxy in the survival of the GC itself. This might be a further support to our machinery results and assumptions.

The mean total BH mass in the system is significantly larger for the IMBH model compared to the BHS and Standard ones. For these

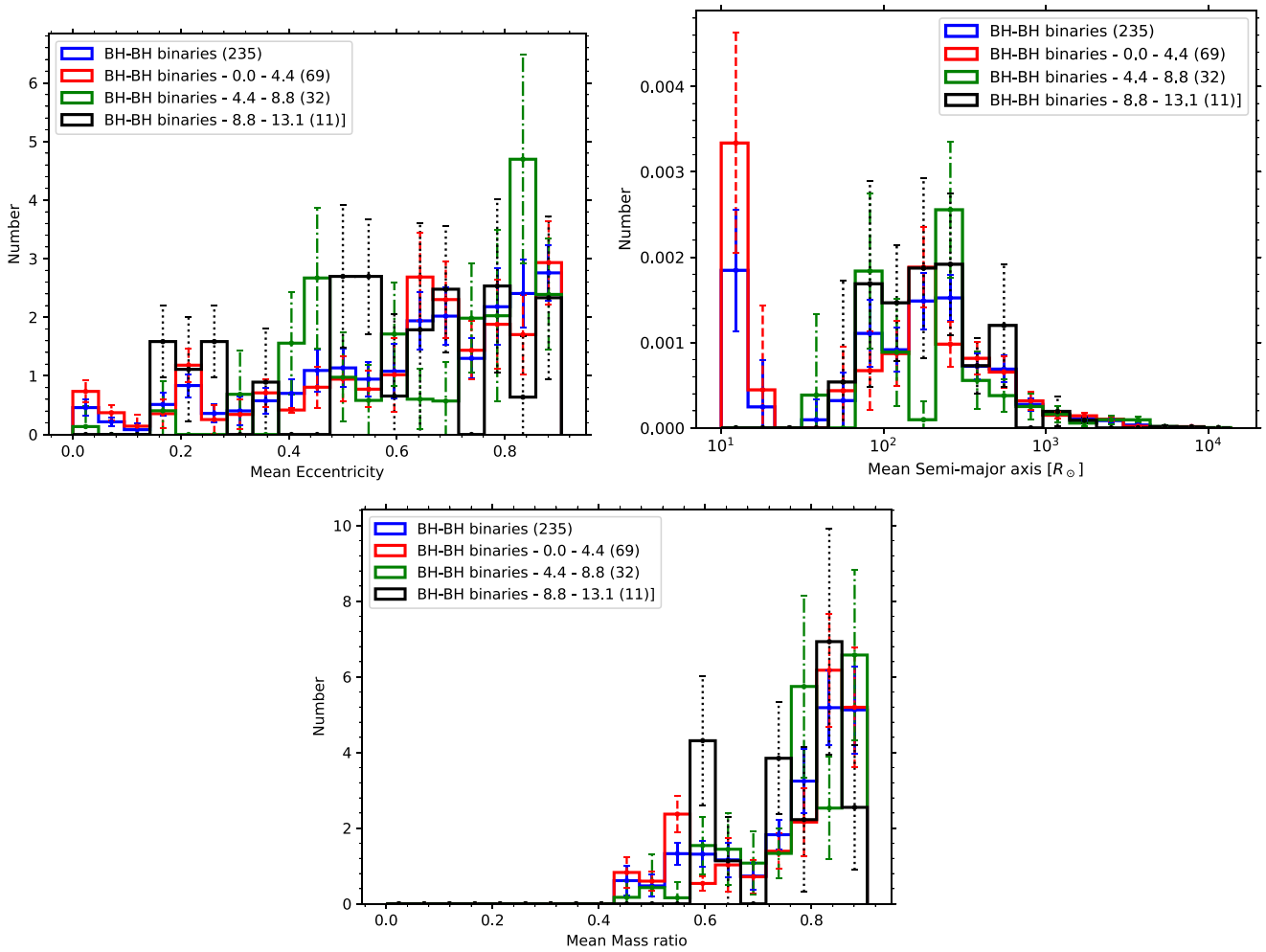

Figure 13. Orbital eccentricity (top-left), semimajor axis (top-right), and mass ratio (bottom) histograms for the BBHs that are present at 12 Gyr in the M31 population. The distribution for all BBHs (blue) and for different galactocentric distance shells are reported. The mean number of BBHs for each population is reported in brackets. The area beneath the histograms have been set to 1.

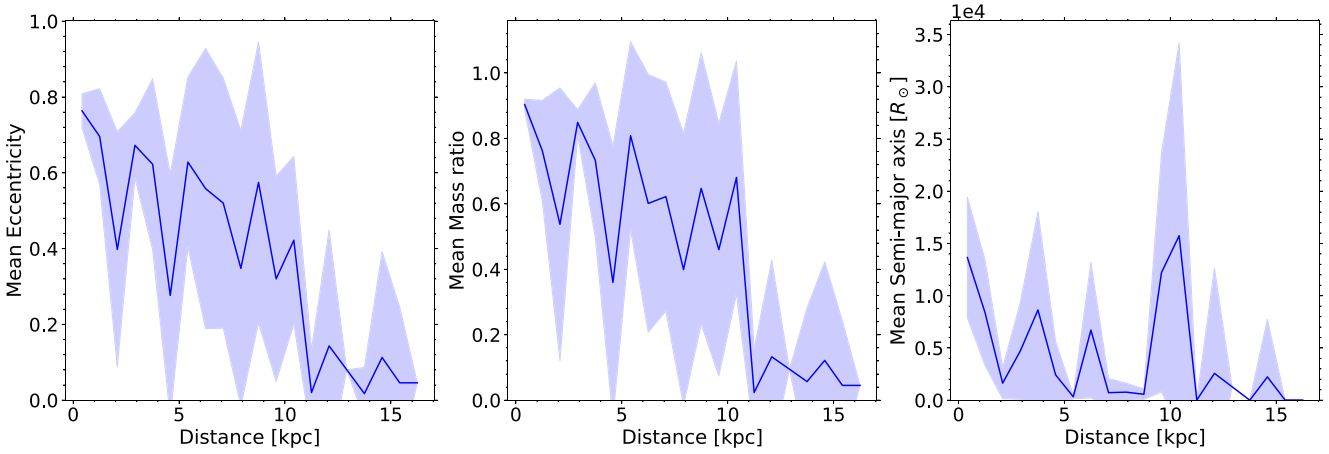

Figure 14. Distributions for mean values in radial galactocentric bins for semimajor axis (left), orbital eccentricity (middle), and mass ratio (left) histograms for the BBHs that are present at 12 in the MW population. The shaded regions represent the standard deviation for both the observed and the simulated GC populations.

models, the total BH mass in the GC is defined by the mass of the IMBH. Indeed, the presence of the IMBH would imply a high density and short dynamical interaction time-scale that would drive out all the massive BHs from the system. Also, the mean total BH mass in the GC for the IMBH models is larger at a smaller galactocentric distance. This might imply a correlation between the formation of an

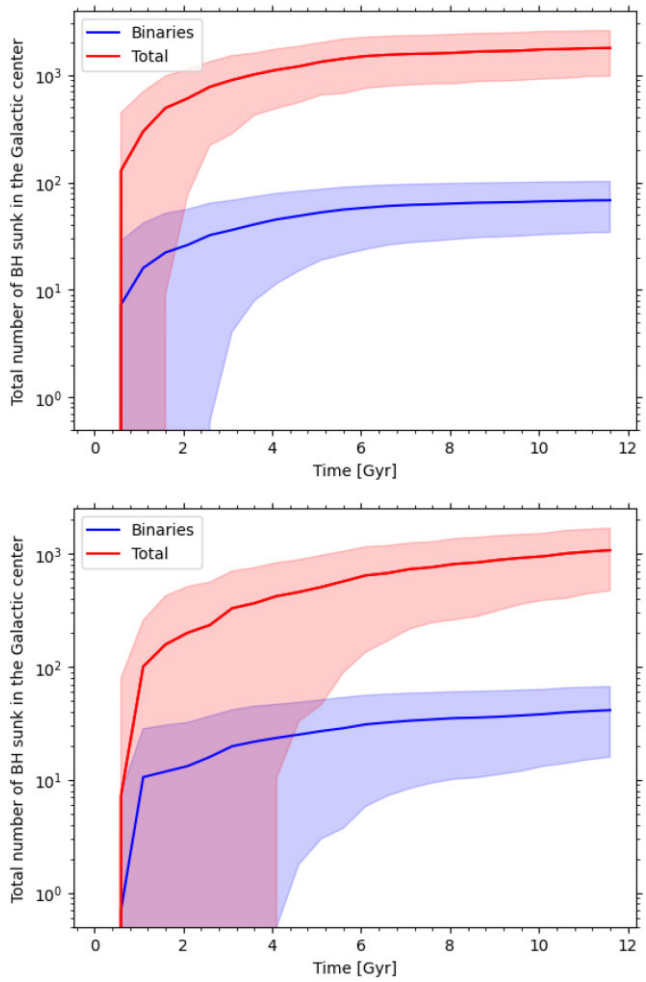

Figure 15. Total number of BH and BBHs delivered to the NSC time evolution for MW (top) and M31 (bottom), respectively.

IMBH in a GC and the galactocentric distance and the local galactic density. Instead, the number of BHs in the Standard models are expected to be small (if any), meaning that it is expected to have an almost null BH mass in the system.

Lützgendorf et al. (2013) examined for the existence of a possible IMBH at the centre of the 14 GCs in their sample using observed surface brightness profiles and velocity dispersion profiles. Six of them have been proposed by Lützgendorf et al. (2013) to host an IMBH in their centre (NGC 1904, NGC 5139, NGC 5286, NGC 6266, NGC 6388, and NGC 6715), and among these, four GCs have a galactocentric distance greater than 5 kpc. The number density of GCs decreases for galacocentric distances greater than about 5 kpc, with a fewer number of GCs observed at larger distances. For this reason, we have set a minimum galactocentric distance of 5 kpc for this comparison. Arca Sedda et al. (2019) classified Galactic GCs IMBH (or BHS) based on how many MOCCA models had a BHS or an IMBH, finding a total of 35 models harbouring an IMBH. 16 of the 35 IMBH reported Galactic GCs in Arca Sedda et al. (2019) are found a distances >5 kpc.

Askar et al. (2018) and Arca Sedda et al. (2019) reported the number of GCs candidates that would harbour a BHS in their centre, both using the MOCCA-Survey Database I results to identify BHS models. In Askar et al. (2018), the authors chose models based on their central surface brightness and the observed current half-mass relaxation time, with a total of 28 Galactic BHS GCs. Arca Sedda et al. (2019) reported a total of 23 models harbouring a BHS. Instead, the authors of Weatherford et al. (2019) found that the mass segregation parameter Δ, which was derived from the 2D-projected snapshots of the models published in the CMC Cluster Catalogue (Kremer et al. 2020) correlates with the number of BHs in the system. A total of 29 Galactic BHS GCs were found in their work (considering only GCs that retain a number of BH $N_{\rm BH} > 50$). More than half of the reported GCs in Askar et al. (2018), Arca Sedda et al. (2018, $\sim$ 70 per cent), and Weatherford et al. (2019) are found at distance >5 kpc. From our models, it might be expected that the probability to discover an IMBH or BHS model is higher at larger galactocentric distances. Indeed, the total number of Standard models seems to be comparable with the IMBH and BHS ones in the outskirts of the galactic halo: the percentage over the whole population of GCs with galactocentric distance >5 kpc is $\sim$ 20 per cent for both IMBH and BHS models. The mean IMBH mass decreases with the galactocentric distances, suggesting a link for the IMBH formation to the galactic field and galactocentric position. However, this is not seen for the BHS models.

The simulated merger rate within a volume $V = 1\,{\rm Gpc}^3$ obtained by our simulations depends on the galaxy density number assumed. Considering the galaxy density number from the Illustris simulations (Vogelsberger et al. 2014), we have a merger rate of $\sim$ 13–23 ${\rm yr}^{-1}$ ${\rm Gpc}^{-3}$, meanwhile considering the interpolated density of MWEGs from Abadie et al. (2010), we obtain a merger rate of $\sim$ 1.0–2.0 ${\rm yr}^{-1}$ ${\rm Gpc}^{-3}$. The results from the Illustris simulation could be interpreted as maximum expected merger rate. Indeed, the galaxy density number used in this work assumes that all galaxies (particularly dwarf ones) in the cosmological cube considered in our study are MW- and M31-like galaxies. On the other hand, the results from the interpolated density of MWEGs should be considered as a minimum expected merger rate, due to the set of assumptions that have been made. Indeed, the merger rates for both MW and M31 in our simulations have been determined for a sub-sample of the whole GC population. As reported in Paper II, we constrained our study for GCs with initial masses between 2×10^5 and $1.1 \times 10^6 {\rm M}_\odot$, and within 17 kpc from the galactic center. The most massive GCs are actually excluded in our study. These might be expected to be host to a large number of BBHs and in particular to BBHs mergers. Also, one additional explanation for the smaller reported value in our simulation is the prescription used in the MOCCA-Survey Database I. As said before, the BH masses obtained in the old prescription are smaller compared to the new updated ones, leading to a larger GW decay time in our simulations. Finally, in our study we did not consider all models that initially populated the studied galaxies. Indeed, we have considered only GCs that would survive up to 12 Gyr, with the dissolved GCs not taken into account. The latter would contribute importantly to the merger rate.

None the less the assumption made in the determination of our merger rate, our values are comparable to the one reported in Mapelli et al. (2022), where a local merger rate $R \sim$ 4–8 ${\rm yr}^{-1}$ ${\rm Gpc}^{-3}$ have been reported. In their analysis, Mapelli et al. (2022) explored the cosmic evolution of isolated BBHs and dynamically formed BBHs in NSCs, GC and young star clusters. In particular, they studied the BBH merger rate considering two main different supernova channels (Fryer et al. 2012) (that are rapid and delayed models) in the BH formation, finding different results according to the chosen prescription: the merger rate in the delayed models are roughly 40–60 per cent smaller compared to the merger rate in the rapid one. The different merger rate can be explained by the different minimum BH mass in the two models ($5{\rm M}_\odot$ for rapid and $3{\rm M}_\odot$ for the delayed),

leading to a larger GW decay time in the delayed model compared to the rapid ones.

Banerjee (2022) investigated the importance of binary evolution and cluster dynamics in producing merging BBHs over cosmic time. The author performed a population synthesis for the modelled universe, deploying direct *N*-body simulations to model the evolution of young massive clusters, and stellar evolutionary models for isolated binaries. The author's estimates of the intrinsic BBH merger rate density and the cosmic evolution are consistent with the findings in the GWTC-2. In particular, the intrinsic merger rate for BBHs considering only young massive clusters determined in Banerjee (2022) is of the order $\sim 1\ \mathrm{yr}^{-1}\ \mathrm{Gpc}^{-3}$ for redshift $z = 0$. This value is comparable to our results, with most of the models computed in Banerjee (2022) used the rapid supernova prescription.

Finally, Askar et al. (2017) determined the local merger rate density using models from the MOCCA-Database I. Assuming a GC star formation rate from Katz & Ricotti (2013), the author determined local merger rate density as function of the star formation rate and the probability of forming a BBH per unit delay time. The authors find a merger rate $R = 5.4\ \mathrm{yr}^{-1}\ \mathrm{Gpc}^{-3}$. Our results are in relatively good agreement with the value reported in Askar et al. (2017). Also, our estimates place in the ballpark of Ligo-Virgo Collaboration predictions for BBH merger rate of $R = 23.9\ \mathrm{yr}^{-1}\ \mathrm{Gpc}^{-3}$ (Abbott et al. 2021), though being on the lower side. Our minimum values are smaller compared to the value reported in Askar et al. (2017). This supports the interpretation that the small value reported by our simulations is connected with the limitations imposed to the GC subpopulation selected in our study.

The number of observable BBH merger rates in a 10 yr span is quite small: our results would suggest that it would be unlikely to observe a BBH merger rate in both MW and M31 galaxies. In the future, results from the MOCCA-Survey Database II could be used to better constrain the BBH mass ratio and properties, taking advantages of the new stellar evolution features (as described in Kamlah et al. 2022) and the GC gas expulsion evolution included in the Monte Carlo method (as described in Leveque et al. 2022a).

The orbital properties of the BBHs that merged within 10 and 13 Gyr strongly depend on the formation channel of the binaries. Dynamical BBHs form due to close few-body encounters, and for this reason their orbits can have higher eccentricities and larger semimajor axis values compared to those BBHs that form through evolution of primordial binaries.

As shown in Fig. 11, the majority of the BBHs observable at 12 Gyr are located in the central galactocentric regions for both MW and M31. On the other hand, a constant mean number of BBHs per GC has been observed. This implies that the larger number of BBHs in the central region is correlated to the total number of GCs being more numerous in this region of the galactic halo, being the mean number of BBHs constant.

The radial distribution and the histograms at different galactocentric distances of semi-major axis, orbital eccentricity and mass ratio of observable BBHs shown in Figs 12 and 13 could suggest stronger dynamical interactions involving BBHs in the central region of the galaxy halo. Indeed, the orbital eccentricity seems to be more thermal and the semi-major axis seems to be larger at smaller galactocentric distances (as shown in Fig. 14). Instead, because of larger and less dense clusters in the outskirt of the galactic halo, the number of interactions that would thermalize the binaries could be expected to be smaller. This would imply a more circular orbital and smaller semimajor axis for BBHs hosted in GCs at larger galactocentric distances. This is supported by the galactocentric distance distribution of dynamical models in the galactic halo. As shown in Fig. 4, the Standard models dominate the central region of the galactocentric halo. Given that the Standard models are more numerous compared to the BHS ones, it might be expected that the number of interactions that a BBHs undergo is larger in a Standard model than a BHS one.

We find around 1000–3000 BHs are transported into the galactic NSC over a 12 Gyr time span. This might have interesting consequences on the overall population of BHs in a galactic nucleus. If NSCs form exclusively *in situ*, the fraction of stars turning into a BH can be retrieved by the IMF, and correspond to $\sim 8 \times 10^{-4}$ for a Kroupa (2001) mass function, thus a number of $N_{\mathrm{BH,in\,situ}} \sim 20\,000$ for a MW-like NSC. If a fraction f of NSC mass is contributed by star cluster dispersal, the actual amount becomes $N_{\mathrm{BH,real}} \sim (1-f)\ N_{\mathrm{BH,in\,situ}} + N_{\mathrm{BH,delivered}}$. In our models, we assumed $f \sim 0.1$, leading to a negligible difference between full *in situ* formation and a 'mixed' formation process. Combining our previous work and the present analysis, we can define a BH-transport efficiency as the ratio between the total number of delivered BHs and the total mass accreted into the galactic nucleus, this being around $\eta = 2000/(3.5 \times 10^6) \sim 5.7 \times 10^{-4}\ \mathrm{M}_{\odot}^{-1}$, and $N_{\mathrm{BH,delivered}} = \eta \times M_{\mathrm{accreted}}$. Thus, if a NSC is totally contributed by infalling clusters, we would expect a number of BHs $N_{\mathrm{BH,infall}} = \eta \times M_{\mathrm{NSC}} \sim 14\,300$. This simplistic analysis provides us with a range of the total number of BHs that might be inhabiting the nuclear regions of MW and Andromeda, being this in the range $(1.4-2.2) \times 10^4$.

4.1 Comparison of BH binary production in GCs and the field

BHs are endpoints of the evolution of massive stars and they should be present in both dense stellar systems such as GCs, as well as in the galactic field. Comparing the expected number of BHs in such environments could be useful to understand the origin and the evolution of BHs and BH binaries as well. Using the results from the simulations carried out in this paper, we report the total amount of BHs present at 12 Gyr for the MW population in Table 4. This includes the number of single BHs and the number of binaries containing at least one BH and different type of companions – main sequence (MS), stars outside the MS phase, white dwarf (WD), neutron stars (NS), and BH – are reported too. For this comparison, we did consider also the BHs and different types of BH binaries that would have been ejected from the GCs and hence would populate the Galactic halo – the numbers from MOCCA also include binaries that escaped their host cluster. These binaries were evolved from the time of escape up to 12 Gyr using the `StarTrack` evolutionary code. For comparison, in the Table 4 we provide the results for Galactic field BH population (Olejak et al. 2020). The authors used `StarTrack` population synthesis code (Belczynski et al. 2008, 2020) to estimate current number of single BHs and BHs in binary systems that formed from the isolated stellar/binary evolution in three Milky Way components: bulge, disc, and halo. They adopted individual star formation rate model and metallicity distribution for each component (see fig. 1–4 of Olejak et al. 2020) and assumed isolated single/binary evolution of stars corresponding to total stellar mass of MW $M_{\mathrm{MW}} \approx 6.10 \times 10^{10}\mathrm{M}_{\odot}$ (Licquia & Newman 2015). The numbers provided for `StarTrack` in Table 4 correspond to total Galactic field population of bulge, disc, and halo.

Our results for the number of BHs are of 3−4 orders of magnitudes smaller compared to `StarTrack` field population, and these differences can be explained by a smaller total stellar-mass in GCs used in our simulations. As already mentioned in Section 2, we constrained our initial models to a small fraction of the total GCIMF, and a region of the galactic potential, implying a total GCs mass population

Table 4. Total number of single BHs, number binaries containing at least one BH and the number of BH binaries with given companion are reported. In the top two rows, the actual number for MOCCA and `StarTrack` simulations are reported. Also, in parenthesis, the percentage of escaping binaries for the MOCCA simulation are reported. In the bottom two rows, the total numbers normalized by the total initial mass are reported. In parenthesis the percentage of each binary in respect of the total number of binaries containing a BH. The initial masses are of 6.3×10^7 $M_\odot$ for the MOCCA simulation and 6.3×10^{10} $M_\odot$ for `StarTrack` (Olejak et al. 2020), respectively.

Model	$N_{\rm BH,\ single}$	$N_{\rm BH,\ binaries}$	$N_{\rm BH-MS}$	$N_{\rm BH-Out\ of\ MS}$	$N_{\rm BH-WD}$	$N_{\rm BH\text{-}NS}$	$N_{\rm BH-BH}$
MOCCA	8.3×10^4 (94 per cent)	6.4×10^3 (98 per cent)	77 (0 per cent)	3 (0 per cent)	42 (0 per cent)	5 (100 per cent)	6.3×10^3 (98 per cent)
`StarTrack` (field)	1.2×10^8	4.9×10^6	1.7×10^5	10^4	1.4×10^6	1.7×10^5	3.1×10^6
MOCCA	10^{-3}	10^{-4}	10^{-6} (1 per cent)	4×10^{-8} (0 per cent)	7×10^{-7} (1 per cent)	7×10^{-8} (0 per cent)	10^{-4} (98 per cent)
`StarTrack` (field)	2×10^{-3}	8×10^{-5}	3×10^{-6} (4 per cent)	2×10^{-7} (0 per cent)	2×10^{-5} (29 per cent)	3×10^{-6} (4 per cent)	5×10^{-5} (63 per cent)

$\sim$ 75 per cent smaller than the whole population. Also, we excluded from our calculation the GCs that would have been dissolved during the Hubble time, that would compose of $\sim$ 10 per cent of the total initial GC population mass in our simulations (and up to $\sim$ 25 per cent if we would consider an initial mass range between 10^3 and 10^7 $M_\odot$). Hence, we would expect that numbers reported from the MOCCA simulations should increase at least by a factor of 2, if we would consider in our simulations the BHs present in the very massive GCs in a full mass-range GCIMF, and the BHs present in dissolved GCs. Indeed, it is expected that the most massive GCs would contribute importantly to the total number of BHs in GCs. Also, the number of BH binaries dynamically formed is expected to be important in such clusters. On the other hand, the contribution of old low mass GCs would be minimal, with small number of BHs formed in such system. Many BHs will escape such host clusters in its early stages of dynamical evolution and thus they are unlikely to form many BBHs (Rastello et al. 2021; Torniamenti et al. 2022).

In Table 4, we also report the number of differed BBHs divided by the total initial stellar mass, which is 6.3×10^7 $M_\odot$ for the MOCCA simulations. When normalized by the total initial mass, our results are comparable (or even larger) to the number reported in `StarTrack` simulations. The difference in the type of companion for the binaries containing a BH is related to the different stellar evolutionary formulae used in our simulations compared to the `StarTrack` ones (for example, the outdated treatment for binary and stellar evolution in MOCCA-Survey Database I strongly underestimated the number of retained NSs in GC models, impacting the number of BH-NS binaries observed in our models), and by the dynamical interactions between BH and other objects inside the GCs. In fact, exchange in binary-single and binary–binary encounters is the most important process in the formation of binary systems with BHs. For example, dynamical encounters within GCs can lead to exchange interactions that can pair BHs with lower mass MS stars. Also, the presence of an IMBH in the GCs would influence the number of BH-MS and BH-WD binaries, preventing their formation, and it would reduce the number of merging BBHs in GCs (Hong et al. 2020). The dynamical interactions between binaries containing at least one BH and other objects in the GCs would strongly influence the fate of such binaries. In fact, according to Heggie-Hills law (Heggie 1975; Hills 1975), hard binaries (generally compact binaries) are more likely to get harder and soft binaries (generally wide binaries) to get softer due to the strong interaction between binary-single stars and binary–binary stars. Consequently, wide binaries (binaries whose stars would evolve or are BHs) would be dissolved, meanwhile hard binaries would get hard enough to survive the supernova (SN) events that their stars will undergo – and hence retrain the BHs that would be formed. Finally, single BHs can also form binaries during the interactions with other single BHs, this being more important in particular for BHS models.

As a result, when compared with the field production, the BH binaries efficiency (that is, the total number per unit of mass) in GCs is much larger than in the fields. In fact, as reported in Table 4, GCs are almost twice more efficient in producing binaries containing at least one BH, and even more efficient in producing BBHs compared to the field. Our results could be considered as a lower limit for the BH binaries efficiency. As mentioned before, a larger number of BHs and BH binaries are expected in clusters with masses larger than the one considered in this study. We would expect that the BH binaries efficiency could be larger of a factor of few, if we would consider such massive clusters. However, the nature of the dynamical formation of BH binaries would be imprinted in the orbital properties of the binaries, as shown in Fig. 9. Finally, it must be cautioned that these results can be sensitive to the differences in binary/stellar evolution

prescriptions used in both MOCCA and `StarTrack`. In a future work, a more thorough comparison of the formation efficiency of BH binaries in the field and in GCs will be made using consistent stellar and binary evolution prescriptions between the two codes.

5 CONCLUSION

In this paper, we expanded the study of the MW and M31 population simulated with the machinery introduced in Paper II, investigating the BH content of their GC population.

Summarizing our main results:

(i) The kinematic properties of the MW population are in agreement with the observed ones (see Figs 1–3). The observed orbital properties distributions (that are, orbital eccentricity, pericenter distance, and the galactocentric distance for a circular orbit determined using the prescription in Cai et al. 2016) in the MW population has been reproduced by our models, further confirming the reliability of our semi-analytic procedure. This is a significant outcome for our machinery, since the GCs in external galaxy have been initially populated on a circular orbit, and subsequently they were modelled in elliptical orbits using the prescriptions in Cai et al. (2016).

(ii) The mean GCs mass and the mean half-light radius for models that would harbour a BHS is larger than Standard and IMBH models (see Figs 4–7). On the other hand, Standard models are more numerous in the central region of the galaxy, with the number of IMBH and BHS comparable to the Standard ones at larger galactocentric distances.

(iii) A maximum and a minimum value observable BBH merger rate has been determined, with value $\sim$ 20–35 yr^{-1} Gpc^{-3} using the galaxy number density from the Illustris-1 simulation (Vogelsberger et al. 2014), and of $\sim$ 1.0–2.0 yr^{-1} Gpc^{-3} using the extrapolated density of MWEGs from Abadie et al. (2010), respectively. The reported value are comparable to the value reported in previous works (Askar et al. 2017; Banerjee 2022; Mapelli et al. 2022), although our results are on the lower-side with respect to other models (e.g. Rodriguez & Loeb 2018). This could be due to the simplistic approach followed in calculating the merger rate. These differences can be explained by a smaller subsample of the whole GC population that have been considered and simulated in our machinery.

(iv) The signature of primordial or dynamically formed BBHs is imprinted in the orbital parameters for the merged binaries. Indeed, the dynamically formed binaries have greater mass ratios and more eccentric orbits than the primordial ones. Furthermore, it appears that the semimajor axis of the dynamically formed binaries is larger than that of the primordial binaries. Conversely, primordial mergers are characterized by a nearly flat eccentricity distribution and a mass-ratio clearly peaked around 0.5. The primordial merger eccentricity distribution subtly implies that dynamics might have aided the merging process, owing to the fact that isolated stellar evolution generally predicts nearly circular BBH mergers.

(v) The observable BBHs at 12 Gyr that have been simulated in our models show different orbital properties for different galactocentric distances. The BBHs do show a larger (thermal) eccentricity, larger mass ratio ($>$0.8) and smaller semimajor axes ($< 10^2\,\mathrm{R}_\odot$) at smaller galactocentric distances. These spatial evolution can be explained by denser GCs in the central region, enhancing the number of strong interactions between the BBHs and the other stars in the GCs.

(vi) Most of the BH and BBH that are delivered to the NSC happens in the first 1$-$2 Gyr of evolution, with a slow increase observed at later times. Also, the total number of BH binaries delivered to the NSC is $\sim$ 5 per cent of the total BH population delivered. A total of 1000–3000 BHs and 100–200 BBHs have transported into the nucleus over a time span of 12 Gyr. This implies a total number of BHs and BBHs lurking in NSCs being of $N_{\mathrm{BHs}} = (1.4-2.2) \times 10^4$ and $N_{\mathrm{BBHs}} = 700$–1100.

(vii) The efficiency of BH binary formation, or the total number per unit of mass, can be significantly enhanced due to dynamics in GCs. In fact, compared to isolated stellar/binary evolution in the Galactic field, GCs are about twice as efficient at producing binaries with at least one BH and even more effective at generating BBHs.

In the future we would like to extend the study of the MW and M31 population to further investigate the super massive BH and NSC masses build up (Askar, Leveque & Giersz, in preparation). Also, we intend to simulate with our machinery other galaxies and the galaxies in the local Universe. We hope to restrict and identify the observational properties, evolutionary paths, and compact object content of GCs (such as IMBH, BHS, BBHs, and X-ray binaries), and also study the gravitational microlensing phenomena in GCs. Our simulation results might be utilized to calculate the BBH merger rate in the local Universe, as well as the event rates of TDEs between the SMBH and infalling GCs.

ACKNOWLEDGEMENTS

We thank the anonymous reviewer for insightful comments that helped us clarify the presentation of the results in this paper. MG and AL were partially supported by the Polish National Science Center (NCN) through the grant UMO-2016/23/B/ST9/02732. AA acknowledges support from the Swedish Research Council through the grant 2017-04217. MAS acknowledges financial support from the European Union's Horizon 2020 research and innovation programme under the Marie Sklodowska-Curie grant agreement no. 101025436 (project GRACE-BH, PI Manuel Arca Sedda). AO acknowledge support from the Polish National Science Center (NCN) grant Maestro (2018/30/A/ST9/00050). AO is also supported by the Foundation for Polish Science (FNP) and a scholarship of the Minister of Education and Science (Poland).

DATA AVAILABILITY

The data underlying this article will be shared on reasonable request to the corresponding author.

REFERENCES

Abadie J. et al., 2010, Class. Quant. Grav., 27, 173001
Abbott R. et al., 2021, ApJ, 913, L7
Abbott R. et al., 2022, A&A, 659, A84
Arca Sedda M., Askar A., Giersz M., 2018, MNRAS, 479, 4652
Arca Sedda M., Askar A., Giersz M., 2019, preprint (arXiv:1905.00902)
Arca Sedda M., Gualandris A., Do T., Feldmeier-Krause A., Neumayer N., Erkal D., 2020, ApJ, 901, L29
Arca Sedda M., Amaro Seoane P., Chen X., 2021, A&A, 652, A54
Arca-Sedda M., Capuzzo-Dolcetta R., 2014a, MNRAS, 444, 3738
Arca-Sedda M., Capuzzo-Dolcetta R., 2014b, ApJ, 785, 51
Arca-Sedda M., Capuzzo-Dolcetta R., Spera M., 2016, MNRAS, 456, 2457
Askar A., Szkudlarek M., Gondek-Rosińska D., Giersz M., Bulik T., 2017, MNRAS, 464, L36
Askar A., Arca Sedda M., Giersz M., 2018, MNRAS, 478, 1844
Bahramian A. et al., 2017, MNRAS, 467, 2199
Bajkova A. T., Bobylev V. V., 2021, Res. Astron. Astrophys., 21, 173
Banerjee S., 2018, MNRAS, 473, 909
Banerjee S., 2022, Phys. Rev. D, 105, 023004
Banerjee S., Baumgardt H., Kroupa P., 2010, MNRAS, 402, 371

Barack L. et al., 2019, Class. Quant. Grav., 36, 143001
Barnard R., Kolb U., 2009, MNRAS, 397, L92
Bash F. N., Gebhardt K., Goss W. M., Vanden Bout P. A., 2008, AJ, 135, 182
Baumgardt H., Sollima A., Hilker M., 2020, PASA, 37, e046
Belczynski K., Kalogera V., Bulik T., 2002, ApJ, 572, 407
Belczynski K., Kalogera V., Rasio F. A., Taam R. E., Zezas A., Bulik T., Maccarone T. J., Ivanova N., 2008, ApJS, 174, 223
Belczynski K., Bulik T., Fryer C. L., Ruiter A., Valsecchi F., Vink J. S., Hurley J. R., 2010, ApJ, 714, 1217
Belczynski K. et al., 2018, A&A, 615, A91
Belczynski K. et al., 2020, A&A, 636, A104
Breen P. G., Heggie D. C., 2013a, MNRAS, 432, 2779
Breen P. G., Heggie D. C., 2013b, MNRAS, 436, 584
Cai M. X., Gieles M., Heggie D. C., Varri A. L., 2016, MNRAS, 455, 596
Chemin L., Carignan C., Foster T., 2009, ApJ, 705, 1395
Conselice C. J., Wilkinson A., Duncan K., Mortlock A., 2016, ApJ, 830, 83
Dage K. C., Zepf S. E., Bahramian A., Kundu A., Maccarone T. J., Peacock M. B., 2018, ApJ, 862, 108
Dehnen W., 1993, MNRAS, 265, 250
Di Carlo U. N. et al., 2021, MNRAS, 507, 5132
Downing J. M. B., Benacquista M. J., Giersz M., Spurzem R., 2010, MNRAS, 407, 1946
Dumont A. et al., 2022, ApJ, 929, 147
Eilers A.-C., Hogg D. W., Rix H.-W., Ness M. K., 2019, ApJ, 871, 120
Fregeau J. M., Cheung P., Portegies Zwart S. F., Rasio F. A., 2004, MNRAS, 352, 1
Freitag M., Gürkan M. A., Rasio F. A., 2006, MNRAS, 368, 141
Fryer C. L., Belczynski K., Wiktorowicz G., Dominik M., Kalogera V., Holz D. E., 2012, ApJ, 749, 91
Galleti S., Federici L., Bellazzini M., Fusi Pecci F., Macrina S., 2004, A&A, 416, 917
Galleti S., Federici L., Bellazzini M., Buzzoni A., Fusi Pecci F., 2006, A&A, 456, 985
Galleti S., Federici L., Bellazzini M., Fusi Pecci F., Macrina S., Buzzoni A., 2014, VizieR Online Data Catalog, 5143, V/143
Gieles M., Baumgardt H., Heggie D. C., Lamers H. J. G. L. M., 2010, MNRAS, 408, L16
Giersz M., Leigh N., Hypki A., Lützgendorf N., Askar A., 2015, MNRAS, 454, 3150
Giersz M., Askar A., Wang L., Hypki A., Leveque A., Spurzem R., 2019, MNRAS, 487, 2412
Giesers B. et al., 2018, MNRAS, 475, L15
Giesers B. et al., 2019, A&A, 632, A3
Gnedin O. Y., Ostriker J. P., 1997, ApJ, 474, 223
González E., Kremer K., Chatterjee S., Fragione G., Rodriguez C. L., Weatherford N. C., Ye C. S., Rasio F. A., 2021, ApJ, 908, L29
Harris W. E., 1996, AJ, 112, 1487
Harris W. E., 2010, preprint (arXiv:1012.3224)
Heggie D. C., 1975, MNRAS, 173, 729
Heggie D. C., Giersz M., 2014, MNRAS, 439, 2459
Hills J. G., 1975, AJ, 80, 809
Hong J., Askar A., Giersz M., Hypki A., Yoon S.-J., 2020, MNRAS, 498, 4287
Kamann S., Wisotzki L., Roth M. M., Gerssen J., Husser T. O., Sandin C., Weilbacher P., 2014, A&A, 566, A58
Kamlah A. W. H. et al., 2022, MNRAS, 511, 4060
Katz H., Ricotti M., 2013, MNRAS, 432, 3250
Kremer K., Ye C. S., Chatterjee S., Rodriguez C. L., Rasio F. A., 2018, ApJ, 855, L15
Kremer K., Chatterjee S., Ye C. S., Rodriguez C. L., Rasio F. A., 2019, ApJ, 871, 38
Kremer K. et al., 2020, ApJS, 247, 48
Kroupa P., 2001, MNRAS, 322, 231
Lanzoni B. et al., 2013, ApJ, 769, 107
Leveque A., Giersz M., Paolillo M., 2021, MNRAS, 501, 5212
Leveque A., Giersz M., Banerjee S., Vesperini E., Hong J., Portegies Zwart S., 2022a, MNRAS, 514, 5739
Leveque A., Giersz M., Arca-Sedda M., Askar A., 2022b, MNRAS, 514, 5751 (Paper II)
Licquia T. C., Newman J. A., 2015, ApJ, 806, 96
Lützgendorf N. et al., 2013, A&A, 552, A49
Maccarone T. J., Servillat M., 2008, MNRAS, 389, 379
Maccarone T. J., Kundu A., Zepf S. E., Rhode K. L., 2007, Nature, 445, 183
Mackey A. D., Wilkinson M. I., Davies M. B., Gilmore G. F., 2007, MNRAS, 379, L40
Mackey A. D., Wilkinson M. I., Davies M. B., Gilmore G. F., 2008, MNRAS, 386, 65
Madrid J. P., Leigh N. W. C., Hurley J. R., Giersz M., 2017, MNRAS, 470, 1729
Maliszewski K., Giersz M., Gondek-Rosinska D., Askar A., Hypki A., 2022, MNRAS, 514, 5879
Mapelli M., 2016, MNRAS, 459, 3432
Mapelli M., Bouffanais Y., Santoliquido F., Arca Sedda M., Artale M. C., 2022, MNRAS, 511, 5797
Massari D., Koppelman H. H., Helmi A., 2019, A&A, 630, L4
Merritt D., Piatek S., Portegies Zwart S., Hemsendorf M., 2004, ApJ, 608, L25
Miller-Jones J. C. A. et al., 2015, MNRAS, 453, 3918
Minniti D. et al., 2015, ApJ, 810, L20
Morscher M., Pattabiraman B., Rodriguez C., Rasio F. A., Umbreit S., 2015, ApJ, 800, 9
Navarro J. F., Frenk C. S., White S. D. M., 1997, ApJ, 490, 493
O'Shaughnessy R., Gerosa D., Wysocki D., 2017, in American Astronomical Society Meeting Abstracts, Vol. 230. American Astronomical Society, Washington, DC, p. 317.07
Olejak A., Belczynski K., Bulik T., Sobolewska M., 2020, A&A, 638, A94
Portegies Zwart S. F., McMillan S. L. W., 2000, ApJ, 528, L17
Portegies Zwart S. F., McMillan S. L. W., 2002a, ApJ, 576, 899
Portegies Zwart S. F., McMillan S. L. W., 2002b, ApJ, 576, 899
Portegies Zwart S. F., McMillan S. L. W., 2007, in St. -Louis N., Moffat A. F. J., eds, ASP Conf. Ser. Vol. 367, Massive Stars in Interactive Binaries. Astron. Soc. Pac., San Francisco, p. 597
Portegies Zwart S. F., Dewi J., Maccarone T., 2004, MNRAS, 355, 413
Rastello S., Mapelli M., Di Carlo U. N., Iorio G., Ballone A., Giacobbo N., Santoliquido F., Torniamenti S., 2021, MNRAS, 507, 3612
Repetto S., Igoshev A. P., Nelemans G., 2017, MNRAS, 467, 298
Rizzuto F. P. et al., 2021, MNRAS, 501, 5257
Rizzuto F. P., Naab T., Spurzem R., Arca-Sedda M., Giersz M., Ostriker J. P., Banerjee S., 2022, MNRAS, 512, 884
Roberts T. P. et al., 2012, ApJ, 760, 135
Rodriguez C. L., Loeb A., 2018, ApJ, 866, L5
Rodriguez C. L., Hafen Z., Grudić M. Y., Lamberts A., Sharma K., Faucher-Giguère C.-A., Wetzel A., 2022, preprint (arXiv:2203.16547)
Taylor M. A., Puzia T. H., Gomez M., Woodley K. A., 2015, ApJ, 805, 65
Torniamenti S., Rastello S., Mapelli M., Di Carlo U. N., Ballone A., Pasquato M., 2022, MNRAS, 517, 2953
Vasiliev E., 2019, MNRAS, 484, 2832
Vogelsberger M. et al., 2014, MNRAS, 444, 1518
Wang L. et al., 2016, MNRAS, 458, 1450
Weatherford N. C., Chatterjee S., Kremer K., Rasio F. A., 2019, preprint (arXiv:1911.09125)
Webb J. J., Leigh N. W. C., 2015, MNRAS, 453, 3278
Webb J. J., Leigh N. W. C., Singh A., Ford K. E. S., McKernan B., Bellovary J., 2018, MNRAS, 474, 3835
Zocchi A., 2015, in IAU General Assembly. Cambridge Univ. Press, Cambridge, UK, p. 2256672

APPENDIX: STATISTICAL TESTING OF THE STUDIED POPULATIONS

To ensure that the obtained results are statistically consistent with the observed distributions and to check whether the GC parameters analysed in this paper show dependence on the galactocentric distance, we used the Kolgomorov–Smirnov test (KS test).

Table A1. We carried out 'two-sample' KS tests by comparing galactocentric distributions for the number, mean mass, mean half-light radius and total BH mass of simulated MW models with an assumed uniform in galactocentric radius distribution. For all these tests, the *p*-value are reported above. For the cases were the *p*-values are larger than 0.05, the null hypothesis cannot be rejected. The results from left to right refers to the data shown in the top row of Figs 4, 5, 7, and 8, respectively.

Dynamical model	Distribution of number of GCs	Mean mass distribution	Mean half-light radius distribution	Total BH mass distribution
BHS	5×10^{-5}	5×10^{-5}	6×10^{-5}	1×10^{-11}
IMBH	5×10^{-8}	10^{-7}	10^{-8}	2×10^{-11}
Standard	5×10^{-19}	5×10^{-5}	9×10^{-6}	-

Table A2. We carried out 'two-sample' KS tests by comparing galactocentric distributions for the number, mean mass, mean half-light radius and total BH mass of simulated M31 models with an assumed uniform in galactocentric radius distribution. For all these tests, the *p*-value are reported above. For the cases were the p-values are larger than 0.05, the null hypothesis cannot be rejected. The results from left to right refers to the data shown in the bottom row of Figs 4, 5, 7, and 8, respectively.

Dynamical Model	Distribution of number of GCs	Mean mass distribution	Mean half-light radius distribution	Total BH mass distribution
BHS	2×10^{-4}	0.03	0.09	0.07
IMBH	2×10^{-5}	2×10^{-4}	2×10^{-4}	2×10^{-4}
Standard	2×10^{-5}	0.07	10^{-3}	-

Table A3. We carried out 'two-sample' KS tests by comparing galactocentric distributions for the mean mass and mean half-light radius of the BHS and IMBH models with the same distributions for the Standard models for the simulated population of GCs in MW (first two columns) and M31 (last two columns). For all these tests, the *p*-values are reported above. For the cases were the *p*-values are larger than 0.05, the null hypothesis cannot be rejected. The results refer to the data shown in Figs 5 and 7.

	MW		M31	
Dynamical Model	Mean mass distribution	Mean half-light radius distribution	Mean mass distribution	Mean half-light radius distribution
BHS	0.08	0.01	7×10^{-7}	7×10^{-7}
IMBH	0.1	4×10^{-3}	0.5	7×10^{-3}

The underlying continuous distributions of two separate samples are compared in the KS test. In particular, the 'two-sample' KS test is used to determine if two samples come from the same distribution. The KS test measures the distance between the two cumulative distribution functions (CDFs) of the two samples. For the 'two-sample', the null hypothesis is that the two samples are drawn from the same distribution. For the KS tests carried out in this work, the null hypothesis is rejected for $p < 0.05$.

The KS test was first applied to compare the observed distributions of the pericenter distance, orbital eccentricity, and circular orbit distance for the MW GC population with the results from our simulations. The p-values for the 'two-sample' KS tests are 0.06 for the orbital eccentricity, 0.15 for the pericenter distance, and 0.05 for the circular orbit distance distribution, respectively. This comparison shows that our sampled models are marginally consistent with the observed distribution of orbital properties of MW clusters. The results refer to the data shown in Figs 1–3.

To verify that the GC property distributions obtained in our models show some dependence on the galactocentric distance we applied the KS test. We compared the galactocentric distance dependence of total number of GCs, mean GC mass, mean GC half-light radius, and total BH mass for different GC dynamic models (GC that includes a BHS, IMBH or neither of those) with a uniform galactocentric distance distribution. For each set of simulation data, we carried out the 'two-sample' KS test against the null hypothesis that the cluster property has a uniform distribution in the galactocentric distance. In Tables A1 and A2, we report the *p*-values from the 'two-sample' KS tests for MW and M31, respectively. For MW, we find that the *p*-values returned from the 'two-sample' KS tests for galactocentric radius distributions of all properties for all types of cluster models are less than 0.05. This indicates that the galactocentric radius distributions of properties of these models are not consistent with a uniform distribution. Additionally, for distributions of the mean mass for the Standard models and the mean half-light radius and total BH mass for the BHS models for M31 clusters, the obtained *p*-values were greater than 0.05. For these cases, the galactocentric radius distribution of properties is consistent with a uniform distribution. For the other properties of M31 models, we found *p*-values lower than 0.05. This suggests that for these properties, our simulated distributions are not consistent with a uniform galactocentric distance distribution. The results reported in Table A1 refers to our results shown in the top row of Figs 4, 5, 7, and 8. Similarly, the results reported in Table A2 refer to our results shown in the bottom row of the same figures.

Furthermore, we have applied the KS test to verify that the relative shape in dependence on galactocentric distance for different types of GC evolution scenario shown in Figs 7 and 8 are statistically meaningful for the mean mass distribution and the half-light radius distribution. For this study, we took as representative the distributions for the Standard model, and we compared it against the BHS and IMBH ones. The *p*-values for the 'two-sample' KS tests are reported in Table A3. For the mean mass distribution for both BHS and IMBH models in MW, and for the mean mass distribution for IMBH in M31 the distributions are comparable to the Standard models ($p > 0.05$ for these tests). Instead, statistically significant differences from the distribution of Standard model properties have been found for the distribution of the half-light radius for both BHS and IMBH models

in both MW and M31, and for the mean mass distribution for BHS models in M31, respectively. This suggests that for the latter cases, the considered simulated distributions are not consistent with the Standard model distributions.

Finally, we applied a KS test for the spatial distribution of the mean values in radial bins for the semimajor axis, eccentricity and mass ratio for non-merging BBHs, comparing them with a uniform distribution in galactocentric distances. The *p*-values for the 'two-sample' KS test are 5×10^{-5} for the orbital eccentricity, 10^{-9} for the mass ratio, and 10^{-5} for the semimajor axis distribution, respectively. As it is possible to note, there are statistical differences for all properties. This suggests that for these cases, our simulated distributions are not consistent with a uniform galactocentric distance distribution. These results refer to the data shown in Fig. 14, from left to right, respectively.

This paper has been typeset from a TEX/LATEX file prepared by the author.

Chapter 5

Embedded gas phase evolution in MOCCA code

Monthly Notices of the ROYAL ASTRONOMICAL SOCIETY

MNRAS **514,** 5739–5750 (2022) https://doi.org/10.1093/mnras/stac1690
Advance Access publication 2022 June 17

A Monte Carlo study of early gas expulsion and evolution of star clusters: new simulations with the MOCCA code in the AMUSE framework

A. Leveque [1]★ M. Giersz [1] S. Banerjee [2,3] E. Vesperini,[4] J. Hong[5,6] and S. Portegies Zwart[7]

[1]*Nicolaus Copernicus Astronomical Center, Polish Academy of Sciences, ul. Bartycka 18, PL-00-716 Warsaw, Poland*
[2]*Helmholtz-Instituts für Strahlen- und Kernphysik (HISKP), Nussallee 14-16, D-53115 Bonn, Germany*
[3]*Argelander-Institut für Astronomie (AIfA), Auf demügel 71, D-53121, Bonn, Germany*
[4]*Department of Astronomy, Indiana University, Swain West, 727 E. 3rd Street, Bloomington, IN 47405, USA*
[5]*Department of Astronomy, Yonsei University 50 Yonsei-Ro, Seodaemun-Gu, Seoul 03722, Republic of Korea*
[6]*Korea Astronomy and Space Science Institute, Daejeon 34055, Republic of Korea*
[7]*Leiden Observatory, Leiden University, PO Box 9513, NL-2300 RA, Leiden, The Netherlands*

Accepted 2022 June 10. Received 2022 June 7; in original form 2022 January 19

ABSTRACT

We introduce a new prescription for the evolution of globular clusters (GCs) during the initial embedded gas phase into a Monte Carlo method. With a simplified version of the Monte Carlo MOCCA code embedded in the AMUSE framework, we study the survival of GCs after the removal of primordial gas. We first test our code and show that our results for the evolution of mass and Lagrangian radii are in good agreement with those obtained with N-body simulations. The Monte Carlo code enables a more rapid exploration of the evolution of systems with a larger number of stars than N-body simulations. We have carried out a new survey of simulations to explore the evolution of globular clusters with up to $N = 500\,000$ stars for a range of different star formation efficiencies and half-mass radii. Our study shows the range of initial conditions leading to the clusters' dissolution and those for which the clusters can survive this early evolutionary phase.

Key words: galaxies: star clusters: general – methods: numerical.

1 INTRODUCTION

Globular clusters (GCs) form through the gravitational collapse of giant molecular clouds (Lada & Lada 2003; Longmore et al. 2014). Newborn clusters are then supposed to be embedded in the leftover gas. The star formation efficiency (SFE), defined as $\epsilon = M_{\rm cl}/(M_{\rm cl} + M_{\rm gas})$, with $M_{\rm cl}$ as the GC star mass and $M_{\rm gas}$ being the embedded gas mass, represents the fraction of gas that is converted into stars.

The ultraviolet (UV) radiation of massive stars and their stellar winds and supernova explosions can lead to the expulsion of primordial gas. Indeed, the UV radiation ionizes the gas, leading to efficient coupling of the stellar radiation (Hills 1980; Krumholz & Matzner 2009), and then to the unbinding and removal of the gas from the cluster. The radiative gas expulsion can be faster than the crossing time of the embedded gas, taking place at the sound speed for ionized hydrogen, that is $\sim 10\,{\rm km\,s^{-1}}$ (Kroupa, Aarseth & Hurley 2001a; Banerjee & Kroupa 2013). The cluster would then expand over its dynamical time-scale. This can be crucial for the survival of the system, which may possibly be dissolved. Different studies have been conducted in order to understand and estimate the importance of the gas expulsion, together with the response of the embedded star cluster (Lada, Margulis & Dearborn 1984; Adams 2000; Geyer & Burkert 2001; Bastian & Goodwin 2006; Baumgardt & Kroupa 2007; Pelupessy & Portegies Zwart 2012; Banerjee & Kroupa 2013, 2014, 2018; Lewis et al. 2021). Due to the gas removal phase and its consequential mass loss, the surviving cluster will have a final half-mass radius, $R_{\rm h}$, 3 or 4 times larger than its initial value (Lada et al. 1984; Baumgardt & Kroupa 2007). In general, the expansion process and final half-mass radius value depend on several factors, e.g. SFE, gas and star density profiles, and gas expulsion time-scale.

Due to the small time-scale of the embedded gas phase ($\sim 1-2\,{\rm Myr}$) and the small time-scale of gas expulsion ($\sim 0.1\,{\rm Myr}$), previous studies have been carried out with NBODY codes only, because they properly account for fast global changes in the potential during the gas removal and violent relaxation phases. In this paper, we introduced and studied the embedded gas removal phase with a Monte Carlo-based code. Due to the computational requirements, N-body simulations are limited to small N, with dense star clusters of millions of stars being a computational challenge (Makino et al. 2003; Gaburov, Harfst & Portegies Zwart 2009; Heggie 2014; Wang et al. 2016). On the other hand, large N and dense clusters can be simulated using a Monte Carlo code. Indeed, a great advantage of the Monte Carlo method is that it provides detailed and fast dynamical evolution of GCs (Giersz 1998; and references therein Joshi, Rasio & Portegies Zwart 2000; Rodriguez et al. 2021; Giersz et al. 2013, 2019)

With a simplified version of the MOCCA code (Hypki & Giersz 2013), in Astrophysical Multipurpose Software Environment (AMUSE) (Portegies Zwart et al. 2009, 2013; Pelupessy et al. 2013; Portegies Zwart & McMillan 2018) framework, we performed a preliminary study on the importance of the embedded gas phase to the survival of the cluster, even for large number of particles.

Our paper is organized as follows: In Section 2 and in Section 3, we introduce the methodology used in this study. In Section 4, we

★ E-mail: agostino@camk.edu.pl

present the main results, and in Section 5, we finally present our discussion and conclusions. In Appendix A, we describe the new updated version of the McLuster code used in this paper to generate the initial conditions for the studied models.

2 METHODS

In this paper, we present a simplified version of the MOCCA code (Giersz 1998; Hypki & Giersz 2013). The MOCCA code simulates and follows the long-term dynamical evolution of spherically symmetric stellar clusters, based on Hénon's Monte Carlo method (and references therein for details about MOCCA code Hénon 1971; Stodolkiewicz 1982, 1986; Giersz et al. 2013), together with stellar and binary evolution and strong interactions. In the original version of the code, prescriptions from the SSE/BSE codes (Hurley, Pols & Tout 2000; Hurley, Tout & Pols 2002) are used to follow stellar and binary evolutions, whereas the FEWBODY code (Fregeau et al. 2004) handles the strong interactions (binary–binary and binary–single). Finally, escaping stars from tidally limited clusters are treated as described in Fukushige & Heggie (2000).

However, in the version presented in this paper, named MOCCA-C, only the relaxation process has been included (Hénon 1971), and the part of the MOCCA code related to the relaxation process was translated from Fortran to C language. This version is specially designed to be easily integrated into the AMUSE[1] (Pelupessy et al. 2013; Portegies Zwart et al. 2009, 2013; Portegies Zwart & McMillan 2018).

AMUSE provides a large set of simulation codes and a uniform interface for different kinds of simulations. Indeed, the philosophy within AMUSE is to divide a multiphysics problem into single physical domains, with a specific module that is responsible for the evolution of the system state within its physical domain. The AMUSE environment can communicate between the specific codes through interfaces. This means that the codes used are interchangeable. In this study, the stellar evolution is handled by the SSE (Hurley et al. 2000) version present in the AMUSE environment, whereas the relaxation is handled by the MOCCA-C code. For simplicity and for purpose of testing the new code, the dynamical interactions among stars (binary formations, 3- and 4-body interactions and collisions) have not been implemented in this work.

The system's initial conditions, i.e. positions and velocities for stars, have to be produced outside of MOCCA-C code. This can be done using the AMUSE initial condition procedure or an external code, such as McLuster (Küpper et al. 2011). In the AMUSE framework, stars are represented by AMUSE particles, and they can be handled (added, removed, and evolved) thanks to the AMUSE interfaces.

2.1 MOCCA-C

The MOCCA-C code contains the relaxation component of the original MOCCA code. The system is first divided in zones and superzones (Stodolkiewicz 1982, 1986), to better represent the relaxation process in different parts of the system (central zones are more frequently relaxed than outer zones - each superzone has its own time step, which increases by a factor of two for each successive superzone); in turn, the relaxation process and new position procedure are applied to all stars in the system (Hénon 1971). The computation of a complete time-step is divided into different cycles according to the number of superzones. For each of those cycles, the new positions for each star in the superzones are computed. The determination of changes of the system structure due to changes of the mass distribution (Stodolkiewicz 1982) is applied when the position for all objects in the superzone has been calculated. Finally, stars are removed from the system according to the escape criteria. The current version of the code does not include binaries, so only single stars are considered.

The effect of relaxation in the time interval is mimicked by consecutive encounters between two neighbour stars, with an exchange of energy and angular momentum, as described in (Hénon 1971; Stodolkiewicz 1982, 1986). The new stars' positions are selected randomly between $r_{\rm min}$ and $r_{\rm max}$, with $r_{\rm min}$ being the star's orbit pericentre and $r_{\rm max}$ being the smallest value between the star's orbit apocentre and the outermost radius of the superzone, with probability inversely proportional to the radial velocity $v_{\rm r}$ at each orbit position. For the outermost superzone in the system, $r_{\rm max}$ is the smallest value between the apocentre distance and the limiting radius ($r_{\rm limit}$), which is set to twice the escape radius ($r_{\rm escape}$). The procedure used to randomly determine the new position is described in Hénon (1971).

Similarly to the standard definitions in NBODY7 code and other versions of these codes (Aarseth 2012), the escape radius is set to twice the tidal radius ($r_{\rm tidal}$) for tidally limited clusters and to 10 times the actual $R_{\rm h}$ for isolated clusters. Alternatively, the escape criteria can be selected from among the following:

(i) distant escape criterion: stars are removed only if their positions are greater than $r_{\rm escape}$;
(ii) tidally limited clusters: the removal of bound stars with energy greater than $E_{\rm crit}$ (tidal binding energy) is not instantaneous, but time delayed. The probability of escape is computed according to the prescription given in Fukushige & Heggie (2000).

In MOCCA-C, the stars' orbits are determined from the potential at the beginning of each time step, meanwhile, the velocities are estimated at the end, that is after the relaxation step and the new position determination. This inconsistency will lead to a small energy flow. Indeed, the kinetic energy of the stars is altered by the time dependence of the potential, caused by sudden changes of the stars' positions inside the system. The kinetic energy corrections are calculated and applied according to the prescription given in Stodolkiewicz (1982). This procedure will be referred to hereinafter as kinetic energy adjustments due to potential changes in time.

3 INITIAL GAS CONDITIONS AND GAS EXPULSION

The complex physical processes involved in the hydrodynamics of gas-removal from an embedded cluster make it difficult to obtain a detailed time evolution of the gas dispersal. In past works, a simplistic analytic representation for the gas expulsion has been used, and the same representation has been used in this work.

The gas is treated as an external potential to the system (Lada et al. 1984; Kroupa, Aarseth & Hurley 2001b; Banerjee & Kroupa 2013, 2014, 2018, and reference therein). The cluster (stars and gas) has been modelled with a Plummer distribution (Plummer 1911) for stars, embedded in a spherically symmetric external potential generated by the initial gas. Even though the spatial distribution of gas particles can be different from that of stars, in this work we used the same distributions for both gas and stars. The study for different spatial distributions between the gas and stars, as in Shukirgaliyev et al. (2017) and Shukirgaliyev et al. (2021), will be conducted in the future.

[1] https://amusecode.github.io/

The gas expulsion has been modelled with an exponential decaying function (Banerjee & Kroupa 2013),

$$M_{\rm g}(t) = \begin{cases} M_{\rm g}(0), & \text{if } t \leq \tau_{\rm delay} \\ M_{\rm g}(0)\ \exp\left(-\frac{t-\tau_{\rm delay}}{\tau_{\rm g}}\right) & \text{if } t > \tau_{\rm delay}, \end{cases} \quad (1)$$

where $M_{\rm g}(0)$ is the initial mass of the gas, $\tau_{\rm g}$ is the time-scale for gas removal, and $\tau_{\rm delay}$ is the delay time for gas removal. The time-scale of gas expulsion is simply given by $\tau_{\rm g} = R_{\rm h}(0)/v_{\rm g}$, with $R_{\rm h}(0)$ as the initial half-mass radius of the system, and $v_{\rm g}$ being the sound speed with which gas expands and becomes removed. The value of $v_{\rm g} \approx 10\,{\rm km\,s^{-1}}$, the typical sound speed in an ionized hydrogen region, has been used in this paper (more details can be found in Banerjee & Kroupa 2013, 2018). The initial total gas mass has been given by

$$M_g(0) = M_{\rm cl}(0)\ \left(\frac{1}{\epsilon} - 1\right),$$

with $M_{\rm cl}(0)$ as the initial total mass of the stars, and ϵ as the SFE. The total number of gas particles was set to be the same as the number of stars. For our test models, a value of $\epsilon = 0.333$ has been used (Banerjee & Kroupa 2018). The gas evolution and expulsion has been treated in the AMUSE environment. During the gas expulsion phase, the gas particles are treated as point mass particles, with mass evolution described by equation (1). During this evolution, the gas particles' positions are not changed. In future works, the spatial evolution of the gas particles will be included. Finally, the gas and stars' potential have been determined separately during the gas expulsion phase. The potential associated with the gas particles has been interpolated at the stars' positions, taking into account the time evolution of the mass of the gas particles. This contribution has been added to the stars' potentials, determined from the total stars' mass interior to the stars' positions, that is

$$u_{{\rm star},i} = -G\left(\frac{M_{{\rm star},i}}{r_{{\rm star},i}} + \sum_{k=i+1}^{N}\frac{m_{{\rm star},k}}{r_{{\rm star},k}}\right),$$

where G is the gravitational constant, $u_{{\rm star},\,i}$ and $r_{{\rm star},\,i}$ are the ith star's potential and position, and $M_{{\rm star,\,i}}$ is the total stars' mass interior to $r_{{\rm star},\,i}$.

3.1 Star cluster evolution phases

The time evolution of an embedded cluster can be divided into three phases: gas expulsion, violent relaxation, and evolution governed by the relaxation process. In the following, we will describe the evolution schemes used for each phase.

3.1.1 Gas expulsion phase

The gas expulsion happens on very short time-scales. For example, for $R_{\rm h} = 1\,{\rm pc}$, $\tau_{\rm g} = 0.1\,{\rm Myr}$ (assuming $v_{\rm g} = 10\,{\rm km\,s^{-1}}$). In order to get reasonable resolution for this phase, the time step was set to be about 10 times smaller than $\tau_{\rm g}$. At the beginning of each time step, the total mass and potential energy of gas has been updated according to equation (1). Due to the very small time step, the system has been divided into only one superzone. Successively, the new positions and then the new potential for each star is calculated. Stars whose energy $E > 0$, are treated as unbound, and the procedure used to find their position will be described in 3.2. Instead, since for bound stars the time step is much shorter than the crossing time, a proper sampling of the orbit is not possible according to the physical principles behind the Monte Carlo method. For this reason, during this phase, the relaxation process has been switched off (kinetic energy between stars is not exchanged). Similarly, no kinetic energy adjustments due to potential changes in time have been applied (as explained at the end of Section 2.1). The changes of the potential due to gas removal are dominant.

The new positions for bound stars are picked randomly by sampling the orbit. However, the procedure to calculate the bound star's movement along their orbits cannot properly respond to very fast potential changes due to gas expulsion. For stars with energy slightly smaller than zero, the apocenter distance can be very large, implying that the new position can be picked further than the distance the star can travel in the time step. Not taking this into account would lead to the too fast escaping of stars and dissolving of the system. To solve this problem, the maximum distance r_{max} a star can reach is increased at each time step according to the distance the star can travel during the time step dt, that is

$$r_{{\rm max};i,n+1} = r_{{\rm max};i,n} + v_{{\rm r},n} \cdot {\rm d}t, \quad (2)$$

where $r_{{\rm max};\,i,\,n}$ is the maximum distance allowed for the i-th star at time step n, $v_{{\rm r},n}$ is the radial velocity of the star, and $r_{{\rm max};\,i,\,0} = v_{r,\,0} \cdot {\rm d}t$. This procedure can lead to an artificial delay in the system expansion, since the new position will be always smaller than $r_{\rm max}$. Again, the probability of picking a random position in the bound orbit in a time-step is inversely proportional to the radial velocity $v_{\rm r}$.

The gas expulsion phase time-scale is determined by $\tau_{\rm g}$, and it is, in general, shorter than 1 Myr. Moreover, a pre-gas expulsion phase can be added by setting a value for $\tau_{\rm delay}$ different from zero. During this phase, the model is evolved according to the procedure described above, with a time step of $\tau_{\rm delay}/2.0$. This time-step has been chosen only from technical reasons to have a minimum time resolution of this phase. For the chosen value of $\tau_{\rm g}$ and the initial cluster parameters used in this work, the pre-gas and gas expulsion phases are in general short compared to the mass segregation time-scale. For this reason, we assumed that the effects of two-body relaxation are negligible over this time-scale. This assumption should not strongly influence the model evolution.

3.1.2 Violent relaxation phase

Just after the end of the gas expulsion phase, the system experiences a violent relaxation phase, which brings the system to equilibrium. Indeed, after an early phase during which the half-mass radius oscillates, $R_{\rm h}$ will eventually settle to an equilibrium value equal to roughly four times the initial half-mass radius (for $SFE = 0.333$; Lada et al. 1984). The time needed for the system to adjust is directly proportional to the half-mass radius crossing time ($t_{{\rm cross,\,Rh}} = 2 \times R_{\rm h}/\sigma_{\rm Rh}$, with $\sigma_{\rm Rh}$ being the velocity dispersion at $R_{\rm h}$) at the system's maximum extension, which is satisfied at the end of the gas expulsion phase. According to Lynden-Bell (1967), the time duration of the violent relaxation phase is on the order of a few orbital periods. A value of four times the $t_{{\rm cross,\,Rh}}$ at the end of the gas expulsion phase was assumed in this work.

The time step during the violent relaxation phase was on the order of 0.2 Myr. As for the gas expulsion phase, the time step is too small for a proper orbit sample. For this reason, the same treatment described above has been applied, with the system being divided into only one superzone. Both, the relaxation process and the kinetic energy adjustments due to potential changes in time have been switched off during this phase too. Also, the determination of the maximum distance a star can reach as described in equation (2) has been imposed when determining the new star position. Because of the relatively long time span of this phase, the lack of relaxation

and mass segregation in this phase can have an impact on the system expansion and the spatial structure of the innermost region of the cluster. This can be important for more compact GCs. In future work, we plan to introduce relaxation processes during this phase and explore their effects, which can be particularly important for very massive stars.

3.1.3 Relaxation

When the violent relaxation phase has ended, the standard Monte Carlo procedure is applied, as described in Section 2.1. The time step used in this phase can be ≥ 1.0 Myr. To properly account for the cluster mass distribution, the system is divided into at least three superzones.

3.2 Unbound stars

In the MOCCA code, stars with binding energy $E > 0$ are removed immediately. This escape criteria is correct only when the time-scale to travel across the system is smaller than the overall model time step (usually around 2–5 Myr), so that stars actually have time to travel the system and be expelled during this time step.

In contrast, during the gas expulsion and violent relaxation phase, the time step is too small, and the escaping stars do not have enough time to travel outside the system within the time step. This will lead to some inconsistencies because the system would too quickly remove escaping stars that would not actually reach the escape radius distance. So the total number of stars bound to the system would decrease faster. Accordingly, the tidal radius would also decrease, resulting in smaller Lagrangian radii and finally faster cluster dissolution.

For this reason, stars with $E > 0$ are not immediately removed. Instead, new positions and velocities for such stars are calculated by an approximated orbit integration. In this treatment, it is assumed that an unbound object can move outward and only radially, i.e. $r_{i,\,n+1} = r_{i,\,n} + |v_{\rm r}| \cdot {\rm d}t$, with $v_{\rm r} = v$ and v being the total velocity of the object. From energy conservation $E_{i,\,n+1} = E_{i,\,n}$, we obtain the radial velocity at the end of the time step, $v_{{\rm r},n+1} = \sqrt{2.0 \cdot E_{i,n} - 2.0 \cdot u_{i,n+1}}$, with $u_{i,\,n+1}$ giving the potential of the star at position $r_{i,\,n+1}$.

This procedure has been applied for the entire simulation (through all different phases). It is important to underline that unbound stars are also considered in the changes in energy and angular momentum estimations during the relaxation process, but they are not taken into account during the kinetic energy adjustments due to potential changes in time. The unbound stars do actually move for small distances in the system during one time step, and the potential changes are not important compared to changes introduced by the relaxation process.

3.3 Pros and cons of the gas expulsion treatment

The gas removal phase and the following violent relaxation phase have been introduced for the first time in the MOCCA code. The procedure of gas expulsion described in this paper was based on a few assumptions that may lead to differences when compared to N-body results for the two initial phases. The movement of bound and unbound stars in the system has been adjusted in order to handle the small cluster evolution time-steps used during those phases. Additionally, the procedure used for the unbound stars' movement is simplistic, lacking proper orbit integration. The lack of primordial and dynamically formed binaries, together with old-fashioned stellar evolution, can lead to slower mass loss and system expansion. The lack of relaxation and mass segregation during the initial phases (particularly during the violent relaxation phase), as explained before, can lead to a slightly slower system expansion and core-collapse. Summing up all those simplifications can lead to some differences in the Lagrangian radii, particularly for the outermost and innermost ones.

We focused our attention on the spatial structure and mass of the cluster after the violent relaxation and aimed at obtaining results matching as closely as possible those from N-body simulations. In this way, we can assume that the final and longest phase of the cluster evolution we simulate will follow the evolution of star cluster in the same way as N-body simulations.

4 SIMULATIONS AND RESULTS

To test our code, a comparison with N-body simulations is needed. For this purpose, we run two different sets of simulations: the first one, a training test, consists of 4 simulations that have been run with NBODY7 (Aarseth 2012); alternatively, in the second set, we try to reproduce the results shown in Banerjee & Kroupa (2013).

The initial conditions have been generated using a newly updated version[2] of the McLuster code[3] (Küpper et al. 2011). For more details, see Appendix A.

4.1 Comparison with new N-body simulations

The training test consists of four simulations with two different numbers of particles $N = [100\,000, 200\,000]$ and two initial half-mass radii $R_{\rm h} = [0.5, 1.0]$ pc. The positions and velocities of stars for each model were selected according to the Plummer model (Plummer 1911). The Kroupa (2001) initial mass function (IMF) ranging from 0.08 to 100 $\rm M_{\odot}$ was applied. For all those models, no primordial binaries were included. The models were run up to 50 Myr. The escape criteria radius $r_{\rm escape}$ was set to a constant value of 100 pc (with $r_{\rm limit}$ set to 50 pc). The gas expulsion time-scales have been set to $\tau_{\rm g} = 0.05$ and 0.1 Myr for models with $R_{\rm h} = 0.5$ and 1.0 pc, respectively. The time delay for gas expulsion was set to 0.1 Myr for all models.

The Lagrangian radii, the evolution of the total mass and of the total number of objects for two of the models are reported in Figs 1 and 2. The other two models show similar evolution. The gas expulsion phase for the model reported in Fig. 1 ended at 0.58 Myr and the violent relaxation phase at ∼6 Myr. Instead, for the model reported in Fig. 2, the gas expulsion phase ended at 0.34 Myr, and the violent relaxation phase at ∼5 Myr. One can clearly see that our prescription can reasonably well reproduce the N-body results, with some differences in the outermost Lagrangian radii, and innermost Lagrangian radii for the model with initial $R_{\rm h} = 0.5$ pc. To quantify the differences between the MOCCA-C and N-Body results for the Lagrangian radii, the total mass, and the total number of bound objects, we integrate the areas below the individual curves for each quantity and calculate the ratio of the difference between these areas to the area under the line for the N-body simulations. The differences shown in Fig. 1 are of the order of 15 per cent, 17 per cent, 20 per cent and 11 per cent for 1 per cent, 10 per cent, 50 per cent, and 75 per cent Lagrangian radii, respectively, at the end of gas expulsion phase, and

[2]The updated version of the code can be found in Github: https://github.com/agostinolev/mcluster.
[3]The original version of McLuster can be found at https://github.com/ahwkuepper/mcluster.

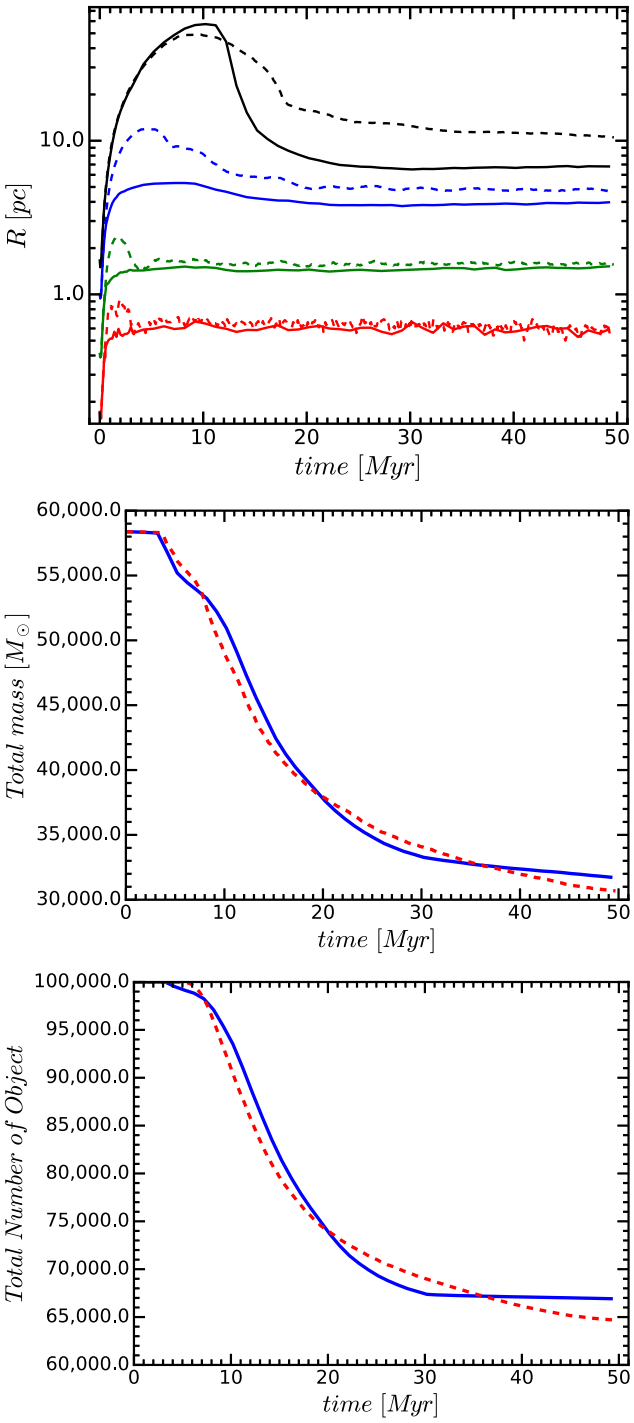

Figure 1. Lagrangian radii (top panel), total mass (middle panel) and total number of bound objects (bottom panel) evolution for the simulation with $N =$ 100 000 and $R_{\rm h} = 1.0$ pc. The continuous and dashed lines correspond to the MOCCA-C and N-body results, respectively. In the upper figure, the curves, from bottom to top, correspond to 1 per cent, 10 per cent, 50 per cent, and 75 per cent Lagrangian radii evolution.The gas expulsion phase for this model ended at 0.58 Myr, while the violent relaxation phase ended at ∼6.0 Myr.

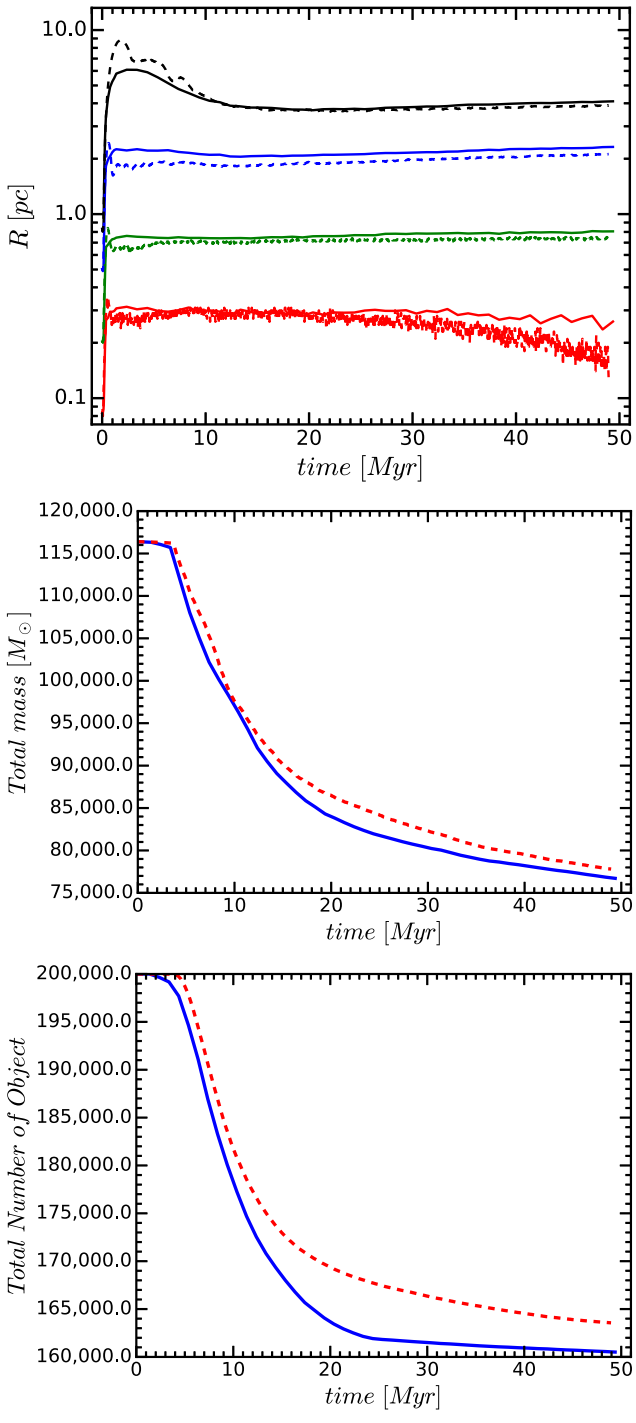

Figure 2. Lagrangian radii (top panel), total mass (middle panel) and total number of bound objects (bottom panel) evolution for the simulation with $N =$ 200 000 and $R_{\rm h} = 0.5$ pc. The continuous and dashed lines correspond to the MOCCA-C and N-body results, respectively. In the upper figure, the curves, from bottom to top, correspond to 1 per cent, 1 per cent0, 50 per cent, and 75 per cent Lagrangian radii evolution. The gas expulsion phase for this model ended at 0.34 Myr, while the violent relaxation phase ended at ∼5.0 Myr.

of the order of 4 per cent, 4 per cent, 18 per cent, and 56 per cent at the end of the simulation. The differences in mass and in total number of bound objects are both of the order of 1 per cent at the end of gas expulsion phase, and of 3 per cent at the end of the simulation. A better comparison is shown in Fig. 2. The differences for the 1 per cent, 10 per cent, 50 per cent, and 75 per cent Lagrangian radii at the end of gas expulsion phase are of the order of 11 per cent, 9 per cent, 4 per cent, and 9 per cent, respectively, with values of 25 per cent, 9 per cent, 9 per cent, and 5 per cent, respectively, at the end of the simulation. The differences in mass and in total number of bound objects are both of the order of 1 per cent at the end of gas expulsion phase, and of 1–2 per cent at the end of the simulation. The evolution of the total mass and total number of bound objects is reproduced reasonably well, with an important part of the mass loss being connected to the number of stars escaping the system.

Those differences can be explained by differences present in the cluster structure connected to the approximate treatment of the star movement and relaxation process. The differences seen in the outermost region of Fig. 1 are related to the approximate treatment for the unbound stars that leads to an important mass loss. Instead, the differences in Fig. 2 are important in the central region of the system. In this case, the lack of the formation of binaries is responsible for causing our model to have a delayed core collapsed when compared to the N-body simulation. Also, during the violent relaxation phase, the energy exchange among stars can be important and induce mass segregation in the N-body simulation that is instead absent in the MOCCA simulation since the effects of relaxation are not included in this phase. Furthermore, the differences in the stellar evolution prescription may play some role in those dissimilarities: in the current version of MOCCA-C, we use the older version of the stellar evolution prescription from Hurley et al. (2000) and Hurley et al. (2000), while the NBODY prescription already includes the most up-to-date, similar to the Level C in Kamlah et al. (2021). Mass loss due to stellar evolution for the same models with the old and new stellar evolution prescriptions is about 14 per cent and 17 per cent, respectively. Likewise, the average BH masses are 20.9 and 25.6 $M_\odot$, for the old and new stellar evolution prescriptions, respectively. Consequently, larger mass loss will lead to a larger cluster expansion (i.e. larger Lagrangian radii, particularly for the outermost ones) in the models with the new stellar evolution. On the other hand, the larger BH masses found in the models with the new stellar evolution will lead to a more rapid evolution towards core-collapse and denser systems. Due to the strong initial cluster expansion, the binary formation efficiency is relatively low, with only 1 or 2 binaries formed during the simulated time span in the N-body simulations.

4.2 Comparison with previous works

As a second comparison, we tried to reproduce the results shown in Banerjee & Kroupa (2013). In that paper, only the initial few *Myr* for the GC R136 and NGC 3603 were simulated. The initial total masses for those models were $M_{\rm cl}\,(0) = 10^5\,M_\odot$ and $M_{\rm cl}\,(0) = 1.3 \times 10^3\,M_\odot$, respectively. The initial half-mass radius followed the Marks & Kroupa (2012) relationship, giving $R_{\rm h} = 0.45$ and 0.34 pc, respectively. For these simulations, we adopt the same escape criterion used in Banerjee & Kroupa (2013) and set the escape radius equal to 10 times the current half-mass radius value. The Kroupa (2001) IMF was used, with the most massive stars set according to the Weidner & Kroupa (2004) relationship.

In our simulations, we used the Kroupa (2001) IMF, with a minimum mass of 0.08 $M_\odot$ and a maximum mass of 150 and 50 $M_\odot$, for GC R136 and NGC 3603, respectively. In order to reproduce the initial total mass for those clusters, an initial total number of stars of 170 000 and 22 000 were used, respectively. The statistical fluctuations for the low-N MOCCA-C models can introduce substantial noise in the global system parameters determination. To reduce the noise, each simulation has been repeated 20 times with a different random seed. All relevant quantities for the model evolution have been computed from the mean of the 20 models. The time delay for gas expulsion was set to 0.0 and 0.6 Myr for NGC 3603 and R136, respectively.

The time evolution of the Lagrangian radii for R136 and NGC 3603 are reported in Figs 3 and 4, respectively. Despite the small time-steps and the short evolution, the system expansion is relatively well accounted for, at least for the R136 model. For NGC 3603, the too

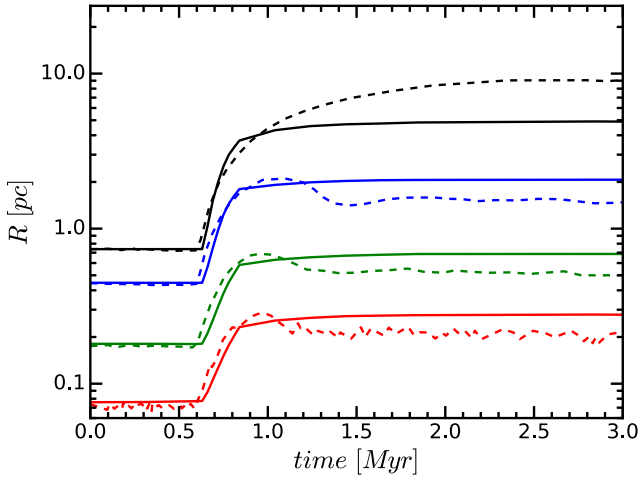

Figure 3. Lagrangian radii evolution for N-body in dashed lines and MOCCA-C in continuous lines for the model with $M_{\rm cl}\,(0) = 1.0 \cdot 10^5\,M_\odot$, and $N(0) = 170\,000$ (the model for R136). The curves, from bottom to top, correspond to 1 per cent, 10 per cent, 50 per cent, and 75 per cent Lagrangian radii evolution. The N-body model is from fig. 1 of Banerjee & Kroupa (2013).

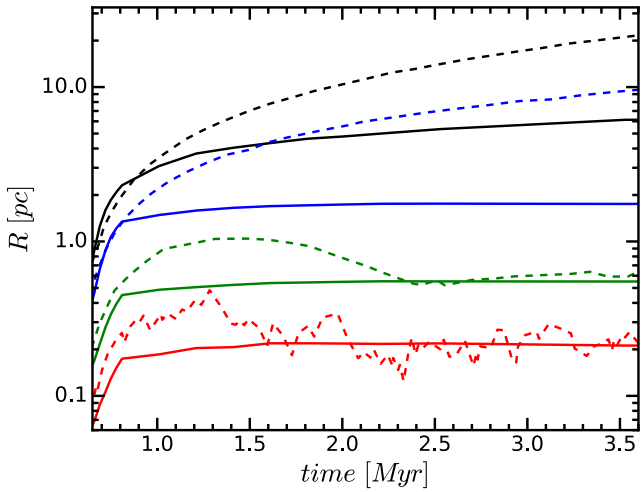

Figure 4. Lagrangian radii evolution for N-body in dashed lines and MOCCA-C in continuous lines for the model with $M_{\rm cl}\,(0) = 1.3 \cdot 10^3\,M_\odot$, and $N(0) = 22\,000$ (the model for NGC 3603). The curves, from bottom to top, correspond to 1 per cent, 10 per cent, 50 per cent, and 75 per cent Lagrangian radii evolution. The N-body model is from fig. 4 of Banerjee & Kroupa (2013).

low number of objects, being at the limit of the Monte Carlo method, introduces important statistical fluctuations. Indeed, for small N, the treatment of unbound objects is probably too simplified and leads to observed differences for larger Lagrangian radii. As for the training set, small differences in the innermost radii are visible. The duration of the gas expulsion and violent relaxation can be relatively long, up to several Myr, and during that time, the massive stars can exchange energy and angular momentum. This will lead to some mass segregation (as seen in N-body simulations), despite the fact that violent relaxation does not depend on stellar mass. On the other hand, the lack of mass segregation in our treatment can lead to a smaller system expansion. Finally, the different starting point shown in Fig. 4 for smaller Lagrangian radii is because the initial time starts at 0.6 Myr (the time of gas expulsion), following the original figure from Banerjee & Kroupa (2013). Using the same procedure described above for Figs 1 and 2, we determined the differences between the MOCCA-C and N-Body results. Our results for R136 differ by 20 per cent, 23 per cent, 27 per cent, and 77 per cent for 1 per cent, 10 per cent, 50 per cent, and 75 per cent Lagrangian radii, respectively; instead, the results for NGC 3603 differ by $\sim$ 5 per cent for 1 per cent and 10 per cent Lagrangian radii, and are 3 and 2 times smaller compared to the N-Body results for 50 per cent and 75 per cent Lagrangian radii, respectively. These values are relatively large since these simulations span a limited time range, including only the gas expulsion phase and the beginning of the violent relaxation phase; as shown in Figs 1 and 2, these are the phases when the differences between the MOCCA and the NBODY simulations are larger.

Despite some of the physical simplifying assumptions adopted in the Monte Carlo procedure, our results show that there is a general satisfactory agreement between the MOCCA-C and N-body simulations and that the Monte Carlo simulations are able to capture the main aspects of these early evolutionary phases.

4.3 MOCCA-C models of large-N clusters

The main advantage of MOCCA over NBODY is in its ability to model systems with large N much more rapidly while still producing reliable results (Giersz et al. 2013; Wang et al. 2016; Kamlah et al. 2021). Indeed, at most several hours were needed to run the models presented in Section 4.1, in contrast to the roughly two weeks needed for NBODY7 to run the same models. MOCCA simulations thus allow to extend the study of the evolution of clusters with large N during the gas expulsion phase. We present here the results of a set of simulations for models following the same prescription for gas removal adopted in the previous section. For the test simulations, which show the correct operation of the code and its effectiveness, we chose Plummer models with $N = 5 \times 10^5$ objects, $R_{\rm h} = 0.5,\ 1.0,\ 3.0,\ 6.0$ pc. The $R_{\rm h}$ has been chosen so that the first two models are tidally underfilling, the third one is tidally filling at the end of the gas expulsion, and the last model to be nearly initially tidally filling. The gas expulsion time-scales $\tau_{\rm g}$ have been set to 0.05, 0.1, 0.3, and 0.6 Myr, and the time delay for gas expulsion was set to 0.1 Myr. The tidal radius was set to 60.0 pc. The IMF was from Kroupa (2001), ranging from 0.08 to 150 $M_\odot$. For each model, we set the SFE $\epsilon = 1.0,\ 0.7,\ 0.5,\ 0.4,\ 0.333,\ 0.2$, and 0.1. Each model has been run up to 2 Gyr. In this preliminary work, as said before, no binaries are allowed (neither initially nor dynamically). For this reason, the evolution of the models is stopped when core collapsed has been reached.

With those simulations, we aimed to investigate the importance of the SFE on the evolution and survival of the system. Indeed, as shown in previous works (Elmegreen et al. 2000; both theoretical Kroupa et al. 2001b; Geyer & Burkert 2001, and observational Lada & Lada 2003; Baumgardt & Kroupa 2007), a minimal SFE of 0.333 is needed to form a bound and gas-free cluster in dynamical equilibrium. So far, this has been tested for small N models only.

The evolution of total mass (scaled by the initial values) is shown in Fig. 5. The importance of the initial state of the system (tidally filling or underfilling) is visible in Table 1, where the ratio between the final mass and the initial mass for each model is reported. The models that were initially tidally filling are unable to survive the embedded gas phase, being dissolved for $\epsilon \leq 0.5$. Indeed, only for the cases with $\epsilon = 0.7$ and 1.0 the models survive, even though an important percentage of the initial mass had been removed, with the final half-mass radius being $\sim$10.0 pc. Models that were initially tidally underfilling ($R_{\rm h} = 0.5$, 1.0 and 3.0 pc) reached an advanced state of evolution, with roughly half (or more) of the initial mass. Interestingly, no model with $\epsilon = 0.1$ has survived. However, models that were strongly tidally underfilling can survive the gas expulsion with $\epsilon \geq 0.2$. Star clusters that were formed as tidally filling or only slightly tidally underfilling can survive the gas expulsion only if $\epsilon \geq 0.7$ and can be observed as star clusters that are advanced in age. This means that star clusters with the observationally suggested values of $\epsilon = 0.333$ have to be formed as tidally underfilled. On the other hand, clusters that are very strongly tidally underfilled can survive under a very low SFE, equal to about 0.2. Also, in Figs 5 and 6, we reported in dashed lines the time when the dissolution of the system started. As discussed in other works (Fukushige & Heggie 1995; Contenta, Varri & Heggie 2015; Giersz et al. 2019), the dissolution of the system happens on a dynamical time-scale, when the system loses its dynamical equilibrium and will not undergo core collapse.

The evolution of the ratio between the actual and the initial half-mass radii for those models is shown in Fig. 6. The value of $R_{\rm h}$ at the end of the gas expulsion strongly depends on the SFE and the initial $R_{\rm h}$. Indeed, for initial values of $R_{\rm h} = 0.5,\ 1.0,\ 3.0$ and 6.0 pc, the $R_{\rm h}$ at the end of gas expulsion is $\sim$34, $\sim$17, $\sim$10, and $\sim$5 times larger than the initial value for $\epsilon = 0.1$, respectively. The drastic expansion of $R_{\rm h}$ is clearly visible for small SFE in all models, and for $\epsilon \leq 0.7$ for the $R_{\rm h} = 6.0$ pc model. In contrast, for $\epsilon = 0.333$ this value is $\sim$3–4 times larger, independent of the initial $R_{\rm h}$. Taking into account the value of the tidal radius, a Plummer model (that can be roughly modelled with a King profile with $w_0 = 5.0$–6.0) is tidally filling when its $R_{\rm h} \simeq 8.0$ pc. Therefore, the model with an initial value of $R_{\rm h} = 3.0$ pc and $\epsilon = 0.333$ will become tidally filling at the end of the gas expulsion. Finally, at the end of the violent relaxation, the half mass radius shows a drastic drop, with the actual half mass radius at that time being only a few pc. The further evolution of $R_{\rm h}$ is principally governed by the relaxation process and mass loss.

5 DISCUSSIONS AND CONCLUSIONS

We have introduced and studied for the first time the embedded gas phase and gas removal phases in the evolution of star clusters with the Monte Carlo MOCCA code. By using the MOCCA code, it is possible to extend the study of these evolutionary phases to systems with a much larger number of starsthan those allowed by direct N-body simulations.

For the study presented in this paper, we have developed a simplified version of MOCCA running within the AMUSE environment. The investigation presented in this paper is a pilot study to show that it is possible to follow the evolution of star clusters during the gas expulsion phase in the Monte Carlo framework and that we can

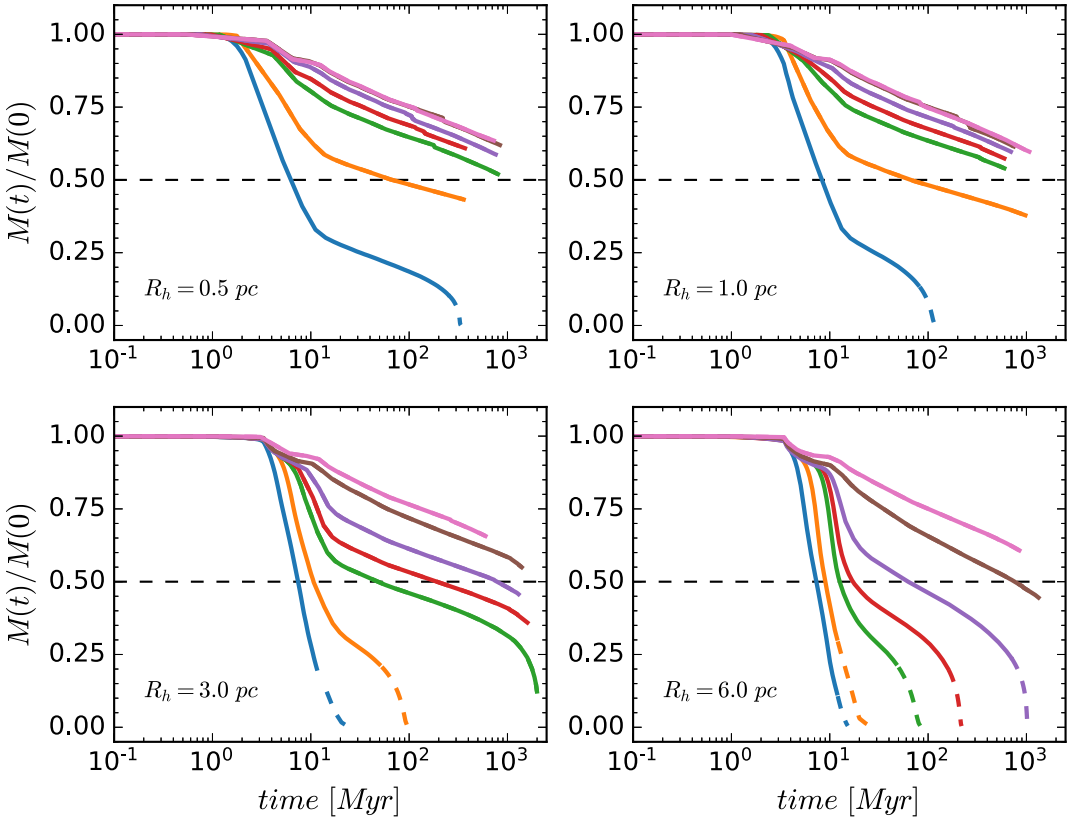

Figure 5. MOCCA-C evolution of the ratio between the actual mass and the initial mass for the model run as a function of SFE. The upper left-hand panel shows runs with $R_{\rm h} = 0.5$ pc, the upper right-hand panel with $R_{\rm h} = 1.0$ pc, the lower left-hand panel with $R_{\rm h} = 3.0$ pc and the lower right with $R_{\rm h} = 6.0$ pc. In each panel, the lines from left to right show the models with SFE $= 0.1$, 0.2, 0.333, 0.4, 0.5, 0.6, 0.7, and 1.0. The dashed part of the lines shows the times for which the tidal disruption of the model has already begun. The plots start at time 0.1 Myr, which is at the beginning of gas expulsion.

Table 1. The ratio between the final and initial masses for model runs with different initial $R_{\rm h}$ and ϵ. Models that were disrupted are reported with a dash, meanwhile all other models undergo a core collapse at the end of the simulations. In brackets, the time (in Myr) for which the models stop is reported. The gas expulsion time-scales $\tau_{\rm g}$ have been set to 0.05, 0.1, 0.3, and 0.6 Myr, for the models with $R_{\rm h} = 0.5$, 1.0, 3.0, and 6.0 pc, respectively.

ϵ	$R_{\rm h} = 0.5$	$R_{\rm h} = 1.0$	$R_{\rm h} = 3.0$	$R_{\rm h} = 6.0$
0.1	– (335.2)	– (121.2)	– (23.5)	– (12.3)
0.2	0.4 (358.8)	0.4 (978.4)	– (94.7)	– (26.1)
0.333	0.5 (799.2)	0.5 (599.4)	0.1 (1997.7)	– (74.1)
0.4	0.6 (370.0)	0.6 (599.0)	0.4 (1597.5)	– (218.9)
0.5	0.6 (759.8)	0.6 (697.6)	0.5 (1299.1)	– (1019.5)
0.7	0.6 (837.6)	0.6 (748.2)	0.5 (1399.3)	0.4 (1327.5)
1.0	0.6 (729.5)	0.6 (1069.0)	0.7 (597.1)	0.6 (849.8)

produce results in general good agreement with those of N-Body simulations.

The new version of MOCCA introduced here includes a new treatment for unbound stars necessary to reproduce the early cluster expansion, while additional dynamical processes will need to be added in future developments of the code. In particular, to reproduce more realistic models of globular cluster evolution and survival after the gas expulsion phase, a better treatment of relaxation and mass segregation in the violent relaxation phase is necessary. Moreover, while a constant SFE and a simplistic treatment of the gas expulsion have been assumed for this initial study, future work will include a more realistic treatment of SFE and gas expulsion.

Despite the differences between the recipes adopted for stellar evolution in the N-body and the Monte Carlo simulations, we do not find significant differences in the dynamics of the systems studied. Instead, the largest differences are seen from the comparison with the models from Banerjee & Kroupa (2013) and can be explained by the small number of stars, which are at the limit of applicability of the Monte Carlo method.

New models have been run in order to investigate the importance of the SFE and tidal field on the evolution and survival of large N systems. In the assumed SFE and the gas removal prescription, models with SFE $= 0.1$ dissolve within 10–100 Myr. Models that were initially tidally filling ($R_{\rm h} = 6.0$ pc) were able to survive only for large SFE ($\gtrsim$0.7). Instead, all other models, formed a bound system and survived the gas expulsion phase.

In Baumgardt & Kroupa (2007), the authors performed a large set of N-body simulations with different SFEs, strengths of the tidal field and gas expulsion time-scales. Each simulation consisted of models with $N = 20\,000$ equal-mass stars, and no stellar evolution was included. As a result, models that were tidally underfilling and with $\epsilon = 0.1$ were able to create bound clusters after the gas expulsion, but only if the tidal fields were weak ($R_{\rm h}/R_{\rm tidal} = 0.01$–$0.03$) and the gas was removed slowly ($\tau_{\rm g}/t_{\rm cross} = 10$). Also, the authors find that no bound clusters were formed for tidally filling models. Our results are in agreement with the ones shown in Baumgardt & Kroupa (2007), considering that the models we run in this paper have a faster gas removal ($\tau_{\rm g}/t_{\rm cross} \lesssim 5$). Nevertheless, our study present more

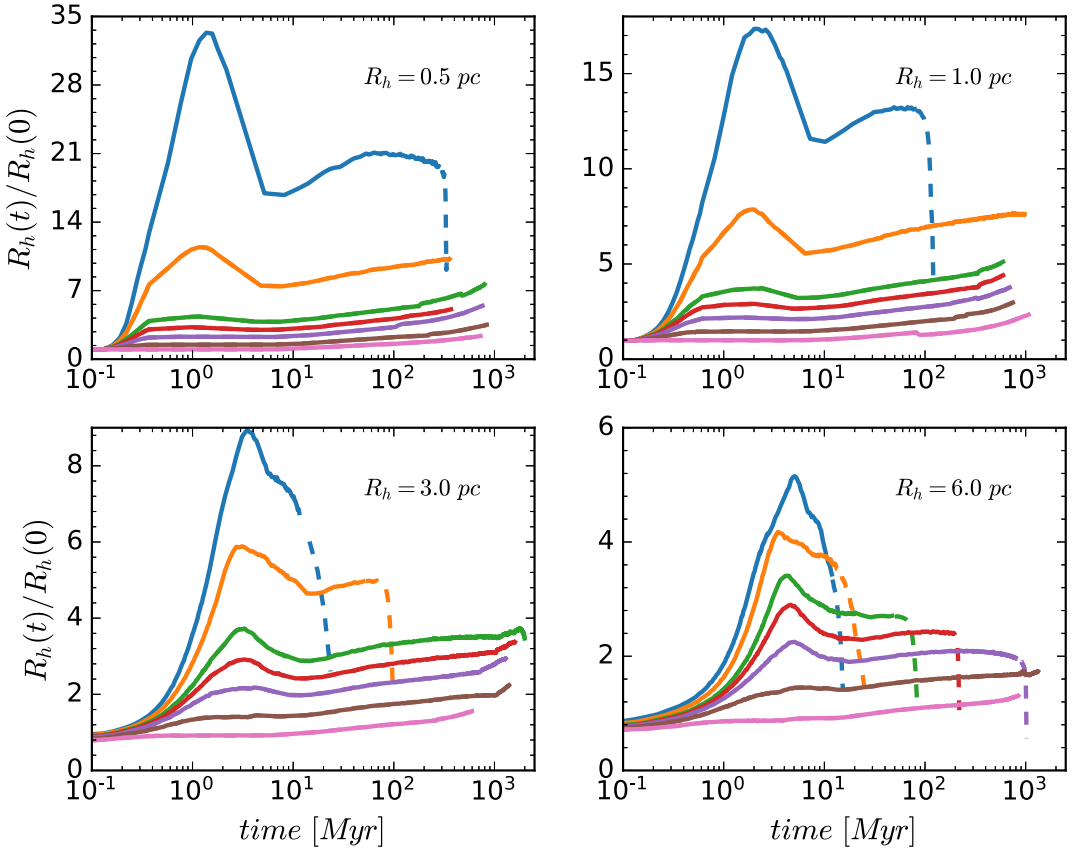

Figure 6. Same as in Fig. 5, but showing the evolution of the ratio between the actual and the initial half mass radii. In each panel, the lines from top to bottom show the models with SFE = 0.1, 0.2, 0.333, 0.4, 0.5, 0.6, 0.7, and 1.0.

realistic models, including the effects of a spectrum of stellar masses and those of stellar evolution. The presence of massive stars in the system and the stellar evolution in the first Myr can be important for the long-term cluster survival. Indeed, the lack of any massive objects can leads to different mass loss efficiencies and dynamical interaction, which in turn leads to not deep enough core collapses and slower dissolutions of the cluster. Their findings still approximately hold also for larger and multimass clusters.

The clusters studied by Brinkmann et al. (2017) also survived the gas expulsion phase, even in a strong tidal field. The authors run several NBODY7 models with initial $R_{\rm h}$ equal to 0.1, 0.3, and 0.5 pc, $M_{\rm cl}$ ranging from 5×10^3 to $5 \times 10^4\,{\rm M}_\odot$, and multimass IMF according to Kroupa et al. (2013). Similarly, as in this work, a Plummer model for the gas and stellar component, and an identical treatment for the gas depletion was used. The models presented in that work are strongly underfilling, and their clusters survived the gas expulsion, as we also see in this paper. The authors also found that the final bound fraction can be sensitive to the relation $\tau_{\rm g}/t_{\rm cross}$, implying a different final bound mass fraction for clusters with the same initial central density. Additionally, similar to our results, their findings show that for fixed gas expulsion velocity, the SFE plays an important role for the survival and bound mass of the system, with larger SFE leading to larger bound fractions. Finally, we find that the stellar evolution can influence the bound mass fraction, due to the different re-virialization timescales after the gas expulsion, with clusters without stellar evolution having higher bound masses than the models with stellar evolution. These results are additionally supported by the MOCCA-C models. This gives us confidence that the gas removal and violent relaxation treatments proposed in this paper can be safely, but with some care, used to simulate large-N embedded systems.

Future work will focus on introducing the embedded gas phase and the procedures introduced in this paper to the standalone MOCCA code. Indeed, the presence and formation of binaries in the system, such as the dynamical interactions and collisions among stars and binaries, strongly influence the evolution of the system. In very dense systems (with initial $R_{\rm h} \sim 0.1$ pc), the collision and dynamical interactions can be important from the very beginning of system evolution, including the violent relaxation phase. Further studies will need to be performed, which will take binaries and interactions into account. Interactions and collisions among stars and binaries, particularly for massive stars and binaries, may strongly influence the early cluster evolution. In fact, the presence of very massive stars, massive BHs, and binaries (primordial and dynamically formed) in the system, together with the energy they may release in the system through dynamical interaction, may have a significant impact on the dynamics and survival of the cluster both during its early and long-term evolutionary phases. These aspects will be studied in a series of future papers.

ACKNOWLEDGEMENTS

MG and AL were partially supported by the Polish National Science Center (NCN) through the grant UMO-2016/23/B/ST9/02732. SB acknowledges support from the Deutsche Forschungsgemeinschaft (DFG; German Research Foundation) through the individual research grant 'The dynamics of stellar-mass black holes in dense

stellar systems and their role in gravitational-wave generation' (BA 4281/6-1; PI: S. Banerjee).

DATA AVAILABILITY

The data underlying this article will be shared on reasonable request to the corresponding author. The AMUSE code is available for download via GitHub at https://amusecode.org. The codes used in this paper are: PYTHON (van Rossum 1995), MATPLOLIB (Hunter 2007), NUMPY (Oliphant 2006), MPI (Gropp et al. 1996; Gropp 2006), SSE/BSE (Hurley et al. 2000, 2002).

NOTE ADDED IN PRESS

Energy consumption of these simulations. We run MOCCA-C for about 2000 single-core CPU hours. This results in about 37.25 kWh of electricity (http://green-algorithms.org/) being consumed by the CAMK supercomputer. With our estimate of the proportion of green electricity used, this process produces ∼30 kg CO_2, which is comparable to driving a car about 170 km.

REFERENCES

Aarseth S. J., 2012, MNRAS, 422, 841
Adams F. C., 2000, ApJ, 542, 964
Banerjee S., Kroupa P., 2013, ApJ, 764, 29
Banerjee S., Kroupa P., 2014, ApJ, 787, 158
Banerjee S., Kroupa P., 2018, The Birth of Star Clusters, Springer, Cham, p. 143
Bastian N., Goodwin S. P., 2006, MNRAS, 369, L9
Baumgardt H., Kroupa P., 2007, MNRAS, 380, 1589
Belloni D., Askar A., Giersz M., Kroupa P., Rocha-Pinto H. J., 2017, MNRAS, 471, 2812
Brinkmann N., Banerjee S., Motwani B., Kroupa P., 2017, A&A, 600, A49
Contenta F., Varri A. L., Heggie D. C., 2015, MNRAS, 449, L100
Duquennoy A., Mayor M., 1991, A&A, 500, 337
Elmegreen B. G., Efremov Y., Pudritz R. E., Zinnecker H., 2000, in Mannings V., Boss A. P., Russell S. S., eds, Protostars and Planets IV, University of Arizona Press, Tucson, AZ, p. 179
Fregeau J. M., Cheung P., Portegies Zwart S. F., Rasio F. A., 2004, MNRAS, 352, 1
Fukushige T., Heggie D. C., 1995, MNRAS, 276, 206
Fukushige T., Heggie D. C., 2000, MNRAS, 318, 753
Gaburov E., Harfst S., Portegies Zwart S., 2009, New A, 14, 630
Geyer M. P., Burkert A., 2001, MNRAS, 323, 988
Giersz M., 1998, MNRAS, 298, 1239
Giersz M., Heggie D. C., Hurley J. R., Hypki A., 2013, MNRAS, 431, 2184
Giersz M., Askar A., Wang L., Hypki A., Leveque A., Spurzem R., 2019, MNRAS, 487, 2412
Gropp W., 2006, in Kranzlmüller D., Volkert J., Kacsuk P., Dongarra J., eds, MPICH2: A New Start for MPI Implementations. Springer Berlin Heidelberg, Berlin, Heidelberg, p. 7
Gropp W., Lusk E., Doss N., Skjellum A., 1996, Parallel Comput., 22, 789
Heggie D. C., 2014, MNRAS, 445, 3435
Hénon M. H., 1971, Ap&SS, 14, 151
Hills J. G., 1980, ApJ, 235, 986
Hunter J. D., 2007, Comput. Sci. Eng., 9, 90
Hurley J. R., Pols O. R., Tout C. A., 2000, MNRAS, 315, 543
Hurley J. R., Tout C. A., Pols O. R., 2002, MNRAS, 329, 897
Hypki A., Giersz M., 2013, MNRAS, 429, 1221
Joshi K. J., Rasio F. A., Portegies Zwart S., 2000, ApJ, 540, 969
Kamlah A. W. H. et al., 2021, MNRAS, 511, 4060
King I. R., 1966, AJ, 71, 276
Kroupa P., 1995a, MNRAS, 277, 1491
Kroupa P., 1995b, MNRAS, 277, 1522
Kroupa P., 2001, MNRAS, 322, 231
Kroupa P., Aarseth S., Hurley J., 2001a, MNRAS, 321, 699
Kroupa P., Aarseth S., Hurley J., 2001b, MNRAS, 321, 699
Kroupa P., Weidner C., Pflamm-Altenburg J., Thies I., Dabringhausen J., Marks M., Maschberger T., 2013, Planets, Stars and Stellar Systems. Springer, Dordrecht, NL, p. 115
Krumholz M. R., Matzner C. D., 2009, ApJ, 703, 1352
Küpper A. H. W., Maschberger T., Kroupa P., Baumgardt H., 2011, MNRAS, 417, 2300
Lada C. J., Lada E. A., 2003, ARA&A, 41, 57
Lada C. J., Margulis M., Dearborn D., 1984, ApJ, 285, 141
Lewis S. et al., 2021, AAS Meeting Abstracts, #232.08
Longmore S. N. et al., 2014, in Beuther H., Klessen R. S., Dullemond C. P., Henning T., eds, Protostars and Planets VI. University of Arizona Press, Tucson, AZ, p. 291
Lynden-Bell D., 1967, Les Nouvelles Méthodes de la Dynamique Stellaire. Editions du CNRS, Paris, p. 163
Makino J., Fukushige T., Koga M., Namura K., 2003, PASJ, 55, 1163
Marks M., Kroupa P., 2012, A&A, 543, A8
Maschberger T., 2013, MNRAS, 429, 1725
Oh S., Kroupa P., Pflamm-Altenburg J., 2015, ApJ, 805, 92
Oliphant T. E., 2006, A guide to NumPy, Vol. 1. Trelgol Publishing, USA
Pelupessy F. I., Portegies Zwart S., 2012, MNRAS, 420, 1503
Pelupessy F. I., van Elteren A., de Vries N., McMillan S. L. W., Drost N., Portegies Zwart S. F., 2013, A&A, 557, A84
Plummer H. C., 1911, MNRAS, 71, 460
Portegies Zwart S. et al., 2009, New A, 14, 369
Portegies Zwart S., McMillan S., 2018, Astrophysical Recipes: The art of AMUSE. IOP Publishing, Bristol
Portegies Zwart S., McMillan S. L. W., van Elteren E., Pelupessy I., de Vries N., 2013, Comput. Phys. Commun., 184, 456
Rodriguez C. L. et al., 2021, Astrophys. J. Suppl. Ser., 258, 22
Sana H. et al., 2012, Science, 337, 444
Shukirgaliyev B. et al., 2021, A&A, 654, A53
Shukirgaliyev B., Parmentier G., Berczik P., Just A., 2017, A&A, 605, A119
Stodolkiewicz J. S., 1982, AcA, 32, 63
Stodolkiewicz J. S., 1986, AcA, 36, 19
Šubr L., Kroupa P., Baumgardt H., 2008, MNRAS, 385, 1673
van Rossum G., 1995, Extending and embedding the Python interpreter, Report CS-R9527. Centrum voor Wiskunde en Informatica, Amsterdam, NL
Wang L. et al., 2016, MNRAS, 458, 1450
Weidner C., Kroupa P., 2004, MNRAS, 348, 187

APPENDIX A: MCLUSTER, A NEW IMPLEMENTATION

The original version of star cluster initial model generator, McLuster, developed by Küpper et al. (2011), has been updated, to better link the generated initial conditions with the MOCCA code.

The main update of the new implementation has been an upgrade to the existing procedure for generating multiple stellar populations (with a maximum of 10) as initial conditions. For a single stellar population, the positions and velocities of stars for each population can be generated according to different models: Plummer (Plummer 1911), King (King 1966), and Subr (Šubr, Kroupa & Baumgardt 2008). Instead, for multiple stellar populations, the velocities of stars are obtained by solving the Jeans equation for dynamical equilibrium. Indeed, for two or more populations which are individually in virial equilibrium, their combination may not be. Moreover, the final system does not follow the distribution of the single population models (i.e. two Plummer models do not sum to a Plummer model). In order to establish virial equilibrium, the velocities of the stars have been modified accordingly. The mass density and the mass profiles for the entire system are determined and used to determine

the velocity dispersion profile for the model solving the Jeans equation. The velocity of each star is then obtained from a normal distribution, with the standard deviation equal to the local velocity dispersion. Additionally, stellar and binary evolution are allowed for each population.

Also, it is now possible to apply a semi-major axis uniform distribution in $\log(a)$ for low mass stars and a distribution for the orbital period for high mass stars based on Sana et al. (2012), Oh, Kroupa & Pflamm-Altenburg (2015). The modified pre-main sequence eigenevolution [Belloni et al. (2017); the original procedure described in Kroupa (1995b), Kroupa et al. (2013)] has been added as an option in generating binary properties. Generally, the pre-main sequence eigenevolution procedure would modify the mass of stars that compose the binaries. For this reason, the total mass of the system and the conversion parameters (from physical units to Nbody) may differ. In order to avoid such an error, the order in which the procedures are called has been modified, with the primordial binary property determination called before the determination of the conversion parameters (opposite to the original version, where the primordial binary property procedure is called last).

A configuration file has been included into the code, in order to modify the initial conditions parameter in a simpler way. The format of the output of the initial model generated can be used for N-body and/or MOCCA simulations.

Finally, the possibility to evaluate the potential energy in spherical symmetry has been added. As an $O(N)$ algorithm, this drastically speeds up the code for models containing millions of objects. This add-on is essential for the MOCCA initial conditions, since the primary assumption in Monte Carlo codes is spherical symmetry of the system.

In Table A1, the initial parameters in the configuration file are reported. From left to right, we reported the name of the parameter, the description of the parameter, and some additional notes.

Table A1. Mcluster initial parameters.

Parameter	Description	Extra note
n	Initial number of objects	$n = n_{\rm singles} + n_{\rm binaries}$
fb	Primoridal binary fraction	$n_{\rm binaries} = fb \cdot n$
initialModel	Initial density distribution	0 - Homogeneous sphere 1 - Plummer (Plummer 1911) 2 - King (King 1966) 3 - Subr (Šubr et al. 2008)
w_0	King model parameter	Values between 1.0–12.0
S	Mass segregation parameter	Values between 0.0–1.0
fractal	Fractal dimensions	Values between 0.0–3.0 (3.0 not fractal)
qvir	Virial ratio	$qvir > 0.5$: expanding; $qvir = 0.5$: equilibrium; $qvir < 0.5$: collapsing
mfunc	Stellar mass function	0 - Equal masses 1 - Kroupa (2001) IMF 2 - Multipower law 3 - L3 IMF (Maschberger 2013)
pairing	Pairing of binary components	0 - Random pairing 1 - Ordered pairing for components with masses $M > 5\,{\rm M}_\odot$ 2 - Random but separate pairing for components with masses $M > 5\,{\rm M}_\odot$ 3 - Uniform distribution of mass ratio for $M > 5\,{\rm M}_\odot$, random pairing for $M \leq 5\,{\rm M}_\odot$
adis	Semimajor axis distribution	0 - uniform distribution in log(a) 1 - Lognormal distribution distribution 2 - Kroupa (1995a) period distribution 3 - Kroupa (1995a) period distribution for $M < 5\,{\rm M}_\odot$; Sana et al. (2012) for $M > 5\,{\rm M}_\odot$ 4 - Flat uniform distribution between amin and amax 5 - Duquennoy & Mayor (1991) period distribution 6 - Uniform distribution in log(a) for $M < 5\,{\rm M}_\odot$; Sana et al. (2012) for $M > 5\,{\rm M}_\odot$
eigen	Eigenevolution	0 - Off 1 - Kroupa (1995b) eigenevolution 2 - Kroupa et al. (2013), rewieved in Belloni et al. (2017)
amin	Min. binary semimajor axis	Value in $R_\odot$
amax	Max. binary semimajor axis	Value in $R_\odot$
tf	Tidal field	No tidal field or point mass galaxy
rbar	Tidal radius	Value in parsec
rh_mcl	Half mass radius	Value for the whole system, in parsec
conc_pop	Concentration radius parameter	Defined as Rh_i/Rh_1, the ratio between the half-mass radii of the i-th and the first generation
potential_energy	Potential energy evaluation	Potential energy evaluated in spherical symmetry sum of gravitational potential for every object
epoch	Age of population	Value in Myr
zini	Initial metallicity	$zini_\odot = 0.02$ for Solar metallicity
seedmc	Random number generator	
outputf	Output format	Initial files for MOCCA and/or N-body simulations
check_en	Make energy check at end	
BSE	Activate SSE/BSE	Swtich on/off stellar/binary evolution

This paper has been typeset from a TEX/LATEX file prepared by the author.

Chapter 6

Submitted Works and Work in Progress

In this chapter, I shortly summarize and present results from submitted works that were and are connected with the MOCCA code development needed to create a new MOCCA-Survey Database which was initially planned to be used to analize GC populations in external galaxies.

6.1 Update of stellar evolution in MOCCA code[1]

The stellar prescription used in MOCCA simulations utilizes the implementation presented in SSE (Hurley, Pols, and Tout, 2000) and BSE (Hurley, Tout, and Pols, 2002). However, new prescriptions that are up to date with the current state-of-the-art for stellar evolutionary codes are essential for the evolution of dynamical models such as GCs. For example, different supernovae (SNe) natal kicks would importantly impact the number of BHs retained in GCs.

The up-to-date prescriptions for SNe include the core-collapse SNe (rapid and delayed models from Fryer et al., 2012), pair-instability and pair-instability pulsation SNe (Heger and Woosley, 2002; Woosley, Blinnikov, and Heger, 2007; Belczynski et al., 2016), electron-capture SNe (ECSNe) and accretion-induced collapse (AICSNe) (Gessner and Janka, 2018). Finally, the remnant masses of the compact objects and their natal kicks depend on the mass fallback prescription.

A strong impact on the SNe event that the star would experience is driven by stellar winds. Indeed, a strong stellar wind would imply a stronger mass loss, and hence a less important mass fallback and a larger natal kick for the newborn BH. The updated metallicity dependent stellar winds (Vink, de Koter, and Lamers, 2001; Vink and de Koter, 2002; Belczynski et al., 2010), and the influence of the surface gravity and effective temperature of the star on its stellar wind, presented in Schröder and Cuntz (2005), are implemented in the stellar evolution prescription in MOCCA.

The new stellar evolution prescription has been also implemented in the `Nbody6++GPU` code, and the results have been compared to the results from the GC evolution simulated with the MOCCA code, with the same stellar evolution prescription. As a result, both approaches for star cluster simulations and the stellar evolution implementations in both algorithms are supported reciprocally. The simulations were followed up to 10 Gyr, and different mechanisms for core-collapse SNe (rapid and delayed SNe), mass ratio distribution for binaries (uniform and Sana et al., 2012), and white dwarfs (WDs) natal kicks were studied. In all simulations, NSs produced by ECSNe and AICSNe would receive a small kick velocity, and hence would stay in the system. On the other hand, NSs formed in SNe II explosions would escape the cluster due to

[1] https://ui.adsabs.harvard.edu/abs/2022MNRAS.511.4060K

large velocity kicks. BHs would escape the system depending on the importance of mass fallback during SNe explosions. On the other hand, the WDs' escape velocity distributions found in MOCCA and N-body results differ significantly from one another. Also, the MOCCA models generate more helium WD and BHs, but the `Nbody6++GPU` models have a significantly higher proportion of WD-WD binaries.

The number of BH-main sequence (MS) stars found is negligible for almost all models except for MOCCA models with delayed SNe and uniform binary distributions. On the other hand, a non-negligible amount of BH-BH binaries were produced in all simulated models after around 100 Myr of evolution. This implies that all BH-BH binaries are dynamically formed: all BHs formed in the system were produced in the first $\sim$ 20 Myr of evolution. The surviving BH-BH binaries found at the end of the simulations will not merge in a Hubble time, and are found mostly in the central regions of GCs. The number of NS binaries is negligible, and they are mostly found in the outskirt regions of the cluster. Most of the NS binaries found are NS-MS binaries, whereas no NS-NS or NS-BH systems are found at the end of the simulation. The compact object binary population is dominated by WD binaries for both MOCCA and N-body models. In particular, N-body models show a larger WD-WD binary fraction when compared to MOCCA models, whereas the latter shows a larger amount of WD-MS binaries. Indeed, the surviving WD-WD binaries are smaller in the MOCCA models, as consequence of the faster evolution in these models, and stronger interactions. Furthermore, these differences could be enhanced by the natal WD kicks switched on in the `Nbody6++GPU` models but not in MOCCA. Due to the different rate of evolution in the `Nbody6++GPU` and MOCCA models, it is not easy to unravel the real reason for these differences.

The mass loss experienced by the MOCCA models is more important than in the N-body ones, with the MOCCA models also being denser than the N-body ones. The different evolution and late core collapses shown in MOCCA is connected to the faster evolution and the larger amount of energy generated in the core in MOCCA as a consequence of the Hénon's principle. The MOCCA models also seems to have larger central densities, implying a larger number of dynamical interactions, and hence larger binary merger rates. However, the fallback kick distribution for both NSs and BHs found in MOCCA were in relatively good agreement with N-body, implying similar retention fractions of compact objects, with the exception of Helium WDs. Similarly, the masses of the retained compact objects are also in agreement between N-Body and MOCCA. Most of the described differences in the cluster structure and properties of objects between the MOCCA and N-body models are connected with the very large tidal radius (500 pc) assumed in the N-body model. This leads to much slower mass loss in N-body than in MOCCA because, by construction, unbound stars escape immediately in MOCCA but in N-body they need up to hundreds Myr to traverse the system.

6.2 Multiple stellar populations in the MOCCA code[2]

The main feature introduced into the new MOCCA code is the ability to follow the evolution of multiple stellar populations. This feature will be strongly studied in the MOCCA Database II. Multiple stellar population are observed in almost all Galactic GCs, evidenced by their color-magnitude diagrams, chemical variations, extreme helium abundance, or anti-correlations of certain elements (Bastian and Lardo, 2018). In different GCs, some spatial and kinematic differences have been observed (Milone

[2] https://ui.adsabs.harvard.edu/abs/2022arXiv220505397H

et al., 2018; Dalessandro et al., 2021). These differences are consistent with the formation scenario proposed by Calura et al. (2019). The formation of multiple stellar populations is still under investigation and debate (D'Ercole et al., 2008; Gieles et al., 2018; Wang et al., 2020), as well as their dynamical evolution (Hénault-Brunet et al., 2015; Vesperini et al., 2021; Sollima, 2021).

Different ratios for the number of objects in the first and second population, their initial binary fraction, and the maximum single star mass in the second population, as well as different concentrations for the whole initial cluster were set as initial conditions for the studied simulations. Different concentration parameters, defined as the ratio between the half-mass radius of the second to the first population, have also been investigated.

At 12 Gyr our models that were initially tidally underfilling show a larger number of first population binaries, compared to those models that were tidally filling. This difference is explained by the different evolution of tidally filling or underfilling models. Indeed, models that were initially tidally underfilling would have enough space to expand before reaching the system's tidal radius, and hence would be able to keep a larger number of first population binaries. Instead, for tidally filling models, the second generation seems to have a larger number of binaries at 12 Gyr in the central region of the cluster. In this case, the cluster loses more and more first generation binaries, due to the influence of the tidal radius, resulting in more numerous second population binaries throughout the entire cluster. Finally, these results seems to not depend on the initial binary fraction of the populations.

Our models show that the binary ratio does not differ much for the different methods of computing the binary count (only MS binaries, binaries selected based on Lucatello et al., 2015, and binaries with at least one red giant), when considering subsets of MS binaries. In general, tidally underfilling models show a smaller binary ratio in the central region of the cluster, with larger values in the outer regions. On the other hand, the tidally filling models show a more numerous second population in the central region, with the first population being more dominant in the outskirts. The binary count for red giants and based on the binary selection described in Lucatello et al. (2015) show larger values, but with similar shapes. These results seem to also be valid if one takes into account only single MS stars to track the mixing between the two populations.

The results presented in this section show that GCs that are tidally underfilling would present a larger number of first than second population stars. Also, the number of binaries in the second population seems to be more easily disrupted in these models, due to their large initial densities. On the other hand, second stellar population seems to be more numerous when the initial cluster is tidally filling, with a similar number of binaries present in the first and second populations. The fraction of second stellar population found in the MOCCA models seems to be in agreement wit the observed values in the MWGCs. Also, the initial binary fractions seems not to importantly affect either the mixing and number fraction between the first and second populations, or the presence of an IMBH. Finally, despite the fact that the MOCCA models explore only a subset of MW GC observational parameters, our results can reproduce the observed distribution of the second population fraction, defined as N_2/N_{tot}, with N_2 being the total number of stars in the second population, and with N_{tot} as the total number of stars in the system.

Galaxy	t_{growth} [Myr]	$[\tau_{min}, \tau_{max}]$	$[f_{NSC,min}, f_{NSC,max}]$
MW	5000	[0.2, 1.1]	[2.0, 8.0]
M31	5250	[0.2, 0.25]	[0.0, 2.5]

TABLE 6.1: Best results reported by our models for t_{growth}, $[\tau_{min}, \tau_{max}]$, and $[f_{NSC,min}, f_{NSC,max}]$ for both the MW and M31 .

6.3 NSC and SMBH mass growth in the Milky Way and Andromeda galaxies

In this section, we show the first application of the machinery introduced in our work to the mass build-up of the NSC and SMBH in the MW and M31 galaxies. As shown by our results in Chapter 4, the final NSC and SMBH masses found in our simulations are 1-2 orders of magnitudes smaller compared to their observed values. This result would suggest that it is necessary to consider the interplay between the infalling galactic gas and its further interactions (and merges) with infalling GCs in order to fully explain the NSC and SMBH observed masses. We applied the prescription introduced in Askar, Davies, and Church (2021a) and Askar, Davies, and Church (2021b) to evolve the NSC and SMBH masses obtained in our results. The prescription assumes that the presence of one (or more) IMBHs in the GCs delivered into the NSC would induce accretion onto the IMBH of the pristine gas present in the central region of the galaxy. The IMBHs are assumed to accrete at 10% of the Eddington rate, with the mass growth evolution for the IMBHs described by the following equation

$$M = M_0 \times 2^{t/\tau},$$

where M_0 is the initial mass of the IMBH, τ is the mass doubling time and t is the time since the IMBH has been delivered. If multiple IMBHs are delivered to the NSC, the first IMBH is accreted until a second IMBH is delivered to the NSC. Also, it is assumed that the pair of IMBHs will merge: the final BH would be ejected if the mass ratio is greater than 0.15, otherwise the merged BH will be retained by system. Finally, accretion onto the IMBH has been followed up to t_{growth}. In the original implementation presented in Askar, Davies, and Church (2021a) and Askar, Davies, and Church (2021b), the authors considered a mass doubling time, τ, of about 300 Myr, assuming the e-folding time for a BH accreting at the Eddington rate is $\sim 30 - 50$ Myr (Madau, Haardt, and Dotti, 2014). Also, for the IMBH, mass accretion was allowed up to $t_{growth} = 4500$ Myr. In addition to the original implementation, in our models we took into account star formation processes triggered in the central region of the galaxy due to the presence of the IMBH, contributing to the final mass of the NSC. Indeed, gas accretion onto the IMBH in the central region of the NSC would trigger a star formation event, and the stellar content formed there would be included in the NSC's overall mass. The total stellar mass formed during this process has been considered to be a fraction of the total IMBH accreted mass, $f_{NSC,stars}$.

With the aim to take into consideration changing accretion rates for the IMBHs, the mass doubling time has been chosen randomly from the range $[\tau_{min}, \tau_{max}]$ for each new IMBH that would be delivered to the NSC. Similarly, the fraction of IMBH accreted mass $f_{NSC,stars}$ has been chosen randomly from the range $[f_{NSC,min}, f_{NSC,max}]$. The best value for these parameters obtained by our results are reported in Table 6.1, whereas the respective initial and the final masses of the NSC and SMBH are reported in Table 6.2. The NSC and SMBH mass growth obtained for the values reported in Table 6.1 are reported in Fig. 6.1 and Fig. 6.2 for MW and M31, respectively.

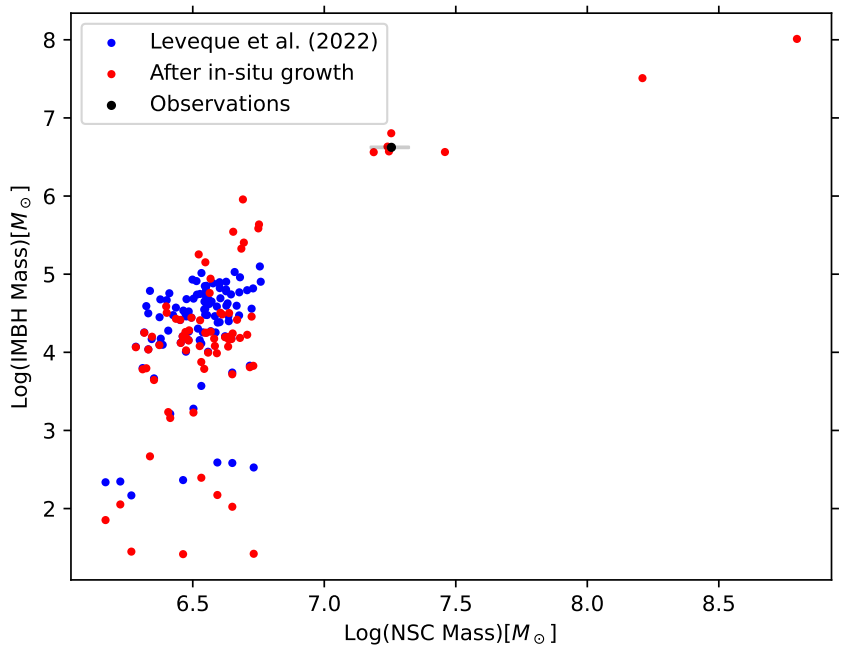

FIGURE 6.1: SMBH mass versus the NSC mass reported in our simulations for the MW. The results with and without the NSC/IMBH mass growth seed are reported in red and in blue, respectively. In black, the observed properties of the MW are shown with the observed errors represented by the grey box.

Galaxy	$M_{Initial,NSC}$ $[M_\odot]$	$M_{Initial,SMBH}$ $[M_\odot]$	$M_{Final,NSC}$ $[M_\odot]$	$M_{Final,SMBH}$ $[M_\odot]$
MW	4.6×10^6	1.1×10^5	1.7×10^7	4.3×10^6
M31	4.6×10^6	8.1×10^4	3.0×10^7	1.6×10^8

TABLE 6.2: The initial and the final masses for the NSC and SMBH (in $M_\odot$) obtained by our prescription for both MW and M31 are reported.

In the figures, the observed properties for MW and M31 are reported as well. In particular, the observed mass of the NSC in the MW has a value of $1.8 \pm 0.3 \times 10^7 M_\odot$ (Chatzopoulos et al., 2015), meanwhile the SMBH at the center of the MW is $4.23 \pm 0.14 \times 10^6 M_\odot$ (Chatzopoulos et al., 2015). Similarly, the NSC mass in M31 is $3.5 \pm 0.8 \times 10^7 M_\odot$ (Lauer et al., 1993; Kormendy and Ho, 2013; Georgiev et al., 2016), while the SMBH in M31 has a mass of $\sim 1.1 - 2.3 \times 10^8 M_\odot$ (Bender et al., 2005).

Our results would suggest that the SMBH growth is less efficient in the MW, implying a limited SMBH mass accretion; consequently, the lower feedback from the SMBH would allow for more efficient *in situ* star formation and hence a larger final NSC mass. On the other hand, a smaller doubling time for the SMBH is needed for M31, therefore the SMBH would accrete much more efficiently. The feedback from the SMBH would then limit star formation in the NSC, resulting in a smaller fraction of *in situ* star formation (as shown in smaller $f_{NSCvalue}$ values).

Our prescription allows us to determine the total gas mass accreted to the SMBH and the total amount of gas initially present in the central region of the galaxy. Indeed, the gas accreted on the SMBH is $4.2 \times 10^6\ M_\odot$ for the MW, meanwhile the stellar mass formed in the NSC is $1.3 \times 10^7\ M_\odot$. Assuming a star formation efficiency of $SFE = 0.333$, the total amount of gas initially present in the NSC is $8.0 \times 10^7\ M_\odot$ for the MW (assuming an accretion rate being 10% of the Eddington limit). Similarly, for

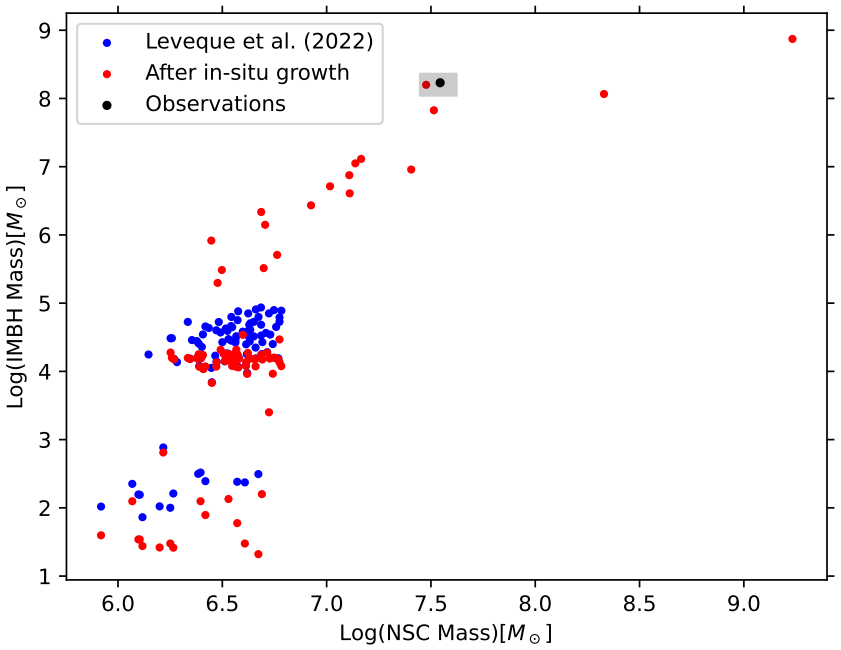

FIGURE 6.2: SMBH mass versus the NSC mass reported in our simulations for M31. The results with and without the NSC/IMBH mass growth seed are reported in red and in blue, respectively. In black, the observed properties of the MW are shown with the observed errors represented by the grey box.

M31 we found that the gas accreted on the SMBH is $1.6 \times 10^8\, M_\odot$ and the total mass of stars formed in the NSC is $2.5 \times 10^7\, M_\odot$. This implies a total amount of gas in the NSC being $1.1 \times 10^9\, M_\odot$.

Chapter 7

Conclusion

We developed a new machinery that combines the results from the MOCCA-Survey Database I with the semi-analytical MASinGA code to reproduce the observational properties of GC populations around galaxies. We compared the results obtained by our machinery with the MW and M31 GC populations, and investigated the NSC and SMBH mass build-up, as well as the BH distribution for such populations. A good agreement of the GCs' global properties between our models and the observed ones around the MW and M31 galaxies have been found in our work. This provides strong arguments and confidence that the developed machinery is working properly. The main results are summarized in the points below:

- A significant portion of the GC population is observed within a galactocentric distance of 5 kpc, with our models reproducing the spatial distributions for the GC populations of the MW and M31 galaxies. The central regions of the galaxies exhibit a significant increase in the observed mass profile of the GC populations, which is not fully covered in our simulations and is likely caused by the various metallicities in these regions (which was actually not investigated in our models). Also, most GCs are rather compact and have a half mass radius less than 4 pc, as shown in both observations and simulations. Finally, the kinematic properties of the MW population found in our models are in agreement with observations.

- Models that contain a BHS have bigger average GC masses and half-light radii than Standard and IMBH models. The number of IMBH and BHS is comparable to the number of Standard models at larger galactocentric distances, but Standard models are more prevalent in the galaxy's center area.

- The orbital parameters for the merged binaries bear the mark of primordial or dynamically produced binary BHs. In fact, our models show that dynamically generated binaries have higher mass ratios and more eccentric orbits, and larger semi-major axes than those of the primordial binaries.

- Depending on the adopted assumptions for the galactic density in the local Universe, we inferred a merger rate for BH binaries in the local Universe of $1.0 - 23\ \mathrm{yr}^{-1}\,\mathrm{Gpc}^{-3}$. Although our results are on the lower side in comparison with other works, they are still comparable. These differences can be accounted for by a smaller sub-sample of the entire GC population that has been taken into account and simulated by our machinery.

- Our models show that the observable binary BHs at 12 Gyr exhibit different orbital properties at different galactocentric distances. At smaller galactocentric distances, the binary BHs do exhibit thermal eccentricity, a higher mass ratio, and smaller semi-major axes. Denser GCs in the central region, which enhance

the number of strong interactions between the binary BHs and the other stars in the GCs, can explain this spatial distribution.

- With values of $\sim 1-3\times10^5\ M_\odot/Gyr$ for both the MW and M31, the mass accretion rate into the NSC in the galactic center seems to be constant over time. However, the final NSC and SMBH masses we estimated from our simulations are a few orders of magnitude lower than the values observed. These differences do indicate that the formation of an initial accreted mass and the interactions and mergers with infalling GCs must be combined in order to adequately explain the NSC and SMBH mass build-up.

- The majority of the BHs and binary BHs which are delivered to the NSC arrive within the first $1-2$ Gyr of its evolution, with a moderate increase at late times. Moreover, only 5% of the total delivered BH population delivered are found in BH binaries. Indeed, we found that over the course of 12 Gyr, a total of 1000–3000 BHs and 100–200 BH-BH binaries have been delivered into the nucleus. This suggests that there are $N_{BHs} = (1.4-2.2)\times10^4$ BHs and $N_{BBHs} = 700-1,100$ binaries BHs lurking in NSCs.

In the future, we plan on using the results from the MOCCA-Survey Database II, with the most updated stellar evolution prescriptions and new features (such as an initial embedded gas phase and multiple stellar populations). We have already started implementing some of these updates to the code. Finally, we plan on applying our machinery to the external galaxies in the local Universe, and provide more insights on the compact object populations, compact object mergers, the NSC and SMBH mass growth evolution, and the spatial distribution for different evolutionary GC histories in future works.

Bibliography

Ahumada, J. A. (Jan. 2005). "CCD photometry of the open clusters NGC 2627, NGC 5617, Pismis 7, and Ruprecht 75". In: *Astronomische Nachrichten* 326.1, pp. 3–18. DOI: 10.1002/asna.200310257.

Antonini, Fabio et al. (May 2012). "Dissipationless Formation and Evolution of the Milky Way Nuclear Star Cluster". In: *ApJ* 750.2, 111, p. 111. DOI: 10.1088/0004-637X/750/2/111. arXiv: 1110.5937 [astro-ph.GA].

Arca-Sedda, M. and R. Capuzzo-Dolcetta (Apr. 2014a). "Dynamical Friction in Cuspy Galaxies". In: *ApJ* 785.1, 51, p. 51. DOI: 10.1088/0004-637X/785/1/51. arXiv: 1307.5717 [astro-ph.CO].

— (Nov. 2014b). "The globular cluster migratory origin of nuclear star clusters". In: *MNRAS* 444.4, pp. 3738–3755. DOI: 10.1093/mnras/stu1683. arXiv: 1405.7593 [astro-ph.GA].

Arca-Sedda, M. et al. (June 2015). "Henize 2-10: The Ongoing Formation of a Nuclear Star Cluster around a Massive Black Hole". In: *ApJ* 806.2, 220, p. 220. DOI: 10.1088/0004-637X/806/2/220. arXiv: 1501.04567 [astro-ph.GA].

Arca-Sedda, Manuel (Dec. 2022). "Formation and evolution of dense star clusters and nuclear clusters in galaxies: implications for NS-NS and BH-BH binary mergers". In: *In prep.*

Ashman, Keith M. and Stephen E. Zepf (1992). "The Formation of Globular Clusters in Merging and Interacting Galaxies". In: *ApJ* 384, p. 50. DOI: 10.1086/170850.

Askar, Abbas, Melvyn B. Davies, and Ross P. Church (Apr. 2021a). "Formation of supermassive black holes in galactic nuclei - I. Delivering seed intermediate-mass black holes in massive stellar clusters". In: *MNRAS* 502.2, pp. 2682–2700. DOI: 10.1093/mnras/stab113. arXiv: 2006.04922 [astro-ph.GA].

— (July 2021b). "Formation of supermassive black holes in galactic nuclei II: retention and growth of seed intermediate-mass black holes". In: *arXiv e-prints*, arXiv:2107.10862, arXiv:2107.10862. arXiv: 2107.10862 [astro-ph.GA].

Askar, Abbas et al. (2017). "MOCCA-SURVEY Database - I. Coalescing binary black holes originating from globular clusters". In: *MNRAS* 464.1, pp. L36–L40. DOI: 10.1093/mnrasl/slw177. arXiv: 1608.02520 [astro-ph.HE].

Bajkova, A. T. et al. (May 2020). "Milky Way Subsystems from Globular Cluster Kinematics Using Gaia DR2 and HST Data". In: *ApJ* 895.1, 69, p. 69. DOI: 10.3847/1538-4357/ab8ea7. arXiv: 2004.13597 [astro-ph.GA].

Bastian, Nate and Carmela Lardo (Sept. 2018). "Multiple Stellar Populations in Globular Clusters". In: *ARA&A* 56, pp. 83–136. DOI: 10.1146/annurev-astro-081817-051839. arXiv: 1712.01286 [astro-ph.SR].

Beasley, Michael A. (2020). "Globular Cluster Systems and Galaxy Formation". In: *Reviews in Frontiers of Modern Astrophysics; From Space Debris to Cosmology*, pp. 245–277. DOI: 10.1007/978-3-030-38509-5_9.

Bekki, K. (July 2007). "The Formation of Stellar Galactic Nuclei through Dissipative Gas Dynamics". In: *Publ. Astron. Soc. Australia* 24.2, pp. 77–94. DOI: 10.1071/AS07008.

Belczynski, K. et al. (Oct. 2016). "The effect of pair-instability mass loss on black-hole mergers". In: *A&A* 594, A97, A97. DOI: 10.1051/0004-6361/201628980. arXiv: 1607.03116 [astro-ph.HE].

Belczynski, Krzysztof et al. (May 2010). "On the Maximum Mass of Stellar Black Holes". In: *ApJ* 714.2, pp. 1217–1226. DOI: 10.1088/0004-637X/714/2/1217. arXiv: 0904.2784 [astro-ph.SR].

Bender, Ralf et al. (Sept. 2005). "HST STIS Spectroscopy of the Triple Nucleus of M31: Two Nested Disks in Keplerian Rotation around a Supermassive Black Hole". In: *ApJ* 631.1, pp. 280–300. DOI: 10.1086/432434. arXiv: astro-ph/0509839 [astro-ph].

Brodie, Jean P. and Jay Strader (2006). "Extragalactic Globular Clusters and Galaxy Formation". In: *ARA&A* 44.1, pp. 193–267. DOI: 10.1146/annurev.astro.44.051905.092441. arXiv: astro-ph/0602601 [astro-ph].

Cai, Maxwell Xu et al. (Jan. 2016). "Evolution of star clusters on eccentric orbits". In: *MNRAS* 455.1, pp. 596–602. DOI: 10.1093/mnras/stv2325. arXiv: 1510.01337 [astro-ph.GA].

Calura, F. et al. (Nov. 2019). "Formation of second-generation stars in globular clusters". In: *MNRAS* 489.3, pp. 3269–3284. DOI: 10.1093/mnras/stz2055. arXiv: 1906.09137 [astro-ph.SR].

Cantiello, Michele and John P. Blakeslee (Nov. 2007). "On the Metallicity-Color Relations and Bimodal Color Distributions in Extragalactic Globular Cluster Systems". In: *ApJ* 669.2, pp. 982–989. DOI: 10.1086/522110. arXiv: 0709.1073 [astro-ph].

Cantiello, Michele et al. (Apr. 2018). "VEGAS-SSS. II. Comparing the globular cluster systems in NGC 3115 and NGC 1399 using VEGAS and FDS survey data. The quest for a common genetic heritage of globular cluster systems". In: *A&A* 611, A93, A93. DOI: 10.1051/0004-6361/201730649. arXiv: 1711.00750 [astro-ph.GA].

Cantiello, Michele et al. (May 2020). "The Fornax Deep Survey with VST. X. The catalog of sources in the FDS area, with an example study for globular clusters and background galaxies". In: *arXiv e-prints*, arXiv:2005.12085, arXiv:2005.12085. arXiv: 2005.12085 [astro-ph.GA].

Capuzzo-Dolcetta, R. and A. Mastrobuono-Battisti (Nov. 2009). "Globular cluster system erosion in elliptical galaxies". In: *A&A* 507.1, pp. 183–193. DOI: 10.1051/0004-6361/200912255. arXiv: 0904.0526 [astro-ph.CO].

Capuzzo-Dolcetta, Roberto (Oct. 1993). "The Evolution of the Globular Cluster System in a Triaxial Galaxy: Can a Galactic Nucleus Form by Globular Cluster Capture?" In: *ApJ* 415, p. 616. DOI: 10.1086/173189. arXiv: astro-ph/9301006 [astro-ph].

Chatzopoulos, S. et al. (Feb. 2015). "The old nuclear star cluster in the Milky Way: dynamics, mass, statistical parallax, and black hole mass". In: *MNRAS* 447.1, pp. 948–968. DOI: 10.1093/mnras/stu2452. arXiv: 1403.5266 [astro-ph.GA].

Colpi, Monica, Lucio Mayer, and Fabio Governato (Nov. 1999). "Dynamical Friction and the Evolution of Satellites in Virialized Halos: The Theory of Linear Response". In: *ApJ* 525.2, pp. 720–733. DOI: 10.1086/307952. arXiv: astro-ph/9907088 [astro-ph].

Côté, Patrick et al. (2004). "The ACS Virgo Cluster Survey. I. Introduction to the Survey". In: *ApJS* 153.1, pp. 223–242. DOI: 10.1086/421490. arXiv: astro-ph/0404138 [astro-ph].

D'Abrusco, R. et al. (Mar. 2016). "The Extended Spatial Distribution of Globular Clusters in the Core of the Fornax Cluster". In: *ApJ* 819.2, L31, p. L31. DOI: 10.3847/2041-8205/819/2/L31. arXiv: 1602.06076 [astro-ph.GA].

Dalessandro, Emanuele et al. (Sept. 2021). "3D core kinematics of NGC 6362: central rotation in a dynamically evolved globular cluster". In: *MNRAS* 506.1, pp. 813–823. DOI: 10.1093/mnras/stab1257. arXiv: 2105.02246 [astro-ph.GA].

Dehnen, W. (Nov. 1993). "A Family of Potential-Density Pairs for Spherical Galaxies and Bulges". In: *MNRAS* 265, p. 250. DOI: 10.1093/mnras/265.1.250.

D'Ercole, Annibale et al. (Dec. 2008). "Formation and dynamical evolution of multiple stellar generations in globular clusters". In: *MNRAS* 391.2, pp. 825–843. DOI: 10.1111/j.1365-2966.2008.13915.x. arXiv: 0809.1438 [astro-ph].

Emsellem, Eric (Aug. 2013). "Is the black hole in NGC 1277 really overmassive?" In: *MNRAS* 433.3, pp. 1862–1870. DOI: 10.1093/mnras/stt840. arXiv: 1305.3630 [astro-ph.CO].

Forbes, Duncan A., Jean P. Brodie, and Carl J. Grillmair (1997). "On the Origin of Globular Clusters in Elliptical and cD Galaxies". In: *AJ* 113, p. 1652. DOI: 10.1086/118382. arXiv: astro-ph/9702146 [astro-ph].

Forbes, Duncan A., Jean P. Brodie, and Søren S. Larsen (Aug. 2001). "Bulge Globular Clusters in Spiral Galaxies". In: *ApJ* 556.2, pp. L83–L86. DOI: 10.1086/323006. arXiv: astro-ph/0106459 [astro-ph].

Fregeau, J. M. et al. (2004). "Stellar collisions during binary-binary and binary-single star interactions". In: *MNRAS* 352.1, pp. 1–19. DOI: 10.1111/j.1365-2966.2004.07914.x. arXiv: astro-ph/0401004 [astro-ph].

Freitag, M. and W. Benz (Aug. 2001). "A new Monte Carlo code for star cluster simulations. I. Relaxation". In: *A&A* 375, pp. 711–738. DOI: 10.1051/0004-6361:20010706. arXiv: astro-ph/0102139 [astro-ph].

Fryer, Chris L. et al. (Apr. 2012). "Compact Remnant Mass Function: Dependence on the Explosion Mechanism and Metallicity". In: *ApJ* 749.1, 91, p. 91. DOI: 10.1088/0004-637X/749/1/91. arXiv: 1110.1726 [astro-ph.SR].

Fujii, M. S. and S. Portegies Zwart (Mar. 2014). "The moment of core collapse in star clusters with a mass function". In: *MNRAS* 439.1, pp. 1003–1014. DOI: 10.1093/mnras/stu015. arXiv: 1304.1550 [astro-ph.GA].

Fukushige, T. and D. C. Heggie (2000). "The time-scale of escape from star clusters". In: *MNRAS* 318.3, pp. 753–761. DOI: 10.1046/j.1365-8711.2000.03811.x. arXiv: astro-ph/9910468 [astro-ph].

Georgiev, Iskren Y. et al. (Apr. 2016). "Masses and scaling relations for nuclear star clusters, and their co-existence with central black holes". In: *MNRAS* 457.2, pp. 2122–2138. DOI: 10.1093/mnras/stw093. arXiv: 1601.02613 [astro-ph.GA].

Gessner, Alexandra and Hans-Thomas Janka (Sept. 2018). "Hydrodynamical Neutron-star Kicks in Electron-capture Supernovae and Implications for the CRAB Supernova". In: *ApJ* 865.1, 61, p. 61. DOI: 10.3847/1538-4357/aadbae. arXiv: 1802.05274 [astro-ph.HE].

Gieles, Mark et al. (Aug. 2018). "Concurrent formation of supermassive stars and globular clusters: implications for early self-enrichment". In: *MNRAS* 478.2, pp. 2461–2479. DOI: 10.1093/mnras/sty1059. arXiv: 1804.04682 [astro-ph.GA].

Giersz, M. (Jan. 2001). "Monte Carlo Simulations of Star Clusters". In: *Dynamics of Star Clusters and the Milky Way*. Ed. by S. Deiters et al. Vol. 228. Astronomical Society of the Pacific Conference Series, p. 61. arXiv: astro-ph/0006438 [astro-ph].

Giersz, M. et al. (Aug. 2019). "MOCCA survey data base- I. Dissolution of tidally filling star clusters harbouring black hole subsystems". In: *MNRAS* 487.2, pp. 2412–2423. DOI: 10.1093/mnras/stz1460. arXiv: 1904.01227 [astro-ph.GA].

Giersz, Mirek (Aug. 1998). "Monte Carlo simulations of star clusters - I. First Results". In: *MNRAS* 298.4, pp. 1239–1248. DOI: 10.1046/j.1365-8711.1998.01734.x. arXiv: astro-ph/9804127 [astro-ph].

Giersz, Mirek and Douglas C. Heggie (Apr. 1996). "Statistics of N-body simulations - III. Unequal masses". In: *MNRAS* 279.3, pp. 1037–1056. DOI: 10.1093/mnras/279.3.1037. arXiv: astro-ph/9506143 [astro-ph].

Giersz, Mirek, Douglas C. Heggie, and Jarrod R. Hurley (July 2008). "Monte Carlo simulations of star clusters - IV. Calibration of the Monte Carlo code and comparison with observations for the open cluster M67". In: *MNRAS* 388.1, pp. 429–443. DOI: 10.1111/j.1365-2966.2008.13407.x. arXiv: 0801.3968 [astro-ph].

Giersz, Mirek et al. (May 2013). "MOCCA code for star cluster simulations - II. Comparison with N-body simulations". In: *MNRAS* 431.3, pp. 2184–2199. DOI: 10.1093/mnras/stt307. arXiv: 1112.6246 [astro-ph.GA].

Gnedin, Oleg Y. and Jeremiah P. Ostriker (Jan. 1997). "Destruction of the Galactic Globular Cluster System". In: *ApJ* 474.1, pp. 223–255. DOI: 10.1086/303441. arXiv: astro-ph/9603042 [astro-ph].

Gnedin, Oleg Y., Jeremiah P. Ostriker, and Scott Tremaine (Apr. 2014). "Co-evolution of Galactic Nuclei and Globular Cluster Systems". In: *ApJ* 785.1, 71, p. 71. DOI: 10.1088/0004-637X/785/1/71. arXiv: 1308.0021 [astro-ph.CO].

Grudić, Michael Y. et al. (Mar. 2022). "Great Balls of FIRE I: The formation of star clusters across cosmic time in a Milky Way-mass galaxy". In: *arXiv e-prints*, arXiv:2203.05732, arXiv:2203.05732. arXiv: 2203.05732 [astro-ph.GA].

Guillard, Nicolas, Eric Emsellem, and Florent Renaud (Oct. 2016). "New insights on the formation of nuclear star clusters". In: *MNRAS* 461.4, pp. 3620–3629. DOI: 10.1093/mnras/stw1570. arXiv: 1606.09537 [astro-ph.GA].

Harris, Gretchen L. H., William E. Harris, and Gregory B. Poole (Feb. 1999). "The Metallicity Distribution in the Halo Stars of NGC 5128: Implications for Galaxy Formation". In: *AJ* 117.2, pp. 855–867. DOI: 10.1086/300749. arXiv: astro-ph/9810134 [astro-ph].

Harris, William E. (1996). "A Catalog of Parameters for Globular Clusters in the Milky Way". In: *AJ* 112, p. 1487. DOI: 10.1086/118116.

Harris, William E., Gretchen L. H. Harris, and Matthew Alessi (Aug. 2013). "A Catalog of Globular Cluster Systems: What Determines the Size of a Galaxy's Globular Cluster Population?" In: *ApJ* 772.2, 82, p. 82. DOI: 10.1088/0004-637X/772/2/82. arXiv: 1306.2247 [astro-ph.GA].

Harris, William E. et al. (Jan. 2006). "Globular Cluster Systems in Brightest Cluster Galaxies: Bimodal Metallicity Distributions and the Nature of the High-Luminosity Clusters". In: *ApJ* 636.1, pp. 90–114. DOI: 10.1086/498058. arXiv: astro-ph/0508195 [astro-ph].

Heger, A. and S. E. Woosley (Mar. 2002). "The Nucleosynthetic Signature of Population III". In: *ApJ* 567.1, pp. 532–543. DOI: 10.1086/338487. arXiv: astro-ph/0107037 [astro-ph].

Heggie, D. C. (Dec. 1975). "Binary evolution in stellar dynamics." In: *MNRAS* 173, pp. 729–787. DOI: 10.1093/mnras/173.3.729.

Heggie, Douglas and Piet Hut (2003). *The Gravitational Million-Body Problem: A Multidisciplinary Approach to Star Cluster Dynamics*.

Hénault-Brunet, V. et al. (June 2015). "Multiple populations in globular clusters: the distinct kinematic imprints of different formation scenarios". In: *MNRAS* 450.2, pp. 1164–1198. DOI: 10.1093/mnras/stv675. arXiv: 1503.07532 [astro-ph.GA].

Hénon, M. H. (1971). "The Monte Carlo Method (Papers appear in the Proceedings of IAU Colloquium No. 10 Gravitational N-Body Problem (ed. by Myron Lecar), R. Reidel Publ. Co. , Dordrecht-Holland.)" In: *Ap&SS* 14.1, pp. 151–167. DOI: 10.1007/BF00649201.

Hills, J. G. (Oct. 1975). "Encounters between binary and single stars and their effect on the dynamical evolution of stellar systems." In: *AJ* 80, pp. 809–825. DOI: 10.1086/111815.

Hurley, Jarrod R., Onno R. Pols, and Christopher A. Tout (2000). "Comprehensive analytic formulae for stellar evolution as a function of mass and metallicity". In: *MNRAS* 315.3, pp. 543–569. DOI: 10.1046/j.1365-8711.2000.03426.x. arXiv: astro-ph/0001295 [astro-ph].

Hurley, Jarrod R., Christopher A. Tout, and Onno R. Pols (2002). "Evolution of binary stars and the effect of tides on binary populations". In: *MNRAS* 329.4, pp. 897–928. DOI: 10.1046/j.1365-8711.2002.05038.x. arXiv: astro-ph/0201220 [astro-ph].

Hypki, Arkadiusz and Mirek Giersz (2013). "MOCCA code for star cluster simulations - I. Blue stragglers, first results". In: *MNRAS* 429.2, pp. 1221–1243. DOI: 10.1093/mnras/sts415. arXiv: 1207.6700 [astro-ph.GA].

Jordán, Andrés et al. (2005). "The ACS Virgo Cluster Survey. X. Half-Light Radii of Globular Clusters in Early-Type Galaxies: Environmental Dependencies and a Standard Ruler for Distance Estimation". In: *ApJ* 634.2, pp. 1002–1019. DOI: 10.1086/497092. arXiv: astro-ph/0508219 [astro-ph].

Joshi, Kriten J., Frederic A. Rasio, and Simon Portegies Zwart (Sept. 2000). "Monte Carlo Simulations of Globular Cluster Evolution. I. Method and Test Calculations". In: *ApJ* 540.2, pp. 969–982. DOI: 10.1086/309350. arXiv: astro-ph/9909115 [astro-ph].

Kamlah, A. W. H. et al. (Apr. 2022). "Preparing the next gravitational million-body simulations: evolution of single and binary stars in NBODY6++GPU, MOCCA, and MCLUSTER". In: *MNRAS* 511.3, pp. 4060–4089. DOI: 10.1093/mnras/stab3748. arXiv: 2105.08067 [astro-ph.GA].

King, Ivan (Oct. 1962). "The structure of star clusters. I. an empirical density law". In: *AJ* 67, p. 471. DOI: 10.1086/108756.

King, Ivan R. (1966). "The structure of star clusters. IV. Photoelectric surface photometry in nine globular clusters". In: *AJ* 71, p. 276. DOI: 10.1086/109918.

Kissler-Patig, M. et al. (Mar. 1997). "Globular cluster systems of early-type galaxies in Fornax." In: *A&A* 319, pp. 470–480. arXiv: astro-ph/9608082 [astro-ph].

Knigge, C. (Jan. 2012). "Cataclysmic variables in globular clusters." In: *Mem. Soc. Astron. Italiana* 83, p. 549. arXiv: 1112.1074 [astro-ph.SR].

Knigge, Christian (Jan. 2015). "Blue Stragglers in Globular Clusters: Observations, Statistics and Physics". In: *Astrophysics and Space Science Library*. Ed. by Henri M. J. Boffin, Giovanni Carraro, and Giacomo Beccari. Vol. 413. Astrophysics and Space Science Library, p. 295. DOI: 10.1007/978-3-662-44434-4_13. arXiv: 1406.3493 [astro-ph.SR].

Kormendy, John and Luis C. Ho (Aug. 2013). "Coevolution (Or Not) of Supermassive Black Holes and Host Galaxies: Supplemental Material". In: *arXiv e-prints*, arXiv:1308.6483, arXiv:1308.6483. arXiv: 1308.6483 [astro-ph.CO].

Korn, A. J. (Jan. 2020). "How stars in globular clusters reveal the depletion of the Spite plateau of lithium." In: *Mem. Soc. Astron. Italiana* 91, p. 105. arXiv: 2111.00913 [astro-ph.SR].

Kremer, Kyle et al. (Apr. 2020). "Modeling Dense Star Clusters in the Milky Way and Beyond with the CMC Cluster Catalog". In: *ApJS* 247.2, 48, p. 48. DOI: 10.3847/1538-4365/ab7919. arXiv: 1911.00018 [astro-ph.HE].

Kundu, Arunav and Bradley C. Whitmore (2001). "New Insights from HST Studies of Globular Cluster Systems. I. Colors, Distances, and Specific Frequencies of

28 Elliptical Galaxies". In: *AJ* 121.6, pp. 2950–2973. DOI: 10.1086/321073. arXiv: astro-ph/0103021 [astro-ph].

Küpper, Andreas H. W. et al. (Nov. 2011). "Mass segregation and fractal substructure in young massive clusters - I. The McLuster code and method calibration". In: *MNRAS* 417.3, pp. 2300–2317. DOI: 10.1111/j.1365-2966.2011.19412.x. arXiv: 1107.2395 [astro-ph.GA].

Larsen, Søren S. et al. (2001). "Properties of Globular Cluster Systems in Nearby Early-Type Galaxies". In: *AJ* 121.6, pp. 2974–2998. DOI: 10.1086/321081. arXiv: astro-ph/0102374 [astro-ph].

Lauer, T. R. et al. (Oct. 1993). "Planetary Camera Observations of the Double Nucleus of M31". In: *AJ* 106, p. 1436. DOI: 10.1086/116737.

Leveque, A., M. Giersz, and M. Paolillo (Mar. 2021). "MOCCA Survey Database: extra Galactic globular clusters. I. Method and first results". In: *MNRAS* 501.4, pp. 5212–5228. DOI: 10.1093/mnras/staa4027. arXiv: 2006.05887 [astro-ph.GA].

Leveque, A. et al. (Aug. 2022a). "A Monte Carlo study of early gas expulsion and evolution of star clusters: new simulations with the MOCCA code in the AMUSE framework". In: *MNRAS* 514.4, pp. 5739–5750. DOI: 10.1093/mnras/stac1690. arXiv: 2206.03404 [astro-ph.GA].

Leveque, A. et al. (Aug. 2022b). "MOCCA-survey data base: extra galactic globular clusters - II. Milky Way and Andromeda". In: *MNRAS* 514.4, pp. 5751–5766. DOI: 10.1093/mnras/stac1694. arXiv: 2206.03967 [astro-ph.GA].

Leveque, A. et al. (Dec. 2022c). "MOCCA-survey data base: extra galactic globular clusters - III. The population of black holes in Milky Way and Andromeda - like galaxies". In: *In prep.*

Loose, H. H., E. Kruegel, and A. Tutukov (Jan. 1982). "Bursts of star formation in the galactic centre". In: *A&A* 105.2, pp. 342–350.

Lovisi, L. et al. (Aug. 2012). "Chemical and Kinematical Properties of Blue Straggler Stars and Horizontal Branch Stars in NGC 6397". In: *ApJ* 754.2, 91, p. 91. DOI: 10.1088/0004-637X/754/2/91. arXiv: 1205.5561 [astro-ph.SR].

Lucatello, S. et al. (Dec. 2015). "The incidence of binaries in globular cluster stellar populations". In: *A&A* 584, A52, A52. DOI: 10.1051/0004-6361/201526957. arXiv: 1509.05014 [astro-ph.SR].

Madau, Piero, Francesco Haardt, and Massimo Dotti (Apr. 2014). "Super-critical Growth of Massive Black Holes from Stellar-mass Seeds". In: *ApJ* 784.2, L38, p. L38. DOI: 10.1088/2041-8205/784/2/L38. arXiv: 1402.6995 [astro-ph.CO].

Madrid, Juan P. et al. (Sept. 2017). "Mass evaporation rate of globular clusters in a strong tidal field". In: *MNRAS* 470.2, pp. 1729–1737. DOI: 10.1093/mnras/stx1350. arXiv: 1706.06635 [astro-ph.GA].

Manchester, R. N. et al. (Apr. 2005). "The Australia Telescope National Facility Pulsar Catalogue". In: *AJ* 129.4, pp. 1993–2006. DOI: 10.1086/428488. arXiv: astro-ph/0412641 [astro-ph].

Marks, M. and P. Kroupa (July 2012). "Inverse dynamical population synthesis. Constraining the initial conditions of young stellar clusters by studying their binary populations". In: *A&A* 543, A8, A8. DOI: 10.1051/0004-6361/201118231. arXiv: 1205.1508 [astro-ph.GA].

Martinez-Medina, Luis A. et al. (Aug. 2022). "On the response of a star cluster to a tidal perturbation". In: *MNRAS*. DOI: 10.1093/mnras/stac2225. arXiv: 2009.06643 [astro-ph.GA].

Milone, A. P. et al. (Oct. 2018). "Gaia unveils the kinematics of multiple stellar populations in 47 Tucanae". In: *MNRAS* 479.4, pp. 5005–5011. DOI: 10.1093/mnras/sty1873. arXiv: 1807.03511 [astro-ph.SR].

Milosavljević, Miloš and David Merritt (Dec. 2001). "Formation of Galactic Nuclei". In: *ApJ* 563.1, pp. 34–62. DOI: 10.1086/323830. arXiv: astro-ph/0103350 [astro-ph].

Neumayer, Nadine et al. (May 2011). "Two-dimensional Hα kinematics of bulgeless disc galaxies". In: *MNRAS* 413.3, pp. 1875–1888. DOI: 10.1111/j.1365-2966.2011.18266.x. arXiv: 1101.5154 [astro-ph.CO].

Ostrov, Pablo, Doug Geisler, and Juan C. Forte (May 1993). "The Metallicity Gradient and Distribution Function of Globular Clusters Around NGC 1399". In: *AJ* 105, p. 1762. DOI: 10.1086/116553.

Pattabiraman, Bharath et al. (Feb. 2013). "A Parallel Monte Carlo Code for Simulating Collisional N-body Systems". In: *ApJS* 204.2, 15, p. 15. DOI: 10.1088/0067-0049/204/2/15. arXiv: 1206.5878 [astro-ph.IM].

Peng, Eric W. et al. (2006). "The ACS Virgo Cluster Survey. IX. The Color Distributions of Globular Cluster Systems in Early-Type Galaxies". In: *ApJ* 639.1, pp. 95–119. DOI: 10.1086/498210. arXiv: astro-ph/0509654 [astro-ph].

Plummer, H. C. (Mar. 1911). "On the problem of distribution in globular star clusters". In: *MNRAS* 71, pp. 460–470. DOI: 10.1093/mnras/71.5.460.

Pooley, David (Apr. 2010). "Globular cluster x-ray sources". In: *Proceedings of the National Academy of Science* 107.16, pp. 7164–7167. DOI: 10.1073/pnas.0913903107.

Puzia, Thomas H. et al. (May 2014). "Wide-field Hubble Space Telescope Observations of the Globular Cluster System in NGC 1399". In: *ApJ* 786.2, 78, p. 78. DOI: 10.1088/0004-637X/786/2/78. arXiv: 1402.6714 [astro-ph.GA].

Ransom, Scott M. (May 2008). "Pulsars in Globular Clusters". In: *Dynamical Evolution of Dense Stellar Systems*. Ed. by Enrico Vesperini, Mirek Giersz, and Alison Sills. Vol. 246, pp. 291–300. DOI: 10.1017/S1743921308015810.

Rhode, Katherine L., Stephen E. Zepf, and Michael R. Santos (Sept. 2005). "Metal-poor Globular Clusters and the Formation of Their Host Galaxies". In: *ApJ* 630.1, pp. L21–L24. DOI: 10.1086/491580. arXiv: astro-ph/0507551 [astro-ph].

Rivera Sandoval, L. E. et al. (Apr. 2018). "New cataclysmic variables and other exotic binaries in the globular cluster 47 Tucanae*". In: *MNRAS* 475.4, pp. 4841–4867. DOI: 10.1093/mnras/sty058. arXiv: 1705.07100 [astro-ph.SR].

Rodriguez, Carl L. et al. (Mar. 2022). "Great Balls of FIRE II: The evolution and destruction of star clusters across cosmic time in a Milky Way-mass galaxy". In: *arXiv e-prints*, arXiv:2203.16547, arXiv:2203.16547. arXiv: 2203.16547 [astro-ph.GA].

Sana, H. et al. (July 2012). "Binary Interaction Dominates the Evolution of Massive Stars". In: *Science* 337.6093, p. 444. DOI: 10.1126/science.1223344. arXiv: 1207.6397 [astro-ph.SR].

Schröder, K. P. and M. Cuntz (Sept. 2005). "A New Version of Reimers' Law of Mass Loss Based on a Physical Approach". In: *ApJ* 630.1, pp. L73–L76. DOI: 10.1086/491579. arXiv: astro-ph/0507598 [astro-ph].

Sollima, A. (Apr. 2021). "Monte Carlo simulations of multiple populations in globular clusters: constraints on the cooling flow versus accretion scenario using million bodies simulations". In: *MNRAS* 502.2, pp. 1974–1989. DOI: 10.1093/mnras/stab154. arXiv: 2102.01707 [astro-ph.GA].

Sollima, A. and A. Mastrobuono Battisti (Oct. 2014). "Treatment of realistic tidal field in Monte Carlo simulations of star clusters". In: *MNRAS* 443.4, pp. 3513–3527. DOI: 10.1093/mnras/stu1426. arXiv: 1407.4169 [astro-ph.SR].

Sollima, A. et al. (May 2022). "Monte Carlo simulations of multiple populations in globular clusters: constraints on the initial size of the second generation from binary stars". In: *MNRAS* 512.1, pp. 776–791. DOI: 10.1093/mnras/stac428. arXiv: 2202.12321 [astro-ph.SR].

Spitzer Lyman, Jr. (Jan. 1958). "Disruption of Galactic Clusters." In: *ApJ* 127, p. 17. DOI: 10.1086/146435.

Spitzer, Lyman (1987). *Dynamical evolution of globular clusters*.

Stodółkiewicz, J. S. (1982). "Dynamical evolution of globular clusters. I". In: *Acta Astron.* 32.1-2, pp. 63–91.

— (1986). "Dynamical evolution of globular clusters. II - Binaries Method". In: *Acta Astron.* 36.1, pp. 19–41.

Thévenin, F. et al. (July 2001). "VLT observations of turnoff stars in the globular cluster NGC 6397". In: *A&A* 373, pp. 905–915. DOI: 10.1051/0004-6361:20010672. arXiv: astro-ph/0105166 [astro-ph].

Tremaine, S. D., J. P. Ostriker, and Jr. Spitzer L. (Mar. 1975). "The formation of the nuclei of galaxies. I. M31." In: *ApJ* 196, pp. 407–411. DOI: 10.1086/153422.

Trujillo-Gomez, Sebastian et al. (May 2020). "The kinematics of globular cluster populations in the E-MOSAICS simulations and their implications for the assembly history of the Milky Way". In: *arXiv e-prints*, arXiv:2005.02401, arXiv:2005.02401. arXiv: 2005.02401 [astro-ph.GA].

Urry, C. Megan and Paolo Padovani (Sept. 1995). "Unified Schemes for Radio-Loud Active Galactic Nuclei". In: *PASP* 107, p. 803. DOI: 10.1086/133630. arXiv: astro-ph/9506063 [astro-ph].

van den Bosch, Remco C. E. et al. (Nov. 2012). "An over-massive black hole in the compact lenticular galaxy NGC 1277". In: *Nature* 491.7426, pp. 729–731. DOI: 10.1038/nature11592. arXiv: 1211.6429 [astro-ph.CO].

Vesperini, Enrico et al. (Apr. 2021). "Dynamical evolution of multiple-population globular clusters". In: *MNRAS* 502.3, pp. 4290–4304. DOI: 10.1093/mnras/stab223. arXiv: 2102.01717 [astro-ph.GA].

Vink, Jorick S. and A. de Koter (Oct. 2002). "Predictions of variable mass loss for Luminous Blue Variables". In: *A&A* 393, pp. 543–553. DOI: 10.1051/0004-6361:20021009. arXiv: astro-ph/0207170 [astro-ph].

Vink, Jorick S., A. de Koter, and H. J. G. L. M. Lamers (Apr. 2001). "Mass-loss predictions for O and B stars as a function of metallicity". In: *A&A* 369, pp. 574–588. DOI: 10.1051/0004-6361:20010127. arXiv: astro-ph/0101509 [astro-ph].

Wang, Long et al. (May 2016). "The DRAGON simulations: globular cluster evolution with a million stars". In: *MNRAS* 458.2, pp. 1450–1465. DOI: 10.1093/mnras/stw274. arXiv: 1602.00759 [astro-ph.SR].

Wang, Long et al. (Jan. 2020). "The possible role of stellar mergers for the formation of multiple stellar populations in globular clusters". In: *MNRAS* 491.1, pp. 440–454. DOI: 10.1093/mnras/stz3033. arXiv: 1910.14040 [astro-ph.SR].

Woosley, S. E., S. Blinnikov, and Alexander Heger (Nov. 2007). "Pulsational pair instability as an explanation for the most luminous supernovae". In: *Nature* 450.7168, pp. 390–392. DOI: 10.1038/nature06333. arXiv: 0710.3314 [astro-ph].

Zepf, S. E. and K. M. Ashman (Oct. 1993). "Globular cluster systems formed in galaxy mergers." In: *MNRAS* 264, pp. 611–618. DOI: 10.1093/mnras/264.3.611.